FACILITATING AN INTEGRATED DATA-CENTRIC APPROACH TO OPTIMIZE DONOR-ACCEPTOR COPOLYMER BASED ORGANIC FIELD EFFECT TRANSISTORS

A Dissertation
Presented to
The Academic Faculty

by

Rahul Venkatesh

In Partial Fulfillment
of the Requirements for the Degree
Doctor of Philosophy in the
School of Chemical and Biomolecular Engineering

Georgia Institute of Technology
May 2024

FACILITATING AN INTEGRATED DATA-CENTRIC APPROACH TO OPTIMIZE DONOR-ACCEPTOR COPOLYMER BASED ORGANIC FIELD EFFECT TRANSISTORS

Approved by:

Dr. Martha Grover, Advisor
School of Chemical and Biomolecular Engineering
Georgia Institute of Technology

Dr. Andrew J. Medford
School of Chemical and Biomolecular Engineering
Georgia Institute of Technology

Dr. Carson Meredith, Advisor
School of Chemical and Biomolecular Engineering
Georgia Institute of Technology

Dr. Chad Risko
School of Chemistry
Georgia Institute of Technology

Dr. Elsa Reichmanis, Advisor
School of Chemical and Biomolecular Engineering
Lehigh University

Dr. Carlos Silva
School of Chemistry
University of Montreal

Date Approved: April 9th, 2024

To my parents, Venkatesh Ramamoorthy and Rajalakshmi Venkatesh, without whom none of this would have been possible

ACKNOWLEDGEMENTS

I would like to express my heartfelt gratitude to my parents, Venkatesh Ramamoorthy and Rajalakshmi Venkatesh, for their unwavering support and sacrifices. Their decision to send me to the United States nine years ago to pursue my dreams has been the cornerstone of my academic journey, and I hope to have made them proud. Special thanks go to my sister, Riya Venkatesh, for her constant help and support. We have shared both the challenges and joys of this journey, making it all the more meaningful.

I extend my deepest appreciation to my advisors, Dr. Martha Grover, Dr. Carson Meredith, and Dr. Elsa Reichmanis. Their guidance and support over the past five years, both in research and professional endeavors, have been invaluable. Additionally, I would like to thank them for nominating me for the fellowships I received over the last few years. I am especially grateful to Martha for her instrumental role in securing my first internship as a data scientist at Dow Chemicals.

I am indebted to my committee members, Dr. Chad Risko, Dr. AJ Medford, and Dr. Carlos Silva, for their availability and valuable advice in their respective areas of expertise. The National Science Foundation deserves special acknowledgment for funding my research over the last five years.

A heartfelt thanks goes out to Dr. Aaron Liu, Dr. Miguel Gonzalez, and Dr.Yulong Zheng for being outstanding lab brothers, mentors, and colleagues. Dr. Aaron was crucial to me being selected for this project and collaboration as he provided the advisors with good feedback based on our first interaction prior to advisor selection. Since then, we have

been inseparable, whether Dr. Aaron Liu liked it or not. We have worked together on several projects and publications, and without his help and support, completing this degree would have been so much more challenging. He provided me with valuable advice outside of research as well, be it financial advice or relationship advice, as well as professional advice. Dr. Miguel Gonzalez was the most positive presence in the office, always motivating me to be the best version of myself and helping me improve my professional skills. It was so much fun to discuss soccer and talk about our clubs that were rivals. Even though he would occasionally take digs at me and call it "tough love," I am truly grateful for him. Dr. Yulong Zheng was the first person I collaborated with and was instrumental in my first publication. Over the last few years, we have collaborated on several projects together, and he was the most patient colleague I have worked with, always available to get on a call and deal with my plethora of questions to which I am very grateful. Their guidance and collaboration have significantly impacted both my professional and personal growth. I would also like to express my gratitude to Dr. Connor Callaway for his crucial contributions to our collaborative project.

I am thankful to Jessica Bonsu, Myeongyeon Lee, and Mengting Sun, whom I had the pleasure of mentoring. This experience has significantly enhanced my leadership skills. Appreciation is also extended to Haoqun Zhao, Caiyi Xiang, Shubham More, Jeffrey Deng, and Emmanuel Bradford for their outstanding contributions as undergraduate students, helping me develop into a better mentor.

Special thanks to Dr. Brian Khau, Dr. Audrey Schulz, and Dr. Caria Evans for mentoring me in the earlier stages of my academic journey, providing essential guidance and training in lab techniques.

I am fortunate to have been part of three labs, and I express my gratitude to Dr. Rupanjali Guruprasad, Steven Crouse, Viviana Cardenas, Dr. Patrick Harris, Dr. Colton Lagerman, Javaz Rolle, Tanner Hickman, Jonathon Rhone, Dr. Yue Li, and Zeyuan Sun for their collaboration and camaraderie.

During my internship at Dow Chemicals as a data science intern, I would like to thank my manager, Mr. Fabio Aguirre, and my mentor, Dr. Sukrit Mukopadhyay, for their instrumental role in developing my professional and data science skills.

Gratitude is extended to my roommates and best friends, Prasad Milner, Nishant Deshmuk, Dr. Rohan Murty, and Tom Piccolo, for their unwavering support and unique contributions to both my personal and professional growth. Prasad imparted invaluable lessons on the importance of living in the present and finding joy in life's little moments. Nishant guided me towards humility and honed my skills as a better listener. Rohan played a pivotal role in refining my interviewing skills, ultimately contributing to my success in securing my first job. Additionally, Tom enhanced my expertise in my cherished pastime of fishing and remained a steadfast presence, offering a listening ear whenever I needed to share my thoughts and concerns. I would also like to express my heartfelt gratitude to my girlfriend, Madeline Lewis, for her unwavering support, patience, and encouragement throughout the completion of this thesis. Her belief in me and her understanding during the

challenging times have been a constant source of strength and inspiration. I am deeply thankful for her presence in my life.

As I reflect on the importance of physical health in recent years, I want to specially thank my workout buddies, Andreas, Biya, and Jonathan, who have been my training companions for marathons and triathlons, pushing me to achieve more.

Last but not least, I want to express my appreciation to all the friends, including Sabrina, Valerie, Dylan, Alexa, Matt, Rachel, Alex, Kunal, Ashley, and Violet, who have been a crucial part of my life during these five years. Their friendship has made the challenges of the Ph.D. journey more bearable, and I will cherish these memories forever.

I would also like to express my gratitude to ChatGPT for its invaluable assistance throughout the process of refining the text in this thesis and providing guidance with Python code. Its capabilities have been instrumental in enhancing the quality of this thesis.

TABLE OF CONTENTS

LIST OF TABLES

LIST OF FIGURES

LIST OF SYMBOLS AND ABBREVIATIONS

AFM	Atomic Force Microscopy
BDOPV	Benzodifuran-dione oligo(p-phenylene vinylene)
BGBC	Bottom-Gate/Bottom-Contact
CB	Chlorobenzene
CP	Conjugated Polymer
CPOM	Cross-Polarized Optical Microscopy
C_i	Capacitance Per Area of the Dielectric
C*	Critical Chain Overlap
D-A	Donor-Acceptor
DPP	Diketopyrrolopyrrole
DPP-DTT	Poly[2,5-(2-octyldodecyl)-3,6-diketopyrrolopyrrole-alt-5,5-(2,5-di(thien-2-yl)thieno [3,2-b]thiophene)]
DPPT-TT	Poly[3,6-di-2-thienyl-pyrrolo[3,4-c]pyrrole-1,4-dione-alt-thieno[3,2-b]thiophene]
DLS	Dynamic Light Scattering
$E_{a,CT}$	Energy of Activation for Charge Transport
F_r	Non-Uniformity of Data Density
G	Paracrystalline Order
GIWAXS	Grazing Incidence Wide Angle X-ray Scattering
HT	High-Throughput
HTE	High-Throughput Experimentation
I_D	Drain Current
MGC	Meniscus-Guided Coating

ML	Machine Learning
M_n	Number Average Molecular Weight
M_w	Weight Average Molecular Weight
NDI	Naphtalene-diimide
NLP	Natural Language Processing
N2200	Poly[N,N'-bis(2-octyldodecyl)naphthalene-1,4,5,8-bis(dicarboximide)-2,6-diyl]-alt-5,5'-(2,2'-bithiophene)
OCAT	One-Composition-At-A-Time
OFET	Organic Field-Effect Transistors
OLED	Organic Light Emitting Diodes
OPV	Organic Photovoltaics
OSC	Organic Semiconducting
PDI	Polydispersity
PDMS	Polydimethylsiloxane
PEDOT:PSS	Poly(3,4-ethylenedioxythiophene) Polystyrene Dulfonate
PSIB	polymer semiconductor-insulator blends
PSPR	process-structure-property relationship
PVME	Poly(vinyl methyl ether)
P3HT	poly(3-hexylthiophene)
RDR	Reduced Design Region
RFID	Radio Frequency Identifications
r_s	Size reduction metric
S	Huang Rays Factor
SANS	Small-Angle Neutron Scattering
SAXS	Small-Angle X-Ray Scattering

SEBS	Polystyrene-block-poly(ethylene-co-butylene)-block-polystyrene
SLS	Static Light Scattering
μ	Mobility
V_G	Gate Voltage
V_T	Threshold Voltage
W	Exciton-Bandwidth
XPS	X-ray Photoelectron Spectroscopy

SUMMARY

The ever-growing demands of consumers in a rapidly expanding global population underscore the need for innovative materials to develop efficient and affordable electronic devices. One such area grappling with this surge in demand is the realm of conjugated polymer (CP)-based electronic materials. These semiconducting polymers have emerged as promising substitutes for traditional silicon, paving the way for flexible, lightweight, and cost-effective electronic devices such as organic field-effect transistors (OFETs), light-emitting diodes, and solar cells. Unlike silicon, CPs can be processed as solutions, rendering them more suitable for developing electronic devices with room for optimization. Unfortunately, progress in organic electronics is hindered by the vast and intricate processing landscape of these polymers, which has been demonstrated to directly impact performance. Moreover, traditional research methodologies have relied heavily on trial-and-error approaches, which not only slow down progress but also hinder the acquisition of insights and impede advancements towards real-world applications. Recent advancements in high-throughput experimentation (HTE) and materials informatics present solutions to these challenges. Thus, this thesis aims to integrate existing knowledge of polymer design and processing with HTE and polymer informatics methods to accelerate the development of OFETs derived from donor-acceptor (D-A) copolymers.

The chapters of this dissertation exemplify the benefits of integrating data-centric approaches into the established polymer electronics framework to streamline the advancement of these materials. Throughout this thesis, a consistent focus lies on carefully

evaluating processing conditions to optimize the performance of CP-based OFETs. Initially, employing data science algorithms on meticulously curated process-property datasets unveils the key processing variables influencing device performance, with algorithm-derived insights guiding future experiments. Subsequently, these informatics insights are validated through relevant experiments investigating the manipulation of CP solution states. These experiments aim to elucidate how variations in solution state parameters, such as concentration, impact the morphology of the final film and the functionality of the device. Lastly, this study delves into the burgeoning domain of polymer semiconductor-insulator blends (PSIBs), highlighting the potential of HTE through the fabrication and characterization of gradient thin-films. This approach complements traditional discrete experiments, facilitating rapid screening of processing spaces for these blend systems, especially concerning blend composition. Moreover, it also provides a pathway to more efficient and comprehensive insights, uncovering trends occurring within narrow windows that might otherwise go unnoticed. In essence, this thesis underscores the integration of HTE and materials informatics into the existing polymer electronics paradigm to expedite the discovery and development of D-A polymer based-OFETs.

CHAPTER 1. INTRODUCTION

1.1 II- Conjugated Polymer-Based Electronic Devices

Silicon, long regarded as the cornerstone of electronic devices, has undeniably propelled the technological era forward. Its reliability and efficiency in circuit boards, solar panels and semiconductor applications have shaped the landscape of modern electronics.[1-3] However, as the demand for flexibility and optimization in electronic devices grows, the inherent limitations of silicon become apparent. The rigid and brittle nature of silicon poses challenges in meeting the dynamic requirements of emerging technologies such as flexible displays, wearable electronics, and portable devices.[4-8]

These limitations propel us toward exploring innovative alternatives, and it is in this context that organic electronics emerge as promising contenders for the future of electronic design. Organic electronics is a branch of modern electronics that deals with organic semiconducting (OSC) materials such as CPs or conducting small molecules.[9, 10] Since the discovery of the first conducting polymer, polyacetylene in 1976,[11] several new CP chemistries have been introduced[12-14] to fabricate light-weight, low-cost and flexible electronic devices such as organic photovoltaics (OPVs),[15-17] OFETs,[18-20] organic light emitting diodes (OLEDs),[21-23] and, biomedical sensors.[24, 25] Despite OSCs exhibiting electrical performance inferior to their inorganic counterpart, silicon, they boast distinct functional and economic advantages.[26-28] One notable advantage lies in the solution processability of OSCs, providing room to optimize synthesis and processing conditions for the fabrication of high-performing electronic devices.[29-33] Moreover, OSCs can be seamlessly blended in small quantities with insulating polymers like polydimethylsiloxane

(PDMS) and poly(3,4-ethylenedioxythiophene) polystyrene sulfonate (PEDOT:PSS), offering the prospect of creating flexible, high-performance electronic devices.[34-37]

The two main classes of CP polymers are homopolymers and D-A copolymers, with the former being extensively studied and the latter being recently discovered (~ 2010).[38-40] Previous work on CP polymers indicates that apart from the polymer intrinsic properties, solution processing and thin-film deposition conditions also impact the morphology, microstructure, and electrical performance of the final thin-film device.[30, 35, 36, 41-44] There exists a large number of possible monomers each with their own potentially unique optimal processing conditions presenting a vast and complex design space **(**Figure 1-1**)** that is inefficient to explore via a trial and error or Edisonian approach.[29, 45] As a result, progress with homopolymer-based devices has been slow, taking almost 30 years to obtain a maximum charge carrier mobility of 1 $cm^2/V.s$.[19] The charge carrier mobility is the target performance metric of interest for OFETs, which is the electronic device that will be the focus of this work. This slow progress is likely due to the majority of process-structure-property relationship (PSPR) studies reported in previous publications being largely single-factor-at-a-time experiments, which can be tedious and inefficient. The more recently discovered, high-performing D-A copolymers have been shown to reach charge mobilities close to 20 $cm^2/V.s$.[13, 38, 46] Unlike homopolymers, there exist knowledge gaps in the PSPRs of D-A copolymers with plenty of room to optimize device performance. However, the concern of the vast design space persists, limiting the rapid discovery and development of these high-performing electronic materials. To address these challenges, this thesis work will focus on improving the performance of D-A polymer-based OFETs using a data-

centric approach, aiming to streamline the exploration of this intricate design space and expedite the progress in developing high-performance electronic materials.

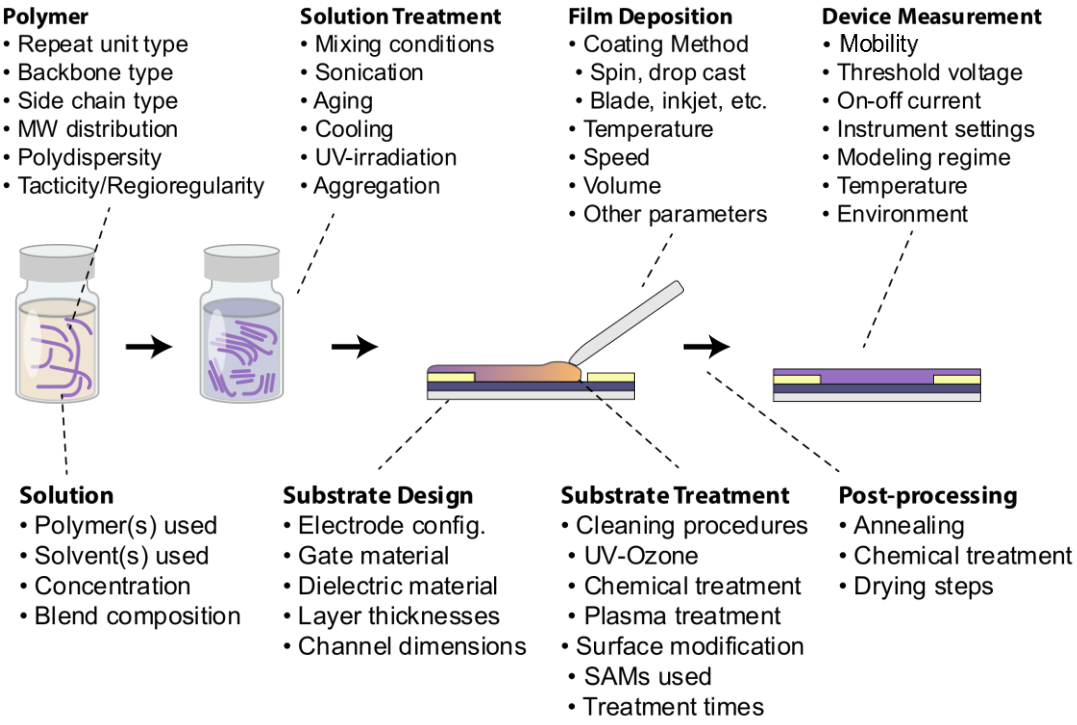

Figure 1-1. Diagram of the methods of fabricating and characterizing a conjugated polymer based organic field effect transistor and associated processing variables. Adapted from Liu et al[47] with permission

1.1.1 Charge Transport in Polymeric Semiconductors

The use of OSCs in large area, low-cost, flexible electronic devices relies on their ability to efficiently transport charge carriers (holes and electrons) through the material, which is influenced by the degree of order within the material.[39, 48, 49] Most CPs consist of ordered (e.g., crystalline domains) and disordered (e.g., amorphous domains) regions as a result of the macromolecular morphologies of the polymer chains.[38, 50] Charges move between ordered aggregates by travelling along tie chains (red lines) that bridge these regions together (Figure 1-2).[39, 51] Disordered regions hinder charge transport by generating

electronic charge traps.[52] Noriega et al, proposed a unified transport model of the mechanism of charge carrier travel in CP films.[39] This model establishes a general relationship between polymer microstructure and macroscopic charge transport by classifying the CPs based on their microstructure and degree of paracrystalline order (g), which is defined as the standard deviation of local, static lattice fluctuations normalized by the average value of the lattice spacing. In simpler terms, it serves as a measure of fluctuations of disorder experienced in the lattice. Highly crystalline materials have g < 1%, while amorphous materials have g > 10-20%. It was identified that the higher the value of g, the deeper the charge traps and resultant larger activation energy for charge transport ($E_{a,CT}$).[38, 39]

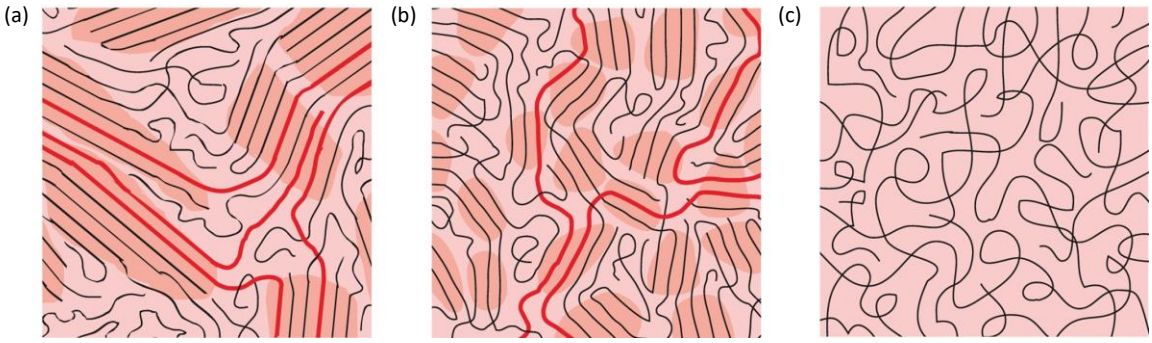

Figure 1-2. Schematic illustration of microstructures for CPs: (a) semicrystalline homopolymer film (b) disordered aggregates commonly observed in many D-A polymers (c) completely amorphous film. The red lines are tie molecules connecting the aggregates. Figure adapted from Noriega et al[39] with permission.

Conjugated homopolymers like poly(3-hexylthiophene) (P3HT), comprise a significant volume fraction of extended crystalline aggregates connected by tie chains (Figure 1-2a).[53-55] These polymers typically exhibit mobilities ranging from 0.1 – 1 $cm^2/V.s$.[38, 39] The typical design guideline for high mobility in homopolymers has been a crystalline lamellar structure with a long-range order and extended π-π stacking/overlap

oriented parallel to the substrate (edge-on) as shown in Figure 1-3.[56-58] The disordered amorphous regions do not hinder charge transport as long as the polymer molecular weight is sufficient enough to maintain a percolating network of tie chains between the ordered aggregates.[59] The energetic disorder encountered by the charges in the form of charge traps is a result of paracrystalline disorder in the π-π stacking within the aggregates (g = 6-8%) resulting in a moderate $E_{a,CT}$ of 72 ± 24 meV.[60]

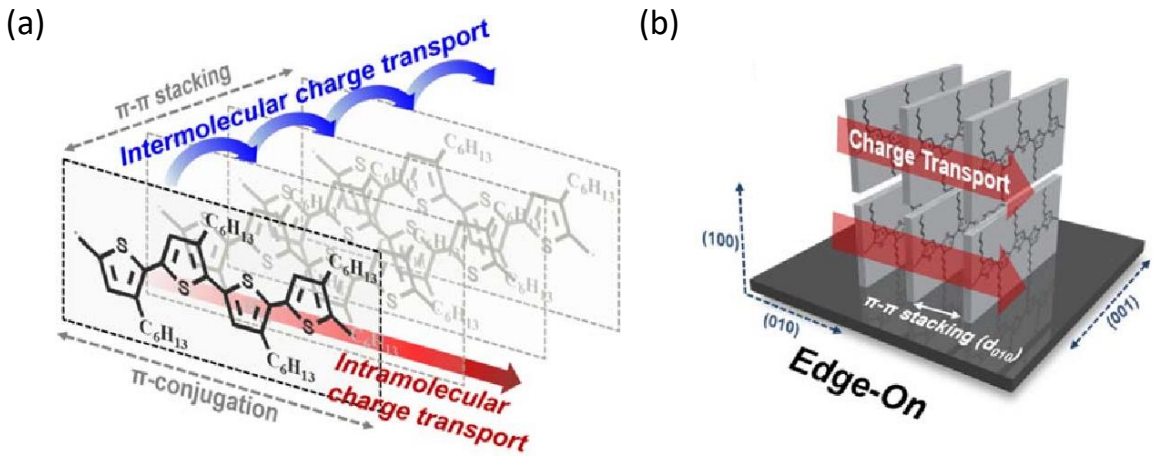

Figure 1-3. (a) Inter- and intramolecular charge transport in crystalline polythiophene. (b) Edge-on stacking orientations of P3HT crystals. Figure adapted from Chu et al.[61]

More recently discovered D-A polymers, with a polymer backbone consisting of alternating electron-deficient (acceptor) and electron-rich (donor) units, have exhibited far higher mobilities (~20 $cm^2/V.s$) compared to the semicrystalline homopolymers.[36] This is surprising because D-A polymers typically have smaller crystalline aggregates and a more disordered microstructure (Figure 1-2b). They typically have a g =10-15 wt.% and $E_{a,CT}$ = 76 ± 23 meV).[38, 39] This comparable $E_{a,CT}$ (to homopolymers) is a reflection of relatively unhindered motion of charge carriers along tie chains connecting aggregates combined with efficient interchain charge transfer within aggregates.[39] The high mobility observed

in D-A polymers despite having a more disordered microstructure is due to the rigid and planar backbone conformation with minimal steric hinderance between the donor and acceptor units.[38, 62-65] This conformation minimizes structural disorders, enabling effective backbone conjugation with a low energetic disorder and close chain packing.[38, 66-68] Hence, interchain charge transfer in D-A polymers is less sensitive to paracrystalline disorder in the π-π stacking within aggregates.[39] Lastly amorphous polymers with g>20 wt.%, adopt highly disordered microstructures with little to no evidence of aggregate formation (Figure 1-2c) and exhibit mobilities lower then < 0.1 cm^2/Vs and high $E_{a,CT} = 230 \pm 100$ meV.[39]

1.1.2 OFETs and Their Functionality

OFETs are not only used as major components in electronic applications such as radio frequency identifications (RFIDs)[69] and sensors[43], but also to characterize the electronic properties of OSC materials.[20, 70] The bottom-gate/bottom-contact (BGBC) configuration (Figure 1-4a) is a common device architecture where the polymer semiconductor is deposited as a thin-film during the final step of fabrication, although other device architectures also exist.[38]

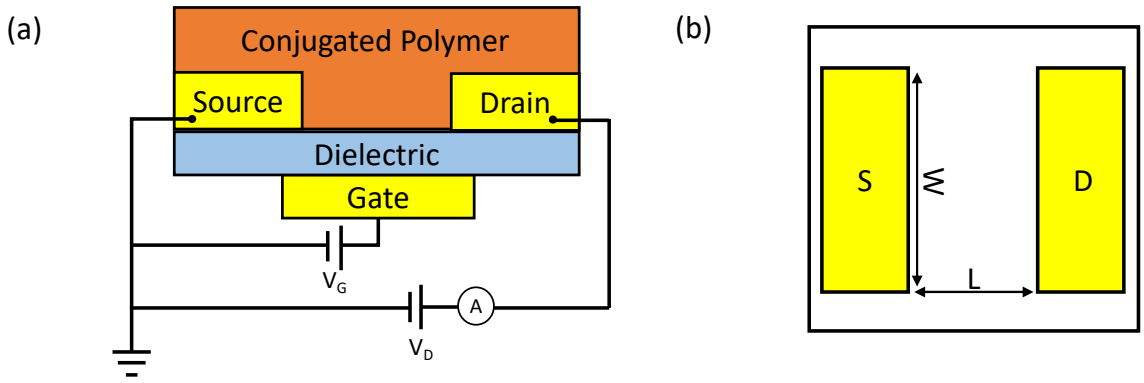

Figure 1-4. (a) Schematic illustration of an OFET with a BGBC configuration connected to a circuit (b) Top-down view of the BGBC OFET.

The source and drain electrodes inject and receive charge carriers respectively through the CP layer. The amount of charge that flows in this layer is modulated by the voltage at the gate electrode (V_G). The relationship between the current and voltage vary in different operating regimes and can be expressed analytically using equations 1 and 3 below. These analytical expressions can be used to extract the charge carrier mobility (μ) and threshold voltage (V_T) which are the target parameters of interest. Mobility, μ, is the speed at which the charge carriers move in the presence of an applied electric field and V_T is the voltage at which the OFET turns on. In these equations, W is the channel width, L is the channel length (Figure 1-4b), and C_i is the capacitance per area of the dielectric.

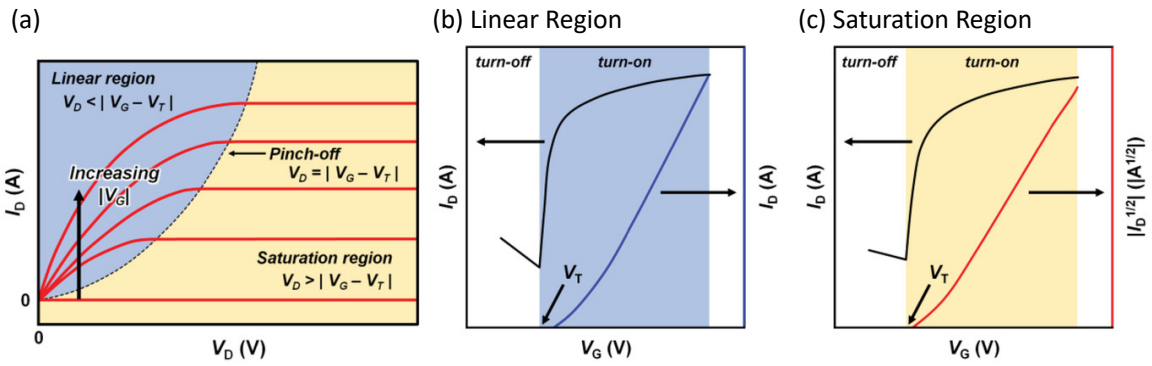

Figure 1-5. (a) OFET output characteristics depending on different gate voltages. Transfer Curves used for extracting OFET parameters in (b) linear and (c) saturation region. Adapted from Kim et al[38] with permission.

In the linear regime (Figure 1-5b), Drain Current (I_D) is proportional to V_G (Equation 1), and is valid when the drain voltage $V_D < V_G - V_T$. In the linear regime, μ can be extracted using Equation 2.

$$I_D = \frac{WC_i}{L}\mu((V_G - V_T)V_D - \frac{1}{2}{V_D}^2)^2 \quad (1)$$

$$\mu_{lin} = \frac{L}{C_i W V_D} \frac{\mathrm{d}I_{DL}}{\mathrm{d}V_G} \tag{2}$$

In the saturation regime (Figure 1-5c), the current cannot increase anymore and saturates (Figure 1-5a). The square root of I_D is proportional to V_G as shown in Equation 3, and is valid when the drain voltage $V_D < V_G - V_T$. μ and V_T in the saturation regime can be extracted using Equation 4.

$$I_{DS} = \frac{W C_i}{2L} \mu (V_G - V_T)^2 \tag{3}$$

$$\mu_{sat} = \frac{2L}{C_i W} \left(\frac{\mathrm{d}\sqrt{I_{DL}}}{\mathrm{d}V_G} \right)^2 \tag{4}$$

1.1.3 The Influence of Processing Conditions on Solution-State Structures, Thin-Film Morphology and Device Performance

CPs used in semiconducting applications like OFETs, OLEDs and OPVs are commonly deposited as thin films from solution-based inks.[29, 71] The literature underscores the crucial roles of solution processing history and deposition parameters in governing thin-film morphology which consequently influences device performance.[42, 72, 73] Traditionally, spin-coating was used as a common deposition technique, but more recently meniscus-guided coating (MGC) techniques like blade coating and solution shearing are gaining

traction.[30] The advantages of MGC techniques include requiring a smaller solution volume and being more suitable for large-scale production processes.[42, 74] Earlier investigations of CP films deposited via MGC identified shear speed, solution concentration, solvent choice, and deposition temperature as crucial factors influencing thin-film morphology and electronic performance.[29, 30, 42, 72]

Traditionally, the focus of most studies in the field of OSC centered on designing new CP molecular structures and optimizing their solid-state morphology to enhance charge-carrier mobilities.[75] However, a crucial factor that was often overlooked was understanding how the self-assembly or aggregation of CPs in solution, prior to device fabrication, influenced device performance.[29, 75] The amount of aggregation in the solution-state can be tuned via parameters including the solvent quality,[75] solution concentration,[76] dissolution temperatures,[77] aging time,[78] UV-induced nucleation,[41] and ternary-component blending.[29, 35]

Unfortunately, prior studies were fixated on establishing correlations between processing conditions, polymer solid-state microstructures, and final device performance, often neglecting an examination of the solution-state structures.[29, 75] This oversight arises from the inherent challenges associated with characterizing the solution state of these conjugated polymers. This is because CP's relatively high absorption coefficients in the visible and near-IR regions make it challenging to probe the polymer solution state directly using regular spectroscopic techniques.[29, 79] The rigid backbone and longer persistence length of D-A polymers further enhances the strong absorption within these regions.[39]

Mitigating this issue involves reducing the optical path length[41, 53, 80] or employing freeze-drying to capture and preserve solution-state conformations for solid-state characterization.[81] Additionally, measuring the solution state viscosity[76, 82] or using scattering techniques like dynamic and static light scattering (DLS and SLS) and small-angle X-ray and neutron scattering (SAXS and SANS) can be used to gain further insights on the chain conformations and polymer aggregation in solution.[29, 75, 81]

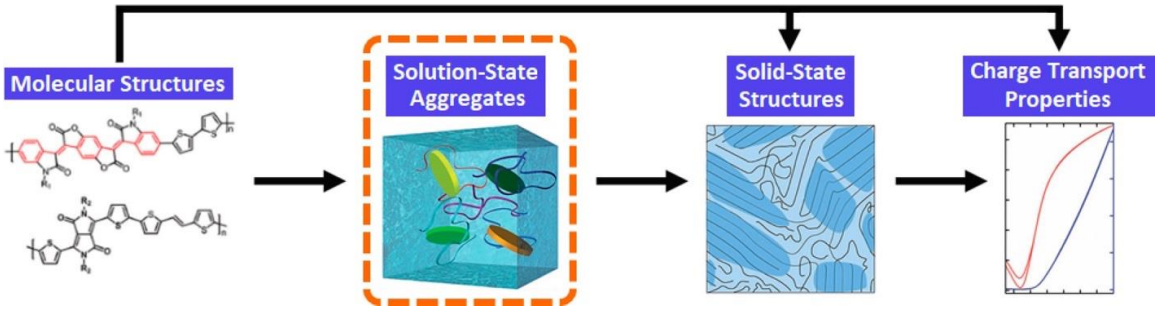

Figure 1-6. Representative pipeline for understanding the structure−property relationship in polymer semiconductors. Reprinted and adapted with permission from Zheng et al.[75]

Recent research has shown that aggregates created in the solution play a direct role in shaping the structural and electronic characteristics of solid-state films upon deposition, as illustrated in Figure 1-6. To optimize the performance of conjugated polymer devices, a nuanced understanding of the intricate relationships between solution-state aggregation, solid-state morphology, and charge-carrier transport is imperative.[29, 75] A study by Zheng et al. found that the thin-film morphology of a CP, benzodifuran-dione oligo(p-phenylene vinylene) (BDOPV), inherits the features of its solution-state assemblies, as revealed by their investigation of the polymer's solution state using various characterization techniques that probed the solution phase[75]. Hence this thesis aims to investigate the solution state prior to deposition in conjunction with thin-film characterization to yield a deeper

understanding of the physicochemical mechanisms influencing the performance in CP based electronics.

1.1.4 H- and J-Aggregate Behaviour In Polymeric Semiconductors

The aggregates observed in CPs typically exhibit two classes of electronic interactions, and the influence of these interactions on the photophysical behavior of CP thin films can be described using the renowned H-J aggregate theory.[83, 84] These interactions include the J-aggregate or intrachain interactions and H-aggregate or interchain interactions, as depicted in Figure 1-7.

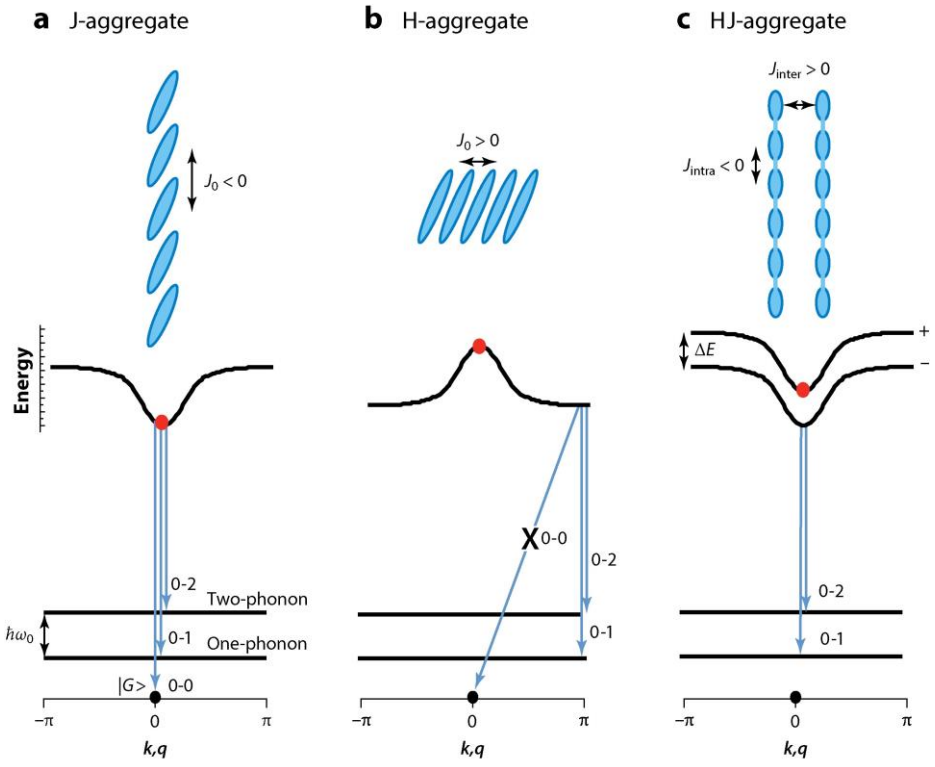

Figure 1-7. (a,b) Molecular orientations within conventional J- and H-aggregates. The sign of the nearest-neighbor coupling J_0 is determined by the through-space Coulombic coupling. Generally, head-to-tail orientations lead to $J_0 < 0$ and J-aggregation, whereas side-by-side orientations lead to $J_0 > 0$ and H-aggregation. (c) In polymer HJ-aggregates, Coulombic interchain coupling is positive ($J_{inter} > 0$),

whereas the effective intrachain coupling between adjacent repeat units is negative ($J_{intra} < 0$) owing to through-bond interactions in 1D direct band-gap semiconductors. Also shown is the energy dispersion, E(k), corresponding to the lowest vibronic band in each aggregate. The band curvature at k = 0 is positive (negative) in J- (H-)aggregates. The red dot indicates the (k = 0) exciton that is optically allowed from the ground state, |G> (black dot). The energies of the one- and two-phonon states within the electronic ground state are also indicated. The dispersionless (Einstein) phonons of wave vector q derive from the intramolecular vibrations with frequency ω0. Arrows indicate emission pathways at low temperatures, such that emission originates primarily from the lowest-energy exciton. Reprinted and adapted with permission from Spano et al.[84]

The photophysical behavior of the CP thin film is determined by the competition between intrachain (favoring J-aggregates) and interchain (favoring H-aggregates) interactions.[84] In the case of J-aggregates, neighboring chromophores are oriented head-to-tail within a single polymer chain, resulting in intrachain interactions and placing the optically allowed exciton at the bottom of the energy band.[84, 85] Conversely, in H-aggregates, chromophores are oriented side-by-side, indicating interchain interactions between different polymer chains and placing the optically allowed exciton at the top of the energy band.[53, 84] An exciton is defined as a quasiparticle resulting from the interaction between an electron excited to a higher energy level and the corresponding "hole" it leaves behind in the material's electronic structure, playing a crucial role in various photophysical processes.[86] The photophysical behavior of CPs, including vibronic absorption and emission spectra, are influenced by inter- and intramolecular interactions and exciton delocalization and can result in significantly different spectral features.

In this work, we primarily focus on analyzing absorption spectra obtained from UV-VIS absorption experiments. The absorption spectrum of CP thin films like P3HT can be comprehensively explained using the weakly interacting H aggregate model.[53, 87-89] This model enables the interpretation of the absorption spectrum and provides quantitative

estimates of the fraction of the film made up of crystalline and amorphous aggregates, as well as the degree of excitonic coupling within the aggregates, referred to as the exciton bandwidth 'W'.[53, 90, 91] The exciton bandwidth relates to the average conjugation length and the crystalline quality in the CP thin film, offering insights into the microstructure correlated with thin-film field-effect transistor OFET characteristics.[83, 84, 92] Figure 1-8 illustrates the absorbance spectrum of a regio regular P3HT spin-coated thin film.[93]

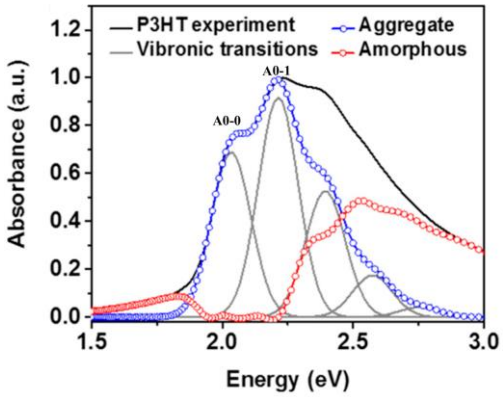

Figure 1-8. Absorption spectrum of P3HT film deposited via spin coating after being subjected to Franck-Condon fit (Equation 6). Reprinted and adapted with permission from Chang et al.[93]

The absorption spectrum comprises a lower energy, dominant part from crystalline regions forming weakly interacting H-aggregate (interchain) states and a higher energy part from more disordered chains forming J-aggregate (intrachain) states.[53, 87, 93] The ratio of the 0-0 and 0-1 absorbance peak is related to W and the energy of the main intramolecular vibration Ep = 0.18, using equation 5, assuming the C=C symmetric stretch dominates the coupling to the electronic transition and a Huang–Rhys factor of 1.[87, 88]

$$\frac{A_{0-0}}{A_{0-1}} \approx \left(\frac{1 - 0.24W/E_P}{1 + 0.073W/E_P}\right)^2 \quad (5)$$

W is inversely related to the conjugation length and degree of intrachain order.[94-96] Additionally, the fraction of the spectrum made up of aggregates can be obtained by the modified Frank-Condon fit (Equation 6) to the absorption spectrum, which accounts for the effect of aggregation on the relative vibronic intensities.[89]

$$A = \sum_{m=0} \frac{e^{-S}S^m}{m!}\left(1 - \frac{We^{-S}}{2E_p}G_m\right)^2 \Gamma\left(\hbar\omega - E_{0-0} - mE_p\right), \text{ where } G_m = \sum_{n \neq m} \frac{S^n}{n!\,(n-m)} \quad (6)$$

Here A = absorbance, S = Huang-Rhys factor, m = vibrational level, G_m is a constant that depends on m, where the sum is over the vibrational quantum number n. For simplicity, a Gaussian line shape is used with the same width for each vibronic transition.

1.2 Tools for Organic Electronics Materials Development

The United Nations predicts the global population to reach 10 billion by 2050, and with it an increase in the demand for clean and high-efficiency energy and personalized consumer products. [97] Recognizing the urgency of this demand and the pivotal role that advanced materials play in meeting these challenges, The Materials Genome Initiative (MGI) was set up under the Obama administration and the goal of this initiative is to

focus its efforts on discovering, manufacturing, and deploying advanced materials at a faster rate and at a lower cost compared to traditional methods.[98] The field of organic electronics is no stranger to the implications of the consumer rapid demand. In the past, discovery of organic electronic materials relied mostly on empirical or experimental trial-and-error approaches.[29, 45] However, with the advent of modern experimental and computational techniques, researchers now utilize a diverse array of data-driven tools to revolutionize the landscape of materials development, which has opened new paradigms for the discovery and rational design of materials.[97] The tools explored in this multifaceted approach include: literature data mining,[82, 99-103] , HTE,[104-118] and materials informatics.[45, 97, 119-137] Each plays a pivotal role in accelerating the discovery, optimization, and deployment of advanced materials. Literature data mining involves extracting meaningful insights from scientific literature, expediting knowledge assimilation, and serving as a catalyst for informed decision-making.[82, 99-103] Meanwhile, HTE simultaneously explores diverse material compositions and processing conditions, reducing the time and resources needed for experiments and characterization.[104, 106-118, 138-142] Finally, Materials Informatics leverages data-driven methodologies like data analytics and machine learning (ML) to model the complex Process-Structure-Property Relationships (PSPRs) and expedite the process of discovery and development of advanced materials.[97, 119-125, 129-137, 142, 143] This thesis delves into recent advancements in these tools, examining how they have evolved to meet current materials research demands. Specifically, we explore their utility in navigating the complexities of organic electronics and developing OFETs with enhanced performance and efficiency.

1.2.1 Literature Data Mining and Process-Structure-Property Database Curation

Thin-film material systems, like CPs, are often linked to an extensive and intricate design space, posing difficulties for researchers in identifying the pertinent processing variables to investigate, determining initial design parameters, and avoiding redundant efforts. To address these challenges, researchers can leverage published scientific literature as a valuable resource, functioning as an extensive repository of materials science knowledge with a wealth of process-structure-property data points.[99-101, 103] Unfortunately, the extraction of valuable information from these scientific texts presents a notable challenge, mainly due to the majority of the data being presented in a semi- or un-structured format, encompassing text, citations, images, captions, and tables.[99, 144, 145] Manually extracting the desired information can be a time-consuming and resource-intensive task, typically necessitating the expertise of a domain specialist. Additionally, a lack of standards for reporting important information such as target performance metrics, processing information, equipment settings, can result in data sparsity.[45, 97, 99, 100, 119] Despite these challenges, there has been a recent surge in interest in literature data mining approaches for experimental design.[146-148] Persson et al. manually curated an excel dataset comprising process-property data for more than 200 OFET devices fabricated from P3HT, sourced from 19 publications.[149] Notably, the hole mobility values for OFETs in the database exhibited a considerable variation spanning six orders of magnitude (from 10^{-6} to 10^{-1} cm^2/V·s). This variance in mobility underscores the significant impact of intrinsic properties and processing conditions on device performance. Initial analysis of the dataset reaffirmed established trends and also unveiled new insights.

Leveraging the capabilities of artificial intelligence and increased computing power, Natural Language Processing (NLP) pipelines emerge as promising tools to automate information extraction from text and organize the data in a structured format for subsequent analysis. Notably, the ChemDataExtractor,[102] an NLP pipeline, has been employed to parse several text documents and establish databases for battery materials,[150] Curie and Néel temperatures of magnetic materials,[151] and synthesis routes for inorganic materials.[152] While NLP has not been widely employed for polymer based applications, there is a growing interest in the field for literature data mining and storing the extracted information in the form of structured databases to facilitate experimental design.[99, 101-103, 153] Shetty et al. recently utilized NLP to extract approximately 300,000 material property records from around 130,000 abstracts of polymer literature within a span of 60 hours.[101] Analyzing the extracted data yielded valuable insights for various applications, such as fuel cells, supercapacitors, and polymer solar cells.

Unfortunately, the domain of CP-based materials remains as a research area in dire need of better data management solutions.[47] While there are a few open-source databases dedicated to organic electronics research, such as the Harvard Clean Energy Project[154] and Organic Crystals In Electronic and Light-Oriented Technologies (OCELOT),[155] these databases predominantly include computational data related to small molecules.[47] Furthermore, the data primarily focuses on structure-property relationships and often overlooks the crucial aspect of process history, which is essential for ensuring reproducibility and accuracy within the field. To address this challenge, Liu et al recently designed and implemented an object-relational database for storing PSP data of OFETs derived from literature and laboratory experiments.[47] The open-source database was

developed to accurately capture the processing history associated with these devices in a standardized manner and serves as a valuable resource for experimental design within the organic electronics community. Data driven methodologies such as data analytics and ML can then be applied to the data stored in these databases to confirm existing trends, develop property prediction models and guide future experimental design.

1.2.2 High-Throughput Experimentation For Efficient Experimental Data Curation

HTE presents a promising approach for efficient acquisition of extensive datasets by simultaneously screening a wide range of relevant processing parameters typically through the use of combinatorial material science techniques.[106-110, 117, 118, 138, 139] HTE methodologies have demonstrated promising results in a variety of technologically important materials including catalysts,[114] alloys,[113] and energy storage materials.[141] The field of polymer research seems to be an appropriate application of HTE due to the vast and complex processing space associated with these material systems.[106, 107, 109-112, 115-117, 138, 140] Within the realm of polymer blend research, HTE methodologies have been enabled by the fabrication and characterization of gradient thin film libraries, where high-throughput (HT) thin film fabrication techniques enable systematic compositional variation.[109, 115, 138] These libraries are typically fabricated through solution-based coating and blending techniques to deposit a continuous thin film library containing a diverse range of blend compositions on a single substrate, that can be used as a foundation for subsequent HT characterization.[109] Meredith et al developed a high throughput gradient film methodology to investigate the influence of blend composition on the polymer phase behavior of polystyrene (PS) and Poly(vinyl methyl ether) (PVME) blends.[111] The influence of other variables like temperature[111] and film thickness[116] on the thin-film

properties have also been investigated using this gradient approach. Liu et al developed a HT solution coating system (Figure 1-9) that is capable of fabricating composition gradient polymer libraries at operating temperatures over 110 °C.[109] In the realm of organic electronics, HT gradient approaches have been primarily applied to polymer solar cells to identify the optimum processing conditions that would result in improved efficiency.[104, 115] To the best of our knowledge, the HT gradient methodology has not been extensively utilized for OFETs. The application of HTE in the realm of CP's holds the potential to revolutionize the way we design and optimize the performance of OFETs.

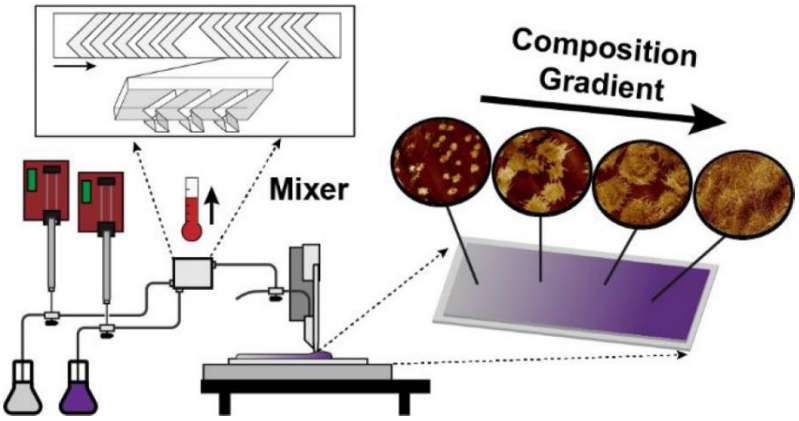

Figure 1-9. Illustration of high-throughput coating system that is capable of coating polymer thin films with varying compositions across the substrate adapted with permission from Liu et al.[109]

1.2.3 Leveraging Polymer Informatics For PSPR Modeling and Experimental Design of OFETs

The large amount of materials data generated from experiments and simulations has given rise to the field of material informatics which is regarded as the 4th paradigm of material science.[97, 119, 121-124, 130, 132-134, 136, 137, 156] Leveraging the power of data science and

ML algorithms, materials informatics has emerged as a transformative paradigm in materials discovery and design. This approach allows us to not only predict the properties of novel material systems with unprecedented accuracy but also guide the efficient design of future experiments, accelerating the development of new material chemistries with tailored functionalities.[97, 120, 122, 125, 132] The typical workflow (Figure 1-10) for informatics-driven materials discovery and design follows a well-defined pipeline: data curation, descriptor generation and dimensionality reduction, model construction and validation, and finally, material/property prediction and experimental verification.[97, 136] For those seeking a deeper dive into this fascinating field, several comprehensive reviews offer valuable insights.[123, 132, 136]

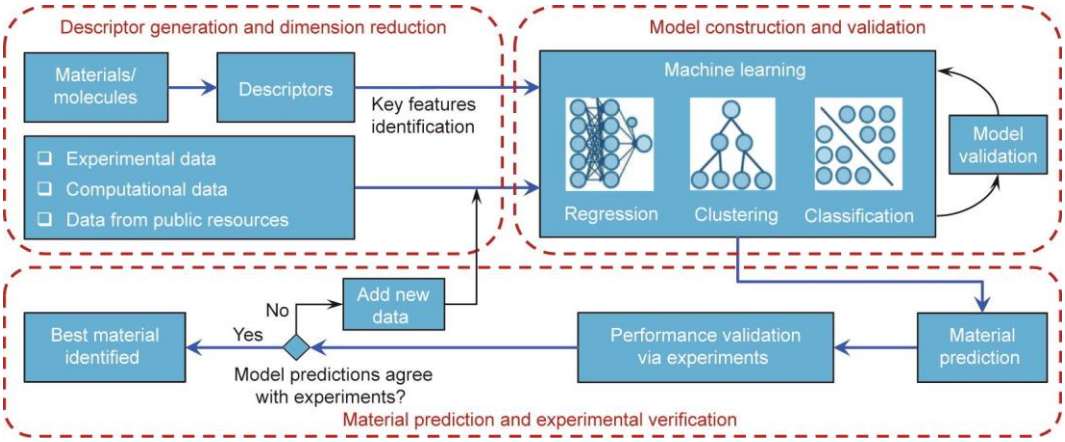

Figure 1-10. Generic workflow for materials discovery and design based on ML adapted with permission from Zhou et al[97]

Traditionally, materials informatics focused on modeling the intricate relationships between material structure and property, leading to the development of quantitative-structure-property-relationship models.[97, 125, 129, 142, 157, 158] These models proved instrumental in discovering new material chemistries with desired properties and predicting the performance of novel materials. More recent models have incorporated processing

variables, acknowledging their significant influence on both material structure and property, resulting in the development of quantitative PSPR models that offer a more comprehensive approach for materials design.[45, 137, 159, 160] For example, Yan et al developed an integrated PSP modeling framework for additive manufacturing, which accurately predicted mechanical properties like yield strength and fatigue life based on manufacturing process parameters and intrinsic material properties.[161] This framework significantly reduced uncertainty in the produced material, minimizing trial-and-error, optimizing material selection, and saving time and resources.

While organic electronics has embraced materials informatics, the majority of progress has been concentrated on organic solar cells.[47, 98, 126, 127, 135, 141, 143] For instance, An et al, designed and implemented a machine learning assisted HT gradient approach to identify the optimum blend composition and deposition parameters that would result in enhanced efficiency for a ternary organic photovoltaic system.[105] Surprisingly, the application of ML for the development of PSPR models remains largely unexplored in the domain of OFETs. This presents a unique opportunity to leverage materials informatics methodologies in this promising field, potentially revolutionizing the way we design and optimize the performance of OFETs. McBride et al, applied a customized classification algorithm to a process-property dataset of P3HT based OFET devices and identified the key processing variables impacting device performance and a reduced experimental design region for those parameters that could potentially improve OFET mobility.[45] By integrating materials informatics tools into the existing paradigm, we can unlock a deeper understanding of the intricate PSPRs governing CP-based OFETs. This approach holds the

potential to unlock a new era of high-performance organic electronics, paving the way for novel applications in various sectors.

1.3 Thesis Overview

The application of HTE methodologies and materials informatics in the realm of organic electronic materials has predominantly centered on the development of D-A based polymer solar cells,[104, 135, 162, 163] with limited exploration in the context of OFETs. Notably, investigations into PSPRs for D-A polymers lag behind their homopolymer counterparts. Traditional trial-and-error approaches are insufficient to meet the demands for rapid advancements in D-A based organic electronics. **Thus, the primary objective of this thesis is to synergize insights from polymer design, processing, materials informatics, and HTE to expedite the development of OFETs derived from D-A polymers.** Materials informatics approaches will be applied to unravel the nuanced relationships between processing parameters, structural features, and final OFET performance and design future experiments. Subsequently, HTE methodologies will be used to efficiently gather data from the expansive design space, complementing the traditional Edisonian approach.

Chapter 2 underscores the benefits of curating centralized data repositories and utilizing informatics methodologies in shaping the experimental design of materials research. In this chapter, a data set containing process-property information for DPP-DTT-based OFET was curated from the scientific literature. Application of a customized classification algorithm to the dataset helped identify a reduced design range for a previously overlooked processing parameter, solution concentration, that would likely

result in an improved hole mobility. Experimental validation revealed a strong influence of solution concentration on the polymer chain excitonic interactions and OFET hole mobility that was previously unidentified. The findings from this work highlight the advantage of materials informatics in identifying new trends and the critical need to further investigate the influence of solution concentration to gain a thorough understanding of the PSPRs of D-A polymers.

Chapter 3 delves deeper into the influence of solution concentration on the optoelectronic properties of D-A polymers, with a focus on diketopyrrolopyrrole (DPP)-based polymers. Experiments performed on different molecular weights of DPP-DTT revealed an interesting trend that films fabricated at the overlap concentration, identified from solution-state viscosity experiments, consistently resulted in improved OFET mobility. Furthermore, similar experiments revealed that the same trend is observed across other types of DPP and naphtalene diimide (NDI) -based polymers as well. This chapter delves deeper into the reasons for the observed improved charge transport and the potential behavior of the polymer chains as they transition from solution to solid state. The findings emphasize the necessity of investigating the solution state prior to film deposition for enhancing thin film morphology and device performance.

Chapter 4 explores the promising domain of PSIBs for OFETs and the current knowledge gaps associated with it. Specifically, this chapter details a case study in investigating the PSPRs for blends of homopolymers and D-A polymers with insulating materials. Integrating traditional experiments and HT gradient film methodologies, the study provides a comprehensive understanding of composition-morphology-device performance space and helps capture transitions in device performance, phase behavior and

morphology that can be potentially overlooked. The findings from this work demonstrate the efficiency of HT methodologies in elucidating PSPRs of CPs.

Finally, Chapter 5 summarizes the key findings and conclusions of this work and provides an outlook on the future work required for the further development of D-A polymer based OFETs and organic electronics research.

CHAPTER 2. DATA SCIENCE GUIDED EXPERIMENTS IDENTIFY CONJUGATED POLYMER SOLUTION CONCENTRATION AS A KEY PARAMETER IN DEVICE PERFORMANCE

In the expansive design space of CPs, how can one strategically navigate the complexity to inform experimental design and decision-making? What criteria should be considered when selecting the initial processing variable to investigate, and how does one determine the appropriate design range for optimal outcomes?

This chapter addresses these questions by employing a data science approach on a curated dataset featuring process-property information of OFETs fabricated from DPP-DTT. The insights from the data science algorithm were validated through experiments and uncovered a key finding. This chapter and Appendix A are adapted from a published article.[82] Reprinted with permission from American Chemical Society:

Venkatesh, R.; Zheng, Y.; Viersen, C.; Liu, A.; Silva, C.; Grover, M.; & Reichmanis, E. (2021). Data Science Guided Experiments Identify Conjugated Polymer Solution Concentration as a Key Parameter in Device Performance. *ACS Materials Letters, 3*(9), 1321-1327. doi:10.1021/acsmaterialslett.1c00320

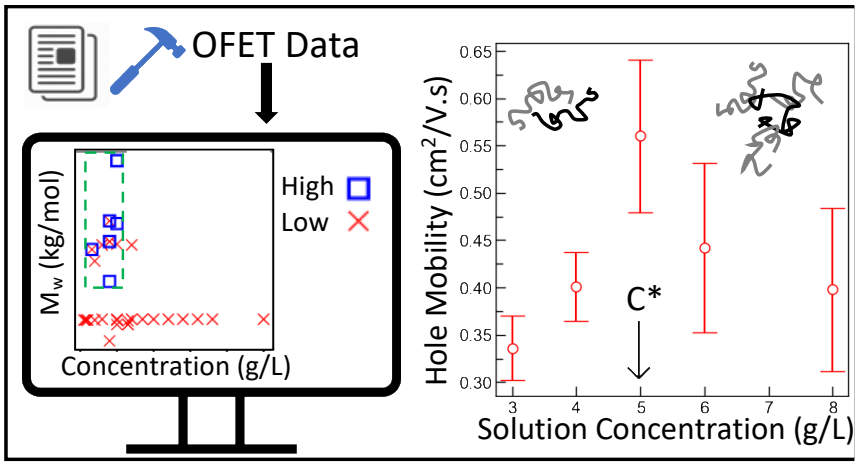

Figure 2-1. Graphical summary of chapter 2. A customized classification algorithm is applied to a dataset of DPP-DTT based OFET devices curated from literature. The algorithm identified a reduced design region for polymer solution concentration that would likely to result in improved hole mobility. Experiments performed to confirm the insights from the data curation exercise revealed a strong influence of solution concentration on the polymer chain excitonic interactions and electronic performance.

2.1 Introduction

CPs have demonstrated great potential in the production of light-weight, low-cost devices such as OPVs,[15] OFETs,[164] OLEDs,[23] and biomedical sensors.[25] The application of these materials in electronic devices relies on their ability to efficiently transport charges within the pi-conjugated network. CPs are believed to be comprised of ordered and disordered regions,[50] whereby charges move between ordered structures by travelling along bridging tie chains. The charge transport mechanism has been extensively studied in conjugated semi-crystalline homopolymers such as P3HT, which possess a significant volume fraction of extended crystalline regions and typically exhibit mobilities in the range of 0.05 – 1 cm^2/Vs.[165] Suggested design guidelines to achieve high mobility in homopolymers include the need for a crystalline lamellar structure with long-range order and extended π-π overlap oriented parallel to the

substrate.[56-58] Previous work on these materials indicates that apart from the polymer intrinsic properties, solution processing and thin-film deposition conditions also impact the morphology, microstructure, and electrical performance of the final thin-film device.[30, 34, 36, 42, 46, 166, 167] There is thus a vast and complex design space that is challenging to explore via solely an Edisonian approach.[45] Additionally, the lack of standardized reporting of processing conditions hinders experimental reproducibility and consequently hampers research progress.[19]

Curating accurate and interpretable process-property datasets helps promote reproducibility and transparency in several fields of research, and enables development of experimental design algorithms for process optimization.[149, 168] Analysis of these datasets can confirm existing hypotheses and guide future experimental studies. In a previous study, Persson *et al.*[149] compiled a database containing process-property information of over 200 P3HT-based OFET devices curated from 19 publications. Despite the CP remaining consistent across all devices, reported values for the charge carrier mobility varied by over six orders of magnitude (10^{-6} to 10^{-1} $cm^2/(V.s)$), indicating the strong influence of intrinsic material properties and processing conditions on charge carrier mobility. Basic analysis on the dataset confirmed well-known trends such as the effect of polymer molecular weight, transistor channel length, and deposition method on hole mobility. Subsequently, McBride *et al.*[168] applied a customized classification approach on the continuous design variables and identified the necessary processing parameters required to confine the high-performing points to a reduced design region (RDR), which can be used to guide future experiments.

More recently discovered push-pull copolymers, commonly referred to as D-A polymers, have exhibited far higher mobilities compared to the semicrystalline homopolymers,[38, 46] even though their microstructure is typically more disordered with smaller crystalline aggregates.[165] The high mobility observed in D-A polymers has been attributed to the rigid, planar backbone conformation with minimal steric hinderance between the donor and acceptor units. Unlike homopolymers, significant knowledge gaps exist in the process-structure-property relationships of D-A copolymers creating opportunities to optimize OFET performance still further. In this work, we compile a process-property dataset derived from 115 published OFET devices fabricated using the commercially available D-A polymer, DPP-DTT. The classification approach developed by McBride *et al.*[168] was extended to this system to gain new insights and guide experimental studies. Interestingly, the algorithm identified polymer solution concentration as a key factor in device performance and recommended a reduced design range for this processing variable expected to result in high performing devices. Whereby to the best of our knowledge, polymer concentration has not been identified as a key metric linked to macroscale device performance. Experimental results correlated very well with the insights gained from the data curation and analysis exercise. Viscosity measurements of the solutions at increasing concentrations revealed a two-regime behavior that is likely attributed to the overlap of polymer chains in solution state. Additionally, UV-Vis absorption spectra of the solid thin-films suggested a likely decrease in intrachain interactions (J-aggregate behavior) and increase in interchain interactions (H-aggregate behavior) with increasing solution concentration. Lastly, OFETs fabricated from DPP-DTT solutions at the concentration range recommended by the classification algorithm

exhibited improved hole-mobility, highlighting the advantage of integrating materials informatics approaches into the existing polymer electronics paradigm.

2.2 Materials and Methods

2.2.1 Materials

DPP-DTT (M_w= 290,000 g mol^{-1}, PDI = 2) was purchased from Ossila Limited, while chlorobenzene(CB)-anhydrous was purchased from Sigma-Aldrich. Heavily n-doped silicon substrates with 300 nm-thick thermally grown SiO_2 dielectric layer were purchased from Rogue Valley Microdevices.

2.2.2 OFET Fabrication

OFETs were used for the electrical characterization of the semiconducting DPP-DTT thin films made from different solution concentrations. The transistors functioned in a bottom gate bottom contact configuration with the n-doped silicon serving as a gate electrode and the SiO_2 serving as a dielectric/insulating layer. The source and drain electrodes were fabricated via a standard photolithography lift-off process followed by E-beam evaporation (Denton Explorer) of Cr (3 nm) as an adhesion layer and Au (50 nm) onto the SiO_2 surface. After electrode deposition, the substrates were then immersed in Acetone and the container was placed in an ultrasonic bath (15 min). This ultrasonication process was then repeated with methanol and IPA followed by sequential rinsing with acetone, methanol and IPA to wash off excess gold deposited on the metal. After drying the substrates with a nitrogen gun, they were then cleaned in a UV-ozone cleaner (Novascan PSD-UV) for 30 minutes to

get rid of any excess photoresist and organic impurities. The cleaned substrates were then immersed in a 0.1 M OTS-18 solution in toluene overnight inside the glove box. The substrates were then sonicated in toluene the following day for 15 minutes followed by sequential rinsing with toluene, acetone, methanol and IPA and were blow dried with nitrogen gas.

2.2.3 Sample Preparation

For sample preparation, a stock solution of 10 g/L DPP-DTT in CB was prepared by heating at 100 ˚C for around 4 hours, followed by heating at 56 ˚C overnight. Solutions with lower concentrations were prepared by diluting the stock solutions. The DPP- DTT thin films are prepared by wire-bar coating the solutions of different concentrations on glass and OFET substrates at 56 ˚C followed by annealing for 10 min. A shearing speed of 80 mm/s was used to deposit the films.

2.2.4 Characterization Methods

2.2.4.1 Viscosity Measurement

The viscosity of the DPP-DTT-CB solutions was measured using a microVISC viscometer (RheoSense, Inc) at 56 °C.

2.2.4.2 Steady-State Linear Absorption Spectroscopy

The steady-state linear absorption measurements were performed using a Cary 5000 UV-Vis-NIR spectrometer on the films deposited on glass substrates.

2.2.4.3 OFET Characterization

OFET properties were measured in a nitrogen glovebox using an Agilent 4155C semiconductor parameter analyzer. The charge carrier mobility and threshold voltage were calculated in the saturation regime ($V_D = -80$ V) by fitting the Equation 3 to the transfer plots of the drain current (I_D) versus the gate voltage (V_G). The mobility is obtained using Equation 4. In these equations, W is the channel width (2 mm), L is the channel length (50 μm), C_i is the capacitance per unit area of the SiO_2 dielectric layer (1.15 x 10^{-8} F cm^{-2}), μ is the hole mobility and V_T is the threshold voltage. The results in this work were averaged over 8-12 OFET devices for each concentration.

2.2.4.4 Atomic Force Microscopy (AFM)

AFM images of the conjugated polymer thin films deposited on glass substrates from varying solution concentrations were obtained using tapping mode on a Bruker-Dimension ICON using HQ:NSC14/No Al (160 kHz, 5.0 N/m) tips purchased from MicroMasch.

2.2.4.5 Profilometry

Thickness of the DPP-DTT thin films on glass substrates was obtained using a Bruker DekakXT profilometer.

2.2.4.6 Cross Polarized Optical Microscopy

Optical Microscopy images of the conjugated polymer thin films prepared from varying solution concentrations deposited on glass substrates were obtained using an Olympus BX51 microscope.

2.2.5 DPP-DTT Literature Dataset Curation

A dataset containing process-property information on OFET devices made from DPP-DTT was curated from 15 publications.[36, 43, 167, 169-180] The database was curated on Excel, with each row containing a unique device obtained from published literature, with the DOI, processing information and target performance metrics (hole mobility) for each device stored as columns. The dataset comprises of 115 OFET devices fabricated from neat DPP-DTT (92 devices) as well as a blend of DPP-DTT with an insulating matrix like PDMS, polystyrene and PCBM (23 devices). In this work, we only focus on the 92 OFET devices fabricated from neat DPP-DTT. Here, 34 design variables/features were identified that were either numerical (21 features) or categorical (13 features). Examples of the numerical features include variables with continuous values such as polymer weight average molecular weight (M_w), polydispersity (PDI), solution concentration, etc. The categorical features include solvent type, deposition type, annealing environment, etc. In this approach we focus on the numerical processing variables.

For mobility values presented as graphs in publications, a semi-automated tool called DataThief[181] was used to extract the mobility values up to three significant figures from the scatter plots. The average OFET hole mobility is the target performance metric that will be focused on in this work and the values reported in this dataset range from 8.5 $cm^2/V.s$ to 1.0 x 10^{-5} $cm^2/V.s$, indicating the strong influence of the processing variables.

2.2.6 Customized Classification Algorithm

A custom classification algorithm developed by McBride *et al.*[168] was applied to only the numerical processing variables to identify the most insightful features that

would confine the "high" performing OFET devices to a reduced design region to gain new insights and guide future experiments. A schematic illustration of the classification approach is shown in Figure 2-2.

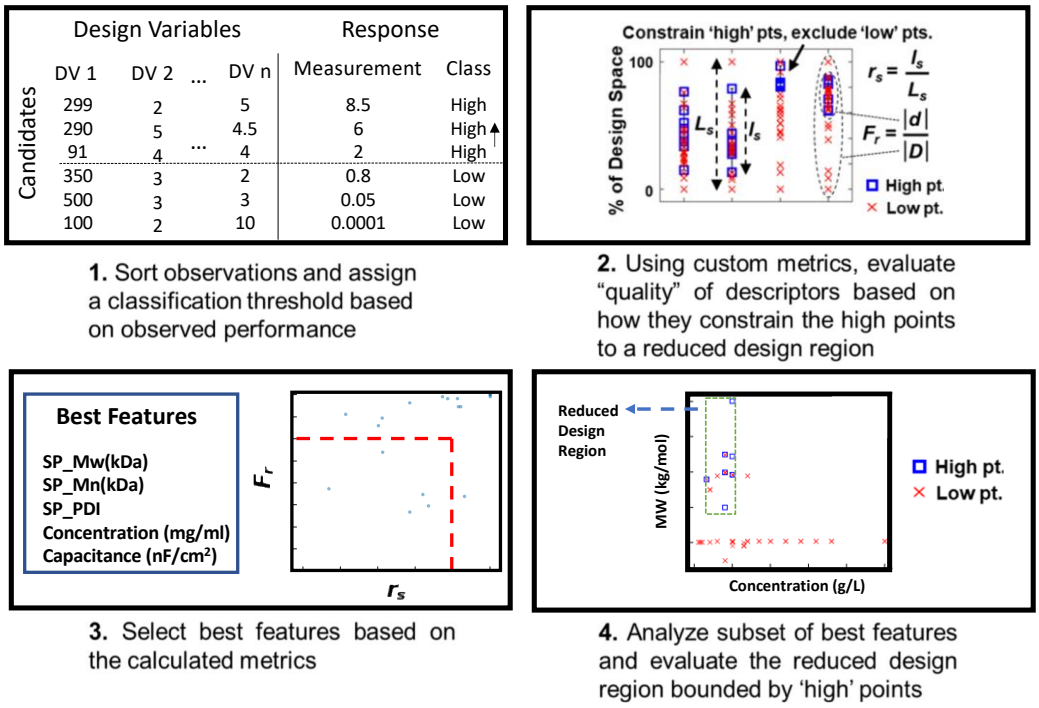

Figure 2-2. Schematic illustration of classification approach to select a smaller set of features that best separate "high" and "low" performers, and construct reduced design regions. Note the 1D reduced design region in Step 2 is not representative of the actual dataset and was created for better visual representation. DV=Design Variables. Diagram adapted from Liu et al. [129]

First, observations were sorted in decreasing order of average OFET hole mobility. A threshold of 1 $cm^2/V.s$ was used to assign a label of "high" or "low" to each data point and this threshold can be adjusted (Figure 2-2, Box1). A total of 16 "high" devices and 76 "low" were identified. Then, a RDR was constructed for each continuous process design variable by calculating the upper and lower bounds of the region containing only the "high" points as shown in Figure 2-3. The quality of the RDR for a specific feature was evaluated by considering two custom metrics that characterize the RDR relative to the total design

space. The size reduction metric r_s aids in searching for features in which the high points were constrained to a small fraction of the total design space. The metric F_r accounts for non-uniformity of data density and finds features that exclude more low observations in the RDR. A visual interpretation of r_s and F_r for a design variable is illustrated in Figure 2-3. A feature with a low r_s indicates that the "high" performing devices have been confined to small subset of the total design space. A feature with a low F_r indicates that the reduced design space excludes more "low" performing devices. Processing variables with a low r_s and low F_r within a dataset are likely to be key indicators of better performance.

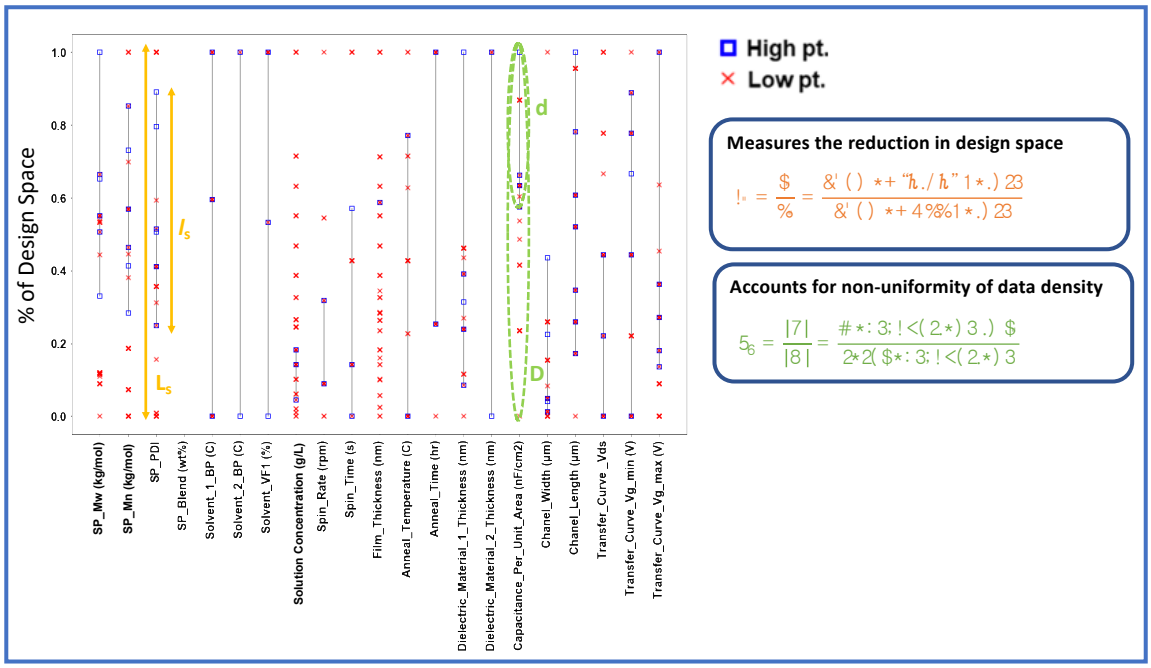

Figure 2-3. Classification approach of one-dimensional reduced design spaces containing OFET devices with hole mobility values exceeding 1 cm^2/V.s. This figure corresponds to box 2 in Figure 2-2. Blue squares represent "high" performing data points which are equal to or above the cutoff of 1 cm^2/V.s, red x markers represent "low" points below the cutoff and the black lines represent the span of the reduced design region in the 1D space.

To identify the most impactful features, the r_s and F_r values for each of the processing variables can be plotted against each other as shown in Figure 2-4. The best

features were selected based on an arbitrary cut-off criteria [r_s & F_r <0.8] which was governed by domain expertise and visual inspection of the separation within the classification metrics. The feature selection approach was integrated with bootstrapping and cross-validation to find a subset of best-performing features as shown in Figure 2-4. These selected features were then analyzed carefully to gain new insights.

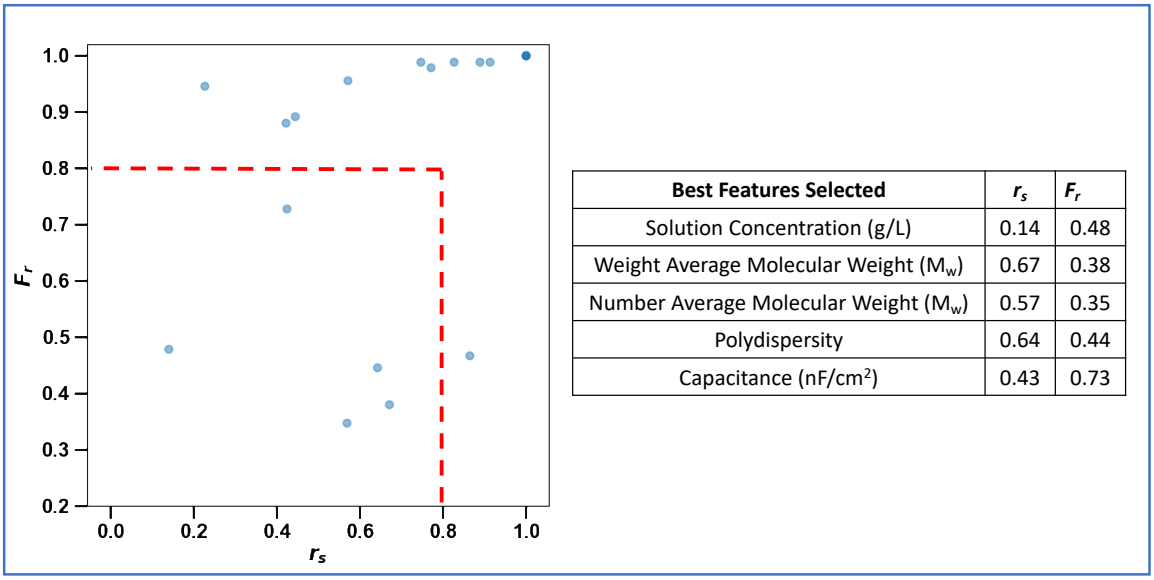

Best Features Selected	r_s	F_r
Solution Concentration (g/L)	0.14	0.48
Weight Average Molecular Weight (M_w)	0.67	0.38
Number Average Molecular Weight (M_w)	0.57	0.35
Polydispersity	0.64	0.44
Capacitance (nF/cm^2)	0.43	0.73

Figure 2-4. Custom metrics r_s and F_r for each numerical processing variable plotted against each other to identify the features/variables that confine the "high" performing points to a reduced design region. This figure corresponds to box 3 in Figure 2-2. An arbitrary threshold of r_s and F_r < 0.8 was selected for both metrics and this was governed by domain expertise and visual inspection of the separation within the classification metrics.

2.2.7 Investigating "High" Performing Devices

Total of sixteen "high" performing devices from 5 different publications

- Ten of the sixteen 'high' performing devices are from the same publication
- Two out of the five publications are from the same research group

Similarities in processing conditions between the high performing devices:

- Majority of the 'high' performing devices used chlorobenzene as the solvent. Of the "high" performing devices, thirteen were processed using CB as solvent, two using chloroform and one using Dichlorobenzene
- Majority of the 'high' performing devices used a concentration of 5 g/L. Ten of the "high" performing devices were made from a concentration of 5 g/L, five devices were made from a concentration of 4g/L and one was made from a concentration of 2g/L
- The solution processing environment for all sixteen 'high' performing devices were performing under ambient conditions
- Majority of the 'high' performing devices used N-doped SI as the substrate. Thirteen devices had N-doped SI as substrate, one had PET and one was unknown.
- Majority of the 'high' performing devices had source drain channels made out of gold. Fourteen devices had source/drain channels as Au, two were unknown.
- Majority of the 'high' performing devices used spin coating as the method for film deposition. Fourteen devices used spin coating for deposition, one inkjet and one blade coating.
- Majority of the 'high' performing devices had films deposited at ambient conditions. Fifteen devices had films deposited in ambient conditions and one was unknown.
- All of the 'high' performing devices used the saturation regime to extract the mobility.

The Excel database along with the python code for the classification algorithm and figure plotting is available for download at : https://github.com/rvenkatesh97/Reduced_Design_Region_Classification_DPPDTT_OFETs

2.3 Results and Discussion

In this work, a dataset comprising processing information and performance metrics associated with 115 DPP-DTT based OFET devices from 15 publications was curated and analyzed. The list of publications utilized for curating this dataset is provided in the supporting information. The classification algorithm developed by McBride *et al.*[129, 168] was applied to the curated dataset to identify the most impactful processing variables from a list of 21 numerical variables that confine the devices with a "high" OFET hole mobility (> 1 $cm^2/(V.s)$) to a reduced design space. The advantage of this algorithm is that it selects the key processing parameters from a long list of variables—thus preventing the need to investigate all the processing variables individually, which can be tedious and time-consuming. The full classification approach is discussed in detail in the methods section 2.2.5 and 2.2.6 along with the corresponding code. The best features selected by the algorithm were plotted as a function of the hole mobility to confirm the existing hypothesis, gain new insights and guide future experiments.

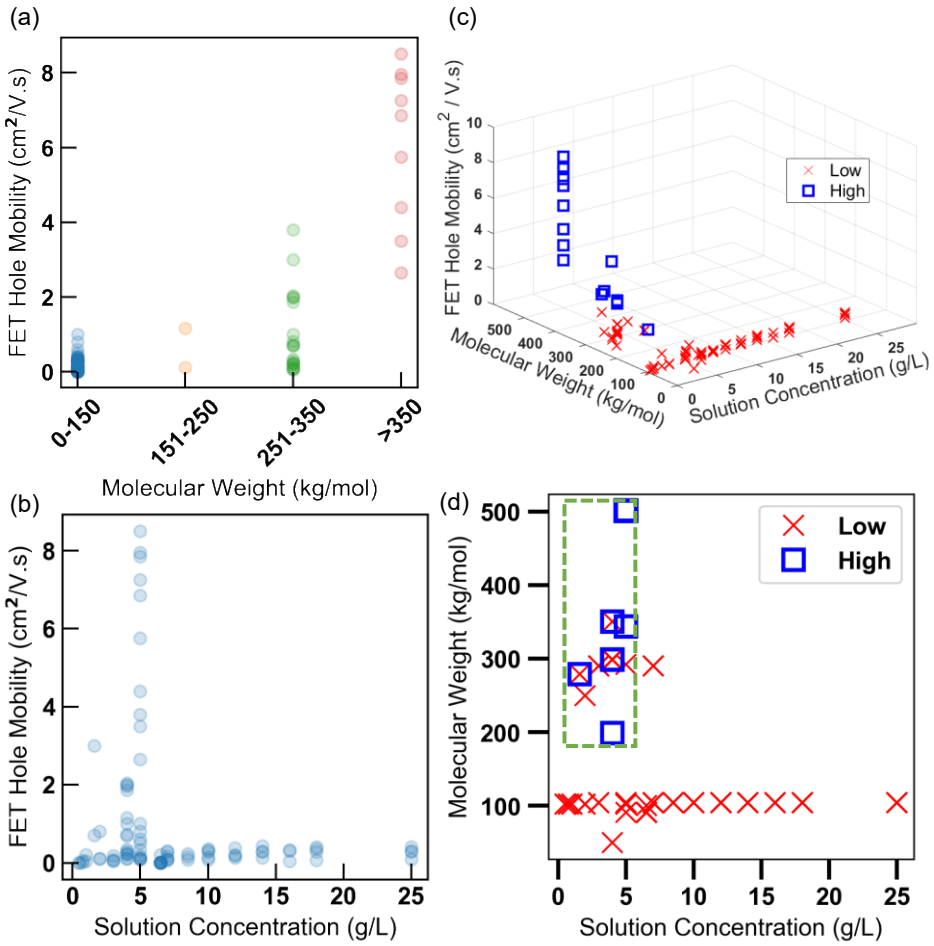

Figure 2-5. FET hole mobility versus (a) groups of weight average molecular weight (kg/mol), (b) solution concentration(g/L) and (c) weight average molecular weight (kg/mol) and solution concentration(g/L) as a three-dimensional plot. (d) Two-dimensional reduced design spaces containing all devices with hole mobility values above and below the cutoff of 1 cm^2/V.s for easier visualization. Blue squares are "High" data points above the cutoff(> 1 cm^2/V.s), red x markers represent "Low" data points below the cutoff(<= 1 cm^2/V.s), and the green dashed-lines represents the boundary of the reduced design region in the 2D spaces containing all the "high" points and some "low" points. Figure 2.5 c and d contain a total of 16 "high" points and 76 " low" points, with some of the points overlapping each other.

The key processing parameters identified by the algorithm based on user-defined specifications (i.e. those that were able to best confine the "high" performing devices to a reduced design space) include M_w, number average molecular weight (M_n), solution concentration (g/L), polydispersity and dielectric capacitance (nF/cm^2) (Figure 2-4). The

FET hole mobility increasing as a function of M_w, is shown in Figure 2-5a. This trend agrees with findings from existing studies on CPs whereby higher polymer M_w typically results in longer polymer chains that can connect ordered crystalline domains and offer enhanced charge transport performance.[38, 46] Perhaps more interesting and as can be discerned from Figure 2-5b, higher mobilities were obtained for devices prepared from solutions having a concentration between 4 and 5 g/L. Ten out of the sixteen "high" performing devices used a concentration of 5 g/L with CB as the solvent. Additional detail comparing the processing conditions for the "high" performing devices is provided in methods section 2.2.7. Conceivably, the majority of studies selected a solution concentration in this range to stay consistent with literature reports. The exact influence of this processing parameter on charge carrier mobility of push-pull polymers has not been widely investigated and provides an opportunity for further studies. Analysis of the other three key processing parameters can be obtained from the code available in the methods section 2.2.7. This insight highlights the advantage of the data curation exercise to uncover knowledge gaps. Finally, subsets of the best features can be analyzed simultaneously, and a RDR bounded by high-performing points can be evaluated to guide future experiments. Results from Figure 2-5 c and d indicate that choosing a value of M_w between 200-500 kg/mol and solution concentration between 2-5 g/L would be more likely to result in a high-performing OFET device.

As recommended by the RDR algorithm, DPP-DTT (Figure 2-6a), with a M_w of 290 kg/mol, in chlorobenzene was used as an initial system of interest. Solution concentrations ranging from 1– 8 g/L were prepared from a stock of 10 g/L. Note, the solution-state of CPs is typically neglected and needs to be studied to establish clear

relationships between solution-state structures, solid-state morphology and charge transport properties.[182] Viscosity measurements of the solutions at different concentrations were conducted to explore the influence of solution concentration on the behavior of polymer chains in the solution state.

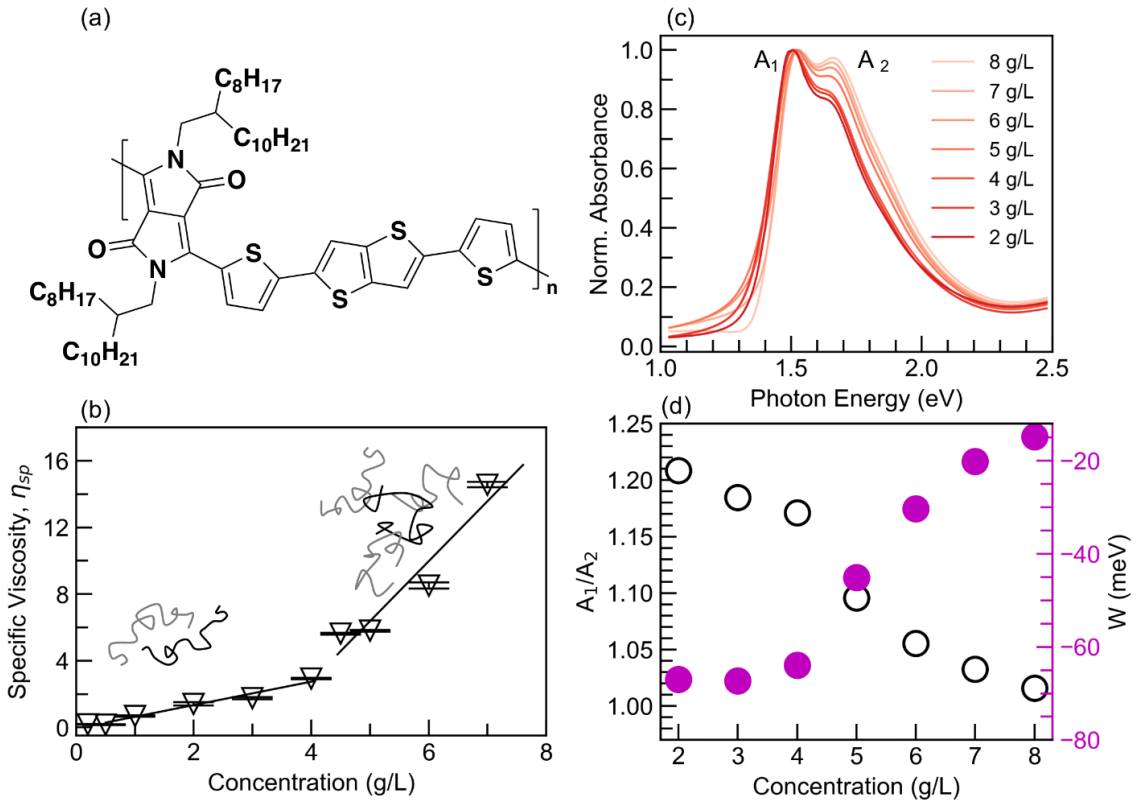

Figure 2-6. (a) Schematic of molecular structure of DPP-DTT. (b) Viscosity measurement of DPP-DTT dissolved in chlorobenzene solutions at 56 °C. The error bars represent the standard deviation of the specific viscosity (open triangles). The schematic illustrates the extended, isolated polymer chains in dilute solutions and kinky, intertwined polymer chains in semi-dilute solutions.(c) Linear absorption spectra of DPP-DTT thin films prepared from solution concentrations ranging from 2 to 8 g/L. (d) A_1/A_2 ratio (open circle) and exciton bandwidth (filled circle) acquired from Franck Condon simulations as a function of concentration.

We discerned an expected increase in the specific viscosity with increasing solution concentration as seen in Figure 2-6b. An interesting observation was the presence of a two-

regime behavior, with the cross-over occurring ~ 5 g/L, which can be attributed to the critical chain overlap point C*.[183, 184] This behavior suggests that the polymer chains or aggregates are more extended and isolated at dilute concentrations (< C* g/L), then start to overlap when the concentration surpasses C* and finally become entangled as displayed in Figure 2-6b. The solution-state absorption spectra of 2 and 8 g/L polymer solutions (Figure A-1), display a more dominant J-like character compared to the corresponding solid-state films, indicating that polymer chains in solution are more isolated than solidified thin films even in semi-dilute regime.

To transfer the chain overlap effect from the solution state to the solid film state, a series of wire-bar coated films were prepared from polymer-CB solutions ranging in concentration from 2 to 8 g/L, with the substrate and solution temperatures being maintained at 56 °C. To probe the influence of solution concentration on the polymer excitonic chain interactions, the photophysical features of the solid thin films were examined using steady-state UV-vis absorption spectroscopy as presented in Figure 2-6c. Here, we focus on the low energy band where localized excitation on the DPP unit is dominant.[185] Analogous to P3HT, the coupling between the electronic excitation and aromatic ring stretching mode could still lead to pronounced vibronic progressions.[186] The ratio of the vibronic progressions of A_1 and A_2 peaks are provided in Figure 2-6d and is observed to be consistently higher than 1, which might be due to the J-type nature of strong intrachain charge-transfer character as investigated recently by Qarai *et al.*[186] A decreasing trend for the A_1/A_2 with increasing solution concentration indicates that films coated from semi-dilute solutions (> C*) may adopt more H-aggregate configurations than films prepared from dilute solutions (< C*). Additionally, the modified

Franck Condon (FC) analysis (assuming a Huang-Rhys factor of 1) was performed within the exciton resonance region from 1.4 to 1.8 eV to extract the *effective* exciton bandwidth (W), which quantifies the effective interchain coupling constant.[53] The complete set of FC fits for the absorption spectra of each concentration along with the parameters obtained for the same is presented in Figure A-2. The magnitude of W decreases with increasing concentration, corresponding to a smaller coupling constant, indicating an increasing H-type interchain interaction (Figure 2-6d).[83, 84] Moreover, with increasing H-type coupling, the A_1 peaks are observed to blue-shift slightly which is consistent with the H-aggregate model.[53, 89] It is worth pointing out, the different electronegativity between donor and acceptor units also modifies the Kasha model which assumes no wavefunction overlap.[83, 187] Nevertheless, the intrachain charge-transfer character/Frenkel exciton mixing as well as interchain Coulombic interactions would give rise to similar Kasha spectral features[83, 186] and the modified FC progression takes into account the contribution from excitonic dispersion in the weak coupling limit. The exciton bandwidth and coupling constant could be understood as an *effective* term. Moreover, the spectral features and the magnitude of exciton bandwidths reproduced by the HJ aggregate model are mostly consistent with situations seen in semicrystalline P3HT within the weakly-coupled limit.[53, 92] Thus, it is suggested that as both the A_1/A_2 and W trends exhibit two regime behavior, analogous to the viscosity results, the chain entanglements inherent in polymer solutions may be preserved in the solidified films. Transient absorption measurements are expected to provide further insight regarding the impact of chain entanglement on the photoinduced absorption line shape. The surface microstructure of thin films at different concentrations were also investigated

using atomic force microscopy (AFM) and cross-polarized optical microscopy (CPOM), and the images are presented in Appendix A. The AFM height and phase images (Figure A-3) indicate fibrillar structures are formed in films prepared from more dilute concentrations which then disappear as solution concentration increases and the films ultimately become featureless. The CPOM images (Figure A-4) indicate a clear change in intensity from low to high concentration, likely due to changes in film thicknesses. It is worth mentioning that the noisy dots in the background of the CPOM images might be attributed to disordered aggregates, which increase in thickness (Figure A-5) with increasing concentration.

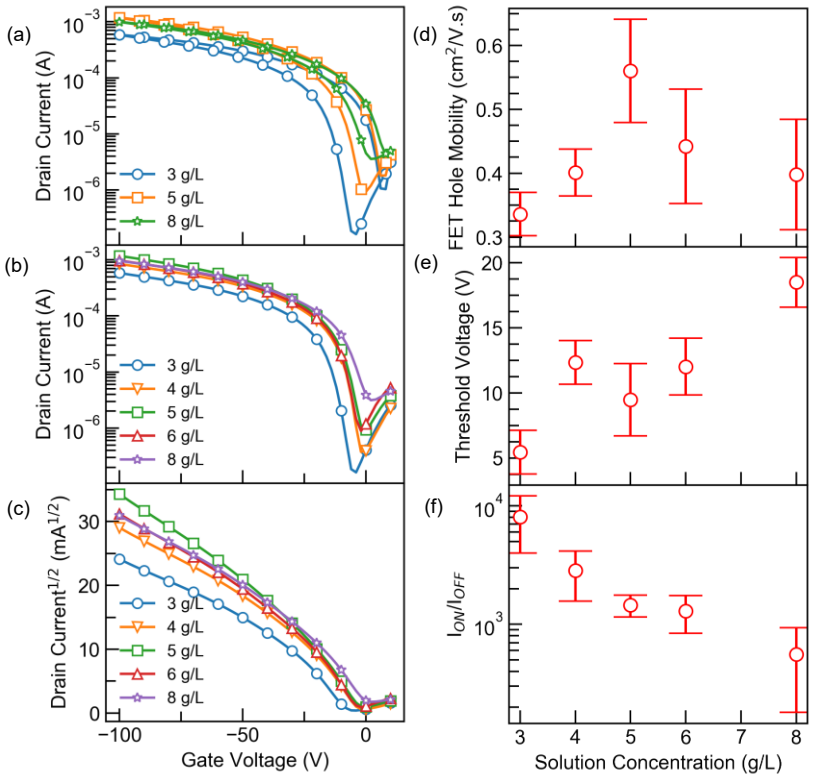

Figure 2-7. Transfer Characteristics (V_{DS} = -80V) and OFET parameters of interest for DPP-DTT thin films as a function of solution concentration. (a) Forward and backward sweep I_D – V_G curves at concentrations of 3, 5 and 8 g/L exhibiting hysteresis. (b) and (c) Backward sweep transfer characteristics (V_{DS} = -80V) as a function of solution concentration. (d) and (e) FET hole mobility and threshold

voltage extracted from the backward sweep transfer curve ($I_D^{1/2}$ - V_G) as a function of solution concentration. (f) I_{on}/I_{off} obtained from the backward sweep transfer curve (I_D – V_G) as a function of solution concentration. The error bars here represent 95% confidence intervals averaged over 8-12 OFET devices.

The electronic performance of the films at different concentrations was investigated by fabricating OFETs using BGBC Si/SiO_2 substrates. The respective transfer and output characteristics are shown in Figure 2-7 (a-c) and Figure A-6, respectively. The transfer curves exhibit hysteresis with the current being higher on the forward sweep towards larger ON voltages than on the reverse sweep as shown in Figure A-7 and Figure 2-8.

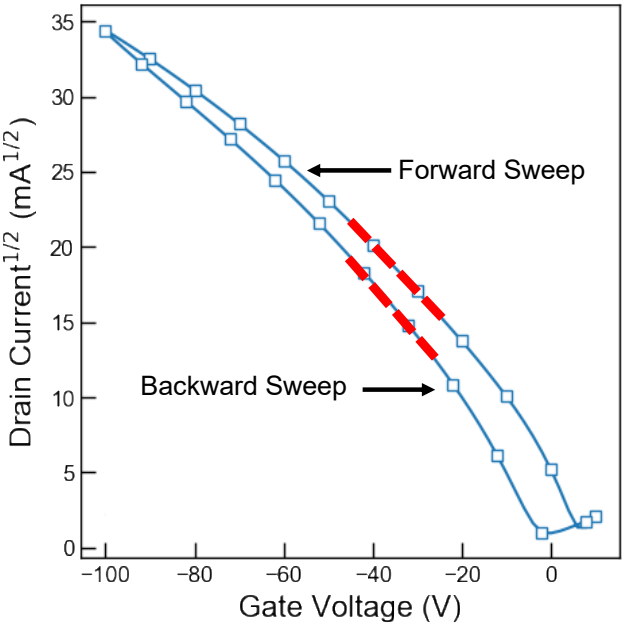

Figure 2-8. Backward and forward transfer characteristics ($I_D^{1/2}$ - V_G) exhibiting regions of different slopes at lower and higher gate voltages. The mobility and threshold voltage for the forward and backward sweeps were extracted by fitting the saturation equation to the red dashed line ranging from V_G = -45 to -25V. This range was selected based on the output characteristics in order to ensure we are in the saturation regime.

This behavior is likely due to the current in the OFET degrading during the timescale of the electrical measurement as a result of dispersive transport or charge trapping in the organic semiconductor or at the interface.[20] For the $I^{1/2}_d$-V_g curves, two regions of different slopes at lower and higher gate voltages were observed. This behavior has been observed previously for other high mobility D-A copolymers in bottom gate OFETs with self-assembled monolayer modified SiO_2 gate dielectric.[46, 166, 188-190] Sirringhaus *et al* suggested that this behavior can be attributed to contact resistance effects, where the current becomes more contact-limited at higher gate voltages and the interfacial accumulation layer becomes more conducting.[18] Another possible explanation is that at higher gate voltages, charges from the accumulation layer are injected into the dielectric or interface and become trapped[20, 191]. As recommended by McCulloch *et al.*[191] and Sirringhaus *et al.* [20] the low slope linear region, depicted by the red line in Figure 2-8, was used to extract a more conservative charge carrier mobility that is closer to the true value.

The hole mobility, threshold voltage and I_{on}/I_{off} as a function of solution concentration extracted from the backward sweep, are presented in Figure 2-7 d, e and f, respectively. Figure 2-7 d indicates a clear increase in hole mobility as the dilute concentrations increase to C* (5 g/L) followed by a decrease in the average mobility. Although, the mobility value at 5 g/L does not cross the threshold (1 $cm^2/V.s$) set during the analysis of the curated OFET dataset, the results in general are in good agreement with the insights from the classification algorithm. It is important to note that device measurements in general can be challenging to compare across the literature due to the different setup conditions[149, 168] and extraction of performance

metrics from different curve regimes.[20, 191] The maximum FET hole mobility of 0.56 cm^2/Vs was obtained at the critical chain overlap concentration, C*, of 5 g/L and the polymer chain overlap in the solution state appears to contribute to improved charge transport in the solid state. This behavior may be analogous to the tie molecules in high molecular weight P3HT that connect crystalline domains together and improve charge transport.[59, 165, 192, 193] A similar trend was observed for hole mobilities extracted from the forward sweep (Figure A-8) as shown in Figure A-9. Additionally, for concentrations greater than 5 g/L, we observe greater variations in the hole mobilities across different OFET devices as represented by the larger error bars. At these concentrations, it is possible that excessive chain entanglement in the solid state leads to spatial defects or charge traps in the thin films. Also, the high viscosity may negatively impact process control during film fabrication, leading to less uniformity. Note that the average threshold voltage increases from 5V to 18V while I_{on}/I_{off} decreases by a factor of 10 with increasing solution concentration, indicating a possible higher density of charge traps.

To confirm if this new insight on the key role of solution concentration is potentially general, the previously curated P3HT dataset[149, 168] was revisited to investigate if the data curation approach yields a similar dependance of mobility on concentration. Unlike the DPP-DTT dataset, the algorithm provided a wider range of concentrations to investigate for the P3HT dataset as shown in Figure 2-9.

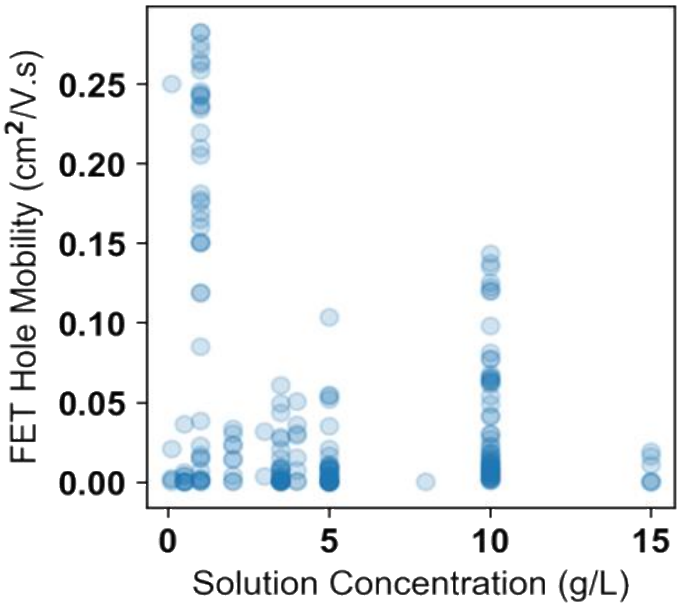

Figure 2-9. FET hole mobility versus solution concentration (g/L) for 202 P3HT devices across the literature. "High" performing devices have a mobility greater than 0.1 cm^2/V.s. The optimum solution concentration range selected by the classification algorithm is from 1-10 g/L.

Concentrations of 5 and 10 g/L suggested by the algorithm do fall in critical chain overlap concentration ranges determined by previous work.[192, 194] It is important to note that the P3HT dataset contains a broader range of M_w's and solvents compared to the DPP-DTT dataset, both of which have been shown to shift the critical overlap concentration.[192] To the best of our knowledge, the influence of solution concentration on FET hole mobility has not been investigated for semicrystalline homopolymers like P3HT, making it difficult to confirm the chain overlap hypothesis suggested by the DPP-DTT exercise. This finding further highlights the need to perform more experiments, not only for D-A polymers like DPP-DTT, but also with semicrystalline homopolymers to investigate the influence of solution concentration on device performance and further strengthen our findings.

2.4 Conclusions

We demonstrated that by integrating a data science approach into the existing polymer electronics paradigm, we can gain new insights and guide future experiments to accelerate learning and optimization. The customized classification algorithm when applied to the curated dataset revealed that the polymer solution concentration is an impactful feature that is able to confine "high" performing OFET devices to a reduced design region. Based on the design guidelines suggested by the classification approach, experiments were performed to investigate the influence of solution concentration on the optoelectronic properties of DPP-DTT and confirmed the insights from the data curation exercise. Viscosity measurements of the solutions at different concentrations identified the critical polymer chain overlap concentration occurs at ~ 5 g/L; a result that can be interrogated through future small angle neutron scattering experiments.[182, 194] Application of the weakly-coupled H-J aggregate model to the linear UV-vis absorption spectra revealed that polymer films deposited from semi dilute solutions exhibited a stronger H-type interaction as compared to films prepared from dilute solutions. To gain further insights on the influence of the solution concentration induced chain entanglement on the absorption line shape, transient absorption measurements will be performed to investigate the energetic landscape. Lastly, the electronic performance of the semiconducting thin films prepared from different concentrations was characterized using OFETs. The experimental device results were in good agreement with the design range suggested by the classification algorithm. An increase in the FET hole mobility was observed as the polymer solution concentration approached C*, suggesting that the effective chain overlap is a critical design parameter that impacts charge carrier transport in D-A

semiconducting polymers. Our findings highlight the importance of polymer solution concentration as a parameter that must be optimized for the fabrication of conjugated polymer-based devices and the critical need to further investigate the impact of this processing parameter to gain a thorough understanding of the process-structure-property relationship.

CHAPTER 3. OVERLAP CONCENTRATION GENERATES OPTIMUM DEVICE PERFORMANCE FOR DPP-BASED CONJUGATED POLYMERS

To what extent can the observed trend in the previous chapter, regarding the impact of solution concentration on device performance, be generalized across various DPP-based polymers and extended to other D-A polymers? Does an optimum value for this processing variable exist, and how does the manipulation of this variable influence solution state aggregation, film morphology, and eventual device performance?

This chapter addresses these questions by investigating the influence of solution concentration, on the optoelectronic properties of D-A polymers, with a focus on DPP-based polymers. Experiments revealed a C* identified through viscosity studies, at which film fabrication consistently led to enhanced device performance. The C* corresponds to a solution state with overlapping polymer chains, shown to promote the formation of ordered morphologies that likely explains the improved charge transport observed in solid films. This chapter and Appendix B are adapted from a published article.[76] Reprinted with permission from Organic Electronics:

Venkatesh, R.; Zheng, Y.; Liu, A. L.; Zhao, H.; Silva, C.; Takacs, C. J.; Grover, M. A.; Meredith, J. C.; Reichmanis, E., Overlap concentration generates optimum device performance for DPP-based conjugated polymers. *Organic Electronics* **2023,** *117*, 106779. doi:https://doi.org/10.1016/j.orgel.2023.106779.

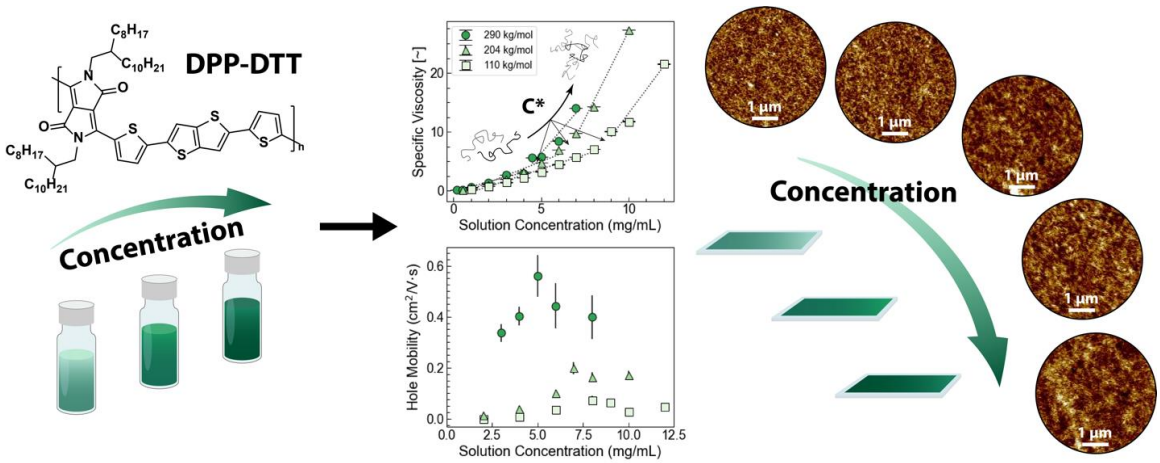

Figure 3-1. Graphical summary of chapter 3. The influence of solution concentration on the optoelectronic properties of DPP-based D-A polymers is investigated. OFET devices fabricated at the critical overlap concentration (C*), obtained from solution viscosity experiments, consistently resulted in improved hole mobility, irrespective of the polymer M_w chosen. The overlapping of polymer chains in the solution state at C*, likely results in ordered morphology in the film state that may explain improved charge transport.

3.1 Introduction

To exploit the full potential of D-A polymers, a detailed investigation of the solution state in conjunction with thin-film characterization is required to obtain understanding of the phenomena that influence and control polymer chain conformation and aggregation, final film morphology, and device performance.[29, 81, 195-197] Disregarding solution state behavior can lead to imperfect understanding of critical PSP relationships and subsequently the final thin-film properties.[29] A common strategy to manipulate the solution behavior of conjugated polymers to achieve desired thin-film morphology and improved device performance is to tune solvent quality[81, 177, 195, 197] or control solution temperature,[77, 198] but other strategies have also been explored. Results from the previous chapter revealed a significant influence of the processing variable, solution concentration, on the optoelectronic properties of DPP-DTT.[82] Interestingly, it was observed that OFET devices

prepared from the C* resulted in improved device performance and thin films prepared at semi-dilute concentrations displayed more interchain (H-aggregate) behavior. Although previous studies have tuned the solution concentration to induce aggregation[167, 199], to the best of our knowledge, the effect of concentration has not been adequately linked to macroscale device performance of D-A polymers and this relationship is yet to be fully understood. Investigating the solution phase will allow us to better understand the transitions taking place from the solution state to the final thin film.

Solution viscosity provides information on the behavior of polymer chains in solution and has been used effectively to probe polymer-solvent interactions, chain conformations, and degree of entanglements of well-known flexible polymers; their solution phase conformations and dynamics are generally well understood.[200, 201] However, the behavior of conjugated polymers in solution differs from that of flexible polymers due to their more rigid, semiflexible backbones with more anisotropic geometries and conjugated backbone interactions, which makes their aggregate structure and chain conformation more difficult to predict using previously developed models.[195, 202, 203] While a few studies on semiconducting polymers such as P3HT point to solution viscosity as an indicator of polymer solution behavior and its impact on solidified thin-film charge transport,[192 59] to the best of our knowledge, the chain overlap concentration is not a factor that has been considered to explain the solution state behavior of D-A polymers or its impact on resultant film morphology and charge transport characteristics.

In this work, using DPP-DTT as a model for other DPP-based candidates, we study the influence of solution concentration on the polymer charge transport characteristics as

determined by OFET device performance. The concentration dependence of DPP-DTT, at different molecular weights, was interrogated in both the solution state and thin films. Photophysical, morphological and electronic performance was explored using UV-Vis absorption spectroscopy, CPOM, AFM, grazing incidence wide angle X-ray (GIWAXS) scattering experiments and OFET device performance. The results were correlated with solution concentration as determined. Notably, similar results were observed for another DPP based polymer; poly[2,5-bis(2-octyldodecyl)pyrrolo[3,4-c]pyrrole-1,4(2H,5H)-dione-3,6-diyl)-alt-(2,2';5',2'';5'',2'''-quaterthiophen-5,5'''-diyl)] (PDPP-4T) as well as an NDI based polymer; Poly[N,N'-bis(2-octyldodecyl)naphthalene-1,4,5,8-bis(dicarboximide)-2,6-diyl]-alt-5,5'-(2,2'-bithiophene) (N2200), suggesting that the observed phenomenon may be applicable to other D-A-based polymers as well.

3.2 Materials and Methods

3.2.1 Materials

DPP-DTT at three different molecular weights, Batch M317 : Mw = 290 kg mol-1 and PDI = 2.03, Batch M0311A2: Mw = 204 kg mol-1 and PDI = 3.09, Batch M0311A3: 110 kg mol-1 and PDI = 2.47, PDPP-4T (Batch M0331A2: Mw = 75 kg mol-1 and PDI = 1.75) and N2200 (Batch M1201A3 : Mw = 202 kg mol-1 and PDI = 2.22) were purchased from Ossila Ltd. CB (anhydrous) was purchased from Sigma-Aldrich.

3.2.2 OFET Fabrication

A detailed description of the OFET fabrication process is provided in the methods section of previous chapter (2.2.2).

3.2.3 Sample Preparation

For DPP-DTT, PDPP-4T and N2200 sample preparation, a stock solution was prepared by dissolving the polymer in CB (anhydrous, Sigma-Aldrich) at 100 °C for 4 h, followed by continued heating at 56 °C overnight. The concentration of the stock solutions used for the respective polymers is shown in Table 3-1 and the smaller concentrations were prepared from the respective stock solution. The thin films were prepared by blade coating the solutions onto the substrates (glass and OTS-18 treated silicon/SiO_2) at coating temperature of 56 °C, with a shearing speed of 2 mm/s followed by annealing at the same temperature for 10 min.

Table 3-1. Stock solution concentration used to prepare samples

Polymer	**Molecular Weight (M_w) (kg/mol)**	**Stock Solution Concentration (g/L)**
DPP-DTT	290	8
DPP-DTT	204	10
DPP-DTT	110	12
PDPP-4T	75	12
N2200	202	10

3.2.4 Characterization Methods

3.2.4.1 Solution Viscosity Measurement

Solution viscosity was measured using a DV2T Brookfield cone and plate viscometer with a CPA-40Z spindle. For DPP-DTT and PDPP-4T solutions dissolved in chlorobenzene at different concentrations, the solution viscosity was measured at 56 °C using a setup consisting of a Brookfield TC-650 water bath.

3.2.4.2 Steady-State Linear Absorption Spectroscopy

A detailed description of the UV-Vis absorption process is provided in the methods section of previous chapter (2.2.4.2).

3.2.4.3 OFET Characterization

A detailed description of the OFET characterization process is provided in the methods section of previous chapter (2.2.4.3).

3.2.4.4 Atomic Force Microscopy (AFM)

A detailed description of the AFM process is provided in the methods section of previous chapter (2.2.4.4).

3.2.4.5 Profilometry

A detailed description of the thickness measurement is provided in the methods section of previous chapter (2.2.4.5).

3.2.4.6 Cross Polarized Optical Microscopy (CPOM)

A detailed description of the CPOM process is provided in the methods section of previous chapter (2.2.4.6).

3.2.4.7 Grazing Incidence Wide Angle X-Ray Scattering (GIWAXS)

GIWAXS measurements were conducted at the SLAC National Accelerator Laboratory on beamline SSRL 11-3. The beam was fixed at an energy of 12.7 keV and the critical angle was 0.12°. Conjugated polymer thin films of varying concentrations were prepared on bare silicon substrates using the same deposition and annealing technique mentioned above.

3.3 Results and Discussion

The impact of solution concentration on the optoelectronic properties of D-A polymers was investigated using DPP-DTT (Figure 3-2 a) dissolved in CB as a model. Three different molecular weight samples were selected, namely DPP-DTT having a M_w of 290 kg/mol, 204 kg/mol and 110 kg/mol. Solutions at different concentrations ranging from 1-12 g/L were prepared from concentrated stock solutions (Table 3-1).

(a)

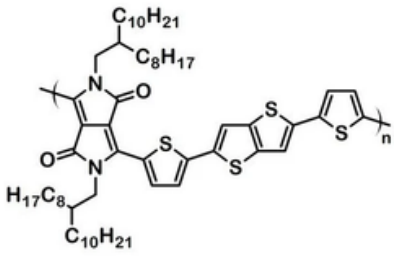

(b)

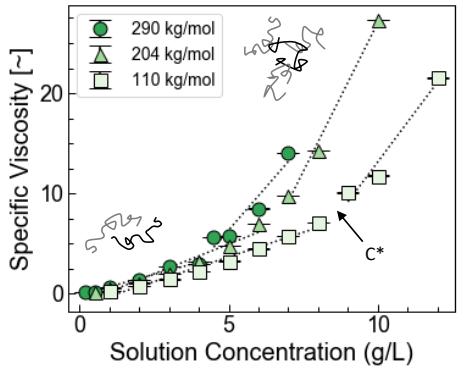

(c)

M_w (kg/mol)	C* (g/L)
290	4.5
204	6.5
110	8.5

(d)

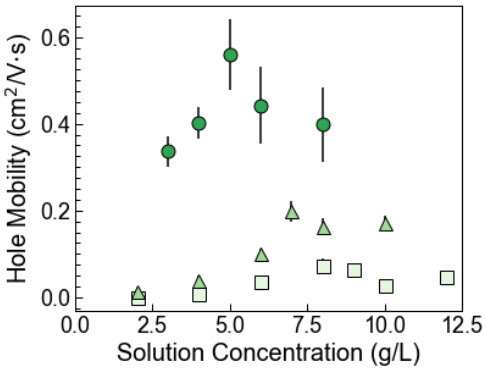

Figure 3-2. (a) Schematic of molecular structure of DPP-DTT. (b) Specific viscosity measurement of DPP-DTT at three molecular weights (290, 204 and 110 kg/mol) dissolved in chlorobenzene solutions at 56 °C. The error bars represent the standard deviation of the specific viscosity. The schematic within the plot illustrates the extended, isolated polymer chains at dilute concentrations and overlapped polymer chains at semi-dilute concentrations. (c) The critical overlap concentration, C*, values extracted from the viscosity-concentration plots for the three different molecular weights of DPP-DTT investigated. C* is the concentration at which the slopes of the two dashed lines intersect. (d) FET hole mobility of DPP-DTT thin films at three molecular weights (290, 204 and 110 kg/mol) extracted from the backward sweep transfer curve (V_{DS} = -80V) as a function of solution concentration. The error bars here represent 95% confidence intervals averaged over 18 OFET devices.

Viscosity measurements of DPP-DTT:CB solutions at different concentrations were performed to investigate the effect of solution concentration on the behavior of polymer chains in the solution state. An increase in the specific viscosity with increasing solution concentration for all three M_w's of DPP-DTT was observed (Figure 3-2b). Each sample exhibited two-regime behavior, with a power law slope increase in the specific viscosity occurring at the corresponding concentrations in Figure 3-2c. Similar behavior

has been observed previously for linear polymer systems and the concentration at which the slope of the viscosity-concentration line changes is referred to as the critical overlap concentration or C*.[204-208] The C* values extracted from the viscosity-concentration plots for the three different M_w's of DPP-DTT investigated are shown in the table in Figure 3-2c. Changes in the slope of the viscosity-concentration line for the three M_w's investigated is provided in Figure B-1 and is in agreement with literature values.[204, 209, 210] C* typically indicates the transition from a dilute to a semi-dilute regime. In the dilute regime, it is believed that the polymer chains are separated from each other and behave independently. In the semi-dilute region, excess polymer chains may act as 'cross linkers' and begin to overlap, eventually resulting in entangled structures at high enough concentrations, thus explaining the significant increase in viscosity.[211] Furthermore, solutions at concentrations of C* and higher tend to form a gel upon aging for one week at room temperature as seen in Figure 3-3, while dilute solutions(<C*) at room temperature remain liquid irrespective of the aging time.

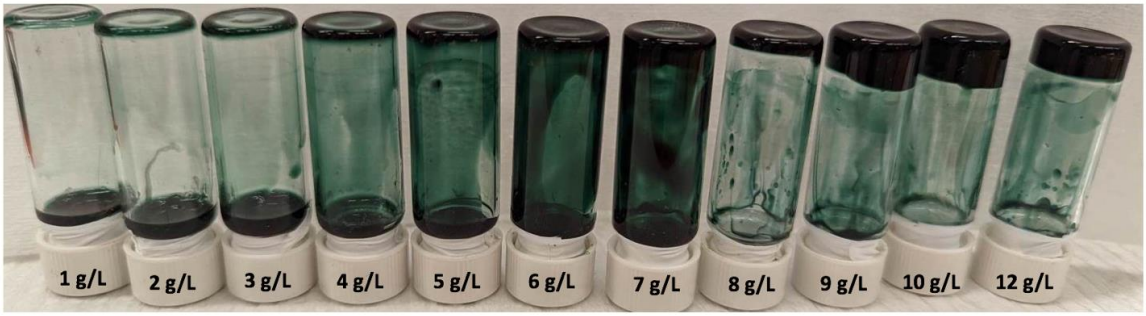

Figure 3-3. DPP-DTT (Mw = 110 kg/mol) solutions at concentrations ranging from 1-12 g/L that were aged for one week and were flipped over to indicate the formation of a gel at concentrations approaching C* (8.5 g/L) and higher. The solutions at concentrations below C* maintained their fluidity and were still a liquid. A similar behavior was also observed for the other two molecular weights of DPP-DTT investigated.

It is expected that C* increases as polymer M_w decreases: at a lower M_w the shorter polymer chains would require a greater solution concentration for the chains to interact and entangle[210]. In addition to experimental determination of C*, a theoretical value was calculated using the Huggins and Kramer equations (Figure B-2).[200, 201, 212] While there is a significant difference between the experimental and theoretical values, the overall inverse relationship of C* vs. M_w holds true. Given that the Huggins and Kramer equations assume that the polymers do not aggregate in the solution state, the observed differences with experimental results is not surprising.[201]

The influence of solution concentration and polymer M_w on the hole mobility of DPP-DTT was investigated in Figure 3-2d. Notably, for each M_w, a peak hole mobility is obtained for OFET devices prepared from the solution concentrations near C*. This observation is in good agreement with our prior result where we hypothesized that the polymer chain overlap in the solution state at a concentration of C* appears to contribute to improved charge transport in the solid state.[82] For all three DPP-DTT samples, hole mobility decreased at solution concentrations greater than C*. It is likely that above C*, excessive chain interactions in the solid state lead to spatial defects or charge traps in the thin films.[59] Higher viscosity solutions were also observed to coat less uniform films, a feature that could also negatively impact performance. An almost identical trend was observed by Sarkar et al as they investigated the influence of film thickness on the device performance of OFETs fabricated from DPP-DTT using spin-coating and the thickness of the films was varied by tuning the solution concentration and spin rate.[167] Furthermore, the peak hole mobility decreases as M_w decreases: higher polymer M_w typically results in improved charge transport as a result of longer polymer chains that connect ordered

domains[38, 174]. A similar trend was observed for the OFET hole mobilities extracted from the forward transfer curve as shown in Figure B-3. *These results indicate that there exists an optimum solution concentration, C*, for each of the M_w's investigated which can maximize charge transport as measured via OFET hole mobility.*

The respective transfer and output curves for the DPP-DTT devices studied here are presented in Figure B-4-Figure B-6 and Figure B-7-Figure B-9, respectively. The transfer curves for the high M_w 290 kg/mol DPP-DTT show deviation from ideal behavior (hysteresis and different slope regions). The hysteresis is likely attributed to the degradation of the current during the measurement due to charge trapping occurring in the organic semiconductor or at the interface.[20] In addition to hysteresis, two regions of different slopes at the lower and higher voltages were observed, which can lead to mobility overestimation - a phenomenon that has been observed for other D-A polymer systems.[166, 174, 188, 189] This behavior is typically attributed to large contact resistance because of a large injection barrier at the contacts.[20, 191, 213] Hence, the linear region with a lower slope (higher V_g) was used to extract a more conservative estimate for hole mobility that is closer to the representative value. These deviations from ideal behavior were significantly reduced for the lower M_w DPP-DTT polymers (204 kg/mol, 110 kg/mol). Although the peak hole mobility decreased, there was a reduction in hysteresis and two-regime behavior was not apparent. Thus, consideration should be given to lower M_w D-A polymers to avoid deviations from ideal transfer curve behavior, even if hole mobility may be somewhat compromised. The average threshold voltage (V_{th}) and I_{on}/I_{off} extracted from the transfer curves for the three different M_w polymers as a function of solution concentration are given in Figure B-10 where it can be observed that all three DPP-DTT samples investigated here

exhibit an increase in V_{th} as a function of solution concentration with no obvious trend for I_{on}/I_{off}.

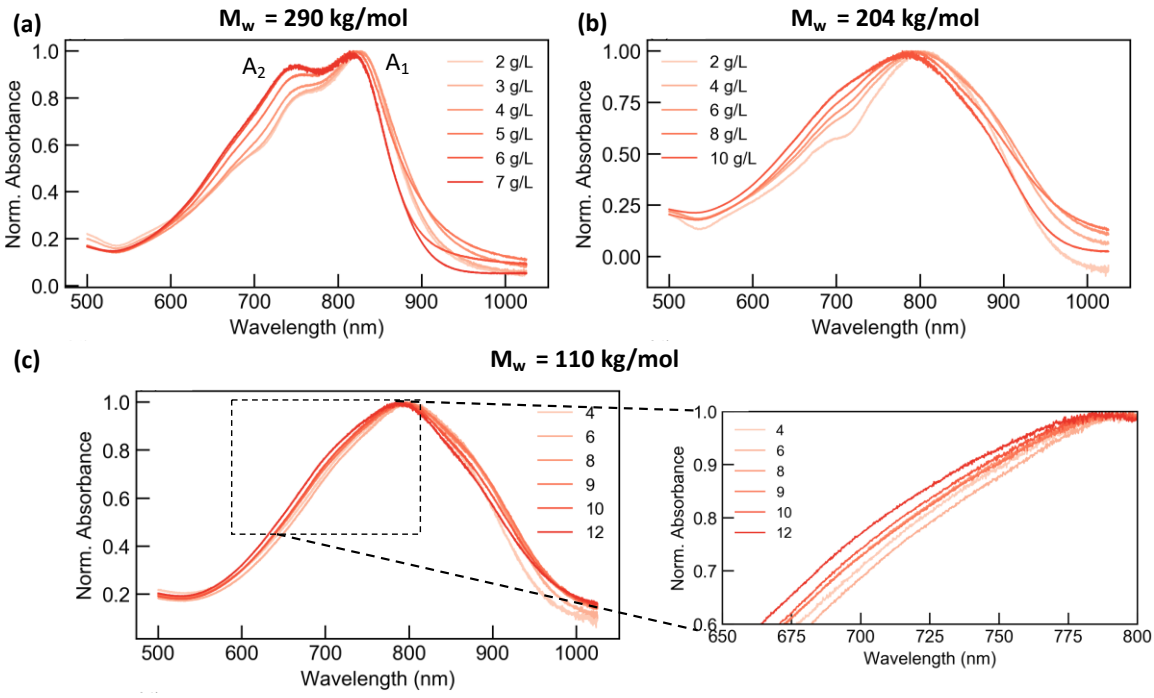

Figure 3-4. Normalized UV-Vis linear absorption spectra of DPP-DTT thin films prepared from the range of solution concentrations investigated respectively for three different weight average molecular weights (a) 290 kg/mol, (b) 204 kg/mol and (c) 110 kg/mol.

UV-Vis absorption spectroscopy was used to probe the influence of solution concentration on the solid-state polymer chain excitonic interactions for the three different M_w's of DPP-DTT as shown in Figure 3-4, with a focus on the absorption band in the low energy range that is assigned to the π-π* transition of the DPP unit.[167, 214, 215] For all three DPP-DTT samples, an increase in the intensity of the spectra in the ~750 nm region with increasing solution concentration can be observed, along with a blueshift which indicates increased excitonic interchain interactions. Such behavior corresponds to the H-type aggregation, as previously seen in spin-coated P3HT thin films, where the chromophores

have a side-by-side geometry, leading to an increased excited state energy.[53, 216] For the high M_w DPP-DTT (290 kg/mol) in Figure 3-4 a, two peaks can be observed at ~820 and 750 nm that are assigned to the A_1 and A_2 peaks of the vibronic transitions of the DPP π-π* transition, respectively. The ratio of the vibronic progressions of the A_1 and A_2 peak and the exciton bandwidth, extracted using the modified Franck-Condon analysis is given in Figure 3-5, and provides information on the packing order of the photophysical aggregates as a function of solution concentration.

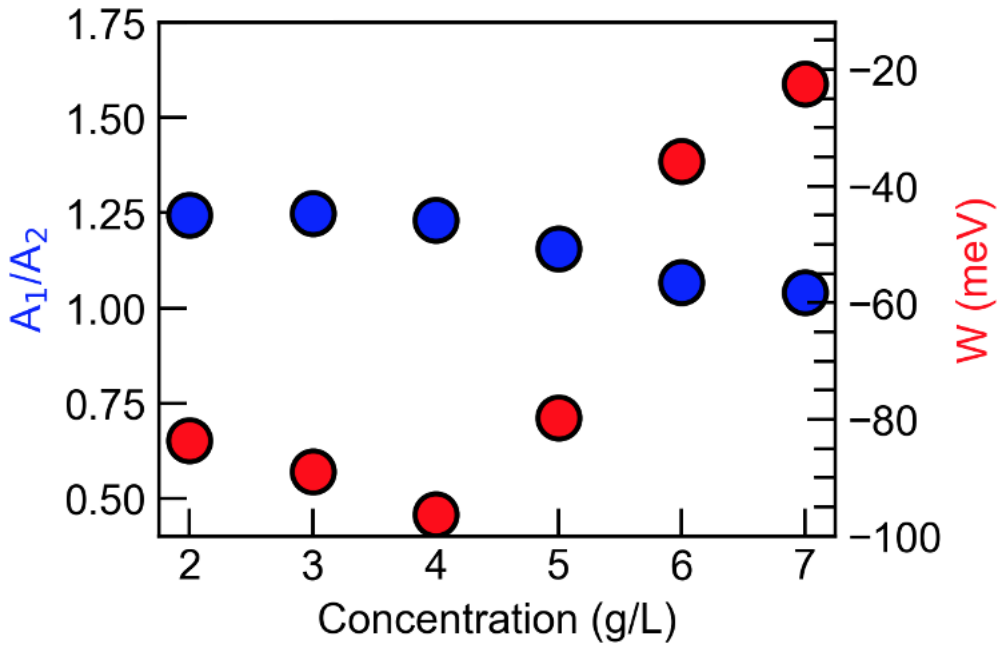

Figure 3-5. A1/A2 ratio (blue circle) and exciton bandwidth (red circle) acquired from Franck−Condon simulations as a function of concentration for DPP-DTT with M_w = 290 kg/mol.

Normally, a lower ratio of the A_1 and A_2 peak, thus larger exciton bandwidth, W, indicates more enhanced interchain Coulombic interactions and/or reduced intrachain excitonic interactions.[217] Therefore, the decreasing trend for A_1/A_2 with increasing solution concentration suggests that films coated at semi-dilute concentrations (>C*) may adopt

more H-aggregate configurations as compared to films prepared from dilute solutions (<C*). For the two lower M_w polymers (204 and 110 kg/mol), a distinctive A_2 peak is no longer observed; rather, the peak becomes broader especially for films prepared from higher solution concentrations (Figure 3-4 b and c). This spectral behavior could be due to the formation of more disordered photophysical aggregates, and the inhomogeneous broadening hides the pronounced vibronic structure. Note that polymorphs have been observed, especially in low molecular weight DPP-based polymers M_w's.[170, 214, 215, 218, 219] The featureless spectral line shapes could originate from the overall absorption of the different aggregates in each polymorph. Nevertheless, the two major vibronic peaks at around 700 and 800 nm can be still ascribed to the absorption of the aggregate in the dominant polymorph as seen in the highest M_w DPP-DTT. The decrease in the A_1/A_2 ratio along with the blue-shift with increasing solution concentration observed for all three Mw's of DPP-DTT verifies that films prepared from higher solution concentrations lead to more H-type aggregation. Recently, Zheng, et al. further investigated the influence of solution concentration on the excitonic interactions and chain conformation of DPP-DTT using additional photophysical techniques including photoluminescence, transient absorption and resonance Raman spectroscopy supported by ab initio calculations.[220] Results revealed that an increase in the solution concentration resulted in the exciton being more dispersed along the polymer chain backbone, indicating that polymer chain order is enhanced when DPP-DTT is processed at higher concentrations.

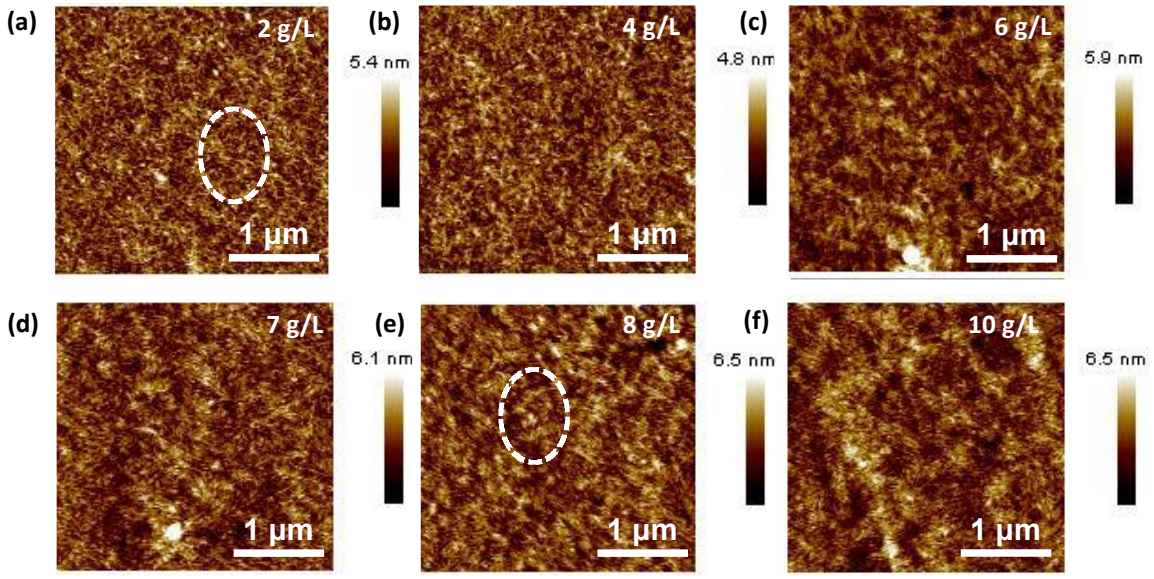

Figure 3-6. Atomic Force Microscopy height images of DPP-DTT (M_w = 204 kg/mol) thin films prepared from the range of solution concentrations (2-10 g/L) investigated. Thin films prepared from semi-dilute concentrations (> C*) exhibit coarser domains that and appear more self-ordered as compared to films prepared from dilute concentrations.

The influence of solution concentration on the surface morphology of the DPP-DTT thin films was investigated using AFM and the height images are provided in Figure 3-6 for M_w of 204 kg/mol and Figure B-11 and Figure B-12 for M_w of 290 and 110 kg/mol, respectively. For all three Mw's investigated here, it can be observed that as the solution concentration increases, there is a shift in the thin-film morphology with a transition in behavior occurring near C*. Films prepared at semi-dilute concentrations (> C*) display relatively coarser domains that overlap and appear more self-ordered, while films prepared at dilute concentrations (<C*) display fine-grained domains with apparently less self-organization and this can be further supported by the increasing surface roughness of the films fabricated from higher concentrations as shown in Table B-1 - Table B-3. In addition to AFM, the CPOM images for the films prepared from different solution concentrations are shown in Figure B-13 - Figure B-15**.** CPOM results reveal relatively smooth films for

the range of concentrations investigated, with no obvious ordered structures observed at the length scale investigated and no birefringence. The thickness of the DPP-DTT films prepared from varying solution concentrations for the samples are presented in Figure B-16. As expected, the film thickness increases with increasing solution concentration, suggesting that the films were fabricated in the evaporation regime.[30, 42]

GIWAXS measurements were conducted on thin films of 290 kg/mol DPP-DTT to explore microstructural transitions and changes in the molecular packing in the films as a function of solution concentration. Examination of the 2-dimensional GIWAXS patterns provided in Figure B-17 shows that most of the films possess an 'edge-on' orientation with respect to the substrate.

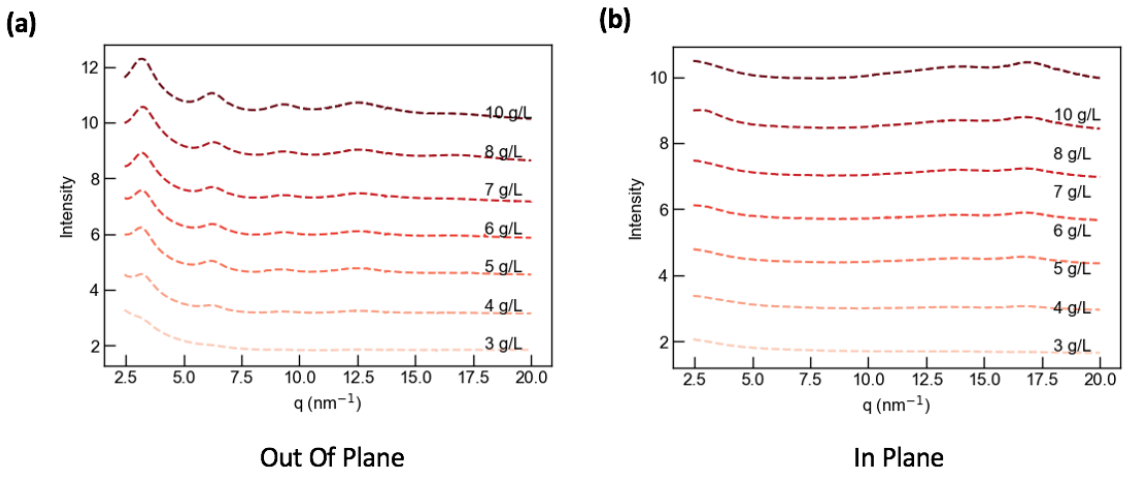

Figure 3-7. (a) Out of plane and (b) in-plane scattering patterns for the DPP-DTT (Mw = 290 kg/mol) thin films prepared from a range of solution concentrations.

Figure 3-7 shows the out-of-plane and in-plane scattering signals extracted from the 2-D GIWAXS patterns. An increase in the intensity of the scattering signal with increasing solution concentration was observed for both the out-of-plane and in-plane

cases, which may imply an increase in the aggregation within the films prepared from higher solution concentrations. The GIWAXS results are in agreement with AFM and UV-Vis observations.[167, 177, 214] The lamellar and π-π spacing, coherence length, full width half maximum and paracrystallinity (g) values extracted from the out-of-plane and in-plane scattering signals are given in Table 3-2.

Table 3-2. GIWAXS parameters for DPPDTT thin films (M_w = 290 kg/mol)

	(100)				(010)			
Conc (g/L)	d(Å)	FWHM (nm^{-1})	L_c	g (%)	d(Å)	FWHM (nm^{-1})	L_c	g (%)
3	-	-	-	-	-	-	-	-
4	19.6	1.68	7.96	6.1	3.7	2.29	2.47	14.7
5	19.7	1.44	8.06	6.5	3.7	2.16	2.62	14.2
6	19.6	1.44	8.04	6.7	3.7	2.16	2.61	14.3
7	19.6	1.32	8.12	6.8	3.7	2.61	2.61	14.3
8	19.4	1.37	7.85	6.7	3.7	2.50	2.50	14.6
10	19.7	1.29	8.03	6.9	3.7	2.78	2.78	13.8

No significant changes in lamellar and π-π spacing values as a function of solution concentration were observed, suggesting that the solution concentration does not impact molecular packing within the film. Lamellar spacing (100) and π-π spacing (010) values were ~19.6 and ~3.7 Å, respectively, which are in good agreement with the reported values.[167, 177, 214]

In addition to investigating the influence of solution concentration on different molecular weights of DPP-DTT, an alternative DPP based polymer, namely PDPP-4T (Figure 3-8a), was examined with 2–12 g/L solutions in CB.

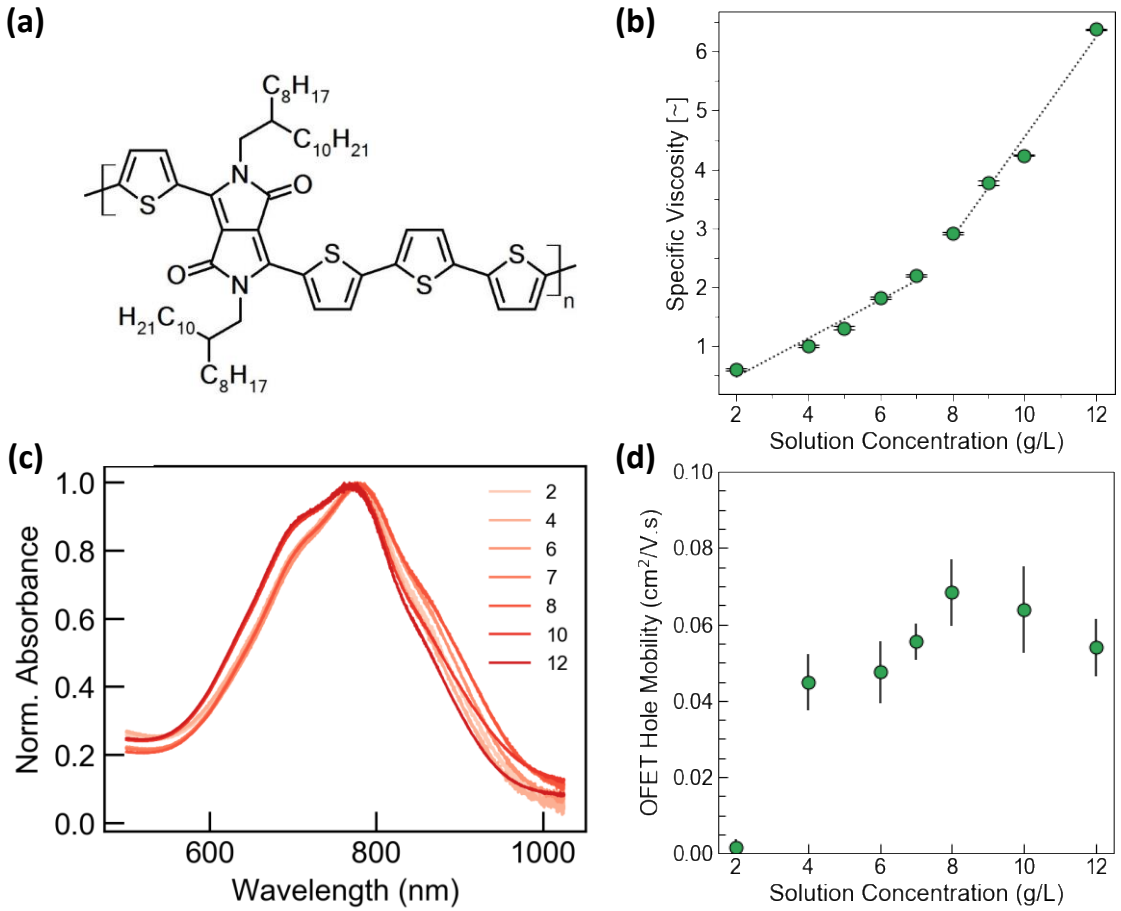

Figure 3-8. (a) Schematic of molecular structure of PDPP-4T (M_w = 75 kg/mol). (b) Specific viscosity measurement of PDPP-4T dissolved in chlorobenzene solutions at 56 °C. The error bars represent the standard deviation of the specific viscosity. The C* extracted from the plot is 8 g/L (c) Normalized UV-Vis linear absorption spectra of PDPP-4T thin films prepared from solution concentrations ranging from 2 to 12 g/L. (d) FET hole mobility of PDPP-4T thin films extracted from the backward sweep Transfer Curve (V_{DS} = -80V) as a function of solution concentration. The error bars here represent 95% confidence intervals averaged over 18 OFET devices.

The solution state viscosity results revealed a similar two regime behavior with the C* occurring at 8 g/L as shown in Figure 3-8b. Further, OFETs prepared from the range of

solution concentrations studied revealed a peak hole mobility at the C* of 8 g/L, followed by a decrease in the average hole mobility at semi-dilute concentrations. *This result indicates that the trend observed previously with DPP-DTT may be generalizable across different DPP based polymers*. In the case of PDPP-4T, the UV-Vis absorption spectra exhibit two distinctive peaks observed at ~720 nm and 775 nm. Although the shape of the spectra differs slightly from DPP-DTT, a similar increase in the intensity of the peak at ~720 nm along with a blue shift with increasing solution concentration is observed. Thus, solution concentration likely influences polymer chain excitonic interactions for not just DPP-DTT but other DPP-based polymers as well. The PDPP-4T transfer curves, output curves, and extracted device parameters (V_{th} and $I_{on/off}$) as a function of solution concentration are shown in Figure B-18-Figure B-20 respectively. Lastly, the PDPP-4T thin-film AFM and CPOM images (Figure B-21 and Figure B-22) reveal a similar trend to that observed for DPP-DTT, with films prepared from semi-dilute concentrations showing mostly self-ordered and overlapped domains as compared to films prepared from dilute concentrations.

This study was further extended to NDI based polymers as well and was done in collaboration with Myeongyeon Lee from Lehigh University. N2200, was examined with 2–10 g/L solutions in CB as shown in Figure 3-9. Interestingly, OFET devices fabricated at the C* ~ 7 g/L revealed a peak electron mobility followed by a decrease in the mobility at semi-dilute concentrations. The transfer curves as a function of solution concentration are shown in Figure B-23. These results reveal that the solution concentration likely influences the optoelectronic properties for not just DPP-based D-A polymers but other D-A polymer systems such as NDI-based polymers as well.

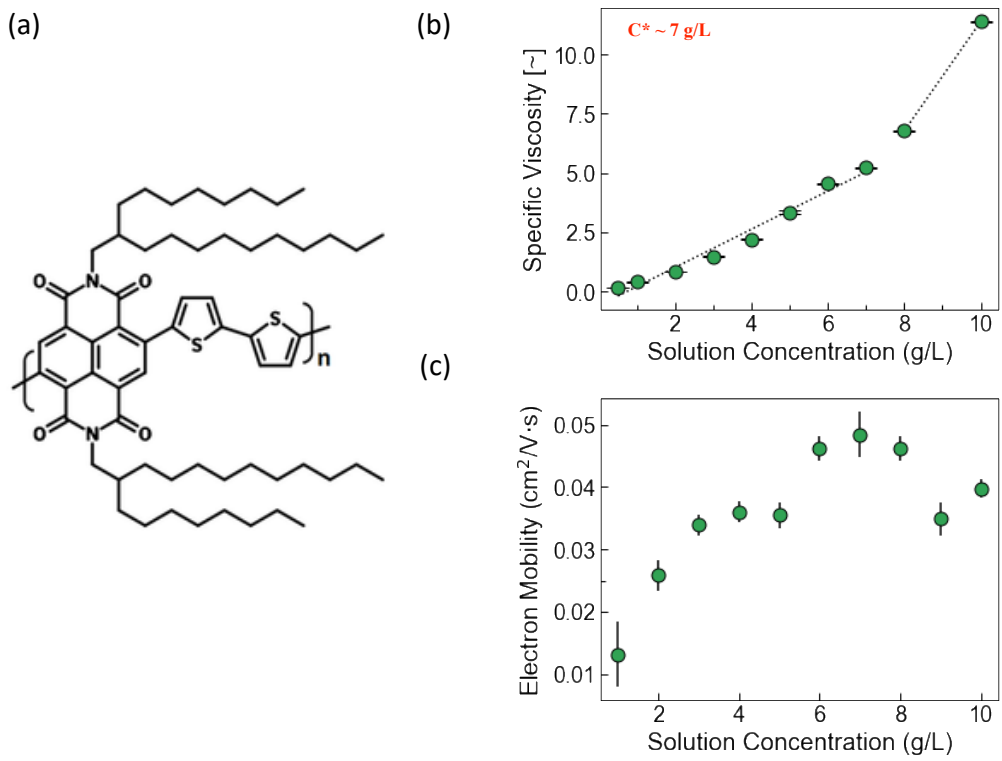

Figure 3-9. Schematic of molecular structure of N2200 (M_w = 200 kg/mol). (b) Specific viscosity measurement of N2200 dissolved in chlorobenzene solutions at 56 °C. The error bars represent the standard deviation of the specific viscosity. The C* extracted from the plot is 7 g/L (c) FET electron mobility of N2200 thin films extracted from the backward sweep Transfer Curve (V_{DS} = 80V) as a function of solution concentration. The error bars here represent 95% confidence intervals averaged over 18 OFET devices.

3.4 Conclusions

In this work, we investigated the influence of solution concentration on the final thin-film morphology and device performance of D-A polymers, with a focus on DPP-based copolymers. DPP-DTT, at three significantly different Mw's, was selected as a model for other DPP based D-A polymer candidates. Viscosity results revealed that an overlap concentration, C*, existed for all three Mw's of DPP-DTT investigated, with the C* scaling

inversely with Mw. Notably, OFET devices prepared from a solution concentration of C* displayed improved hole mobilities irrespective of the Mw, although the improvement at C* was most pronounced at the highest Mw explored. UV-Vis spectroscopic interrogation revealed that films prepared at semi-dilute concentrations are more aggregated and display more interchain interaction than at dilute concentrations, while AFM imaging revealed that films prepared from dilute concentrations (<C*) displayed a lack of aggregates and mostly fine-grained domains with less self-organization. For films prepared from concentrations approaching C*, increased aggregation was observed, with the formation of coarser domains that overlap and become more ordered at increasing solution concentrations. These results were confirmed through GIWAXS studies demonstrating that films prepared from higher solution concentrations displayed increased aggregation. Significantly, a similar correlation between solution concentration and device performance was observed with an alternative DPP-based polymer, PDPP-4T, and an NDI-based polymer, N2200, further strengthening our findings.

This work further highlights the importance of probing the solution state of conjugated polymers prior to deposition in order to control the final thin film morphology and improve device performance. Our findings highlight that polymer solution concentration is an important processing parameter linked to macroscale device performance of D-A polymers and there exists an optimum solution concentration that results in improved charge transport, C*, which can be obtained from relatively straightforward viscometry experiments. This study also opens up questions about how the solution concentration influences the polymer chain conformations and aggregation in the solution state. In addition to the viscosity experiments, more comprehensive techniques

such as DFT calculations and/or MD simulations in tandem with SANS/SAXS experiments would help obtain a better understanding of the influence of the parameter on the solution phase behavior of D-A polymers and the transition to the final film state.

CHAPTER 4. HARNESSING COMPOSITIONAL GRADIENTS TO ELUCIDATE PHASE BEHAVIORS TOWARDS HIGH PERFORMANCE POLYMER SEMICONDUCTOR BLENDS

In the realm of polymer semiconductor/insulator blends, how can researchers effectively navigate the intricate interplay between composition, morphology, and device performance to optimize OFET performance?

This chapter addresses this critical question by introducing a novel high-throughput gradient thin film library approach. This work aims to efficiently explore the vast composition space of polymer semiconductor/insulator blends systematically, uncovering nuanced transitions in performance, morphology, and phase behavior that may otherwise be overlooked.

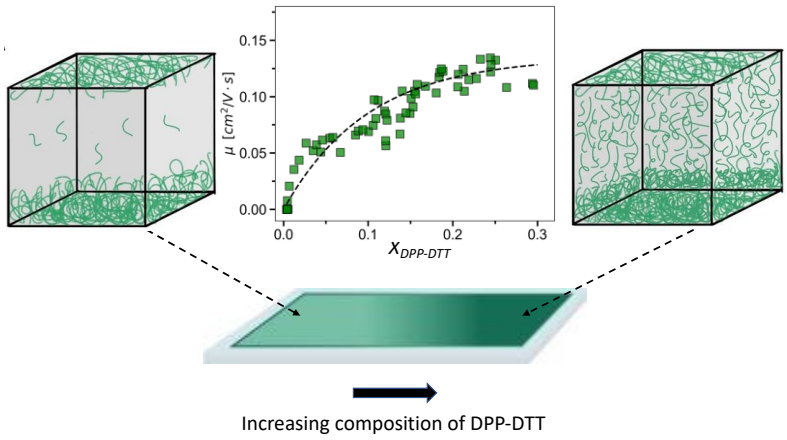

Figure 4-1. Graphical summary of chapter 4. In this work, High-throughput gradient film methodologies are integrated with traditional discrete experiments to obtain a more comprehensive understanding of the composition-morphology-device performance relationships of polymer semiconducting insulating blends.

4.1 Introduction

PSIBs offer opportunities to induce thin film morphological motifs that provide improved overall environmental, mechanical and electronic performance in resultant devices, such as OFETs.[35, 37, 221-225] For OFETs that employ a conjugated polymer as the active layer, incorporating an insulating polymer such as polystyrene (PS) or PDMS has been shown to induce formation of a connected or 'networked' semiconducting polymer structure with improved charge transport characteristics.[36, 179, 180, 221, 226-229] Even blend compositions with low weight fractions of the semiconducting component can achieve charge-carrier mobilities that match or even exceed those of devices made with only the semiconducting component.[36, 179, 180, 221] Notably, blend systems may also offer cost advantages due to reduced semiconductor source material requirements.[230] Contingent upon the experimental conditions, phase separation between the organic semiconductor and insulating polymer within the blends can significantly influence final film morphology and device performance.[35, 228, 230-233] In PSIBs, reported phase separation characteristics are diverse, ranging from vertical phase separation to apparently uniform material dispersion.[35, 37] Such variations depend on polymer intrinsic characteristics (e.g., chemical structure, molecular weight, solubility, substrate interaction) and the deposition conditions.[35, 37, 234, 235]

Despite the substantial promise of PSIBs, notable knowledge gaps persist. Phase transitions and morphological changes that are critical to understanding the performance of PSIBs can occur within narrow composition windows, which could be overlooked if the entire composition space is not comprehensively examined under the same deposition conditions. Moreover, the complexity escalates when exploring composition-performance

trends with respect to different polymers/solvents or incorporation of additional solution processing steps (e.g., UV-irradiation[221], ultrasonication[236], aging,[223] etc.).[237] Additionally, identifying the blend composition where improved device performance is first achieved with minimal semiconductor content can be challenging and costly. To realize the full potential of PSIBs, in-depth understanding of the intricate composition-performance relationship governing PSIB behavior is needed.

Consequently, HTE has emerged as an effective approach to address the lack of sufficient data for materials optimization.[106-108, 110, 112-114, 118, 142, 238] Within the realm of polymer blend research, HTE methodologies have been applied to the synthesis and characterization of gradient thin film libraries, where HT thin film fabrication techniques enable systematic compositional variation on a single substrate.[109, 112, 115, 138, 239, 240] The application of HTE in the realm of PSIBs enables efficient screening of compositions deposited under the same conditions, allowing thorough phase-space exploration and reduced risk of overlooking composition-dependent phenomena.[109, 111, 115, 239, 241] Furthermore, the large amount of data generated from HTE can then be integrated with data science techniques (e.g. machine learning) to model the relationship between processing conditions and OFET device performance.[105, 141, 242, 243]

In this study, we explored the influence of polymer blend composition on the optoelectronic properties of PSIBs, employing DPP-DTT as a model conjugated polymer and PS as the insulating material of interest to understand how variations in blend composition affect device performance, morphology, and phase behavior. To achieve this goal, two complementary approaches, namely HTGF and discrete or one-composition-at-a-time (OCAT) methods were employed. Gradient film libraries covering a wide range of

compositions were fabricated to efficiently screen the composition-performance relationship. Characterization of the resultant thin films unveiled unexpected trends and facilitated the observation of onset behaviors and transitions in device performance, morphology and phase behavior as a function of composition. Results obtained using the OCAT method validated the findings and provided a deeper understanding of key composition-performance relationships. Insights revealed through X-ray photoelectron spectroscopy (XPS) depth profiling conducted on OCAT films highlighted the complex interplay between composition and 3D spatial distribution within the film. The generalizability of the gradient approach was confirmed by its application to P3HT under different solution processing conditions and across a broader composition spectrum.

4.2 Materials and Methods

4.2.1 Materials

DPP-DTT (*Mw* = 204 kDa, PDI = 3.09, Ossila Ltd) kDa, P3HT (*Mw* = 74 kDa, RR = 95%, Rieke Metals, Inc.), PS (*Mw* = 37 kDa, MilliporeSigma), chloroform (MilliporeSigma, anhydrous, amylenes as stabilizer) and CB (anhydrous, Sigma-Aldrich) were used as obtained.

4.2.2 Overall Flow Coating Design

The coating system employed in this study represents a minor modification of a previously described gradient pumping system design,[109] with the only difference being the replacement of the herringbone mixer with a 1/8-inch, T-joint union (Swagelok, SS-41GXS2). The polymer solutions are introduced into the T mixer positioned at the

convergence of the two inlet streams. At this point, mixing is facilitated by the fitting and the collision of the two feeds. The remaining components of the coating system remained unchanged.

4.2.3 OFET Fabrication

A detailed description of the OFET fabrication process is provided in the methods section of previous chapter (2.2.2).

4.2.4 Constant Composition Film Preparation for OCAT experiments

Prior to film deposition, substrates were cleaned by sequential sonication in acetone, methanol, and isopropanol (10 min each), followed by cleaning in UV–ozone for 30 min (Novascan PSD- UV).

The preparation of DPP-DTT/PS samples at different blend ratios involved the initial preparation of a stock solution of 7 g/L by dissolving DPP-DTT in chlorobenzene at 100 °C for 4 hours, followed by continued heating at 56 °C overnight. Similarly, a polystyrene (PS) solution at 7 g/L was prepared by dissolving polystyrene pellets in chlorobenzene at 60 °C for 30 minutes. Blend solutions at varying compositions were then obtained by mixing the DPP-DTT and PS stock solutions at desired ratios. To prepare DPP-DTT/PS thin films for the OCAT experiments, the blend solutions were blade-coated onto glass and OFET substrates at a temperature of 56 °C, with a shearing speed of 2 mm/s, followed by annealing at the same temperature for 10 minutes.

The preparation of P3HT/PS samples at different blend ratios involved the initial preparation of separate stock solutions (10 g/L) of P3HT and PS dissolved in chloroform

at 55°C for 30 minutes. Blend solutions at varying compositions were then obtained by mixing the P3HT and PS stock solutions at desired ratios. The blend solutions were further pre-processed by UV-irradiation using a handheld lamp (Entela, Model UVGL-15, 5 mW cm^{-2} , 254 nm) for 8 minutes according to the procedure in Chang et al.[221] To create P3HT/PS thin films for the one-composition-at-a-time experiments, the blend solutions were blade-coated onto glass (Electron Microscopy Sciences) and OFET substrates at a temperature of 25 °C, with a shearing speed of 2 mm/s, followed by annealing at the same temperature for 10 minutes.

4.2.5 Gradient Film Sample Preparation

DPP-DTT/PS blend solutions were first prepared and dissolved in chlorobenzene at the desired blend ratio (30 wt% DPP-DTT). Films were coated onto OFET gradient arrays using the HTGF coater. First, a cleaning procedure was followed in which the system at 60 °C was flushed with chlorobenzene (2-3 runs) and air (2 runs) to remove any residual material. The syringes feeding the flow system were then filled with DPP-DTT/PS (blend ratio of 30 wt% DPP-DTT) and PS solutions. Prior to coating, the system was initially infused with PS solution until droplets at a consistent drip rate were visible at the outlet purge. Next, approximately 0.3 ml of the DPP-DTT/PS solution was pumped into the system so that the blend solution reached the mixer. The PS was then pumped at the maximum flow rate to remove excess blend solution until colored droplets of blend solution appeared at the outlet purge followed by clear PS solution. Once the substrates had been cleaned and positioned under the distributor outlet, the pump containing the DPP-DTT/PS blend solution was set to a constant flow rate of 20 mL/h and the blend solution was continuously infused into the system. Prior to diverting flow to the distributor for film

coating, flow was directed to the purge stream for a prescribed initial delay period of 10 s. Once the desired length of the substrate was coated, pump flow was paused, stage position reset, and a the substrate was replaced before flow was resumed.

The constant composition flow coated samples that were prepared for the composition calibration curves where coated in the same manner, without flowing any PS solution. P3HT/PS pristine and UV-irradiated gradient films were prepared in the same manner, with the only difference being the use of chloroform as the solvent instead of chlorobenzene and the system was maintained at room temperature.

4.2.6 Characterization

4.2.6.1 OFET Characterization

A detailed description of the OFET characterization process is provided in the methods section of previous chapter (2.2.4.3).

4.2.6.2 UV-Visible Spectroscopy (UV-Vis)

A detailed description of the UV-Vis absorption process is provided in the methods section of previous chapter (2.2.4.2).

The solution-state spectra were acquired by sandwiching 5 μL of P3HT solution between two coverslips at room temperature, followed by spectral analysis using the Cary UV-VIS spectrometer.

4.2.6.3 X-ray Photoelectron Spectroscopy (XPS)

The composition across different points of the gradient thin film samples were obtained using X-ray photoelectron spectroscopy (XPS) using a Thermo K-Alpha XPS system equipped with a monochromatic Al-K X-ray source (1468 eV). Spectra were collected using a flood gun with high purity Argon gas and an X- ray spot size of 400 μm. Survey scans were collected with pass energy of 200 eV with 1 eV increments. High resolution point and line scans for carbon, silicon and sulfur were collected with pass energy of 50 eV with 0.1 eV increments. The element distributions in the blend films were analyzed using the depth profiling feature (50 etches, 30 seconds per etch, Sputter Rate Estimate : Ta_2O_5 = 0.20 nm/sec).

4.2.6.4 Atomic Force Microscopy

A detailed description of the AFM process is provided in the methods section of previous chapter (2.2.4.4).

4.2.6.5 Profilometry

A detailed description of the thickness measurement is provided in the methods section of previous chapter (2.2.4.5).

4.3 Results and Discussion

In this study, a HTGF coating apparatus (Figure 4-2a) was used to screen the composition-morphology-performance relationships for the DPP-DTT/PS blend system. Operationally, the coating system employs a T-joint mixer design, which is a modification from a previously published apparatus having characteristics of both slot-die and blade coating.[109]

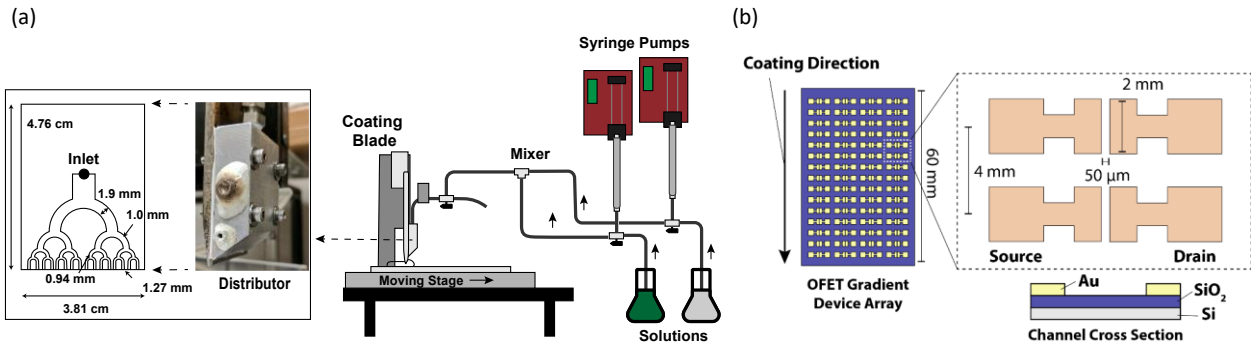

Figure 4-2. Overview of the HTGF coating system and OFET gradient device array. (a) Schematic flow diagram of the gradient film coating system, including syringe pumps, T-joint mixer, coating blade, distributor and moving stage. The subset shows Image and design of microchannel distributor . (b) Depiction and schematic of custom-designed transistor array (15 x 4) containing 60 OFET devices per substrate. The apparent mean residence time and mixing volume for this system are 57 s and 0.31 ml respectively. Figure was adapted from Liu et al.[237]

To enable gradient film device fabrication, a custom gradient BGBC OFET array was designed, as depicted in Figure 4-2b**.** Each gradient array contained 60 devices, organized into 4 columns with 15 devices each. This design allowed for the fabrication of multiple devices on a single substrate, with each row of 4 devices representing a distinct blend composition. The inclusion of 4 columns was deliberate to provide replicates for enhanced experimental reliability. The composition profile was verified for each deposited film coordinate (i.e., each discrete OFET spaced at 4 mm increments) using automated XPS array scans from instrument calibration based on measurements of the S2p peaks on DPP-DTT/PS films of known composition fabricated via flow coating (Figure C-1).

A DPP-DTT/PS gradient film spanning from 0 to 30 wt % DPP-DTT was fabricated by maintaining the temperature of the solution, substrate and HTGF system at 60 °C. The composition-device performance relationship and the corresponding changes in film morphology are shown in Figure 4-3. A total of 83 OFET devices representing distinct blend compositions across one and one-half device arrays was obtained in less than 1 min,

with 55 devices exhibiting detectable mobility. The upper composition bound of 30 wt% DPP-DTT was determined based on previous work, [36, 228] where optimal device performance with minimized semiconducting content was observed. The selection of the 0 wt% lower boundary was made to enable observation of the onset of charge transport. The composition and mobility measurements for each coordinate on the DPP-DTT/PS gradient film are presented in Figure C-2.

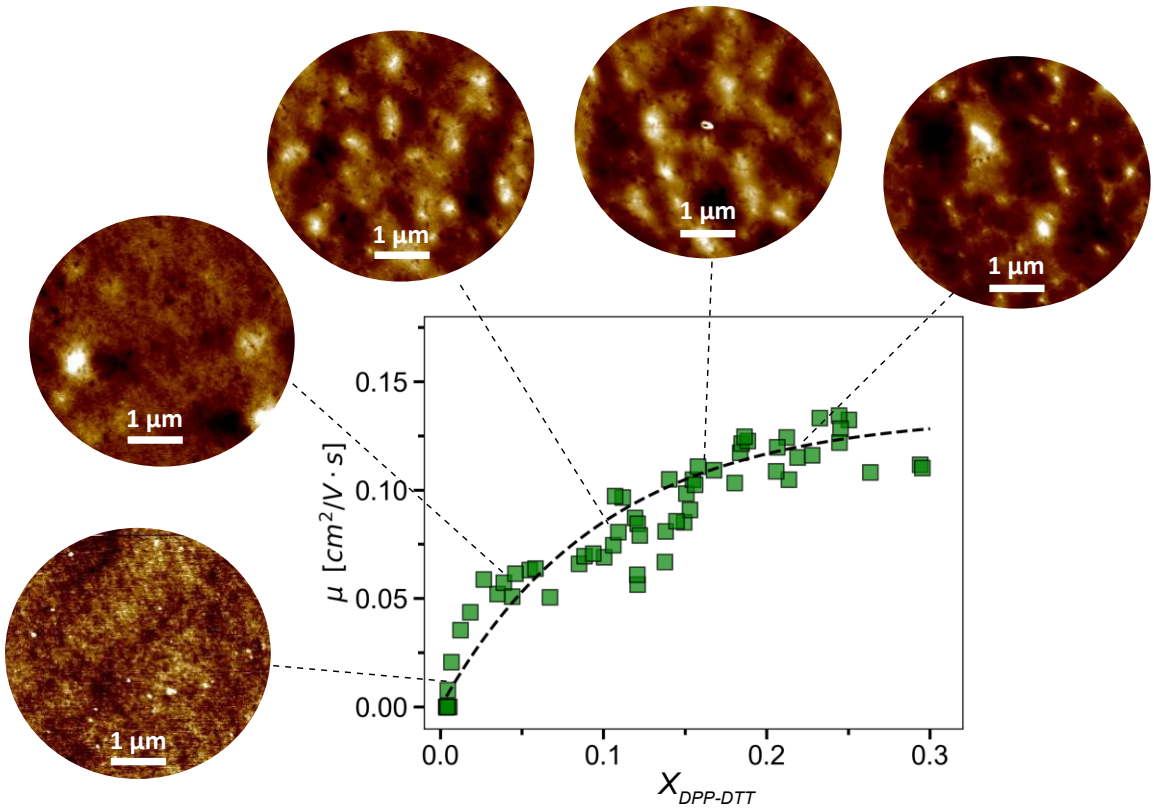

Figure 4-3. Hole mobility measurements of DPP-DTT/PS devices deposited as gradient thin film libraries along with the resultant thin film morphology obtained from AFM (height images). Gradients were prepared using 30/70 DPP-DTT/PS solutions. Dashed trendline represents an exponential fit of y = a[(1-exp(-bx)] to facilitate visual comparison, where y is the hole mobility, x is the composition range of DPP-DTT investigated, a = 0.14 and b = -8.4. The light-colored regions in the AFM images represent the DPP-DTT domains.

Figure 4-3 illustrates a monotonic increase in hole mobility up until $X_{DPP\text{-}DTT} \sim 0.30$, after which either a plateau or drop in device performance can be expected based on previous findings.[36, 228, 229] Measurable device transfer curves were obtained even at compositions as low as $X_{DPP\text{-}DTT} \sim 0.005$. This observation underscores the advantage of the gradient film methodology to efficiently capture the onset of charge transport in PSIBs. Access to multiple compositions on a single substrate enabled efficient characterization at various points along the gradient film. Furthermore, the gradient approach reduced sample-to-sample variability due to changing environmental conditions, enhancing the reliability and robustness of the acquired data. Atomic force microscopy (AFM) was used to evaluate changes in film surface morphology with increasing composition. As presented in Figure 4-3, DPP-DTT domains (light-colored) became noticeable at $x_{DPP\text{-}DTT} \sim 0.1$, and progressively increased in size as the proportion of DPP-DTT increased. When the proportion of the semiconducting component reached xDPP-DTT ~ 0.15, a connected network structure that may contribute to the observed improved device performance was observed.[36, 228, 229, 244]

The gradient film libraries also provide a convenient platform to investigate changes in polymer distribution through the film thickness as a function of composition. XPS depth profiling provided mechanistic insights in this regard. Figure 4-4 presents the normalized relative atomic contribution of sulfur (as determined by the S2p signal) plotted against etching time, specifically examining points with 5 wt% and 20 wt% DPP-DTT along the gradient. Given that sulfur is present only in DPP-DTT, it serves as a qualitative indicator of the proportion of DPP-DTT at different depths within the blend film. The corresponding atomic contributions for carbon (representative of both DPP-DTT and PS)

from the C1s signal and silicon (representative of the silicon substrate) from the Si2p signal, at the same points along the film are provided in Figure C-3. Note that although nitrogen and oxygen are exclusive to DPP-DTT, they were not used as unique identifier elements in this study, considering their potential for physisorption at the surface.[245, 246] Additionally, based upon the molecular structure of DPP-DTT, the atomic contribution of nitrogen and oxygen is considerably lower compared to sulfur.

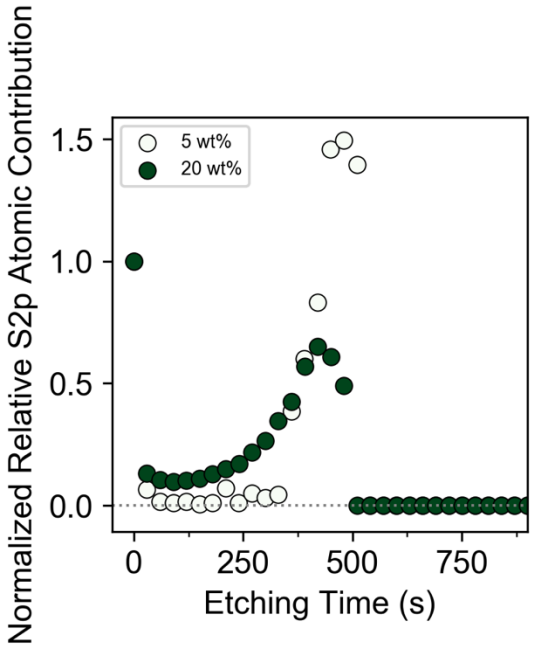

Figure 4-4. Atomic contribution of sulfur as determined by the S2p signal plotted against etching time as obtained from XPS depth profiling on gradient film library points with 5 wt% and 20 wt% DPP-DTT ratios. Normalizing the S2p atomic contribution relative to the surface level prior to etching (etching time = 0) allows for comparison of spectra acquired from the different points on the gradient film which may have slight differences in film thickness. Etching was conducted at a Ta_2O_5 sputter rate of 0.2 nm/sec.

Notably, Figure 4-4 reveals a distinct pattern for both points, the sulfur signal appeared to decrease precipitously during the initial stages of etching, followed by a sustained low level within the bulk, subsequently increasing in the range of 250 – 300 s to

peak around 450 s as etching progressed towards the film-substrate interface. To delve deeper into the rapid initial decrease in sulfur, additional etching was conducted at a slower rate on another 20 wt% DPP-DTT sample point from the same gradient, focusing specifically on etching only the initial few layers (~10 nm) of the film, with the results depicted in Figure 4-5. The slower etching rate revealed a more gradual decrease in the sulfur signal, providing confirmation of diminishing DPP-DTT content as the film's bulk was approached. In both instances, carbon (Figure C-3b) was detected throughout the film thickness, diminishing towards the film-substrate interface, suggesting the presence of mainly polystyrene throughout the bulk. . These results unveil the presence of a PSIB layer comprising DPP-DTT and PS at the air-film interface, the presence of mainly polystyrene in the bulk, while the film-substrate interface again presents with DPP-DTT and some proportion of PS, suggesting a pattern of vertical tri-layer phase separation (semiconductor/insulator/semiconductor), a phenomenon previously observed in other blended conjugated polymer systems.[35, 230, 247-253] Additionally, it is noteworthy that as the composition increases from 5 wt% to 20 wt% DPP-DTT, there is a slight increase in the proportion of DPP-DTT within the bulk film, with virtually no DPP-DTT detected in the bulk at 5 wt%.

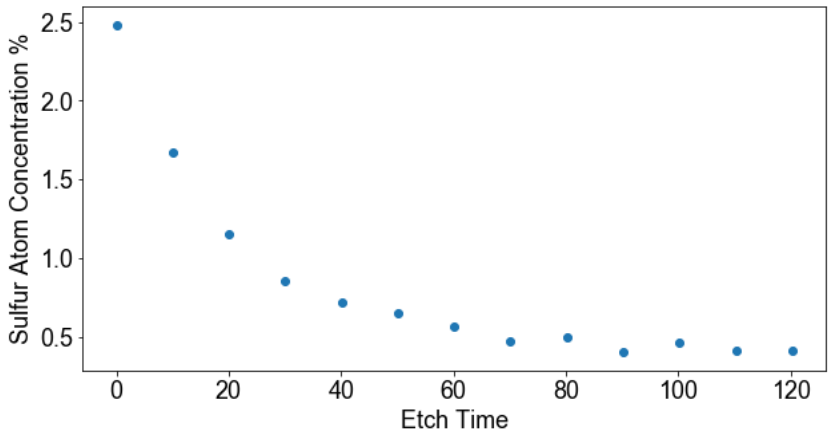

Figure 4-5. Atomic % of sulfur as determined by the S2p signal plotted against etching time. Results were obtained from XPS depth profiling performed on the DPP-DTT/PS gradient on a point having 20 wt% DPP-DTT . The measurement focused on etching only the initial few layers (~10 nm) of the film and etching was conducted at a slower Ta2O5 sputter rate of 0.05 nm/sec (low current). The atomic percentage on the Y-axis represents the proportion of the S2p signal intensity relative to the total signal intensity of all elements being analyzed, which in this case is only Sulfur (S2p), Carbon (C1s), and Silicon (Si2p).

To validate and further explore the insights obtained from the gradient experiments, OCAT experiments were conducted. Blend solutions of DPP-DTT/PS at various compositions, both within and outside the gradient range, were prepared as described in the methods section. Subsequently, these PSIBs were blade-coated onto glass and silicon BGBC OFET substrates for relevant characterization. Blade coating was selected for its precise control during film deposition, potential to enhance film order, and scalable applications.[30, 37, 42, 244]

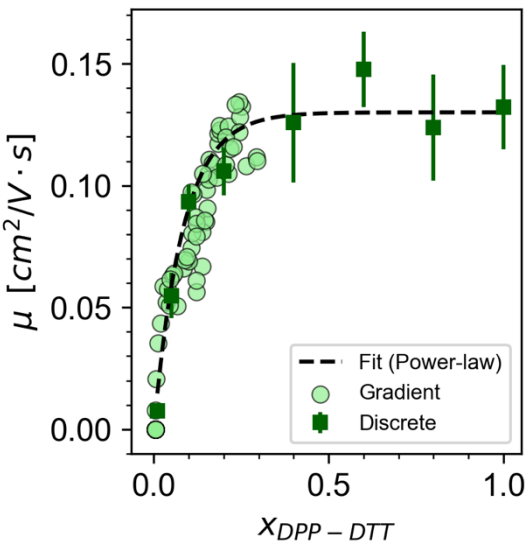

Figure 4-6. Comparison plot of OFET hole mobilities for gradient films (circles) and OCAT blade-coated films (squares) of DPP-DTT/PS blends at varying wt% of DPP-DTT. Dashed trendline represents an exponential fit of y = a[(1-exp(bx)] to facilitate visual comparison, where y is the hole mobility, x is the composition range of DPP-DTT investigated, a = 0.132 and b = -10.45.

Figure 4-6 presents a comparison plot of the average OFET hole mobilities obtained from blade-coated OCAT films and flow-coated gradient films (*vide supra*). Notably, within the composition range selected for the preliminary gradient experiments, the mobilities from the OCAT films are consistent with those fabricated using the gradient method. These results underscore the efficacy of the gradient film to accurately capture the composition-device performance trends. Moreover, following the anticipated monotonic increase, the mobility of the OCAT devices gradually reaches a plateau at compositions exceeding 40 wt% DPP-DTT. This plateau can be identified as the 'optimal' composition for improved device performance while minimizing the semiconducting component. The mobilities presented in Figure 4-6 for the OCAT films were extracted from the forward transfer curve, with similar results observed for mobilities extracted from the backward transfer curve (Figure C-4). The OFET device transfer and output curves for the OCAT

experiments are provided in Figure C-5 and Figure C-6, respectively. Additionally, Table C-1 contains extracted average V_{th} and I_{on}/I_{off} ratios for the OCAT films as a function of blend composition. Devices fabricated from low wt% DPP-DTT exhibited higher I_{on}/I_{off} ratios, while the threshold voltage showed no obvious trend.

The consistent OFET mobility of the PSIB films at low compositions of DPP-DTT (~20-40 wt%) and its similarity to the mobility observed at 100 wt% DPP-DTT has been observed previously and may attributed to the formation of a connected network structure of the semiconducting polymer within the PS matrix, as evidenced by AFM (Figure 4-7).[36, 228, 229, 244] Similar to the gradient results, OCAT films exhibit gradual formation of a networked structure that increased in density as the DPP-DTT content increased to 80 wt%, eventually resulting in formation of an apparently amorphous and featureless film at 100 wt% DPP-DTT. The connected network morphology likely provides percolation pathways for the charge carriers improving charge transport within the film.[36, 226, 230] Furthermore, organic/polymer transistors are interface-driven devices, wherein charge transport predominantly occurs within a very thin semiconductor layer at the semiconductor/dielectric interface connecting the source and drain electrodes.[35, 254, 255] As observed by the XPS depth profiling in Figure 4-4**,** the formation of a contiguous DPP-DTT enriched layer at the substrate interface may enable blend films with low compositions of DPP-DTT to exhibit charge carrier mobilities that approach those of the 100 wt% DPP-DTT films.[35]

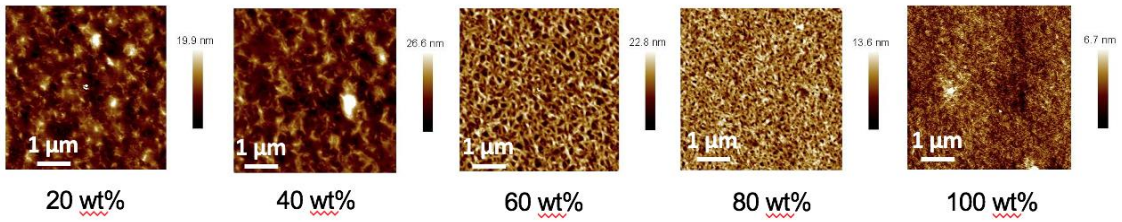

Figure 4-7. Tapping-mode AFM height images of the top surface of DPP-DTT/PS OCAT blend films at different weight compositions of the semiconducting component.

The influence of blend composition on the solid-state polymer chain excitonic interactions for the OCAT DPP-DTT/PS films was also investigated using UV–Vis absorption spectroscopy. Figure 4-8 presents the spectra of DPP-DTT/PS blend films at discrete compositions ranging from 20 to 100 wt% DPP-DTT and reveals a spectral red shift associated with decreasing DPP-DTT content, which is attributed to intermolecular π-π stacking and points to a more planarized conjugated backbone in films comprising lower wt% DPP-DTT.[66, 256] The slight increase in intensity of the shoulder at 830 nm suggests that PS facilitates DPP-DTT aggregation during film formation.[36]

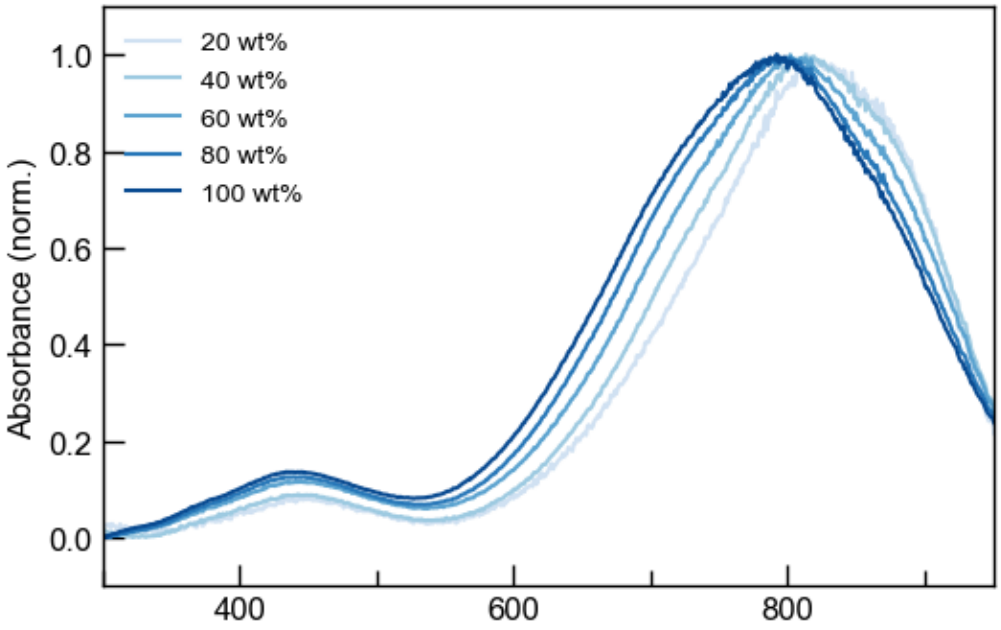

Figure 4-8. Normalized UV-vis absorption spectra of DPP-DTT/PS blend thin films obtained by blade coating with different weight ratios of conjugated polymer.

XPS depth profiling was conducted on the OCAT films to validate and further explore insights gained from the preliminary gradient experiments, specifically focusing on the observed vertical phase separation phenomenon (Figure 4-4). Figure 4-9 presents a plot of the normalized relative atomic contribution of sulfur within the blend films, plotted against etching time for the 20 and 40 wt% DPP-DTT/PS OCAT films; the corresponding profiles for carbon and silicon are provided in Figure C-7. Additionally, for comparison purposes, depth profiling of the 100 wt% DPP-DTT film was also carried out, and the corresponding results are presented in Figure C-7.

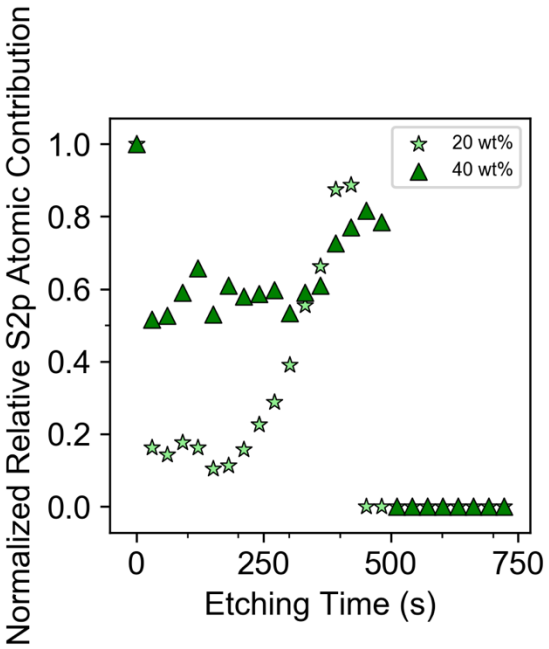

Figure 4-9. Atomic contribution of sulfur as determined by the S2p signal plotted against etching time as obtained from XPS depth profiling on OCAT blend films with 20 wt% and 40 wt% DPP-DTT ratios. Normalizing the S2p atomic contribution relative to the surface level prior to etching (etching time=0) enables comparison of spectra acquired from different OCAT films with varying thicknesses. Etching was conducted at a Ta2O5 sputter rate of 0.2 nm/s.

Figure 4-9 reveals that for the 20 wt% and 40 wt% blend films, the silicon substrate was reached after approximately 450 s and 500 s of etching, respectively. The slight differences in the required etching time are attributed to differences in film thickness (Figure C-8). In the 20 wt% DPP-DTT case, the etching profile appeared identical to that of the gradient film, again suggesting that at 20 wt% DPP-DTT, the blend undergoes vertical, tri-layer phase separation. The 40 wt% DPP-DTT film also displayed the presence of the semiconducting component at the air and substrate interfaces. In behavior that is consistent with findings in previous studies,[36, 228] the proportion of sulfur in the bulk of the film appeared higher than that observed for the film prepared with only 20 wt% DPP-DTT, suggesting a more uniform distribution of DPP-DTT throughout the film. A similar

observation was made by Xu et al.[252] for blends of poly[3,6-di-2-thienyl-pyrrolo[3,4-c]pyrrole-1,4-dione-alt-thieno[3,2-b]thiophene] (DPPT-TT) and polystyrene-block-poly(ethylene-co-butylene)-block-polystyrene (SEBS). At low DPPT-TT compositions, vertical tri-layer phase separation was observed, where the semiconducting component appeared to segregate at the air and substrate interfaces with SEBS primarily occupying the bulk of the film; and as the proportion of DPPT-TT increased, a more uniform distribution was observed throughout.

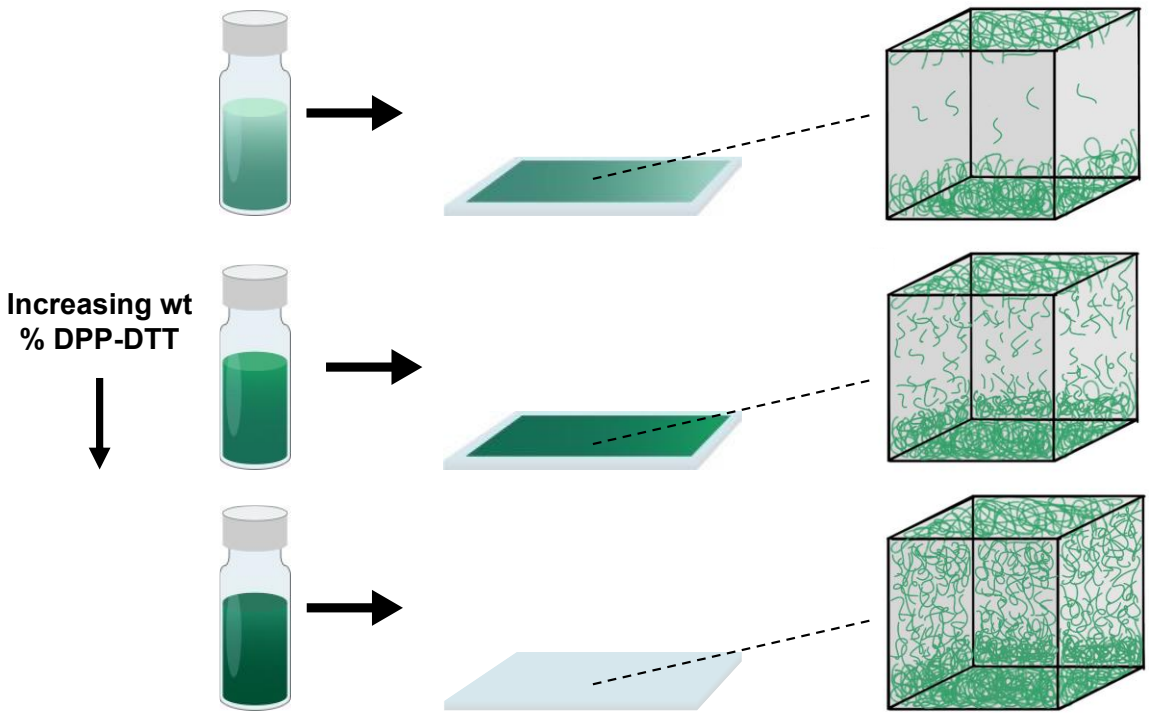

Figure 4-10. Illustration of the potential phase separation mechanism occurring during film formation. The green chains represent domains of DPP-DTT, while the grey space represents PS. At lower compositions there is a presence of DPP-DTT at the air/film interface and enrichment of DPP-DTT at film/substrate interface, with majority of the film bulk containing PS. As the ratio of DPP-DTT within the film increases, a more uniform distribution of the two polymers within the film is observed.

From a mechanistic perspective and as illustrated in Figure 4-10, the observed accumulation of DPP-DTT at the air and substrate interfaces is most likely driven by energy minimization,[35, 230, 257, 258] in addition to factors such as polymer intrinsic characteristics[251, 259] and deposition conditions.[36, 228, 244] Given that reported solubility parameters for DPP-DTT, PS, and chlorobenzene are similar,[36, 228] the vertical phase separation observed here may be due to the substantial differences in DPP-DTT (~200 kDa) *vs.* PS (~37 kDa) molecular weight,[251, 260] high polydispersity (~3) of DPP-DTT,[259] polymer solution characteristics,[179, 261-263] and parameters associated with blend film fabrication,[36, 228, 244, 264, 265] etc.[35, 230, 235] An increase in wt% DPP-DTT within the film,

leads to a more substantial proportion of DPP-DTT in the bulk, suggesting a more uniformly distributed blend;[36, 228, 252] however, DPP-DTT continues to be enriched at both the substrate and air interfaces. Most likely, the increase in DPP-DTT concentration in the bulk of the film is linked to the length scale of phase separation, whereby the XPS sampling spot size (400 μm) is sufficiently large to encompass both DPP-DTT and PS domains. At higher wt% DPP-DTT, the semiconducting polymer domain size could be augmented, leading to a networked structure within the bulk parallel to the substrate.[36, 228] Clearly, phase separation in PSIBs is a complex phenomenon that depends on a multitude of parameters. As a consequence, optimization of the blend systems requires careful selection of materials and processing conditions to match desired performance targets.[29]

In collaboration with my colleague Dr. Aaron Liu, we expanded our study beyond the DPP-DTT/PS system, and used the HTGF coater to generate untreated and UV-irradiated P3HT/PS gradient films at room temperature, spanning a wide composition range, showcasing the generalizability of this approach.[237] UV-irradiated P3HT blend solutions were prepared alongside the pristine alternatives to assess the system's ability to capture the effects of pre-processing the blend solution prior to film deposition.[221] The resulting composition-device performance relationships and changes in film morphology are illustrated in Figure 4-11.

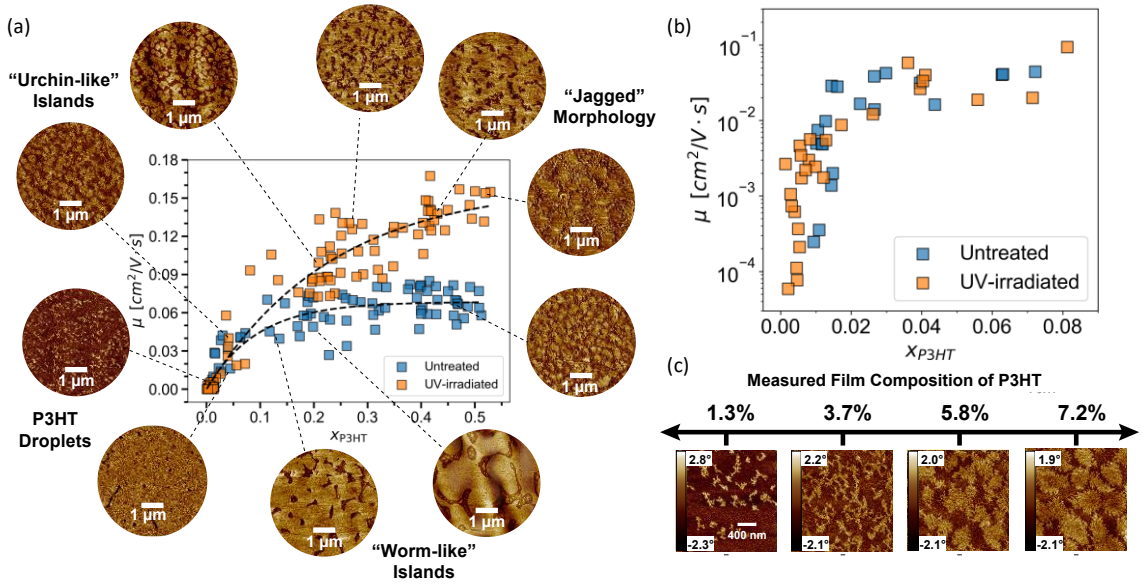

Figure 4-11. (a)Hole mobility and surface morphology (AFM phase images) measurements of P3HT/PS devices deposited as gradient thin film libraries. Final solutions were either derived from 50/50 P3HT/PS solutions that were either used as dissolved without treatment (pristine) or UV-irradiated for 8 minutes prior to loading. Dashed trendline represents an exponential fit of y = a[(1-exp(-bx)] to each dataset to facilitate visual comparison, where y denotes the hole mobility, x signifies the composition range of P3HT investigated, and a and b are constants derived from the fit. In the case of the untreated system, a = 0.068 and b = -10.65, while for the UV-irradiated system, a = 0.16 and b = -4.24. (b) Zoomed-in window of the composition vs. mobility plot at compositions below x_{P3HT} = 0.10, with mobility values plotted in log-scale to emphasize onset. (c) AFM phase images of the UV-irradiated gradient film at compositions below x_{P3HT} = 0.10. Similar results were observed for the untreated system. Figure adapted from Liu et al.[237]

Screening the PSPRs of untreated and UV-irradiated P3HT/PS was conducted by generating a gradient spanning a 0–50 wt% P3HT using chloroform as the solvent as detailed in the methods section. Composition calibration curves obtained from known compositions of flow coated untreated and UV-irradiated P3HT/PS films are shown in Figure C-9. The composition and mobility measurements for each coordinate on the untreated and UV-irradiated P3HT/PS gradient films are presented in Figure C-10 and Figure C-11. Similar to the DPP-DTT/PS system, composition boundaries were chosen

based on previous work[221], with the intent of observing the onset of charge transport and identifying the optimum blend composition. Over 100 OFET devices, encompassing distinct blend compositions distributed across two arrays, were fabricated. The composition-mobility profiles derived from the gradient device screening (Figure 4-11a) highlights a distinct enhancement in FET hole mobility when devices are fabricated from UV-irradiated solutions, particularly at the higher compositions. This differentiation becomes particularly pronounced as the two exponential trendlines begin to diverge at compositions exceeding 10-15 wt% P3HT. Both sets of devices initially exhibit a positive and incremental trend in mobility. The mobility of the untreated devices gradually reaches a plateau at compositions exceeding 40 wt% P3HT, which can be identified as the 'optimal' composition. Conversely, devices produced from UV-irradiated solutions display a continuous mobility improvement as the P3HT composition increases. These findings align well with the trends observed in the previous studies.[221] Figure 4-11b offers a detailed examination of the performance at lower compositions of P3HT (below 10 wt%), highlighted at the log-mobility scale, where both pristine and UV-irradiated exhibit comparable trends. For both sets of P3HT films, OFET transfer curves (I_d-V_g) were detectable even at compositions below 1 wt% P3HT, with devices derived from the UV-irradiated solutions showing a higher frequency of measurable mobility.[237]

The P3HT/PS composition gradient libraries also underwent AFM analysis to establish links between changes in thin-film surface morphology and corresponding improvements in device performance. Upon examination, it becomes evident that for compositions below 5 wt% P3HT, there are distinct droplet-like features, approximately 100 nm in size, which gradually enlarge and merge as the P3HT composition increases

(refer to Figure 4-11c). Conversely, at higher P3HT compositions (10-15 wt%), AFM surface images (see Figure 4-11a) illustrate the formation of island-like structures of P3HT domains, which progressively merge into a more interconnected network. Notably, disparities in mobility between untreated and UV-irradiated films at higher P3HT compositions (>20 wt%) may stem from subtle distinctions in their morphologies. Specifically, the untreated blend library displays smoother, more globular domains, while the UV-irradiated blend library exhibits P3HT domains with irregular edges resembling "finger-like" protrusions which appear to facilitate interconnectivity between domains as the P3HT composition increases.[237] This enhanced connectivity potentially facilitates charge transport, leading to improved device performance in the UV-irradiated films.[1, 51, 52]

Depth profiling conducted on the untreated P3HT/PS gradient film at two significantly distinct composition points also revealed vertical phase separation, as depicted in Figure 4-12. It is evident that for the 5 wt % and 50 wt % blend films, the silicon substrate was reached after approximately 900 s and 1000 s of etching, respectively. The slight differences in the etching time required to reach the substrate could be attributed to variances in film thickness. In the case of the 5 wt% P3HT, the proportion of sulfur initially decreased upon etching and remained at a consistently low level for approximately 500 s. As etching progressed towards the film-substrate interface, the proportion of sulfur increased to its maximum value at around the 875 s mark, ultimately disappearing upon reaching the silicon substrate. These results suggest that at 5 wt% P3HT, there is a very thin layer of P3HT at the air-film interface, with the majority of the P3HT enriched at the film-substrate interface and this behavior aligns well with previous findings.[41] Notably, the

50 wt% P3HT film displayed enrichment of the semiconducting component at the air and substrate interfaces. Moreover, the proportion of sulfur in the bulk of the film appeared higher than that observed for the film prepared with only 5 wt% P3HT, indicating a more uniform distribution of P3HT throughout the film at higher compositions of P3HT in the blend. Previous work by Chang et al. suggested that during film formation, initially, a PS-top/P3HT-bottom vertical phase separation is formed temporarily.[41, 266] This is likely due to the lower solubility of P3HT ($\delta \approx 14.8$ MPa$^{1/2}$)[267] in chloroform ($\delta \approx 19$ MPa$^{1/2}$)[268] compared to PS ($\delta \approx 17.9$ MPa$^{1/2}$),[267] causing P3HT to be depleted more rapidly from the solution and settle on the SiO2 substrate, while PS tends to remain in the liquid phase for longer and gets enriched at the air interface.[41, 266] However, this bilayer structure eventually gets disrupted, and P3HT ($\gamma \approx 21.0$ mJ/m^2)[269] is likely to migrate to the air/film interface, while the PS ($\gamma \approx 40.2$ mJ/m^2)[270] will tend to migrate toward the SiO2 ($\gamma \approx 36.5$ mJ/m^2)[266] substrate for energy minimization.[41, 266, 271] Walheim et al suggested that voids emerge within the upper layer abundant in PS solution, subsequently occupied by the lower layer containing a higher concentration of P3HT.[221, 272] This hypothesis corresponds with the findings depicted in Figure 4-12, illustrating a sparse layer of P3HT at the air interface at low compositions. As the composition of P3HT in the blend increases, it is proposed that the voids become increasingly filled with P3HT, leading to greater enrichment of P3HT at the air interface.

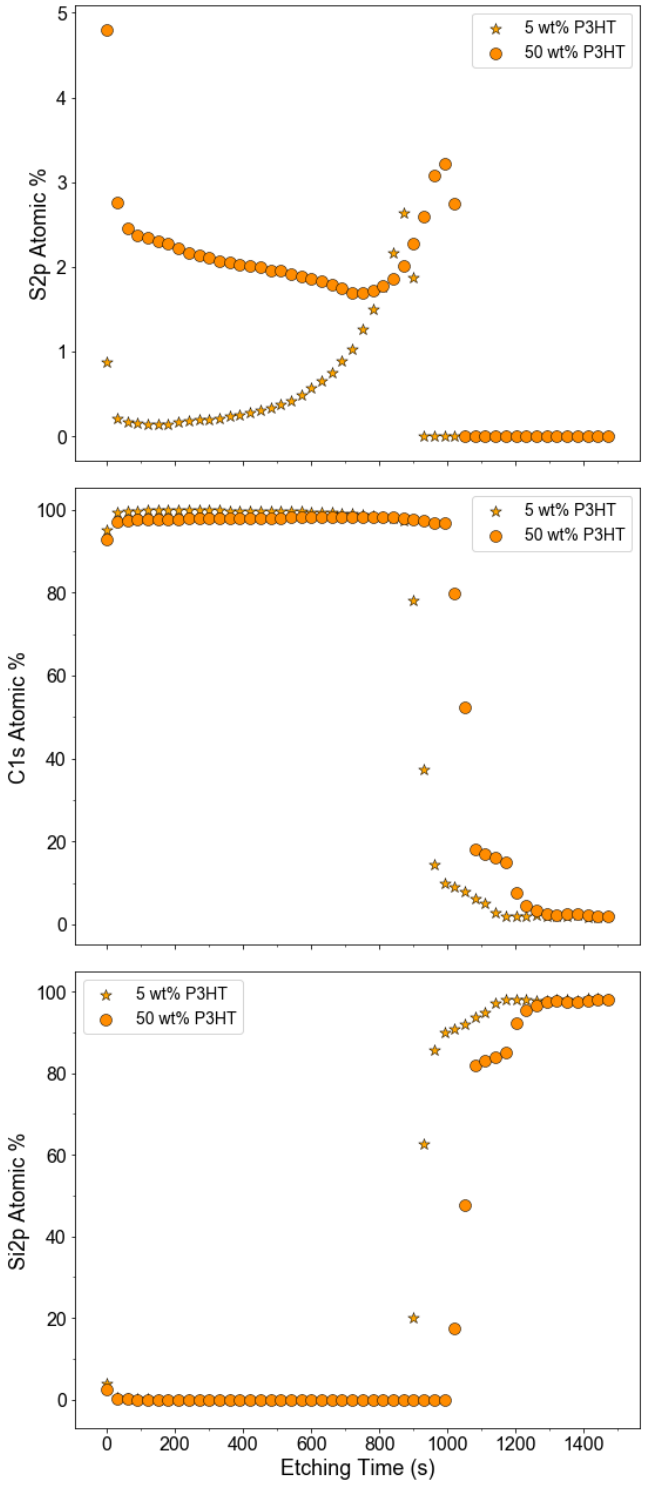

Figure 4-12. Atomic % of sulfur (top), (b) carbon (middle), and (c) silicon (bottom) as determined by the S2p, C1s, and Si2p signals, plotted against etching time obtained from XPS depth profiling on untreated P3HT/PS gradient film library points with 5 wt% and 50 wt% P3HT ratios. The atomic percentage on the Y-axis represents the proportion of the S2p signal intensity relative to the total signal intensity of all

elements being analyzed, which in this case is only Sulfur (S2p), Carbon (C1s), and Silicon (Si2p). Etching was conducted at a Ta2O5 sputter rate of 0.2 nm/sec.

Similar to the DPP-DTT/PS system, the P3HT/PS system underwent detailed analysis through OCAT experiments, covering both the composition gradient range and external compositions. OFET devices were fabricated by blade-coating untreated and UV-irradiated P3HT/PS blend solutions at various P3HT compositions onto BGBC silicon substrates. Figure 4-13 depicts the average OFET hole mobilities of blade-coated untreated P3HT/PS and UV-irradiated P3HT/PS films, plotted against P3HT wt%. As anticipated, devices fabricated from UV-irradiated blend solutions consistently exhibited higher mobilities compared to their untreated counterparts. This enhanced performance can be attributed to the presence of well-ordered P3HT nanofibrillar structures that create pathways between P3HT regions within the film (See Figure 4-15), thereby enhancing charge transport.[221, 273, 274] In the case of untreated P3HT/PS, the mobility remained steady at approximately 1.50 $\times$ 10-2 $cm^2/V\cdot s$ across P3HT content ranging from 20 to 100 wt%. Conversely, devices fabricated using UV-irradiated blend solutions showed a gradual improvement in mobility as P3HT content increased, with detectable mobility even at 5 wt% P3HT. The OFET device transfer (Figure C-12 and Figure C-13) and output curves (Figure C-14 and Figure C-15) are presented in Appendix C. Note the OFET hole mobilities shown in Figure 4-13 are extracted from the forward transfer curve, with similar results being obtained when extracted from the backward transfer curve (Figure C-16). The extracted average Vth and Ion/Ioff ratios for the untreated P3HT/PS and UV-irradiated P3HT/PS systems as a function of blend composition are provided in Table C-2 and Table C-3, respectively. The performance characteristics of the P3HT/PS systems presented

above are consistent with results reported by Chang et al.,[221] despite differences in deposition method (i.e., spin coating) and polymer molecular characteristics.

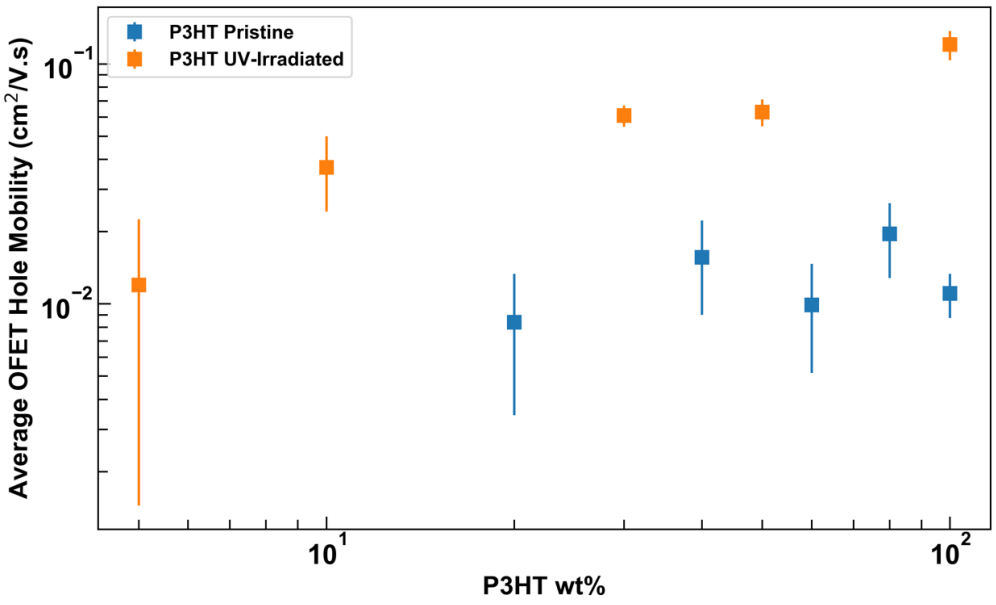

Figure 4-13. Comparison of average FET hole mobilities of blade coated P3HT/PS blend films and P3HT/PS blend films from 8-min UV-irradiated blend solutions as a function of the weight percentage of P3HT in the blend solution plotted in log scale. The mobilities were extracted from the forward sweep transfer curve (V_{DS} = -80 V) and the error bars here represent 95% confidence intervals averaged over 18 OFET devices.

When comparing the gradient film and OCAT OFET results (Figure 4-14), it becomes evident that, despite following a similar trend, the mobilities derived from the gradient film approach consistently outperform those from the OCAT experiments across the investigated composition range. This performance variation is likely attributed to inherent mechanistic distinctions linked to the two coating methods: the gradient film approach utilizes a slot die + blade coating technique, whereas the OCAT approach relies strictly on blade coating. It is hypothesized that flow-induced nucleation of fibril-like

aggregates might occur during the mixing stage or while passing through the distributor in the gradient film system, potentially leading to the self-assembly of P3HT morphological motifs conducive to higher mobilities.[275]

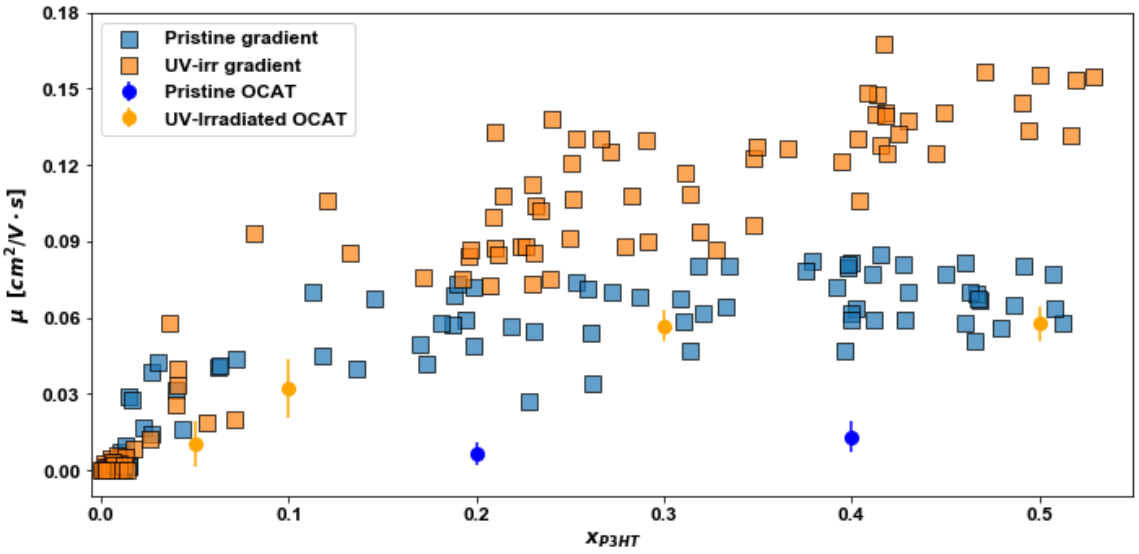

Figure 4-14. Comparison plot of OFET hole mobilities for flow-coated gradient films (squares) and OCAT blade-coated films (circles), depicting untreated/pristine (blue) and UV-irradiated (orange) P3HT/PS blends at varying compositions of P3HT.

The surface morphology of the OCAT P3HT blend films at different weight fractions of P3HT was investigated using atomic force microscopy (AFM) (Figure 4-15). In the case of the untreated P3HT, films prepared with 40 wt% P3HT show domains of isolated spherical clusters (~ 0.6 μm) of P3HT (light domains) that increase in number with increasing wt% P3HT, eventually appearing amorphous as the P3HT composition increases to 100 %. In the case of the UV-irradiated blend films, P3HT islands have already appeared in films prepared from 20 wt% P3HT and eventually become interconnected, presumably via P3HT nano fibers, as the proportion of P3HT increases (see for instance the 60 wt% film). Unlike the untreated, 100 wt% P3HT films, the UV-irradiated films

revealed ordered nano fibers that were likely formed in the solution phase as P3HT aggregated, and were subsequently transferred to the film during deposition. This ordered and interconnected morphology observed in the UV-irradiated films is likely responsible for the improved charge transport observed in Figure 4-13.

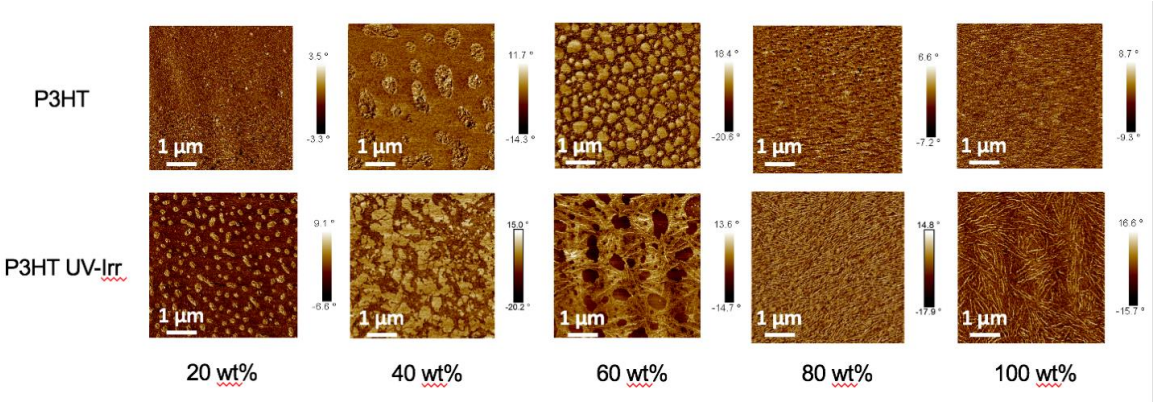

Figure 4-15. Tapping-mode AFM phase images of the top surface of untreated P3HT/PS (top) and UV-irradiated P3HT/PS (bottom) blend films at different weight % of P3HT.

The influence of blend composition on the solution (Figure 4-16) and solid-state (Figure 4-17) polymer chain inter- and intra-molecular interactions for the P3HT-based PSIB's was probed using UV–Vis absorption spectroscopy. Figure 4-16a presents the solution spectra of untreated P3HT and the corresponding blends, which exhibit dominant high-energy features at ~450 nm (π–π* intraband transition) convoluted with less pronounced aggregation peaks at 605 nm (i.e. $A_{0\text{-}0}$ vibronic peak) that are enhanced at low-compositions of P3HT blends. These results reveal that the P3HT chains are likely to be fully dissolved in solution, and the presence of PS does not lead to the aggregation of P3HT in solution.[221, 236, 273, 276] Unlike the pristine solutions, the UV irradiated counterparts show a strong enhancement in the features at ~575 nm and 750 nm with increasing PS content

(Figure 4-16b). This result suggests that upon exposure to UV, PS facilitates the P3HT aggregation in the solution.[221]

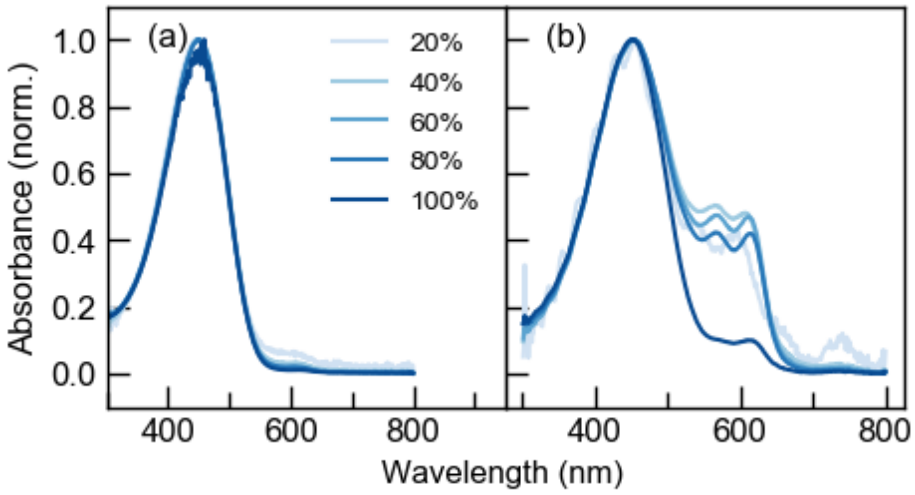

Figure 4-16. Normalized UV-vis absorption spectra of (a) untreated P3HT/PS, and (b) UV-irradiated P3HT/PS blend solutions obtained by capturing a drop of solution in between two coverslips

In the case of the pristine blend films shown in Figure 4-17a, an enhancement of the peak at ~605 nm can be observed with increasing PS content. This trend is associated with increased intrachain coupling as the PS content increases, suggesting that the PS likely facilitate P3HT backbone planarization via favorable intra-molecular interactions within chains during film formation.[221, 236, 273, 277] Figure 4-17b demonstrates a nonmonotonic variation at the 605 nm peak, interestingly. The absorption spectra of thin films, prepared from UV-irradiated solutions, initially exhibit an increase in peak intensity at 605 nm as the PS content increases to 40 wt%. Subsequently, the peak diminishes as the PS content further increases to 80 wt%. This result suggests that UV-irradiation and addition of PS have synergistic effects in the P3HT aggregation. Above 60% of the P3HT component, the conjugated polymer chain backbone planarizes with addition of PS, just like untreated case.

However, at compositions below 60 wt % P3HT, the UV-irradiation undermines further P3HT chain planarization with excessive use of PS.

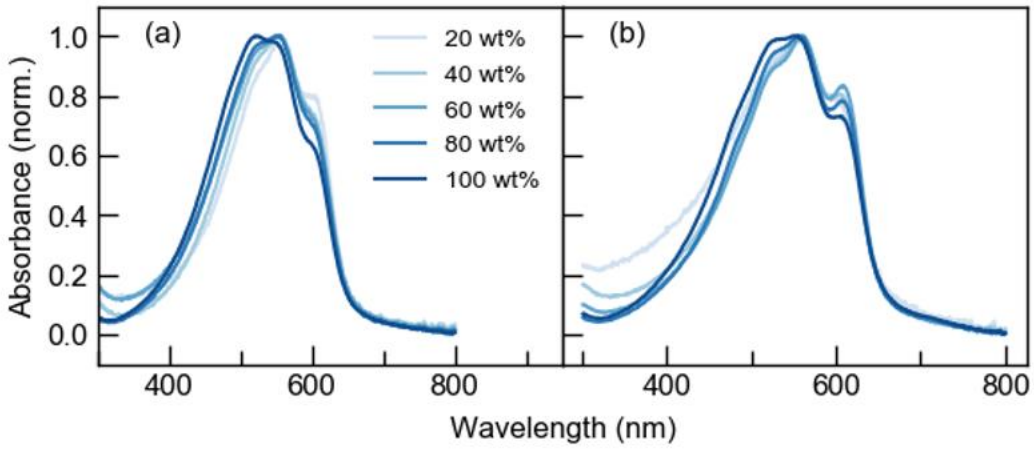

Figure 4-17. Normalized UV-vis absorption spectra of (a) untreated P3HT/PS, and (b) UV-irradiated P3HT/PS blend thin films obtained by blade coating with different weight ratios of conjugated polymer

To quantify the degree of aggregation and interchain excitonic interactions under different processing conditions, we further employed a modified Franck-Condon model developed by Spano.[84, 276] The simulation results are shown in Figure C-17, where the modified FC progression precisely captures the first and second vibronic peaks. In general, the W values in observed in Figure 4-18 reveal enhanced interchain excitonic interactions with increasing P3HT content, meanwhile the addition of PS aids the P3HT intrachain interactions, indicating enhanced backbone planarization, with similar effects observed with UV irradiation. However, simultaneous use of both PS addition and UV-irradiation lead to adverse effects to the chain planarization above 60 wt% PS as mentioned above. As for the degree of aggregation, it decreases with increasing P3HT content in the pristine samples as seen by the increasing presence of the non-aggregated (amorphous) region as observed in Figure C-17a, confirming that PS induces aggregation during film formation.

In contrast, the UV-radiated P3HT films show a maximum aggregate percentage at around 60 wt% P3HT as seen in Figure 18b. The trend is consistent with the aggregate absorption peak (Figure C-17b), where the 0-0 transition is the sharpest among all components. The result suggests that an optimal processing condition exists with nonmonotonic variations. Overall, this combinatorial approach contributed to a deeper understanding of the structure-property relationships in not just D-A polymer based blends but in and homopolymer-based blend systems as well and this approach paves the way for the rational design of PSIBs with improved performance and stability.

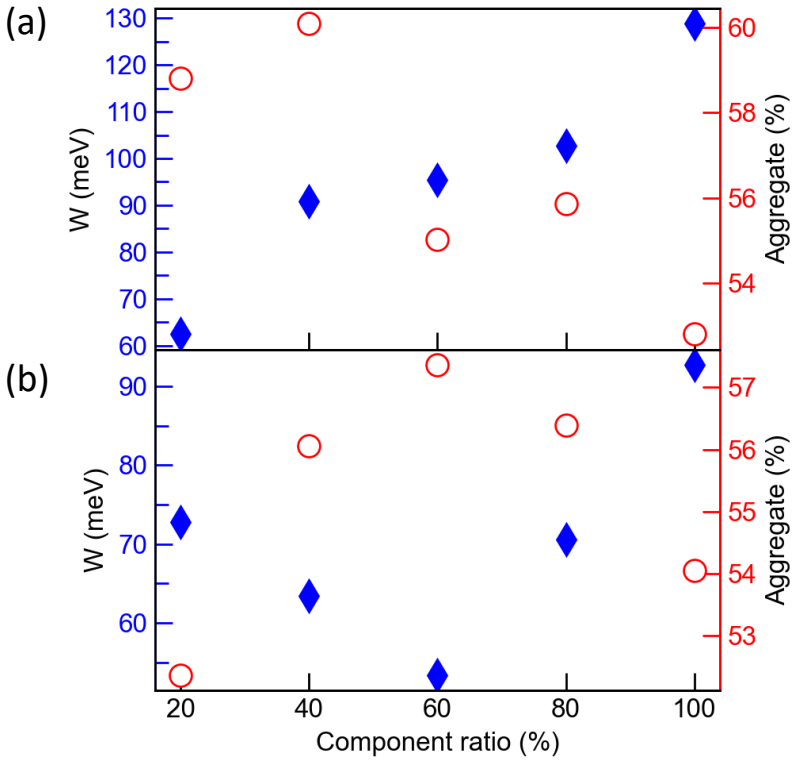

Figure 4-18. The Exciton bandwidth – W (left) and percentage of aggregates (right) plotted as a function of the weight percentage of (a) untreated P3HT and (b) UV-irradiated P3HT for blade coated thin film blends.

4.4 Conclusion

In this work, an exploration of PSIBs achieved through a HTGF library approach, coupled with traditional discrete experiments, revealed key insights into the relationships between blend composition, thin-film morphology, phase-separation and device performance. The HTGF approach allowed for efficient screening of a broad composition range of DPP-DTT blends with PS as the insulating material. Clear advantages in capturing the nuances of onset behaviors and transitions in device performance, phase separation and morphology based on composition were demonstrated. Such aspects can often be elusive, making the HTGF approach valuable for gaining a comprehensive understanding of PSPRs in PSIBs. The insights from the gradient approach were also investigated and validated through OCAT experiments, which provided a targeted approach to investigate specific blend compositions within and beyond the gradient range. The OCAT trends observed for DPP-DTT agreed with those from the gradient films, highlighting the effectiveness of the gradient approach in capturing key PSPRs in PSIBs. XPS depth profiling unveiled findings such as the presence of DPP-DTT at air interface with enrichment of DPP-DTT at the substrate interface at lower blend ratios of the semiconducting component, transitioning to a more even distribution within the bulk at higher blend ratios. The gradient approach was also employed with P3HT/PS blends under different solution processing conditions and spanning a wider composition range. The outcomes validated the versatility of the HTGF approach, demonstrating its applicability to diverse conjugated polymer blend systems. The observed device performance differences between HTGF and OCAT coated films for DPP-DTT vs. P3HT point to the impact of polymer molecular structure on the solution behavior of semiconducting polymers during the thin film deposition process, particularly

under dynamic flow conditions. The results emphasize the complexity PSIBs and support the critical need to develop effective high-throughput characterization techniques such as automated microscopy, spectroscopy, and device testing. Access to such methods to efficiently unravel the behavior of these complex systems will expedite their scalability and deployment for practical applications.

CHAPTER 5. CONCLUSION, FUTURE WORK AND PERSPECTIVE

5.1 Conclusion

Conjugated polymers (CP) have emerged as promising candidates for the development of lightweight, cost-effective, and flexible electronic devices like OFETs, OLEDs, and solar cells, which found applications across various industries spanning from consumer electronics to renewable energy systems. Unlike traditional inorganic silicon, CPs offered the advantage of being processed from solutions, allowing for further optimization and cost-savings. However, progress in CP research had been impeded by the complexity of their processing space, coupled with a predominant reliance on discrete or trial-and-error experimental approaches, hindering both the pace of advancement and depth of insights. This thesis, focusing on D-A-based OFETs, aimed to overcome these challenges through a data-centric approach. It demonstrated how the application of informatics on curated process-property datasets could unveil crucial insights and guide future experiments (CHAPTER 2). Furthermore, it explored how the manipulation of CP solution states could influence final film morphology and device performance (CHAPTER 3), and how HTE could complement discrete experiments, facilitating rapid screening of processing spaces for PSIBs resulting in more efficient and comprehensive insights (CHAPTER 4). In summary, this work bridged the gap between theory and practice, propelling the field of CP-based electronic devices toward a faster and more efficient future.

CHAPTER 2 delved into the benefits of harnessing data science methodologies to uncover pivotal insights and steer future experiments within the domain of materials research. The study involved the curation of a comprehensive dataset from scientific literature, focusing on DPP-DTT based OFET devices and encompassing crucial process-property information. A significant obstacle encountered during dataset curation was the manual extraction process, compounded by the absence of data for several pertinent processing variables, which could be attributed to the absence of standardized reporting measures within the community. Leveraging a customized classification algorithm, this dataset was analyzed to pinpoint the key processing variables influencing hole mobility, thereby suggesting a reduced experimental design region conducive to enhanced device performance. Notably, the algorithm's analysis revealed polymer solution concentration as an overlooked factor significantly impacting hole mobility, advocating for a narrowed design region to optimize this parameter. Experiments conducted to validate these computational insights, confirmed the influence of solution concentration on excitonic interactions and hole mobility, a previously unrecognized phenomenon. These discoveries underscored the efficacy of employing material informatics approaches to navigate the intricate PSPRs inherent in D-A based CPs, validating existing hypotheses, uncovering novel insights, and providing guidance for future experimentation. The compelling outcomes of this study warranted further exploration and investigation.

CHAPTER 3 further explored the insights garnered from CHAPTER 2, with a specific focus on investigating the influence of solution concentration on the optoelectronic properties of D-A polymers, particularly focusing on DPP-based CPs. Intriguingly, experimental investigations conducted across various molecular weights of DPP-DTT

unveiled a consistent trend: OFET devices fabricated at C*, as determined through solution viscosity experiments, consistently exhibited enhanced hole mobility. This trend persisted across alternative D-A polymers such as PDPP-4T and N2200, confirming a previously unidentified trend. To unravel the underlying reasons behind these observations, relevant characterizations were performed. These investigations aimed to understand the solution state behavior of CPs prior to deposition, as it exerted a profound influence on the final film morphology and device performance. This study emphasized the importance of understanding and optimizing solution parameters for CPs to harness their full potential in optoelectronic applications. The results from this study helped identify that the C* is the optimal solution concentration for improved device performance of D-A polymer-based OFETs, highlighting the critical role of solution concentration in achieving enhanced optoelectronic properties.

CHAPTER 4 delved into the advantages of HTE in efficiently exploring the intricate processing space of PSIBs. This emerging area of interest held promise for next-generation OFETs. In this study, P3HT and DPP-DTT were selected as the respective homopolymer and D-A model polymers, while PS served as the insulating material of focus. In this work, a synergistic approach combining HTGF methodologies with traditional discrete experiments allowed us to gain a comprehensive understanding of the composition-morphology-device performance space and identify critical knowledge gaps. The HTGF methodology efficiently captured a wide composition range on fewer substrates, facilitating the identification of the onset of charge transport and transitions in device performance, phase behavior, and morphology that might otherwise be overlooked. Insights from the gradient film methodology were corroborated by preparing OFETs at

discrete compositions both within and outside the gradient range, and the results from the relevant characterizations closely mirrored the findings from the gradient experiments. Notably, XPS depth profiling revealed an intriguing trend: at lower blend ratios of the semiconducting component, there was an enrichment of the CP at air and substrate interfaces. As the blend ratios increased, a more even distribution within the bulk of the film emerged. This observation underscored the complex interplay between composition and spatial distribution within PSIB films, adding an additional layer of nuance to our understanding of multicomponent polymer systems. In summary, the strategic combination of HTGF and OCAT methodologies enhanced our comprehension of PSPRs in PSIBs, providing valuable insights for optimizing various optoelectronic applications.

A recurring theme across all three chapters of this thesis underscores the importance of carefully assessing processing conditions in the pursuit of optimizing the performance of CP-based OFETs. CHAPTER 2 and CHAPTER 3 meticulously examined the impact of solution concentration, while CHAPTER 4 delved into the influence of blend composition on the optoelectronic properties of D-A polymer-based OFETs. Despite the focus on these variables, numerous other processing variables as depicted in Figure 1-1, await exploration. The methodologies employed herein hold promise for a more streamlined investigation of these variables in future endeavors. Collectively, these chapters represent a cohesive journey through the realm of materials research, culminating in a deeper understanding of the intricacies surrounding D-A polymer-based OFETs. The overarching message resonates: **by integrating HTE and materials informatics into the existing polymer electronics paradigm, we can accelerate the discovery and development not only of OFETs but of other polymer-based electronic devices as well.**

5.2 Recommendations for Future Work

5.2.1 Advancing Understanding of Concentration Trend and Solution Parameters in D-A Polymers

For future work, delving further into the concentration trend observed in CHAPTER 2 and 3 presents an exciting avenue for exploration. To gain deeper insights into the behavior of polymer chains in solution and the solution-state structures formed, advanced solution state characterization techniques such as SANS, SAXS, and freeze drying techniques could be employed.[75, 81] These methods would elucidate the structural arrangement of polymer chains in solution and provide valuable information on how solution properties influence the morphology and performance of solid-state films. Additionally, Molecular Dynamics (MD)[278, 279] simulations offer a powerful tool to simulate the behavior of polymer chains in solution and their transition to the solid-state during the film deposition process. By integrating MD simulations with the aforementioned advanced solution characterization techniques, a more comprehensive understanding of the processes governing film formation can be attained, thus enabling the optimization of solution parameters for enhanced device performance.

In addition to investigating the observed concentration trend across different types of D-A polymers (NDI-based, BDOPV-based, IID-based, etc.), conducting experiments with various solvents, encompassing both poor and good solvents, provides an

opportunity to explore the influence of solvent quality on the observed concentration trend. Previous studies have shown that solvent quality can induce aggregation in the solution state of D-A CPs, which subsequently impacts film morphology and charge transport properties.[75, 280] By varying the solvent quality, we can evaluate how different solvents affect the behavior of polymer chains in solution and, consequently, impact device performance. This comprehensive approach to future experimentation will deepen our understanding of the concentration trend and pave the way for optimizing solution state parameters to engineer high-performance D-A polymer-based OFET devices.

5.2.2 Integrating Temperature Gradients into High-Throughput Gradient Film Experiments

In addition to the composition gradient method discussed in CHAPTER 4, incorporating an additional gradient in annealing temperature perpendicular to the composition gradient presents a novel avenue for exploring multiple processing parameters (2-D gradients) simultaneously, as depicted in Figure 5-1.

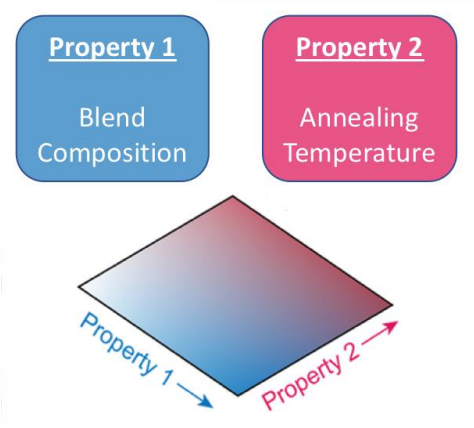

Figure 5-1. Blend composition can be varied in the coating direction (Property 1), while annealing temperature can be varied perpendicular to the coating direction

(Property 2), creating a thin film library with two continuous and orthogonal varied processing parameters.

Previous research has underscored the significant impact of post-deposition annealing on film morphology and device performance.[169, 265, 281, 282] Preliminary results for a 40 wt% DPP-DTT/PS OFET demonstrate enhanced mobility and distinct transfer curve characteristics when the device is annealed at 200°C for 60 minutes in a nitrogen environment, compared to the as-cast film as shown in Figure 5-2.

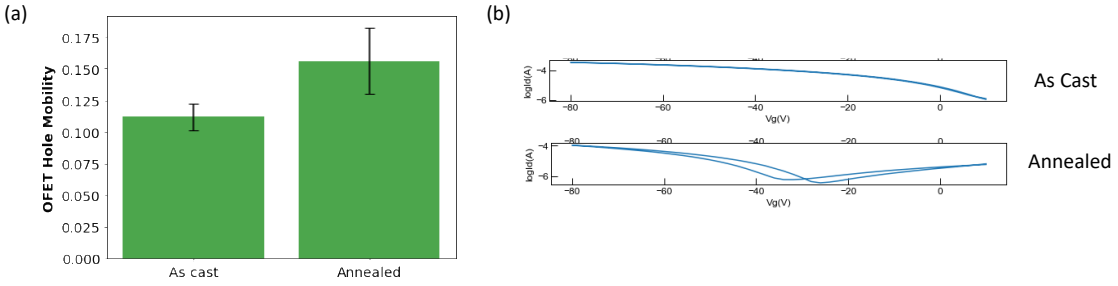

Figure 5-2. (a) FET hole mobility and (b) transfer curves of OFET devices fabricated from a 40 wt% DPP-DTT/PS blend as cast and annealed at 200°C for 60 minutes in a nitrogen environment.

Recently, an annealing stage was set up in the Meredith lab to facilitate the creation of a gradient in the annealing temperature, enabling testing of a broad range of annealing temperatures on a single substrate, as depicted in Figure 5-3. An OFET array similar to the one used in CHAPTER 4 can be employed for this experiment as well.

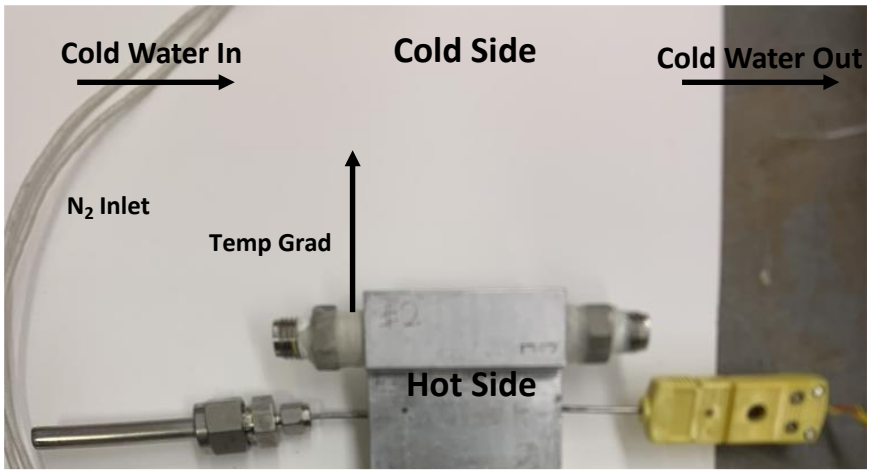

Figure 5-3. High-throughput annealing stage that can be used to generate a gradient of annealing temperatures on the substrate

Initial experiments should involve inspecting a broad range of annealing temperatures on a flow-coated constant composition substrate to comprehensively investigate the influence of annealing on morphology and OFET performance. A blend composition of 40 wt% DPP-DTT can be selected based on the insights from CHAPTER 4 suggesting it as the optimum composition. Next, multiple processing variables can be investigated simultaneously by fabricating a 2-D gradient. An OFET array comprising a gradient in composition established using the method outlined in CHAPTER 4 can then be subsequently transferred to the gradient annealing stage to introduce a gradient in annealing temperature perpendicular to the composition. This integrated approach offers several advantages, including the ability to explore diverse processing conditions efficiently and comprehensively. This work holds a promising direction for future research and can help further strengthen our understanding of the intricate interplay between processing variables, film morphology, and device performance of CP-based devices.

5.2.3 Modeling OFET Process-Property Data Using Machine Learning (ML)

In this section, I propose harnessing ML techniques to model PSPR for OFET experimental data. This endeavor capitalizes on the wealth of available OFET data accumulated from laboratory experiments, published literature, and previously curated datasets, offering an opportunity to extract new insights and guide future experiments. Notably, ML methodologies have yet to be systematically employed in this domain, representing unexplored territory suitable for exploration. Establishing an organized pipeline for ML analysis is crucial, involving defined steps such as problem identification, data collection, feature selection/representation, model selection, model training and testing, addition of prediction intervals (PI), model interpretation, and design of experiments for the curation of new data. A potential pipeline that could be followed for this project is shown in Figure 5-4. A logical starting point (step 1) would involve developing ML models capable of predicting OFET mobility based on processing conditions, thus laying the foundation for understanding the influence of these parameters on device performance.

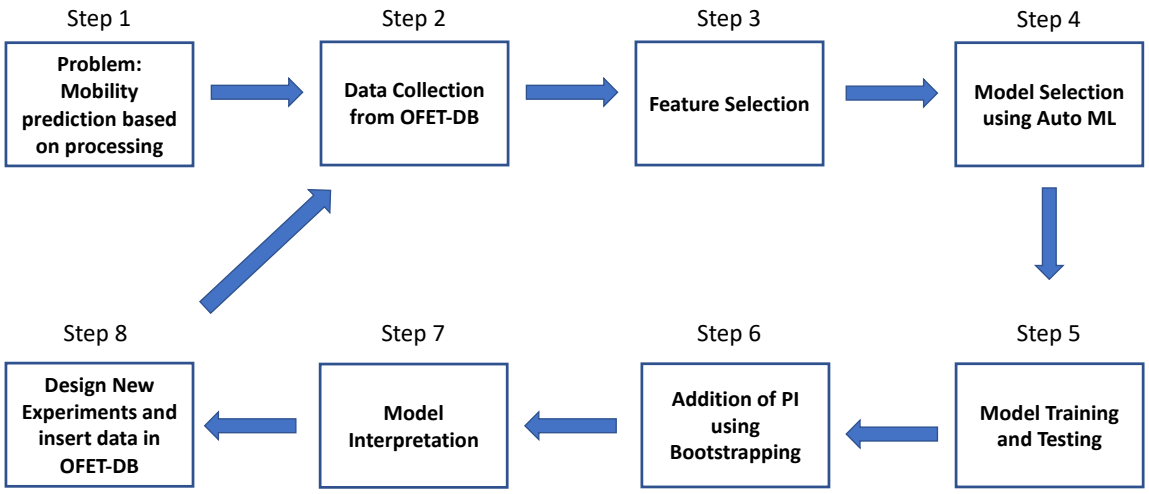

Figure 5-4. Potential pipeline for developing a ML that can predict the performance of an OFET device based on the processing conditions

5.2.3.1 Data Collection

Acquiring data for ML is facilitated through the recently implemented OFET-DB,[47] a valuable resource meticulously documenting the processing history and characterization data of experimentally fabricated OFET devices. Developed by Dr. Aaron Liu, this open-source database meticulously documents the process stages, order, meta-information and characterization data. The database was initially built upon three curated OFET datasets for model polymer systems: P3HT, DPP-DTT, and N2200, totaling 640 data points from peer-reviewed journal articles and laboratory experiments. To streamline data addition, an experimental data entry template (Figure 5-5), adapted from MaterialsMine,[283] simplifies data recording for experimentalists and domain experts, reducing backend workload.

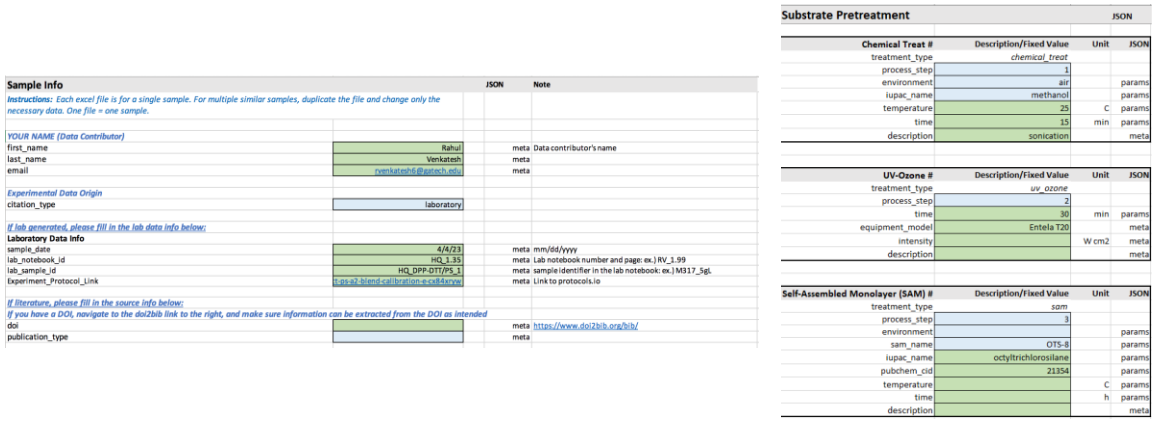

Sample Info		JSON	Note
Instructions: Each excel file is for a single sample. For multiple similar samples, duplicate the file and change only the necessary data. One file = one sample.			
YOUR NAME (Data Contributor)			
first_name	Rahul	meta	Data contributor's name
last_name	Venkatesh	meta	
email	rvenkatesh6@gatech.edu	meta	
Experimental Data Origin			
citation_type	laboratory		
If lab generated, please fill in the lab data info below:			
Laboratory Data Info			
sample_date	4/4/23	meta	mm/dd/yyyy
lab_notebook_id	HQ_1_35	meta	Lab notebook number and page: ex.) RV_1.99
lab_sample_id	HQ_DPP-DTT/PS_1	meta	sample identifier in the lab notebook: ex.) M317_5gL
Experiment_Protocol_Link	dx.doi.org/10.17504/protocols.io.ewov1qkzkvr2/v1	meta	Link to protocols.io
If literature, please fill in the source info below:			
If you have a DOI, navigate to the doi2bib link to the right, and make sure information can be extracted from the DOI as intended			
doi		meta	https://www.doi2bib.org/bib/
publication_type		meta	

Substrate Pretreatment			JSON
Chemical Treat #	**Description/Fixed Value**	**Unit**	**JSON**
treatment_type	*chemical_treat*		
process_step	1		
environment	air		params
iupac_name	methanol		params
temperature	25	C	params
time	15	min	params
description	sonication		meta
UV-Ozone #	**Description/Fixed Value**	**Unit**	**JSON**
treatment_type	*uv_ozone*		
process_step	2		
time	30	min	params
equipment_model	Entela T20		meta
intensity		W cm2	meta
description			meta
Self-Assembled Monolayer (SAM) #	**Description/Fixed Value**	**Unit**	**JSON**
treatment_type	*sam*		
process_step	3		
environment			params
sam_name	OTS-8		params
iupac_name	octyltrichlorosilane		params
pubchem_cid	21354		params
temperature		C	params
time		h	params
description			meta

Figure 5-5. Example pages of the data entry template designed in excel that can be used to document experimentalist details, process stages, order, meta-information and characterization data.

With the assistance of colleagues Jessica Bonsu, Myeongyeon Lee, and Mengting Sun, automation of data extraction from the template and insertion to the database was achieved through a Python code employing SQL queries, enabling rapid integration. This approach updated 100 existing records in the database and added 240 more within two weeks, a significant improvement over previous data curation timelines. Furthermore, collaborative efforts with Dr. Ying Diao's lab at the University of Illinois-Urbana Champaign facilitated the incorporation of additional experimental data, enriching the database with OFETs based on DPP2T and PII2T. Notably, hosting the data on the Microsoft Azure cloud further enhances accessibility for collaborators, fostering seamless collaboration and data sharing within the scientific community. However, the current template workflow may not be suitable for the HTE data as seen in Chapter 4, warranting future modifications. Constant database updates with data from future experiments, either from laboratory or publications, are recommended to maintain relevance and improve ML model performance.

5.2.3.2 Feature Selection/Representation

To enable ML, it is imperative to represent polymer structure, processing variables, and structural information in a machine-readable format.[132] However, in the realm of polymer-based OFETs, this task presents challenges due to the vast array of processing variables available, making feature selection complex. It is advisable to start with the simplest representation of processing variables and progressively augment dataset complexity by incorporating more detailed processing information. Monitoring model performance throughout this process is crucial. If the model's performance declines as additional processing information is added, it suggests that these features negatively impact model accuracy and should be removed. Moreover, in cases of highly correlated descriptors, one can be eliminated, retaining the other. Various feature selection techniques, such as principal component analysis (PCA)[284] and linear discriminant analysis (LDA),[285] exist to reduce feature space dimensions.

The relevant data for ML can be extracted from the OFET-DB database using Python commands and SQL queries. This data can then be structured into a table containing descriptors [X] as model inputs and mobility [Y] as the output. The polymer structures of P3HT, DPP-DTT, N2200 etc. within the dataset can be effectively represented using BigSMILES, a compact representation method that captures the stochasticity of polymers.[286] Polymer genome[287] is another tool that can be used to numerically represent the polymers using their custom fingerprinting feature. Representing processing information as descriptors demands some ingenuity. Numerical variables like polymer M_w, M_n, channel width, etc. are relatively straightforward to

include. However, categorical data such as deposition method or dielectric material must be encoded in a machine-readable format. One-hot encoding is a common method for this purpose, as illustrated in Figure 5-6.

Sample #	Deposition Method
1	Spin
2	Blade
3	Drip

Sample #	Deposition_ Spin	Deposition_ MGC	Deposition_ Other
1	1	0	0
2	0	1	0
3	0	0	1

Figure 5-6. Using one-hot-encoding to represent categorical information like deposition method in a digital/numerical format

Moreover, certain processing details, like solution/substrate/post-process treatments such as aging time or UV-irradiation time, may only apply to a subset of OFET data points, potentially resulting in rows with empty values. To address this, a single column could be used, named 'solution_treatment_aging' or 'solution_treatment_UV-irradiation', with a value of 0 indicating no treatment and 1 indicating treatment (refer to Figure 5-7).

Sample #	Solution_ Aging_Time (hr)	Solution_UV-irr_Time (hr)
1	1	-
2	-	2
3	2	-

Sample #	Solution_ Aging	Solution_ UV-irr
1	1	0
2	0	1
3	1	0

Figure 5-7. Simplifying the representation of solution/substrate/post-processing treatment information to avoid missing information.

Maintaining the order of these treatment steps is also crucial and may require a creative approach to incorporate into the dataset. One possible technique is demonstrated in Figure 5-8.

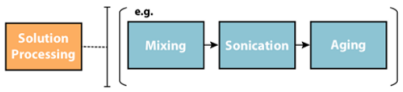

Sample #	SP_Mixing	SP_Aging	SP_Sonication	SP_UV
1	1	3	2	0

Figure 5-8. Custom approach to representing the order in which process treatments take place.

Eventually, incorporating film structural information, such as d-spacing values from GIWAXS measurements or W values from UV-Vis measurements, should be considered as descriptors to build PSP models rather than solely process-property models. However, a challenge arises as not all records in the database may contain values for these structural parameters, potentially leading to missing information in the dataset.[45, 47, 149]

5.2.3.3 Auto ML for Model Selection and Building

With the curated and pre-processed dataset ready, the next crucial step involves selecting an appropriate ML algorithm for training. A supervised learning regression model capable of predicting OFET mobility for new data post-training is appropriate for this work. The careful selection of an algorithm is pivotal in any ML workflow, significantly influencing prediction accuracy.[123] While various supervised regression algorithms are readily available online through packages in Python (such as scikit-learn,[288] Keras,[289] PyTorch[290] etc.), testing each algorithm and optimizing hyperparameters through trial and error can be both exhaustive and time-consuming. However, recent advancements in Auto-ML model screening software offer a solution by

enabling rapid comparison of multiple ML models and recommending the most suitable model and parameters for our data, making it easier for users to build highly performant predictive models without extensive manual effort.[132, 291] Both paid software solutions like JMP,[292] Microsoft Azure,[293] H2O,[294] and open-source alternatives like TPOT[295, 296] exist, each with its own set of advantages and disadvantages. While user-friendly tools such as JMP, Azure, and H2O boast good interfaces and ease of use, they come with substantial costs, often exceeding $10,000 in yearly subscriptions. On the other hand, AutoML tools like TPOT, though less user-friendly compared to their counterparts, are free to use and serve as an excellent starting point. Despite relying on AutoML tools, it remains crucial to possess a basic understanding of the underlying models' functionality and not blindly trust the recommendations.

5.2.3.4 Addition Of Prediction Intervals Using Bootstrapping

In addition to developing a model capable of accurately predicting the mobility of an OFET, it is recommended to compute prediction intervals/errors for each data point to enhance the model's reliability. The inspiration for this approach stemmed from my colleague Xiaohan Yu during our data science internship at Dow Chemicals, where we constructed ML models to predict the performance of polyurethane foams. Utilizing bootstrapping, prediction intervals for the data points can be calculated, providing a measure of uncertainty surrounding each prediction.[297] Bootstrapping involves repeatedly sampling with replacement from the original dataset to generate multiple bootstrap samples. For each sample, the model is trained, and predictions are made for the entire dataset. The variability in predictions across the bootstrap samples is then used to estimate the prediction interval for each data point. This process offers a robust approach to quantify

the uncertainty inherent in the predictions. An example of using bootstrapping to add prediction intervals to a sample P3HT dataset is shown in Figure 5-9 below.

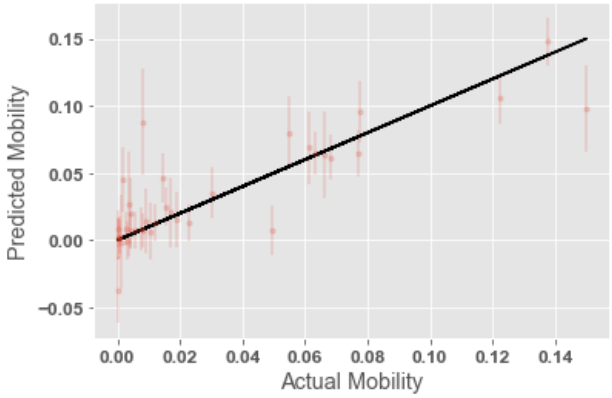

Figure 5-9. Using bootstrapping to obtain prediction intervals for a sample P3HT process-property dataset.

5.2.3.5 Model Interpretation and Designing Future Experiments

As crucial as it is to develop a model with high predictive capability (accuracy), understanding and interpreting its functionality is equally important for gaining deeper insights.[132, 298] For instance, in the case of optimizing OFET mobility, understanding the influence of each processing variable enables better design of experiments. There are two strategies that are commonly adopted to explain and interpret a model's functionality: glass-box models, which are inherently explainable and interpretable, and posthoc methods, which are suitable for explaining black-box models like neural networks.[132] Glass-box models such as least absolute shrinkage and selection operator (LASSO),[299] sure independence screening and sparsifying operator (SISSO),[300] and genetic programming symbolic regression (GPSR),[301] inherently shed light on how the ML model makes predictions and how the features are related to the output. Conversely, for

more complex ML models like neural networks, posthoc analysis methods like SHapley Additive exPlanations (SHAP)[302] can be employed. SHAP, rooted in game theory, assigns a SHAP value to each feature, offering both local interpretability for specific instances and a global understanding of the model's behavior across the dataset. In polymer research, SHAP has been utilized to discern the predictive significance of various features, such as functional groups and polymer intrinsic properties on performance metrics like membrane permeability.[303-306] An example of SHAP applied to a neural network model built on a sample P3HT dataset is depicted in Figure 5-10. Here, we can observe the correlation between each feature and the mobility, utilizing the SHAP value to discern the order of importance of each feature. This enables us to prioritize the processing variables accordingly while designing future experiments.

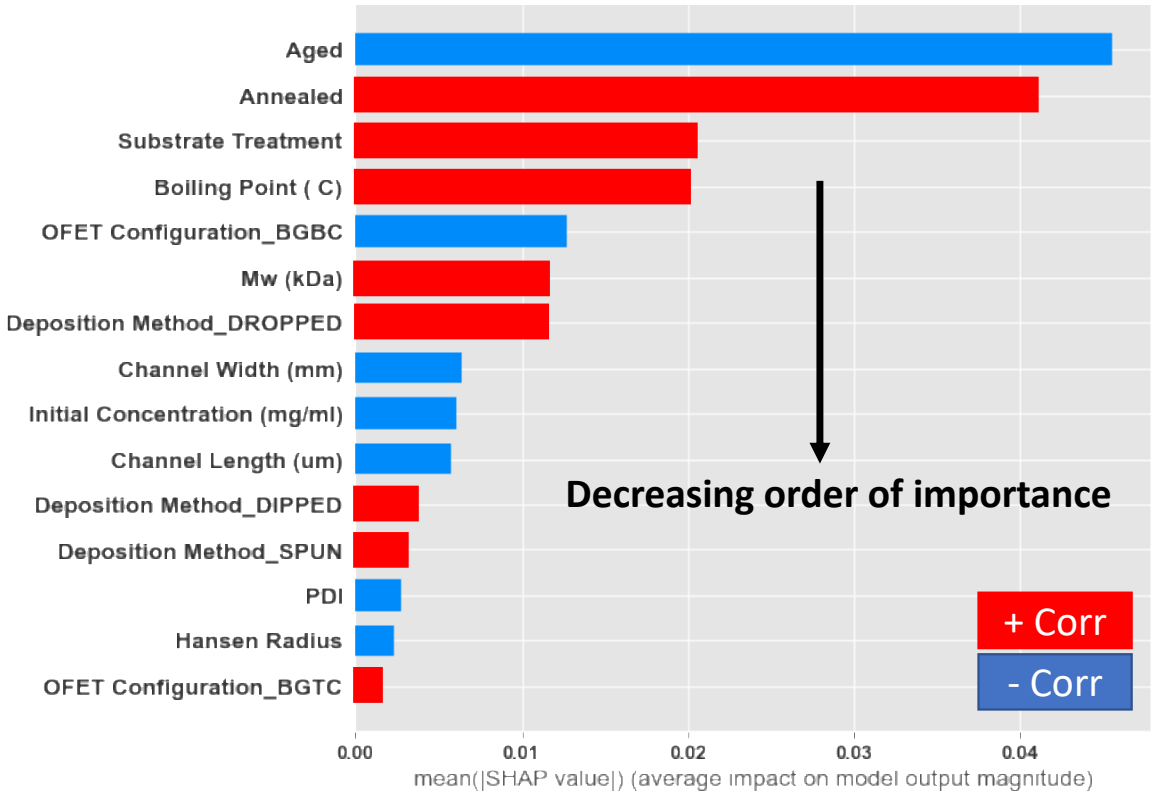

Figure 5-10. Using SHAP to interpret a neural network model built on a sample P3HT dataset. SHAP can be used to identify the order of importance of each descriptor and how It impacts the target property of interest (mobility in this case).

In addition to model interpretation, integrating active learning tools can aid in the design of new experiments and improve the predictive capabilities of ML models.[132, 307] Active learning algorithms for materials design, iteratively select the most informative data points for experimentation, with a focus on regions where the model's predictions exhibit the highest uncertainty.[303, 305] Bayesian Optimization, a prevalent type of active learning, utilizes probabilistic or surrogate models like Gaussian process regression[308] to intelligently explore the experimental space.[309] This technique identifies the optimal set of experiments (i.e., processing conditions) based on the model's predictions and uncertainty estimates, effectively guiding experimentation towards regions of interest.

By following the outlined workflow (*vide supra*) and incorporating the suggested methodologies, we can expect to gain new insights and drive advancements in the development of polymer-based OFETs. This comprehensive approach would not only enhance our understanding of underlying principles but can also accelerate the translation of research findings into practical applications.

5.2.4 Mobilizing a Knowledge Platform for Organic Thin-Film Electronics

5.2.4.1 Motivation

Initiated in 2023, this project is deeply significant to me as it represents my inaugural experience leading a team. It stands as a culmination of the skills acquired throughout my PhD journey, offering an opportunity to apply and expand upon my expertise. The driving force behind this endeavor stems from the issue of missing data and non-standardized reporting, particularly concerning processing conditions, within the field of polymer-based electronics. This deficiency not only impedes experimental reproducibility but also acts as a significant barrier to research progress.[45, 47, 310] Moreover, the lack of collaboration exacerbates these challenges, underscoring the urgent need for concerted efforts to address them. Leveraging the wealth of OFET experimental data available through resources like the recently developed online repository, OFET-DB,[47] served as a pivotal starting point for this project. Inspired by successful initiatives within the polymer community, including CRIPT[125], Polymer Genome,[287] and Materials Mine,[283] we embarked on the development of a shared database and knowledge platform. This platform aims to empower researchers in the organic electronics community by providing access to existing OFET experimental device data and facilitating the

contribution of new data through an intuitive web interface. Our vision for this platform extends beyond mere data storage. We envision it as a dynamic hub for collaboration among researchers in the organic electronics community. By integrating advanced data visualization and analysis tools, the platform seeks to enable users to explore data, extract insights, and leverage materials informatics techniques. Ultimately, our goal is to enhance experimental design, foster the development of PSP models, and facilitate informed scientific decision-making. Through these efforts, we aim to accelerate the integration of next-generation conjugated polymer-based materials into real-world applications. Furthermore, an initiated collaboration with the Ying Diao group at University of Illinois Urbana-Champaign facilitated the addition of new OFET device data to the database and will assist in testing the interoperability of the web interface across research groups, further enhancing the project's scope and impact.

5.2.4.2 Proposed Features and Development Plan

The platform will leverage the model from the OFET-DB database, enabling researchers to input, store, and retrieve various types of data and metadata related to the processing, characterization, and performance of conjugated polymers-based OFETs. A user-friendly web interface, featuring a web form resembling the previously mentioned Excel template, will provide researchers with a convenient option to contribute OFET data. Moreover, the platform will incorporate robust features for data visualization and analysis features to assist researchers in identifying trends and patterns in their data. Users will also have the capability to download customized versions of the dataset for data science and machine learning purposes.

The platform's development plan encompasses both backend and frontend aspects. We plan on using Gin, a HTTP web framework written in GoLang, to develop the backend framework, GORM for data modeling, and PostgreSQL as the database hosted on the Azure cloud. For the frontend, authentication functionalities will be implemented using Firebase, while React.js and CSS will be employed for user interface design. React and D3.js will be utilized to create dynamic and interactive data visualization pages. Continuous integration and deployment (CI/CD) pipelines will be established using Github Actions, and the connection between the front and back ends will be facilitated through a Docker container environment. The beta version of the platform is anticipated to be ready by the summer of 2024.

To further enhance the platform's capabilities, it is recommended to pursue continued collaboration with partners and stakeholders, while also welcoming new collaborators from diverse research groups and national labs to enrich the dataset. Dedication of resources to execute planned development tasks, adoption of an iterative development approach, and establishment of mechanisms for monitoring progress and evaluating the platform's effectiveness are crucial for ensuring the project's success. The development of a robust experimental knowledge platform for organic thin-film electronics holds significant promise for advancing research in the field. Through collaboration and innovation, the project aims to expedite the translation of research findings into practical applications, thereby contributing to the ongoing evolution of organic electronics.

5.3 Perspective and Outlook

5.3.1 Embracing A Data Centric Approach In Research

Incorporating a data-centric workflow within research offers numerous advantages. Firstly, it facilitates the adoption of clear guidelines for data organization, storage, and sharing, thereby enhancing the reproducibility of research.[311, 312] Secondly, by adopting such workflows, researchers can streamline data handling, enabling them to concentrate on scientific discovery rather than routine data processing. Additionally, proper management of data can lead to higher citation rates for publications.[313] Moreover, data-centric approaches foster collaboration by making datasets accessible and usable across various research projects.[125] Furthermore, these approaches empower researchers to identify hidden trends or new areas for exploration, thereby accelerating the pace of discovery.[82]

Although there have been several examples of successful data management case studies at universities,[314, 315] incorporating this workflow into smaller groups like research groups is challenging. This is because the major bottleneck lies in convincing skeptical or apprehensive researchers about investing time and energy in these resources and changing their existing workflow.[311] However, the availability of resources such as online courses, textbooks, documentation, tutorials, coding platforms, and tools like ChatGPT makes it easier to adopt. It is recommend to make incremental adjustments to the existing workflow by integrating tools like virtual lab notebooks,[316, 317] which offer an efficient way to organize and document research activities. Additionally, hosting lab data on a secure online database managed by a lab member ensures easy access and preservation of valuable research data while maintaining confidentiality.[311] To facilitate the adoption of these tools, I suggest incorporating training sessions during research group meetings, providing hands-on guidance on their usage and benefits. This approach not only enhances collaboration

within the team but also maximizes the utility of these technological resources in advancing research endeavors.

Reflecting on my experience, I recommend that all students, regardless of their immediate research focus, invest in acquiring basic data science skills and proficiency in Python coding, and consider adopting a data-centric workflow within their research groups. By equipping ourselves with the necessary skills and tools, we can navigate the complexities of modern research, advance innovation, and drive progress in our respective fields.

5.3.2 Revolutionizing OFET Research by Integration of Autonomous Experimentation

In the domain of materials research, autonomous experimentation has emerged as a powerful tool for expediting the discovery and development of novel materials with tailored properties.[125, 132, 318-323] Researchers have ushered in a new era of experimentation by integrating advanced technologies such as robotics, computation, artificial intelligence (AI), and ML into the established framework. This integration has given rise to autonomous experimental systems, often referred to as self-driving laboratories, which can streamline various aspects of the experimental process, from synthesis and characterization to data analysis and decision-making, in a continuous, closed-loop fashion.[125, 319, 324-326]

Extensive efforts have been dedicated to developing autonomous platforms for synthesizing, testing and optimizing the performance of various materials, including small molecules,[320, 327, 328] colloids,[329, 330] and additive manufacturing materials.[325, 331] While autonomous experimentation has seen significant advancements in multiple fields, its application in polymer science has only recently garnered attention.[125, 132, 332-335] A notable

example is the Polybot system at Argonne National Laboratory, which offers several stations for synthesis, characterization, and processing of polymer thin-films.[336] Samples can effortlessly shuttle between these stations using a mobile platform equipped with a robot arm, highlighting the potential of autonomous experimentation to revolutionize workflows within polymer research.

Combining human ingenuity with autonomous experimentation offers numerous advantages for materials research. These platforms can augment existing workflows and enable faster experimentation and data collection, ultimately enhancing efficiency and throughput.[320, 325] The precision and consistency of autonomous systems can further improve the accuracy of results.[319, 326] Moreover, their ability to operate continuously frees up researchers' time from repetitive or labor-intensive tasks, allowing them to focus on more complex tasks.[326, 337] Additionally, autonomous experimentation utilizes fewer resources and enables the exploration of complex parameter spaces that would be impractical with traditional methods.[323, 325, 326] Real-time data collection and analysis, facilitated by ML methods like active learning, enhance data-driven decision-making, accelerating discovery.[132, 303, 305, 307, 320] Moreover, these systems foster collaboration by enabling remote access and sharing of experimentation platforms, thereby facilitating interdisciplinary research and knowledge exchange.[125, 320-322, 325]

When designing autonomous platforms, several key considerations should be kept in mind. Integrating existing laboratory equipment, workflows, and protocols alongside new components into the autonomous system is crucial for ensuring seamless operation.[322-324] Leveraging APIs can facilitate seamless communication and coordination between machines within the automated system, enhancing interoperability and scalability.[125, 320,

[323] Effective data handling and interpretation are other critical aspects, requiring the establishment of robust databases with tailored data models and advanced algorithms capable of efficiently managing vast amounts of experimental data for seamless real-time analysis and informed decision-making.[125, 320, 324, 325] Additionally, it is crucial to ensure that the automated system can effectively handle unexpected situations, errors, and variations in experimental conditions. Moreover, safety protocols and ethical guidelines must be strictly adhered to, preventing hazardous situations and minimizing risks to researchers and the environment.[338] Finally, defining clear roles for human researchers and AI systems is necessary, striking the right balance between automation and human expertise to maximize efficiency and scientific discovery.[325, 339, 340]

Recently, the capabilities of autonomous experimentation have extended to the development of polymer electronics like OPVs,[341] with significant potential for expansion into other areas such as OFETs. The PolyBOT system stands at the forefront of these advancements, demonstrating notable progress in this field.[323] However, developing such complex autonomous systems tailored to the specific demands of OFET research presents certain distinct challenges. Integrating robotics into OFET fabrication processes necessitates expertise spanning materials science, engineering, and robotics, which may not be readily available within a single research group. Moreover, the stringent requirements for precision and cleanliness in OFET fabrication mandate access to specialized equipment and facilities (e.g. clean room), which can be both costly and challenging to acquire. Nevertheless, systems like PolyBOT serve as exemplary models, inspiring research groups to make incremental advancements to their existing approach and participate in meaningful collaborations. For instance, adopting a data-centric workflow or

automating testing/characterization procedures are key steps toward eventually reaching similar stages of autonomous experimentation. Additionally, collaborative efforts with other research groups and industry partners specializing in automation can offer effective solutions to the challenges mentioned above.

Our research endeavors align closely with this trajectory as we aim to eventually integrate autonomous systems into our own laboratory workflows. We can initiate this process by implementing small yet impactful changes into our existing methodologies to streamline sample preparation, mixing, and characterization processes. For instance, the semiconductor parameter analyzer stored inside the glove box, which is used to measure the mobility of OFET devices, currently involves a laborious and time-consuming process of manually moving each probe to a new device on the substrate. By integrating a robotic system, we can significantly improve efficiency and accuracy, mitigating the potential for human error and ensuring consistency across measurements. Automating the individual steps of the OFET fabrication and seamlessly connecting them not only expedites the process but also minimizes variability in results, a critical factor in our field. In conclusion, the integration of autonomous experimentation into existing workflows represents a paradigm shift in materials research, offering unprecedented opportunities for discovery and innovation. By embracing and leveraging the power of autonomous capabilities, researchers can contribute to the broader goal of the MGI of developing high-performing, more sustainable, and cost-efficient materials for all.

APPENDIX A. SUPPORTING INFORMATION FOR CHAPTER 2

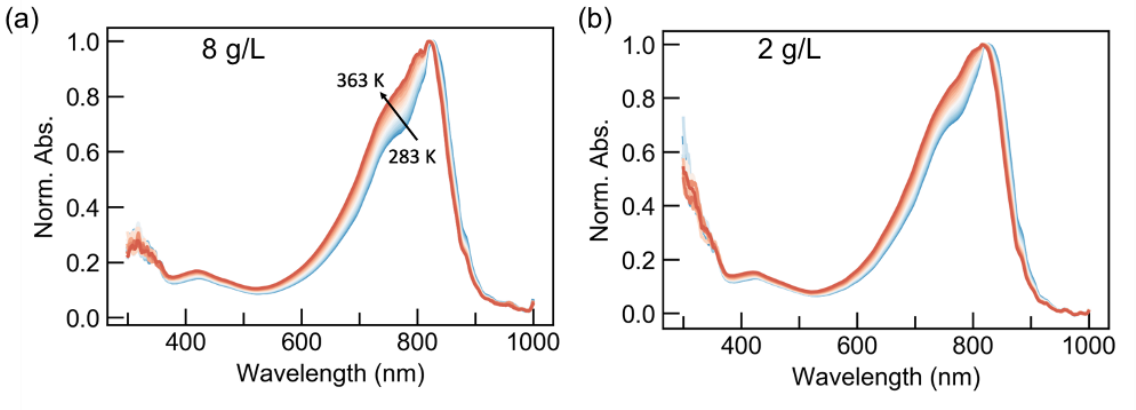

Figure A-1. Solution-state absorption spectra of (a) 8 and (b) 2 g/L DPP-DTT-CB solution measured from 283 K to 363 K with an 5 K temperature interval.

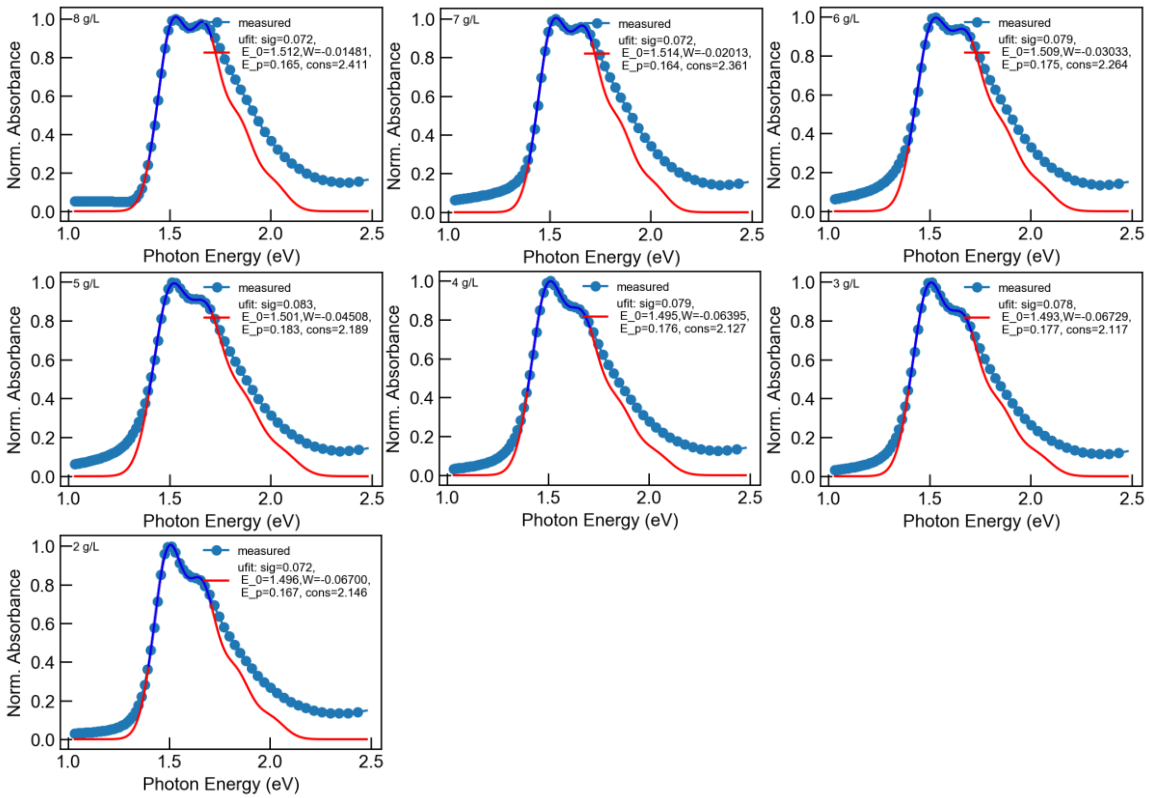

Figure A-2. Modified FC fit for all absorption spectra at different concentrations along with the fit parameter.

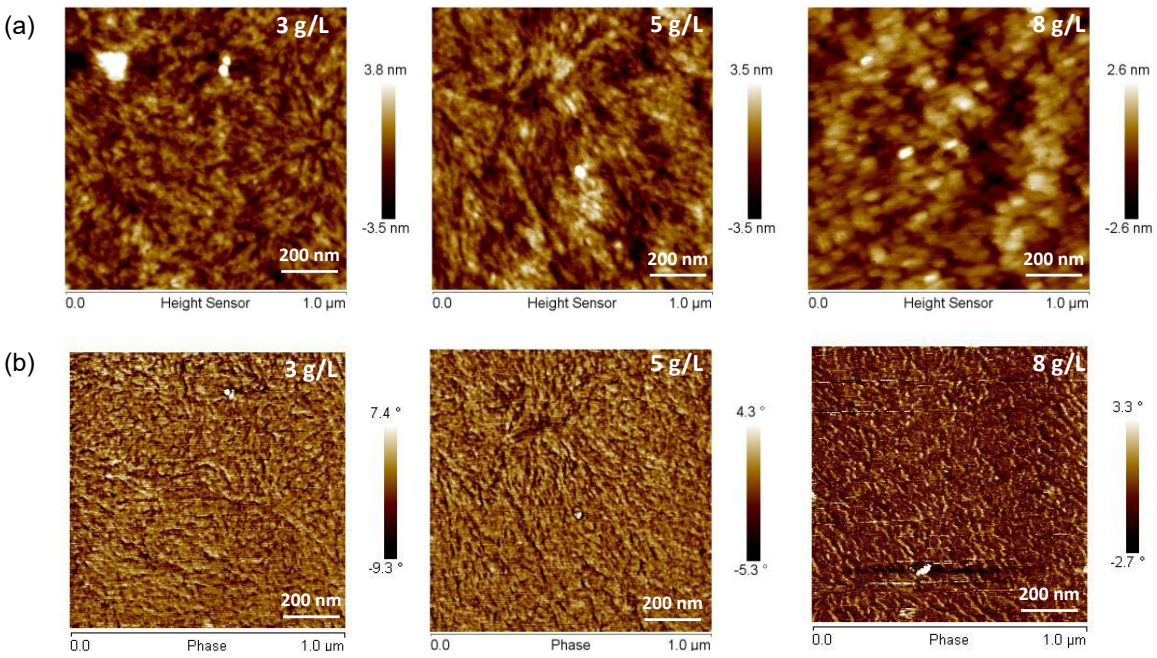

Figure A-3. (a) Height and (b) Phase, Atomic Force Microscopy images of the DPP-DTT thin film samples prepared from solutions of different concentrations.

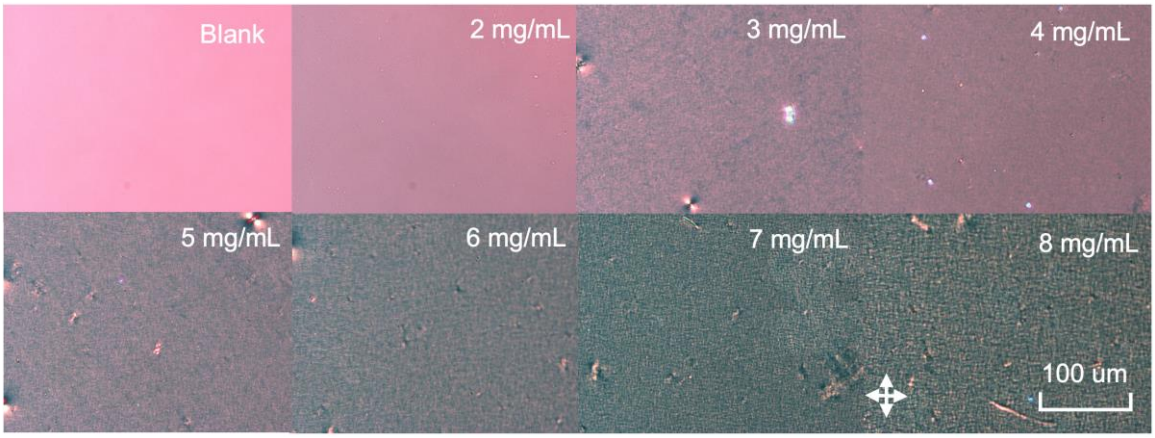

Figure A-4. The cross-polarized optical microscopy images of the samples prepared from solutions of different concentrations. The directions of the polarizations are indicated with the cross signs.

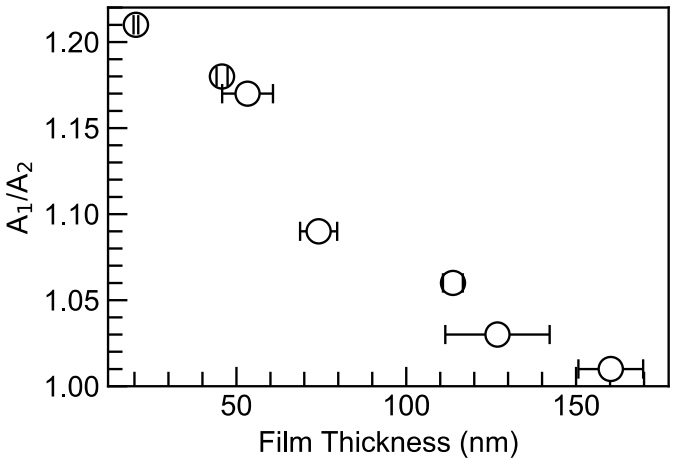

Figure A-5. Film thickness of samples of 2 to 8 g/L in chlorobenzene measured from profilometry as a function of A_1/A_2. The error bars represent 95% confidence interval averaged over 3 different points on the film.

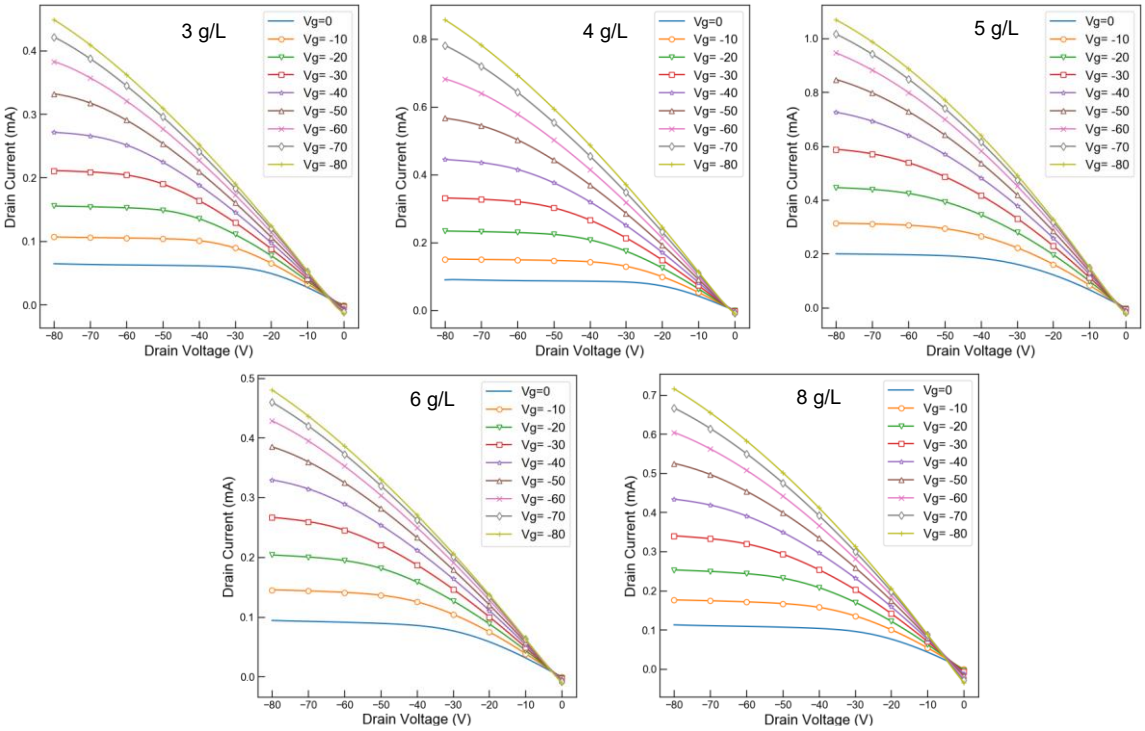

Figure A-6. Output Characteristics for DPP-DTT thin films as a function of solution concentration averaged over 8-12 FET devices.

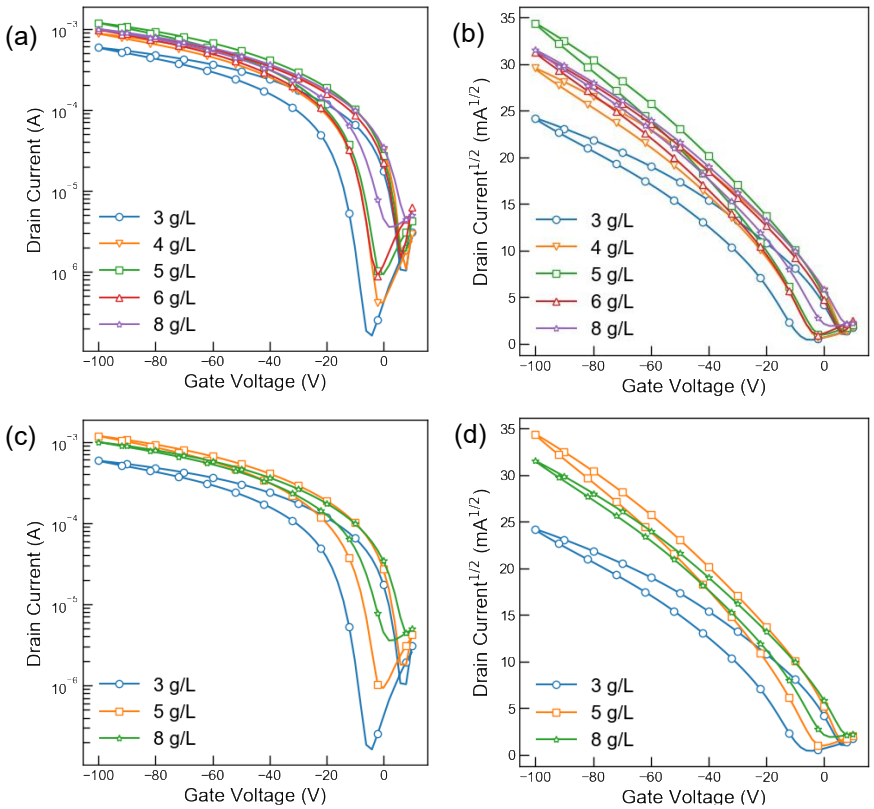

Figure A-7. (a) and (b) Transfer characteristics at concentrations of 3, 4, 5, 6 and 8 g/L exhibiting hysteresis. (c) and (d) Same transfer characteristics as in (a) and (b) but only for three concentrations for clearer visualization.

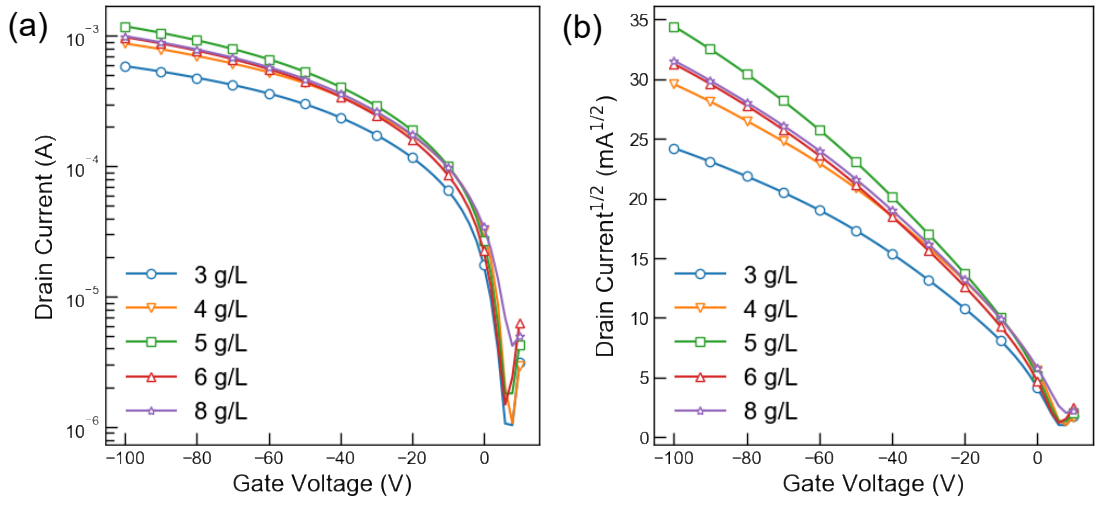

Figure A-8. Forward sweep transfer characteristics (V_{DS} = -80V) as a function of solution concentration.

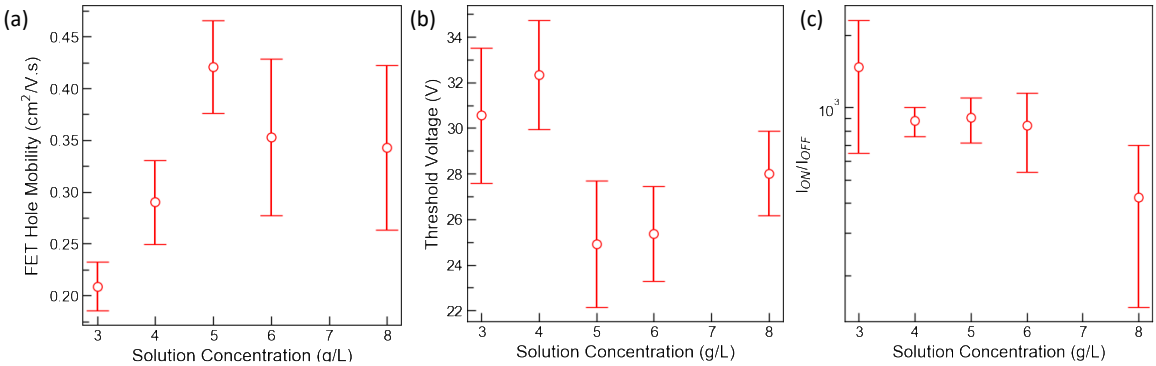

Figure A-9. (a) and (b) FET hole mobility and threshold voltage extracted from the low slope region of the forward sweep transfer curve ($I_D^{1/2}$ - V_G) as a function of solution concentration. (c) I_{on}/I_{off} obtained from the forward sweep transfer curve (I_D – V_G) as a function of solution concentration. The errors bars represent 95% Confidence interval averaged over 8-12 OFET devices.

APPENDIX B. SUPPORTING INFORMATION FOR CHAPTER 3

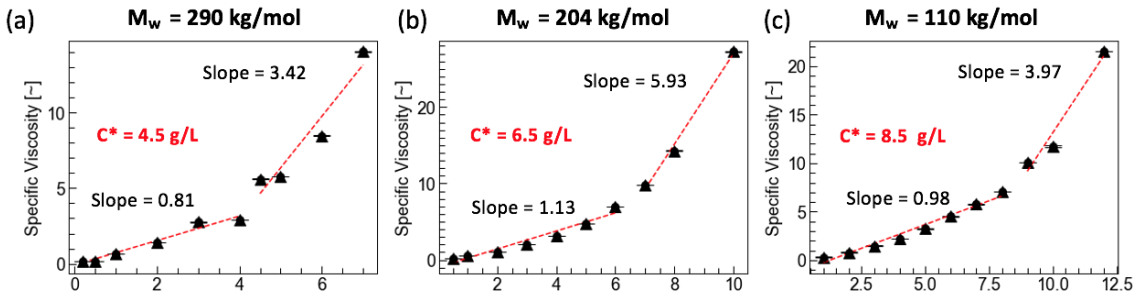

Figure B-1. Specific viscosity measurement of DPP-DTT at three molecular weights (a) 290, (b) 204 and (c) 110 kg/mol dissolved in chlorobenzene solutions at 56 °C. The error bars represent the standard deviation of the specific viscosity. The critical overlap concentration C* is the point where there is a change in the slope of the viscosity as a function of concentration. The point of intersection of the two extrapolated red dashed lines is the C*.

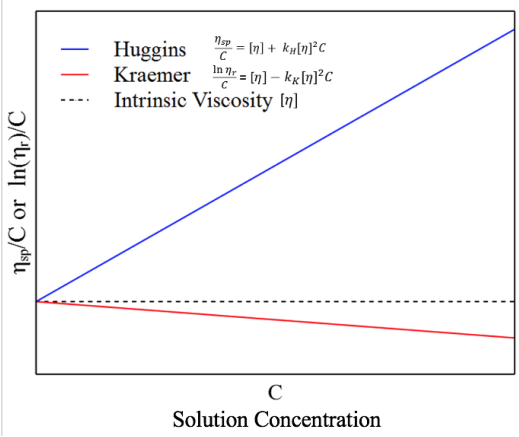

η_{sp} = specific viscosity

η_r = reduced viscosity

Assumption : C* ~ 1/ $[\eta]$

M_w (kg/mol)	C* from Huggins Equation (g/L)	C* from Kramer Equation (g/L)
290	1.57	1.67
204	3.11	2.72
110	4.21	3.41

Figure B-2. A schematic of how C* can be calculated using the Huggins and Kramer equation. The y-intercept of the red and blue lines gives the intrinsic viscosity [η]. The C* can then be obtained from the intrinsic viscosity using the assumption C* ~ 1/[η].

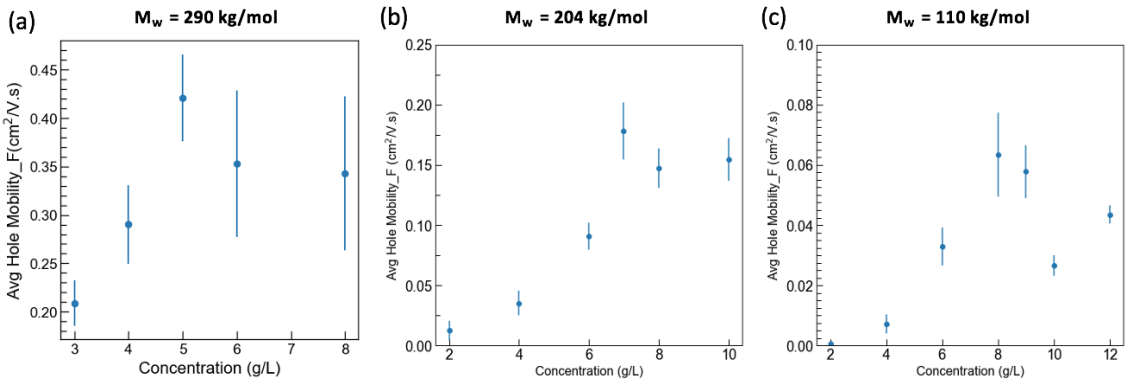

Figure B-3. FET hole mobility of DPP-DTT at three molecular weights (a) 290, (b) 204 and (c)110 kg/mol extracted from the forward sweep transfer curve (V_{DS} = -80V) as a function of solution concentration. The OFET hole mobility was averaged over 18 devices and the error bars represent 95% confidence intervals.

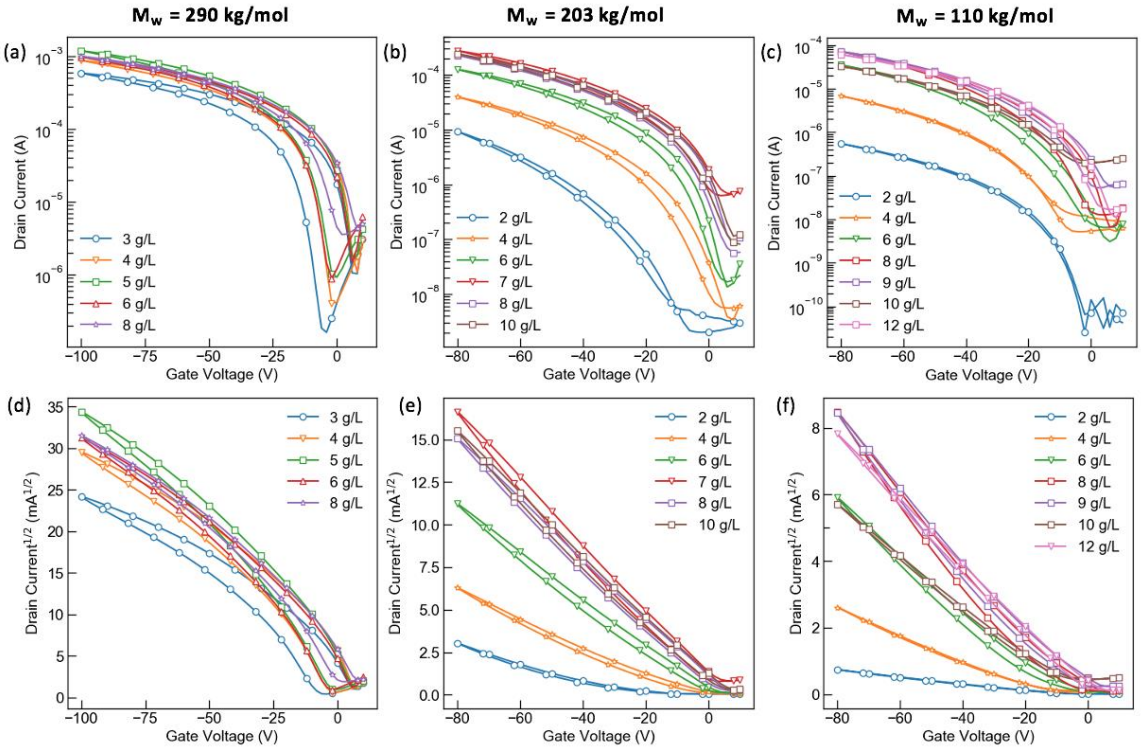

Figure B-4. Transfer characteristics for the three different M_ws of DPP-DTT investigated at the range of concentrations studied. (a-c) $I_d - V_g$ curves for the forward and backward transfer regime (d-f)) $(I_d)^{1/2} - V_g$ curves for the forward and backward transfer regime.

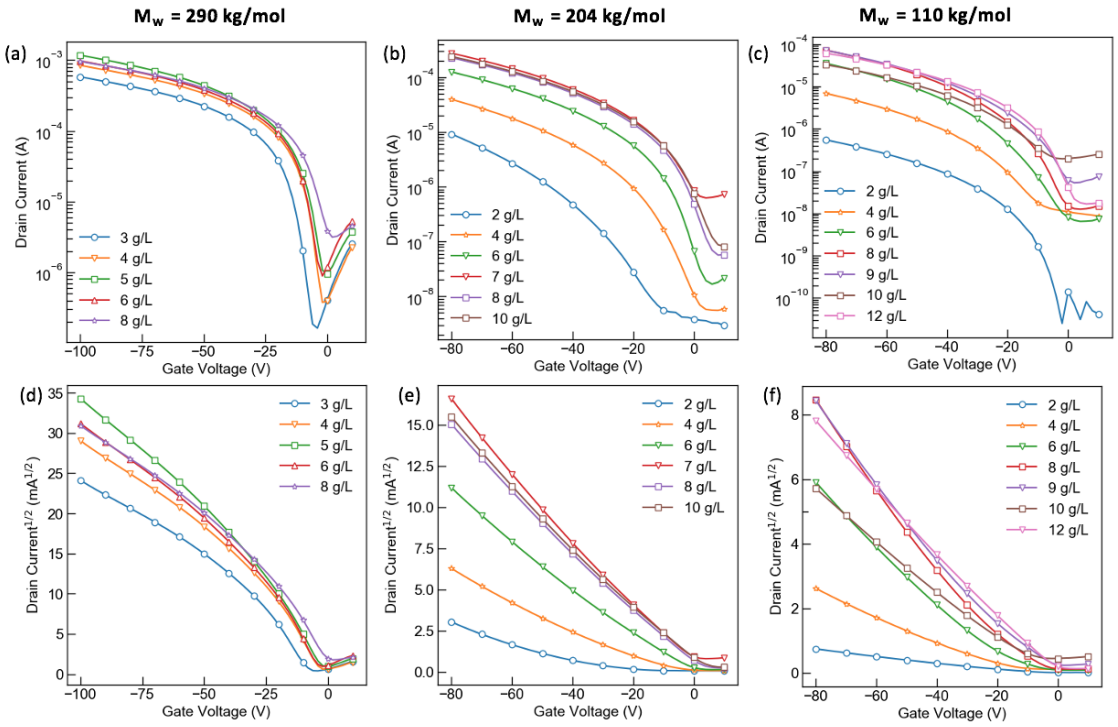

Figure B-5. Transfer characteristics for the three different M_ws of DPP-DTT investigated at the range of concentrations studied. (a-c) I_d – V_g curves for the backward transfer regime (d-f)) $(I_d)^{1/2}$ – V_g curves for the backward transfer regime.

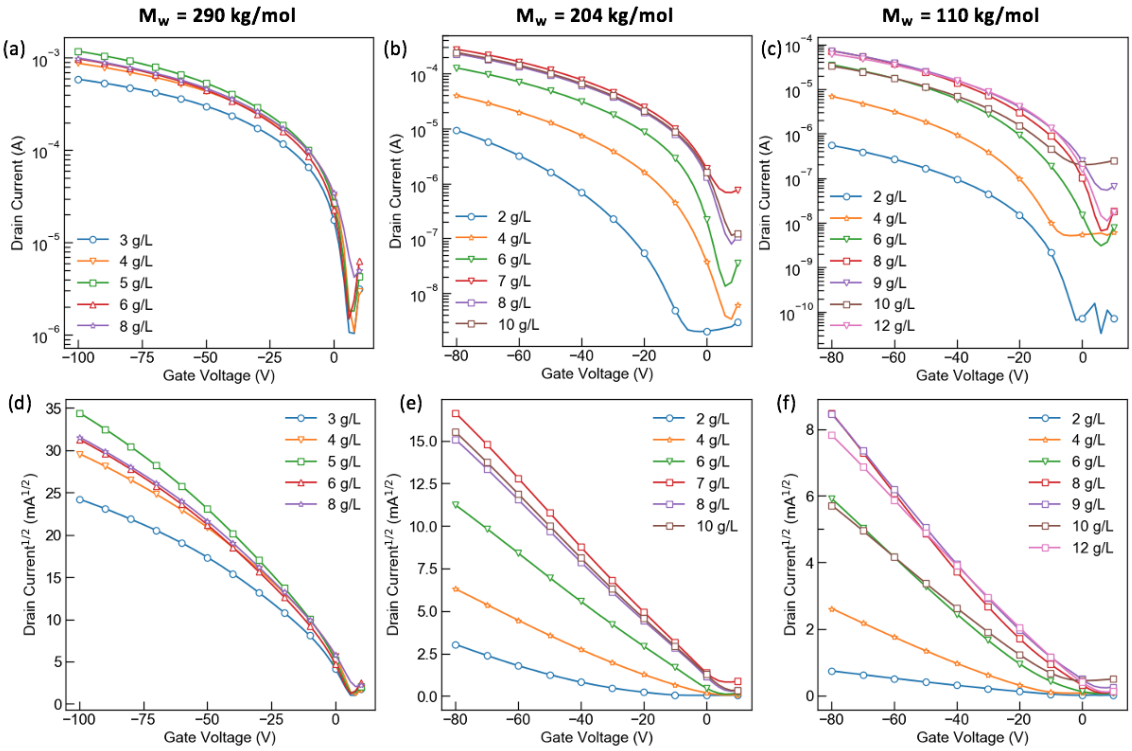

Figure B-6. Transfer characteristics for the three different M_ws of DPP-DTT investigated at the range of concentrations studied. (a-c) $I_d - V_g$ curves for the forward transfer regime (d-f)) $(I_d)^{1/2} - V_g$ curves for the forward transfer regime.

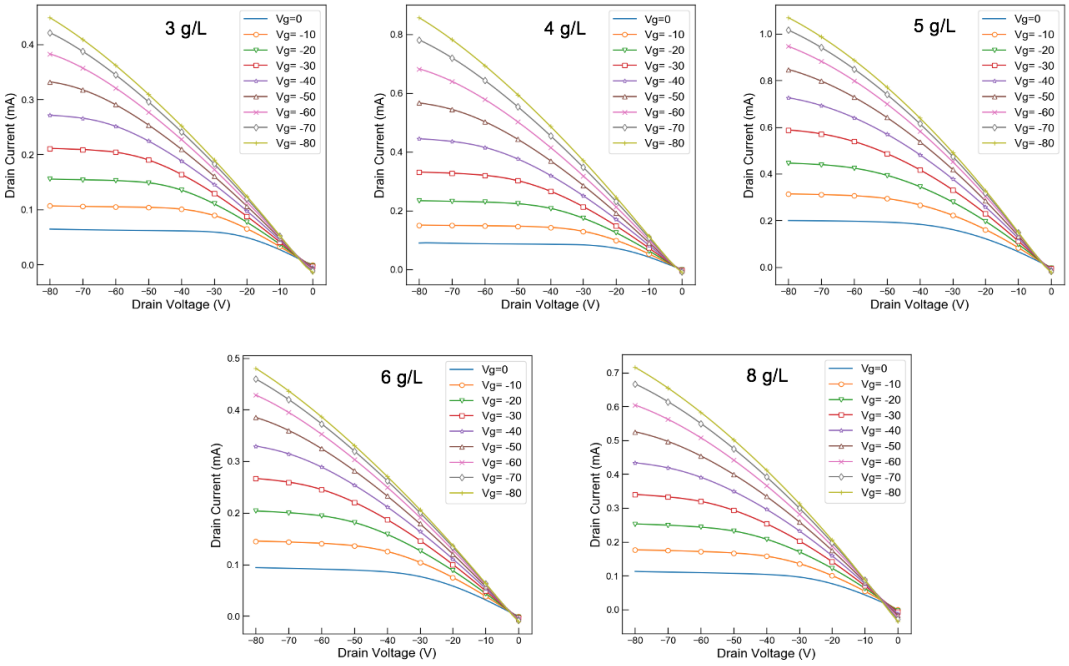

Figure B-7. Output Characteristics for DPP-DTT thin films as a function of solution concentration averaged over 18 FET devices for M_w = 290 kg/mol.

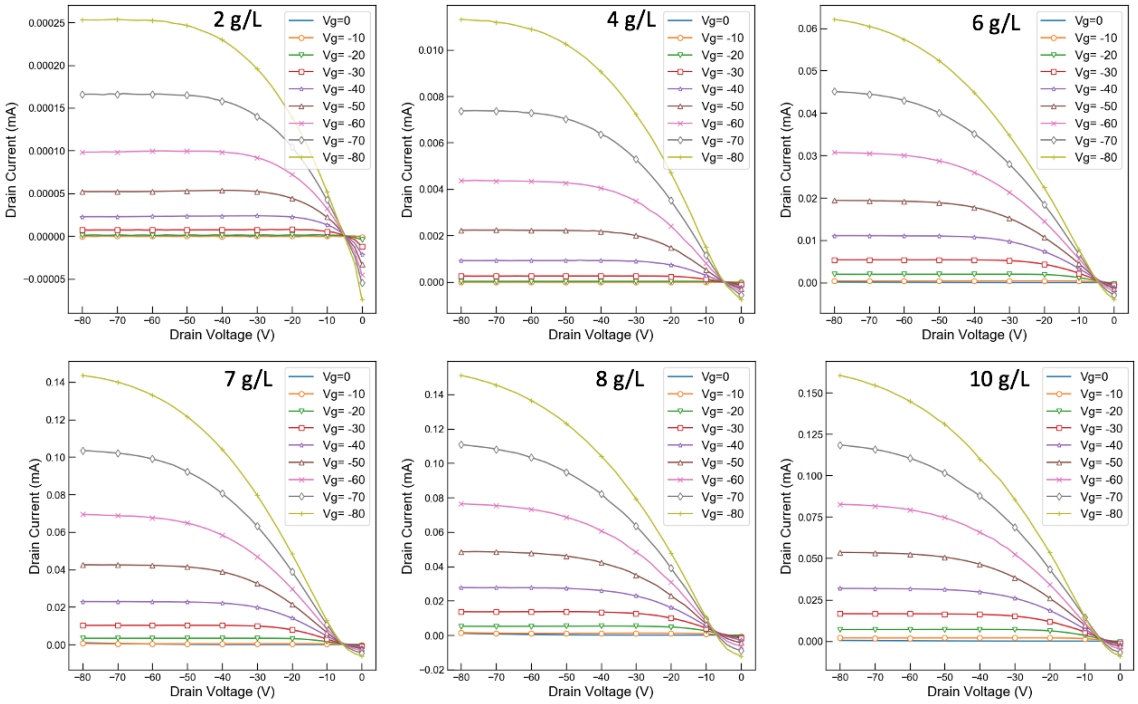

Figure B-8. Output Characteristics for DPP-DTT thin films as a function of solution concentration averaged over 18 FET devices for M_w = 204 kg/mol.

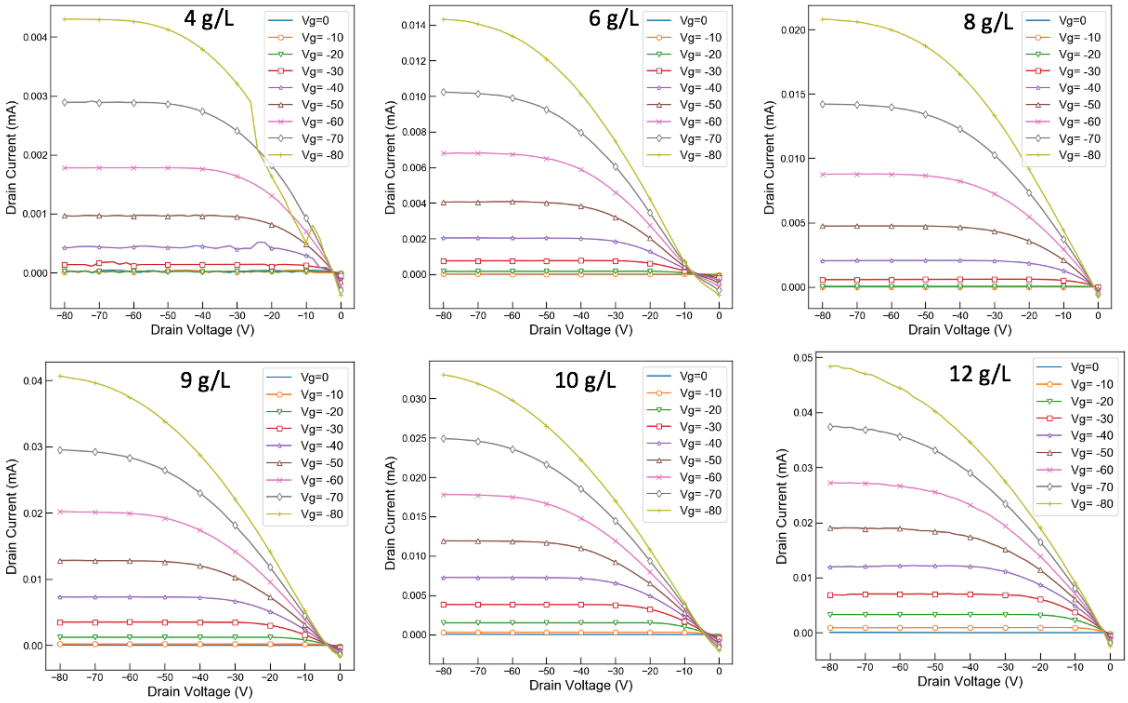

Figure B-9. Output Characteristics for DPP-DTT thin films as a function of solution concentration averaged over 8-12 FET devices for M_w = 110 kg/mol.

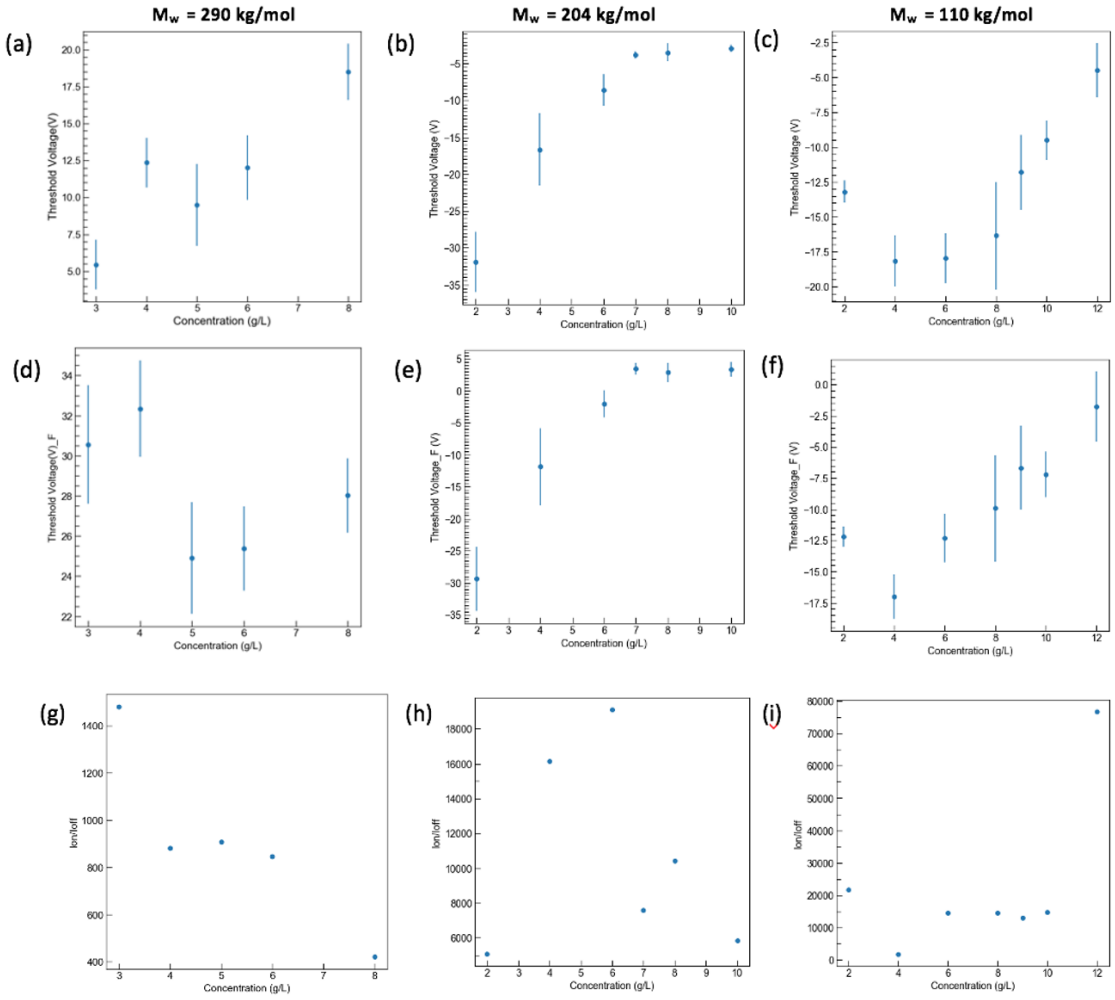

Figure B-10. (a-c) Threshold voltage obtained from the backward sweep transfer curve $(I_d)^{1/2} - V_g$ as a function of solution concentration for the three Mw's investigated. (d-f) Threshold voltage obtained from the forward sweep transfer curve $(I_d)^{1/2} - V_g$ as a function of solution concentration for the three Mw's investigated. (g-i) Ion/Ioff obtained from the transfer curve $(I_d)^{1/2} - V_g$ as a function of solution concentration for the three Mw's investigated.

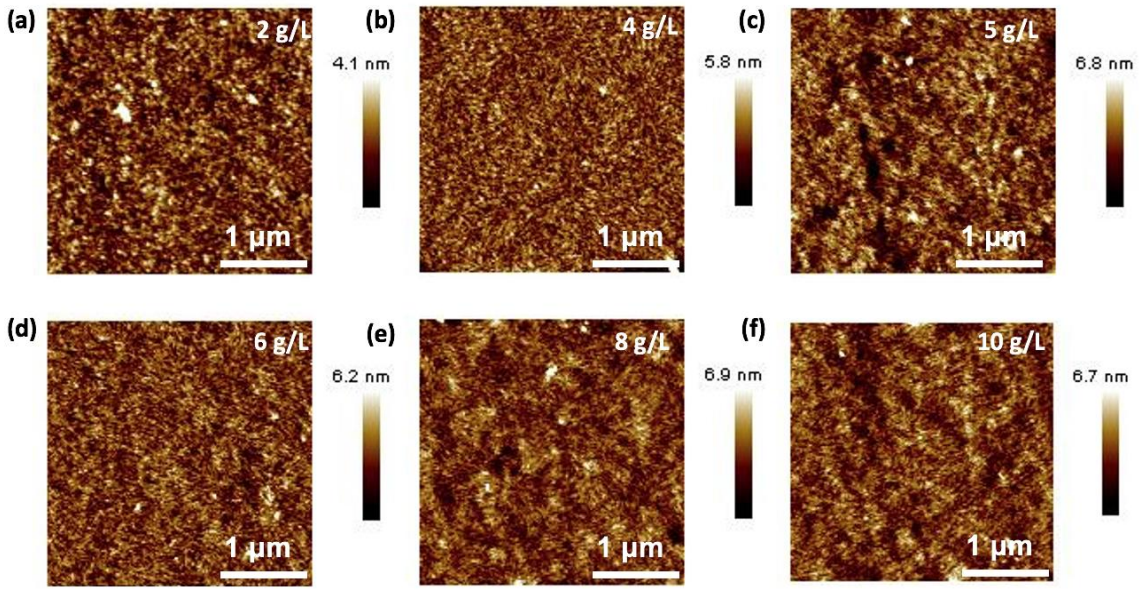

Figure B-11. Atomic Force Microscopy height images of DPP-DTT (M_w = 290 kg/mol) thin films prepared from a range of solution concentrations.

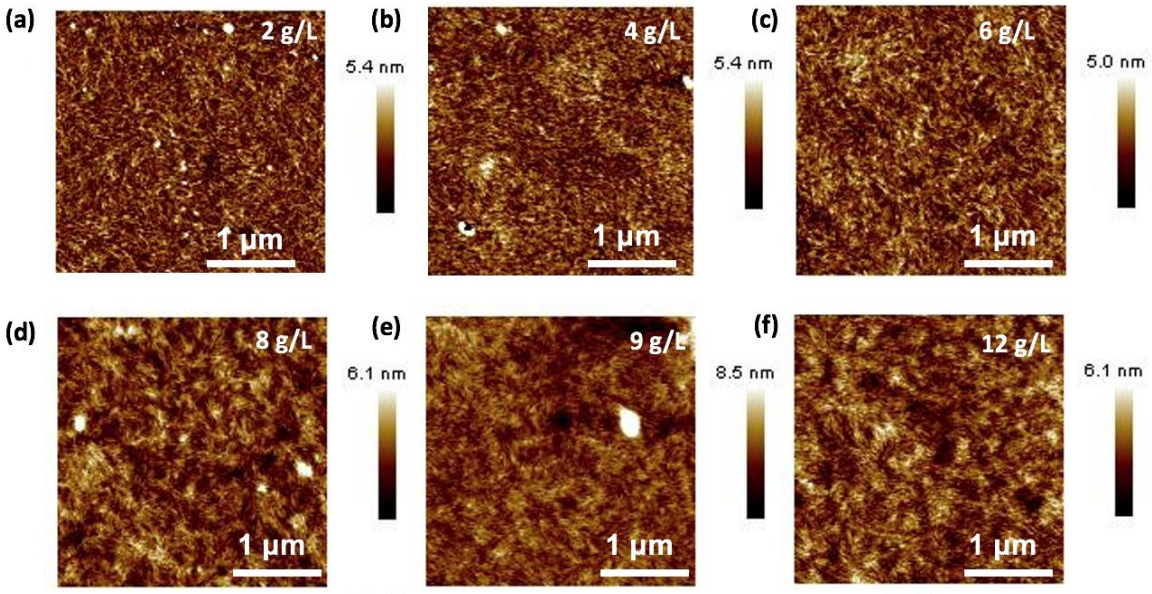

Figure B-12. Atomic Force Microscopy height images of DPP-DTT (M_w = 110 kg/mol) thin films prepared from a range of solution concentrations.

Table B-1. AFM Surface Roughness DPPDTT – 290 kg/mol.

Concentration (g/L)	Arithmetic Mean - Surface Roughness (R_a)	Root Mean Square-Surface Roughness (R_q)
2	0.601	0.762
4	0.523	0.66
6	0.621	0.833
7	0.689	0.894
8	0.736	0.931
10	0.749	0.939

Table B-2. AFM Surface Roughness DPPDTT – 209 kg/mol.

Concentration (g/L)	Arithmetic Mean - Surface Roughness (R_a)	Root Mean Square-Surface Roughness (R_q)
2	0.514	0.644
4	0.63	0.796
5	0.64	0.801
6	0.68	0.851
8	0.753	0.948
10	0.747	0.938

Table B-3. AFM Surface Roughness DPPDTT – 110 kg/mol.

Concentration (g/L)	Arithmetic Mean - Surface Roughness (R_a)	Root Mean Square-Surface Roughness (R_q)
2	0.565	0.713
4	0.581	0.732
6	0.567	0.714
8	0.652	0.819
9	0.663	0.828
10	0.637	0.799
12	0.674	0.847

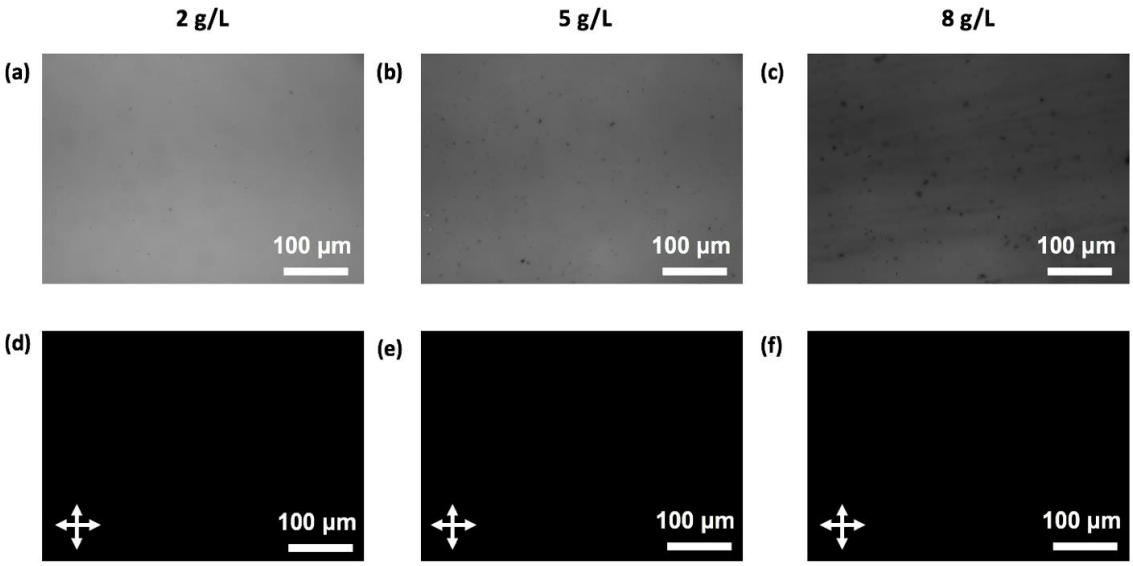

Figure B-13. The cross-polarized optical microscopy images of the DPP-DTT samples (M_w = 290 kg/mol) prepared from solutions of different concentrations and the directions of the arrows indicates the orientation of the polarizers. (a-c) The polarizers are oriented parallel to each other (0 degrees) (d-f) The polarizers are oriented perpendicular to each other (90 degrees).

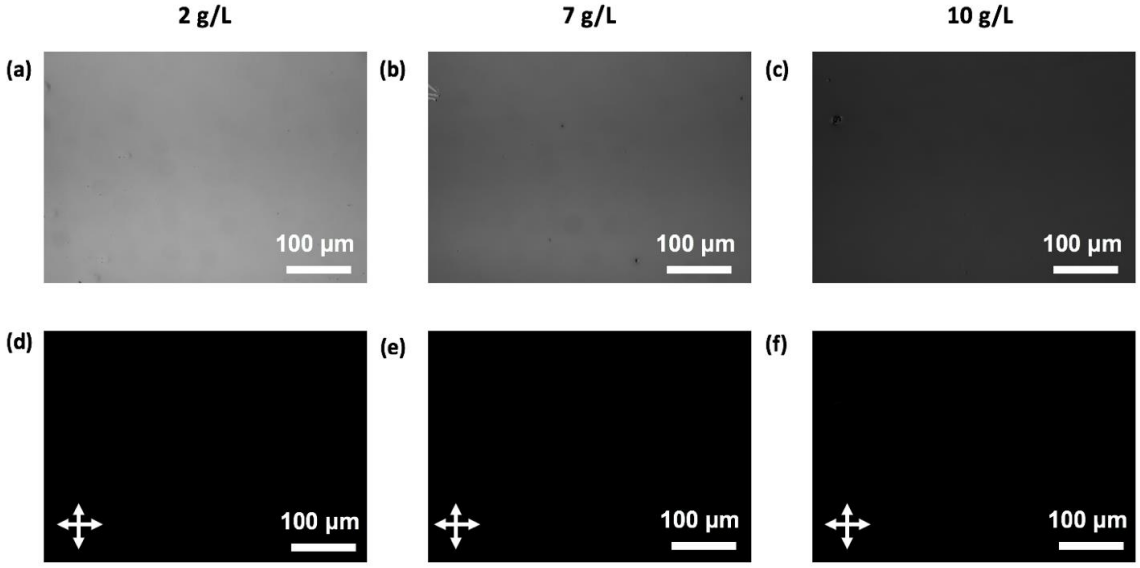

Figure B-14. The cross-polarized optical microscopy images of the DPP-DTT samples (M_w = 204kg/mol) prepared from solutions of different concentrations and the directions of the arrows indicates the orientation of the polarizers. (a-c) The polarizers are oriented parallel to each other (0 degrees) (d-f) The polarizers are oriented perpendicular to each other (90 degrees).

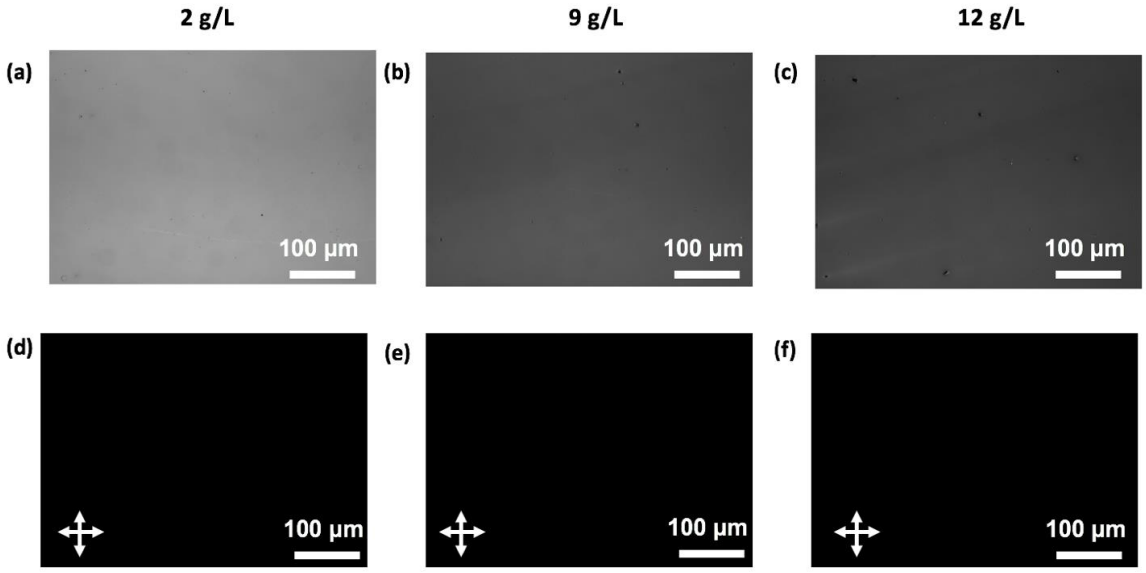

Figure B-15. The cross-polarized optical microscopy images of the DPP-DTT samples (M_w = 110 kg/mol) prepared from solutions of different concentrations and the directions of the arrows indicates the orientation of the polarizers. (a-c) The polarizers are oriented parallel to each other (0 degrees) (d-f) The polarizers are oriented perpendicular to each other (90 degrees).

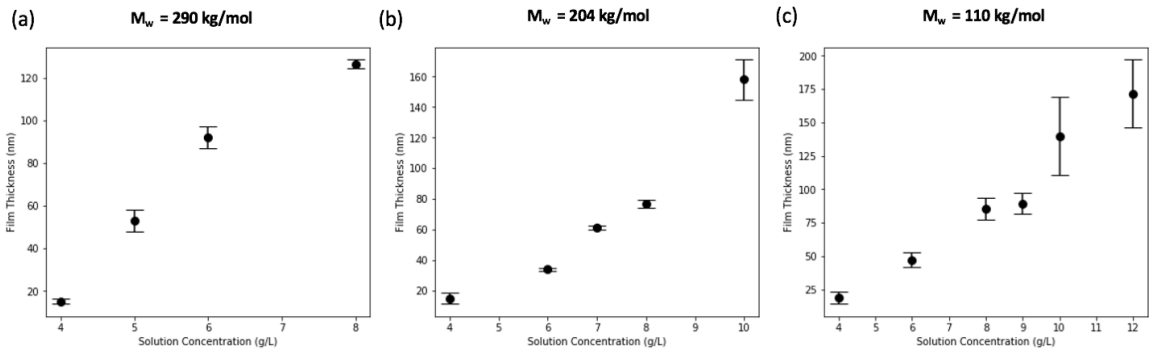

Figure B-16. Film thickness as a function of solution concentration for the three different molecular weights of DPP-DTT investigated (a) 290 kg/mol, (b) 204 kg/mol and (c) 110 kg/mol.

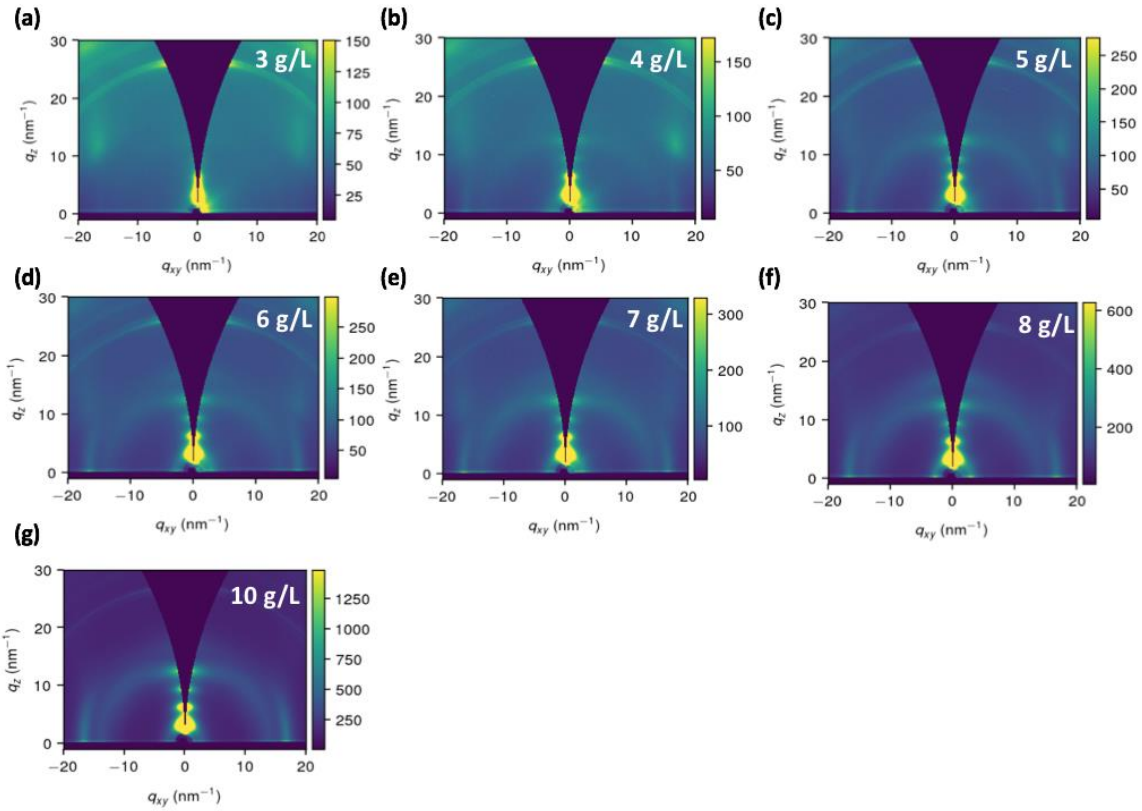

Figure B-17. 2-dimensional GIWAXS patterns for the DPP-DTT (Mw = 290 kg/mol) thin films prepared from a range of solution concentrations.

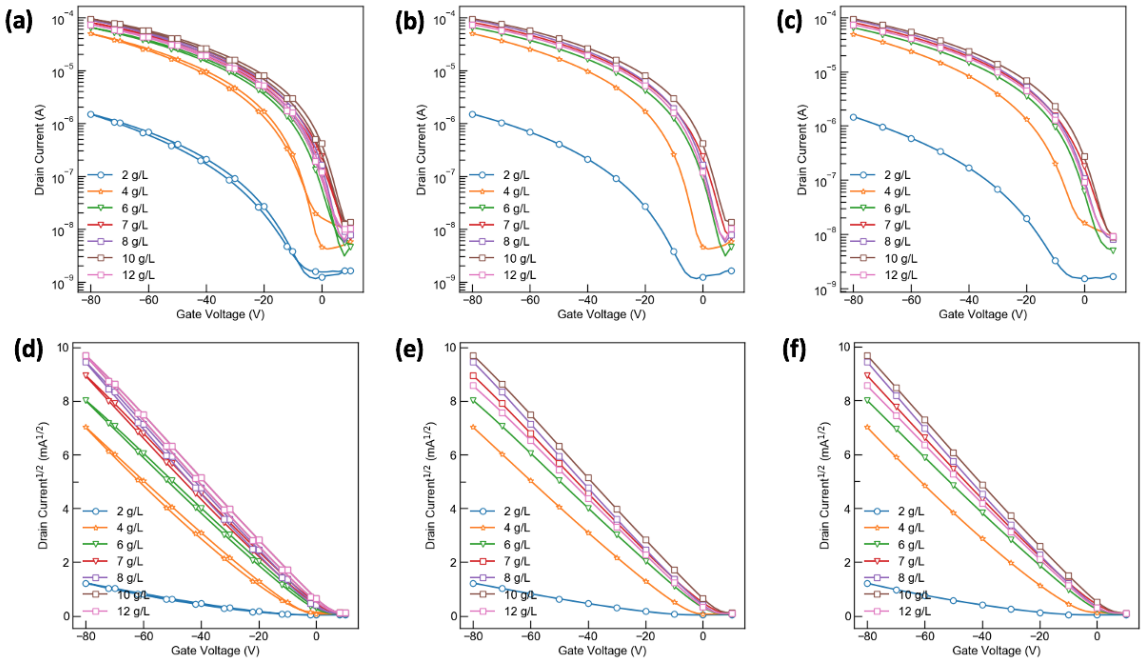

Figure B-18. Transfer characteristics for PDPP-4T at the range of concentrations studied averaged over 18 FET devices. (a) I_d – V_g curves for the forward and backward transfer regime (b) I_d – V_g curves for the forward transfer regime (c) I_d – V_g curves for the backward transfer regime (d) $(I_d)^{1/2}$ – V_g curves for the forward and backward transfer regime (e) $(I_d)^{1/2}$ – V_g curves for the forward transfer regime (f) $(I_d)^{1/2}$ – V_g curves for the backward transfer regime.

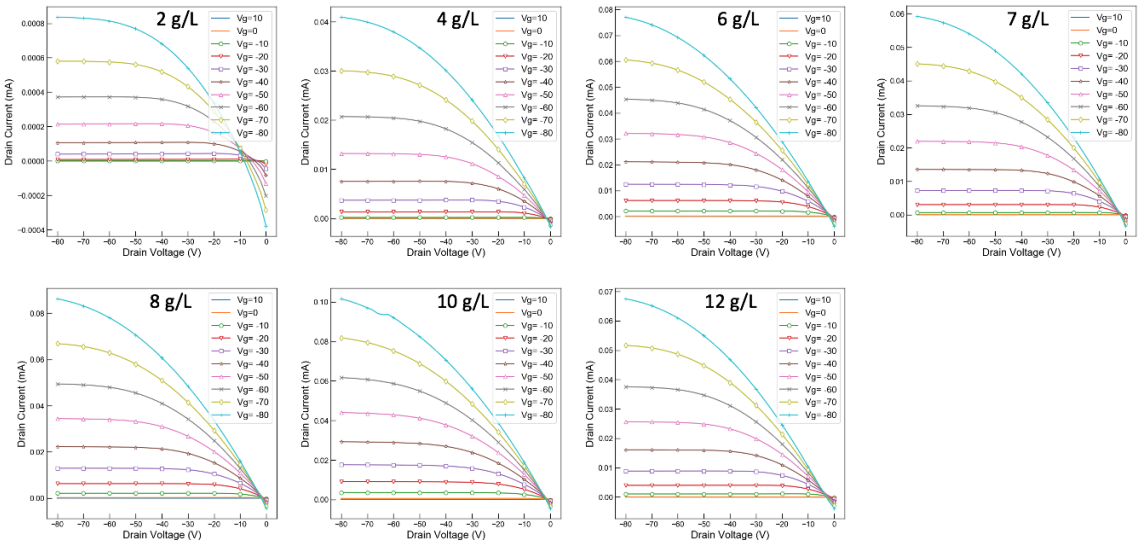

Figure B-19. Output Characteristics for PDPP-4T thin films as a function of solution concentration averaged over 18 FET devices.

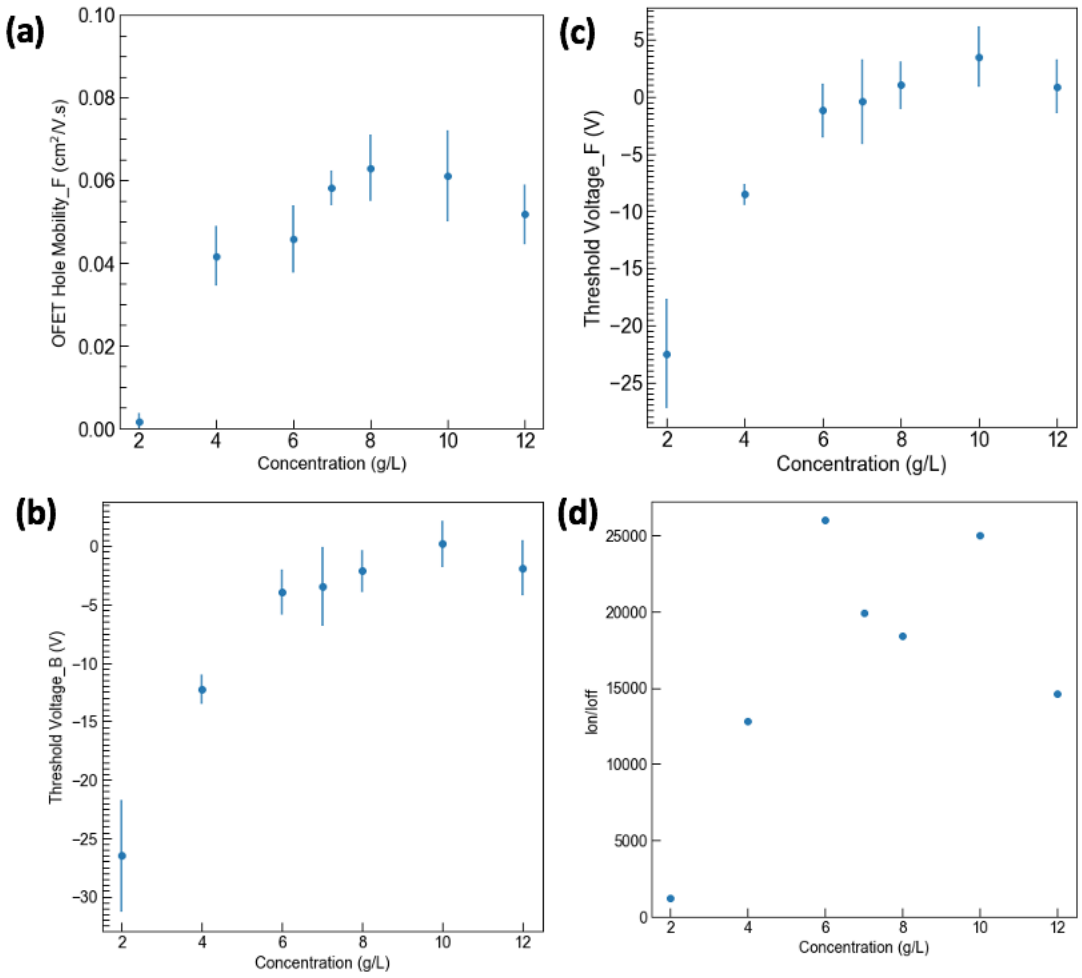

Figure B-20. (a) FET hole mobility of PDPP-4T extracted from the forward sweep transfer curve (V_{DS} = -80V) as a function of solution concentration. The OFET hole mobility was averaged over 18 devices and the error bars represent 95% confidence intervals. (b). Threshold voltage obtained from the backward sweep transfer curve $(I_d)^{1/2} – V_g$ as a function of solution concentration for PDPP-4T. (c) Threshold voltage obtained from the forward sweep transfer curve $(I_d)^{1/2} – V_g$ as a function of solution concentration for PDPP-4T. (d) Ion/Ioff obtained from the transfer curve $(I_d)^{1/2} – V_g$ as a function of solution concentration for PDPP-4T.

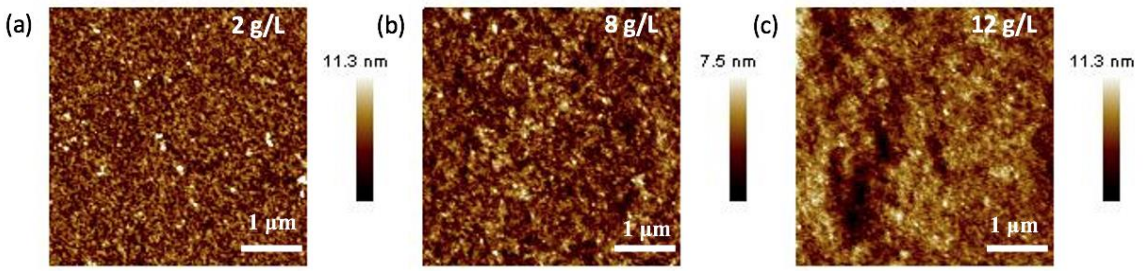

Figure B-21. Atomic Force Microscopy height images of PDPP-4T thin films prepared from solutions at (a) dilute concentration, (b) at the critical overlap concentration and (c) a semi-dilute concentration.

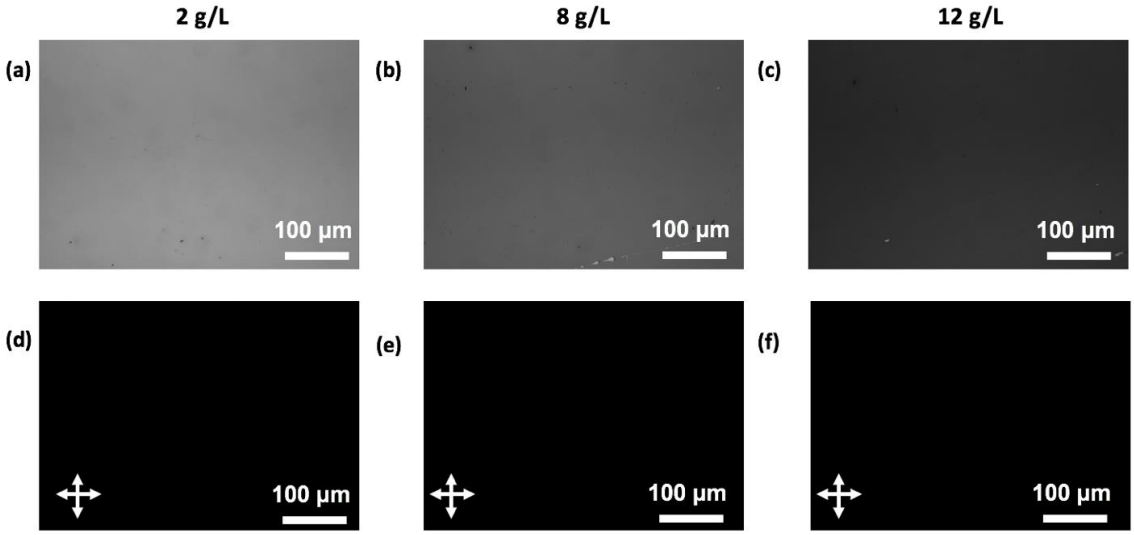

Figure B-22. The cross-polarized optical microscopy images of the PDPP-4T samples prepared from solutions of different concentrations and the directions of the arrows indicates the orientation of the polarizers. (a-c) The polarizers are oriented parallel to each other (0 degrees) (d-f) The polarizers are oriented perpendicular to each other (90 degrees).

Table B-4. AFM Surface Roughness PDPP-4T.

Concentration (g/L)	Arithmetic Mean - Surface Roughness (R_a)	Root Mean Square-Surface Roughness (R_q)
2	1.19	1.55
8	0.889	1.15
12	1.18	1.49

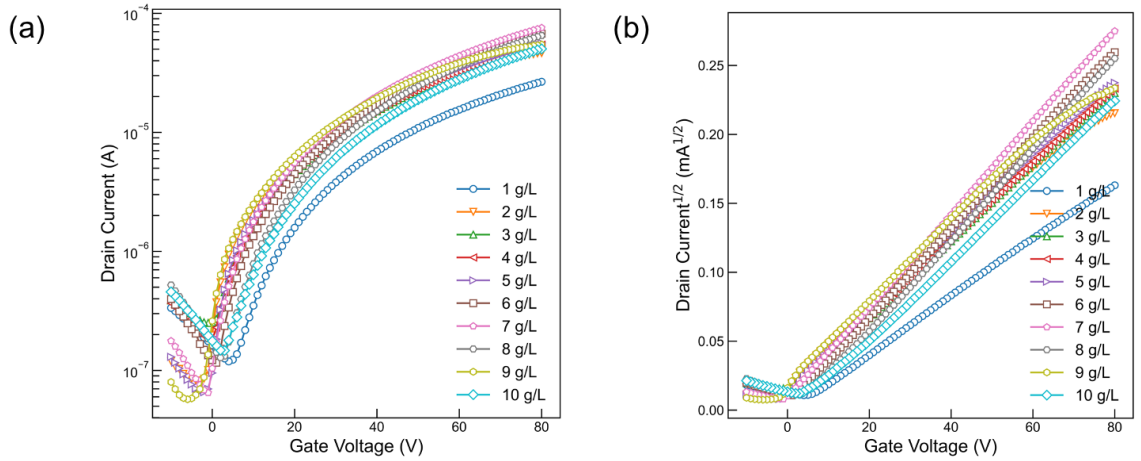

Figure B-23. Transfer characteristics for N2200 at the range of concentrations studied averaged over 18 FET devices. (a) $I_d - V_g$ curves for the backward transfer regime (b) $(I_d)^{1/2} - V_g$ curves for the backward transfer regime.

APPENDIX C. SUPPORTING INFORMATION FOR CHAPTER 4

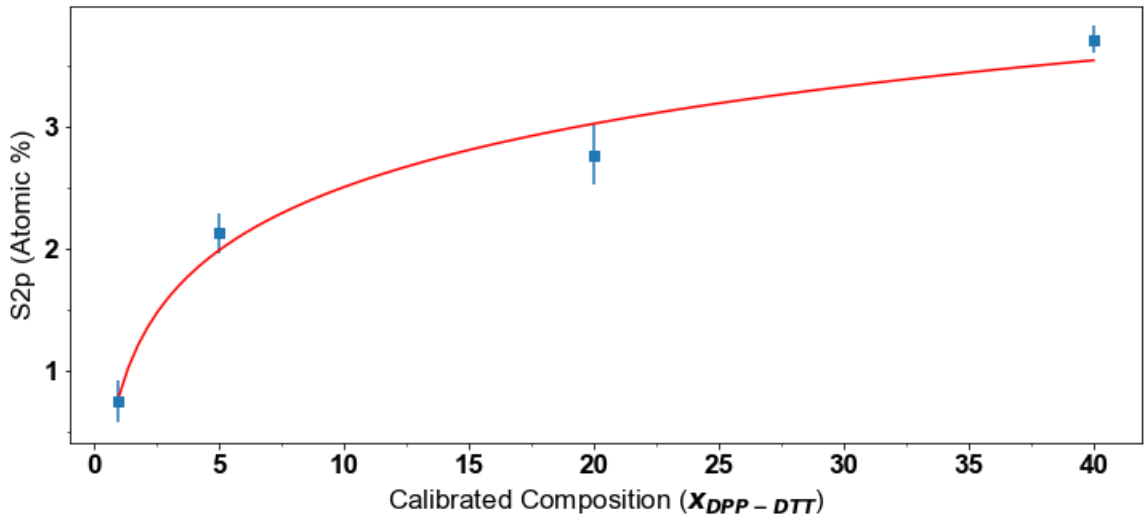

Figure C-1. Calibration curves based on XPS measurements of the S2p atomic % on known DPP-DTT/PS constant composition films fabricated using the high-throughput coater without flowing any PS solution. The atomic percentage on the Y-axis represents the proportion of the S2p signal intensity relative to the total signal intensity of the elements being analyzed, which in this case is only Sulfur (S2p) and Carbon (C1s).

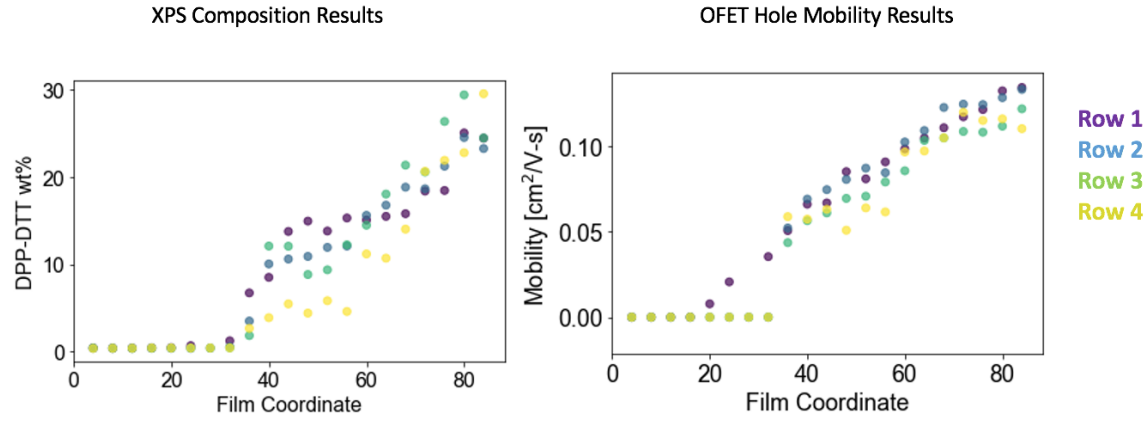

Figure C-2. (a) DPP-DTT composition measurements for each coordinate on the DPP-DTT/PS gradient films obtained via XPS measurements of the S2p peaks and converted to composition value using calibration curve from Figure S1 (b) OFET hole mobility measurements for each coordinate on the DPP-DTT/PS gradient films.

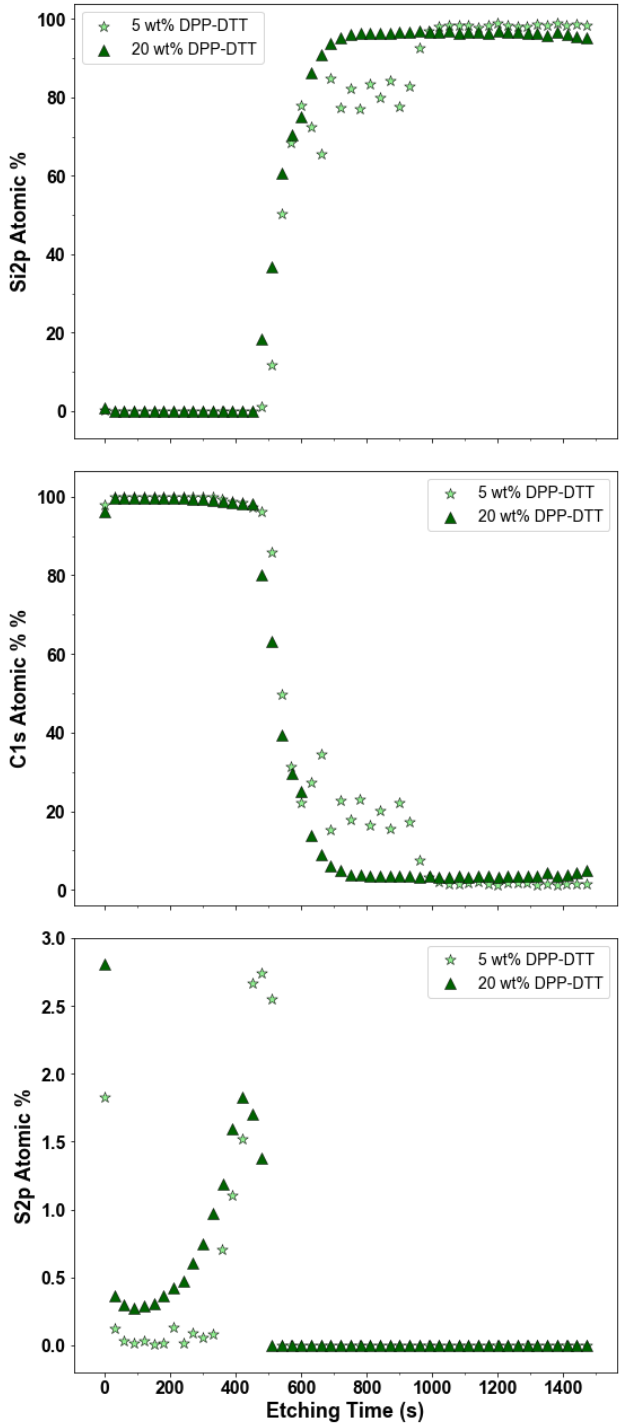

Figure C-3. Atomic % of silicon (top), (b) carbon (middle), and (c) sulfur (bottom) as determined by the Si2p, C1s, and S2p signals, respectively, plotted against etching time. Results were obtained from XPS depth profiling performed on two different points on the gradient film library having ratios of 5 wt% and 20 wt % DPP-DTT. The atomic percentage on the Y-axis represents the proportion of the Si2p/C1s/S2p signal intensity relative to the total signal intensity of all elements being analyzed,

which in this case is only Sulfur (S2p), Carbon (C1s), and Silicon (Si2p). The sum of the atomic percentages for the three elements at each etching time adds up to 100%. Etching was conducted at a Ta2O5 sputter rate of 0.2 nm/sec.

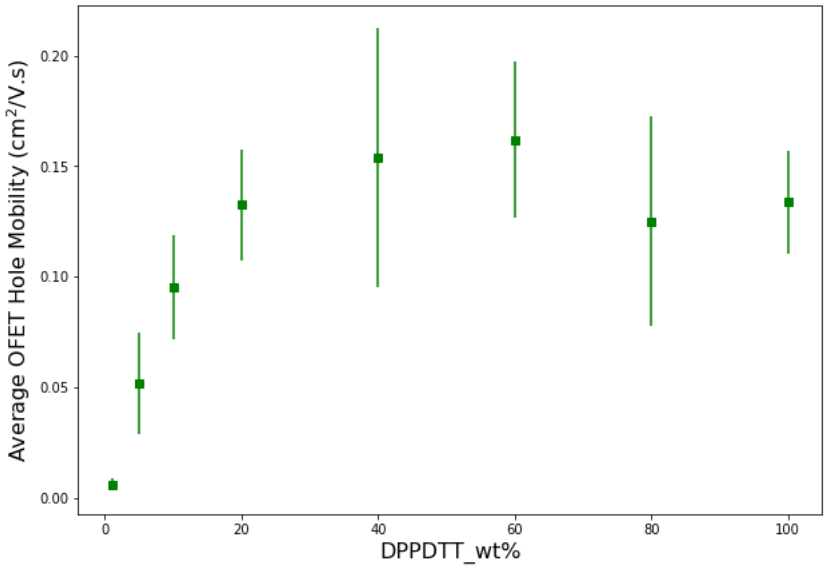

Figure C-4. Average FET hole mobilities of blade coated OCAT DPP-DTT/PS films as a as a function of the weight percentage of the conjugated polymer in the blend solution. The mobilities were extracted from the backward sweep transfer curve (V_{DS} = -80 V) and the error bars here represent 95% confidence intervals averaged over 18 OFET devices.

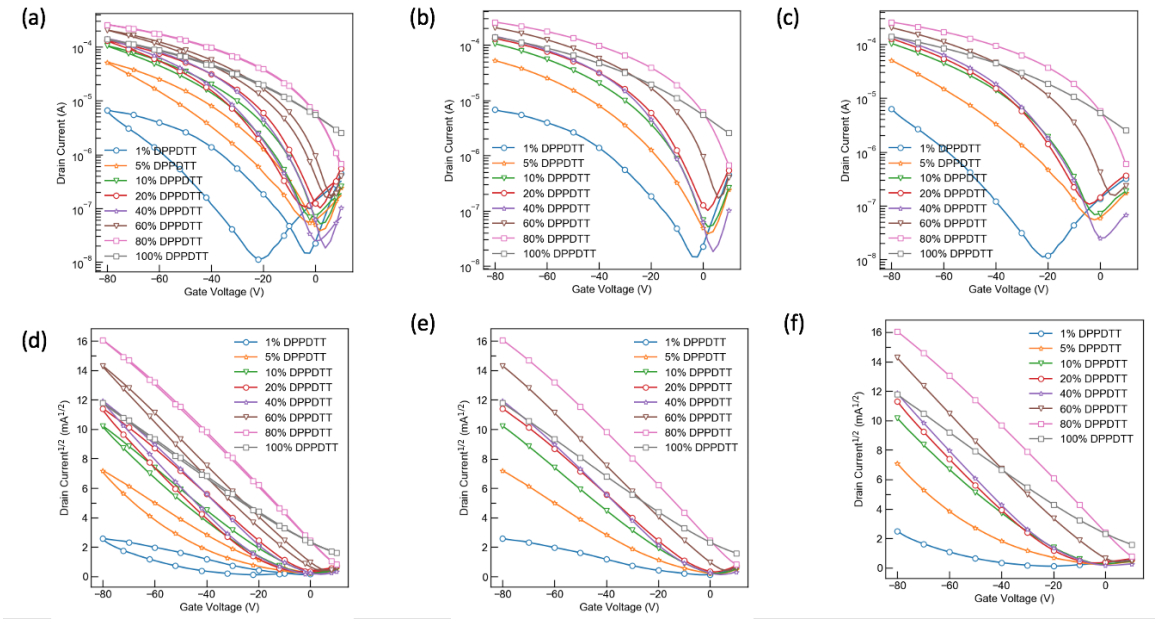

Figure C-5. Transfer characteristics for the DPP-DTT and DPP-DTT/PS OFETs at the range of compositions studied for OCAT experiments. (Top) $I_d - V_g$ curves for (a) forward and backward, (b) forward only, and (c) backward only transfer regime. (Bottom) $(I_d)^{1/2} - V_g$ curves for (d) forward and backward, (e) forward only, and (f) backward only transfer regime.

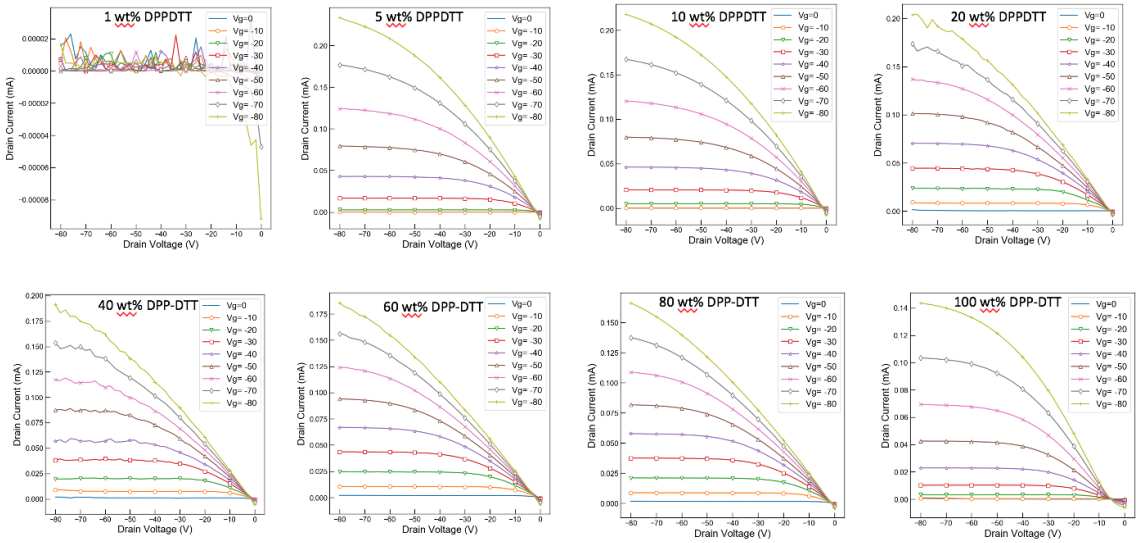

Figure C-6. Output Characteristics for neat DPP-DTT and DPP-DTT/PS blade coated OFETs at the range of blend compositions investigated for the OCAT experiments.

Table C-1. Threshold voltage obtained from forward and backward transfer curves and I_{on}/I_{off} ratio for neat DPP-DTT and DPP-DTT/PS OFETs at the range of compositions investigated for the OCAT experiments.

DPP-DTT wt%	V_t forward	V_t backward	I_{on}/I_{off}
1	-15 ± 10	-31 ± 3	3×10^2
5	-18 ± 3	-30 ± 4	3×10^4
10	-10 ± 2	-15 ± 1	7.6×10^2
20	-4 ± 1	-17 ± 2	1.65×10^3
40	-9 ± 2	-20 ± 3	2×10^4
60	2 ± 1	-4 ± 2	1.6×10^3
80	20 ± 2	18 ± 2	5.6×10^2
100	7 ± 2	5 ± 3	2×10^2

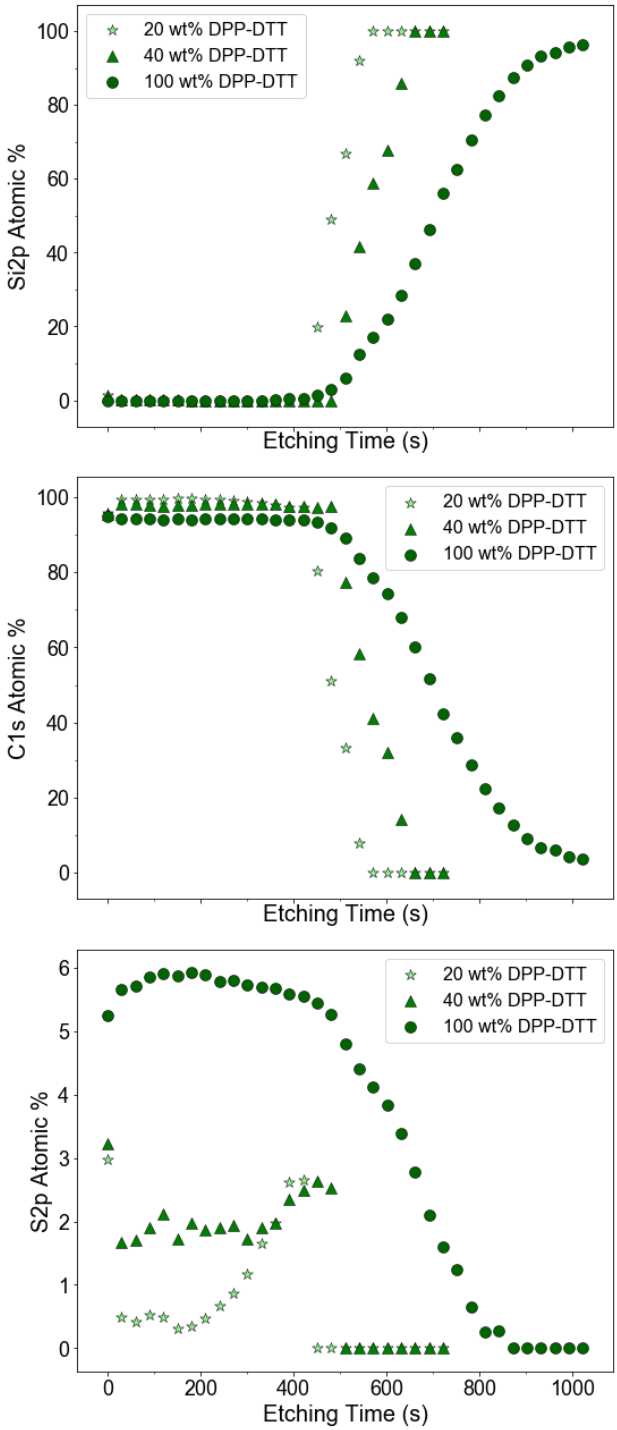

Figure C-7. Atomic % of silicon (top), (b) carbon (middle), and (c) sulfur (bottom) as determined by the Si2p, C1s, and S2p signals, respectively plotted against etching time. Results were obtained from XPS depth profiling performed on OCAT films having 20, 40 and 100 wt% DPP-DTT ratios. The atomic percentage on the Y-axis represents the proportion of the Si2p/C1s/S2p signal intensity relative to the total signal intensity of all elements being analyzed, which in this case is only Sulfur (S2p),

Carbon (C1s), and Silicon (Si2p). The sum of the atomic percentages for the three elements at each etching time adds up to 100%. Etching was conducted at a Ta2O5 sputter rate of 0.2 nm/sec.

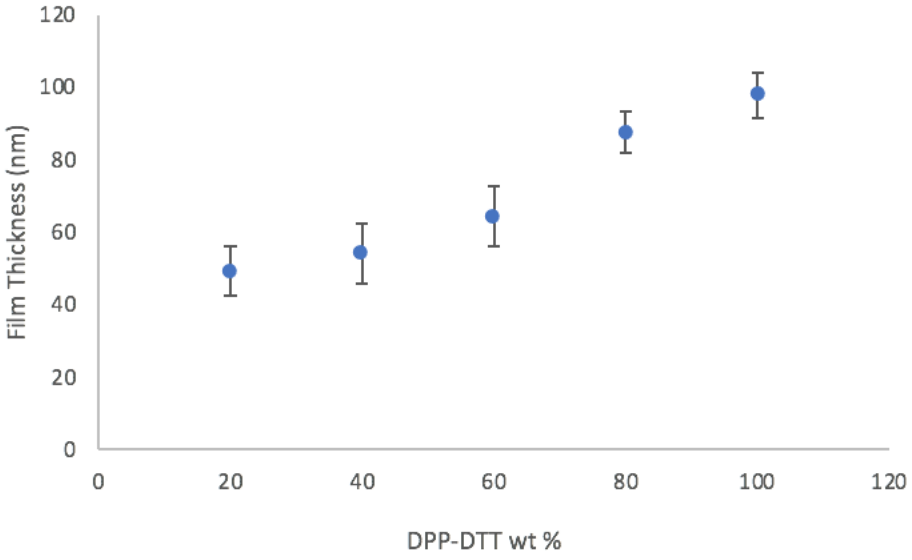

Figure C-8. Film thickness of the blade coated OCAT DPP-DTT/PS films obtained from profilometry plotted as a function of the wt% of DPP-DTT in the film.

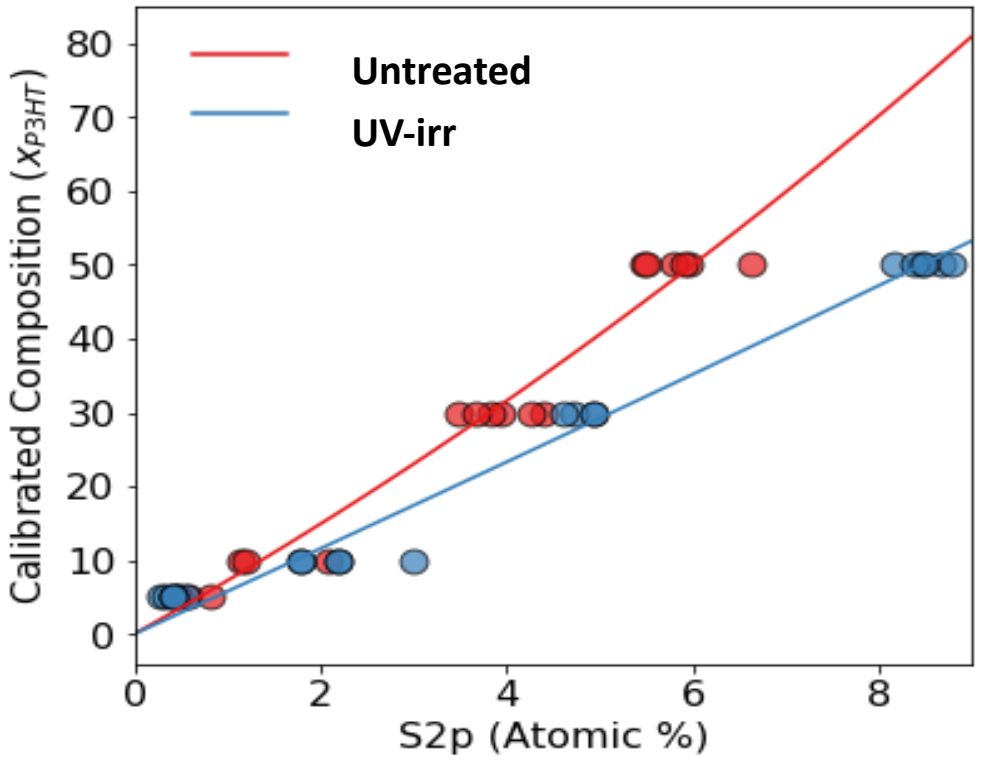

Figure C-9. Calibration curves based on XPS measurements of the S2p peaks on known P3HT/PS (untreated and UV-irradiated) composition films fabricated via flow coating.

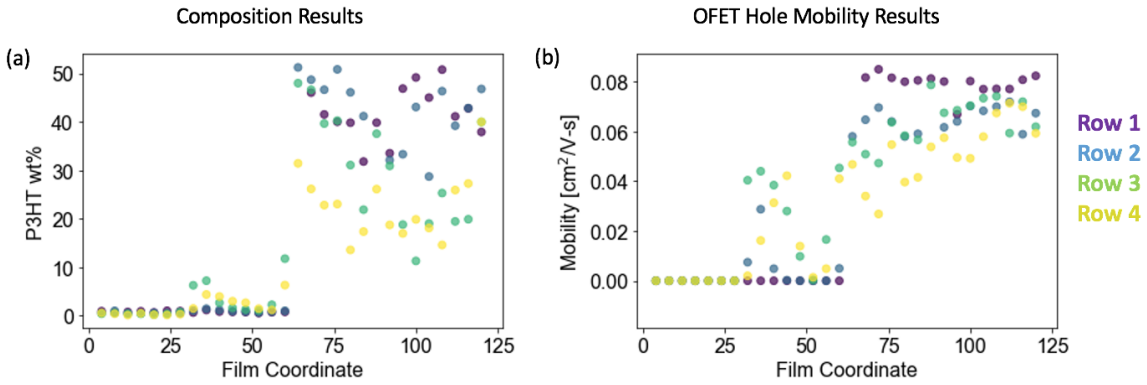

Figure C-10. (a) P3HT composition measurements for each coordinate on the untreated P3HT/PS gradient films obtained via XPS measurements of the S2p peaks and converted to composition value using calibration curve from Figure C-9 (b) OFET hole mobility measurements for each coordinate on the untreated P3HT/PS gradient films.

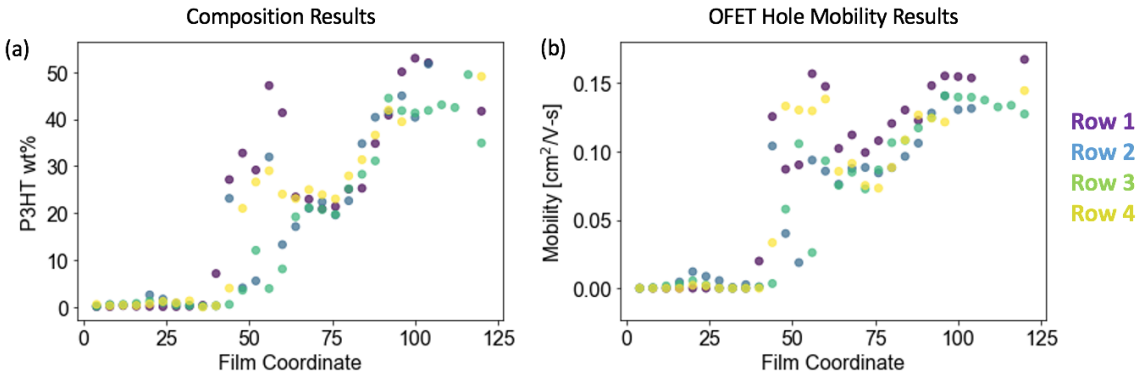

Figure C-11. (a) P3HT composition measurements for each coordinate on the UV-irradiated P3HT/PS gradient films obtained via XPS measurements of the S2p peaks and converted to composition value using calibration curve from Figure C-9 (b) OFET hole mobility measurements for each coordinate on the UV-irradiated P3HT/PS gradient films.

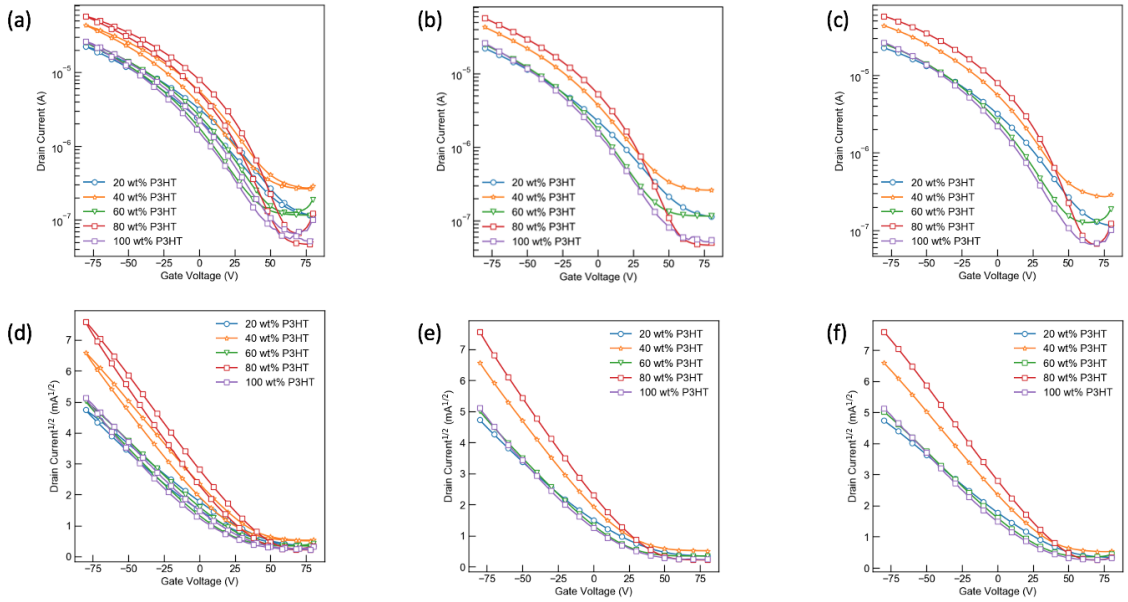

Figure C-12. Transfer characteristics for the blade coated neat P3HT and P3HT/PS OFETs at the range of compositions studied. (Top) $I_d - V_g$ curves for (a) forward and backward, (b) forward only, and (c) backward only transfer regime. (Bottom) $(I_d)^{1/2} - V_g$ curves for (d) forward and backward, (e) forward only, and (f) backward only transfer regime.

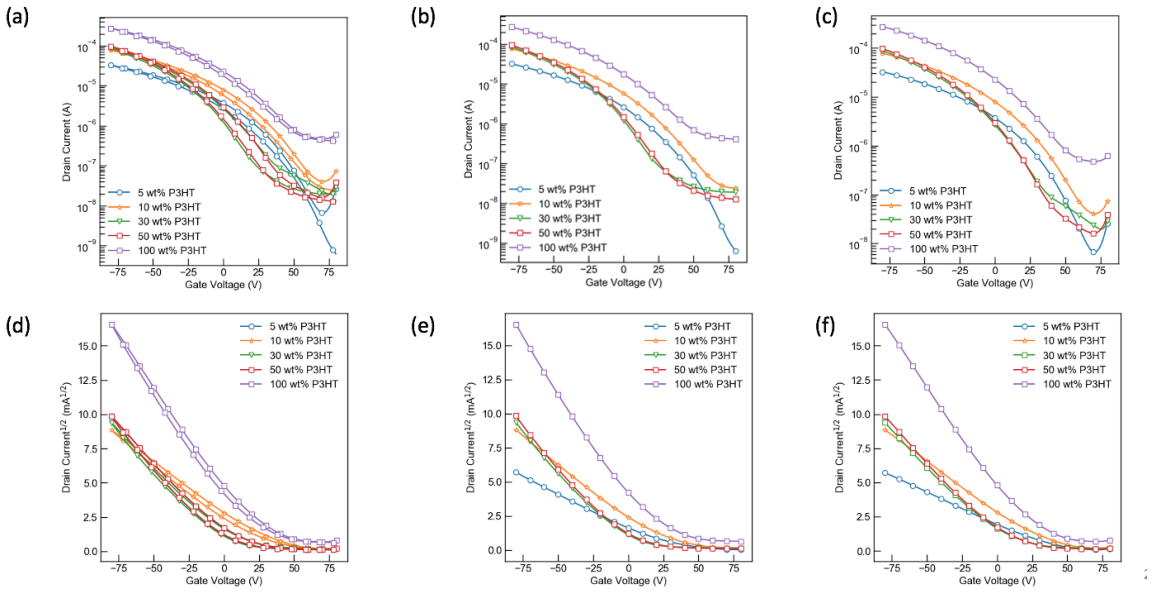

Figure C-13. Transfer characteristics for the blade coated UV-irradiated P3HT and P3HT/PS OFETs at the range of compositions studied. (Top) $I_d - V_g$ curves for (a) forward and backward, (b) forward only, and (c) backward only transfer regime. (Bottom) $(I_d)^{1/2} - V_g$ curves for (d) forward and backward, (e) forward only, and (f) backward only transfer regime.

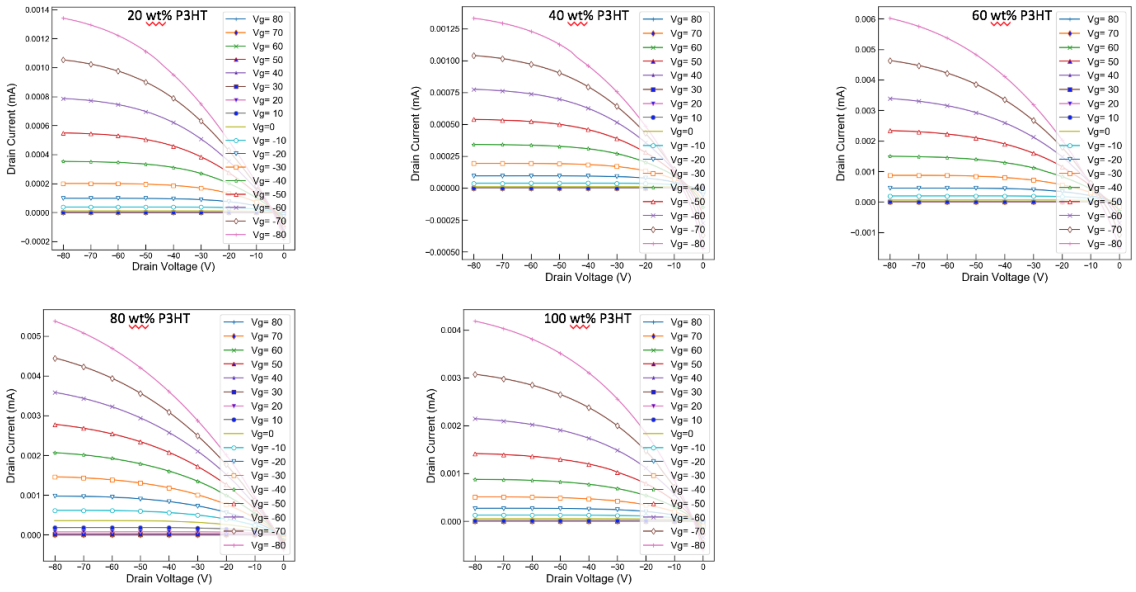

Figure C-14. Output Characteristics for neat P3HT and P3HT/PS blade coated OFETs at the range of blend compositions investigated.

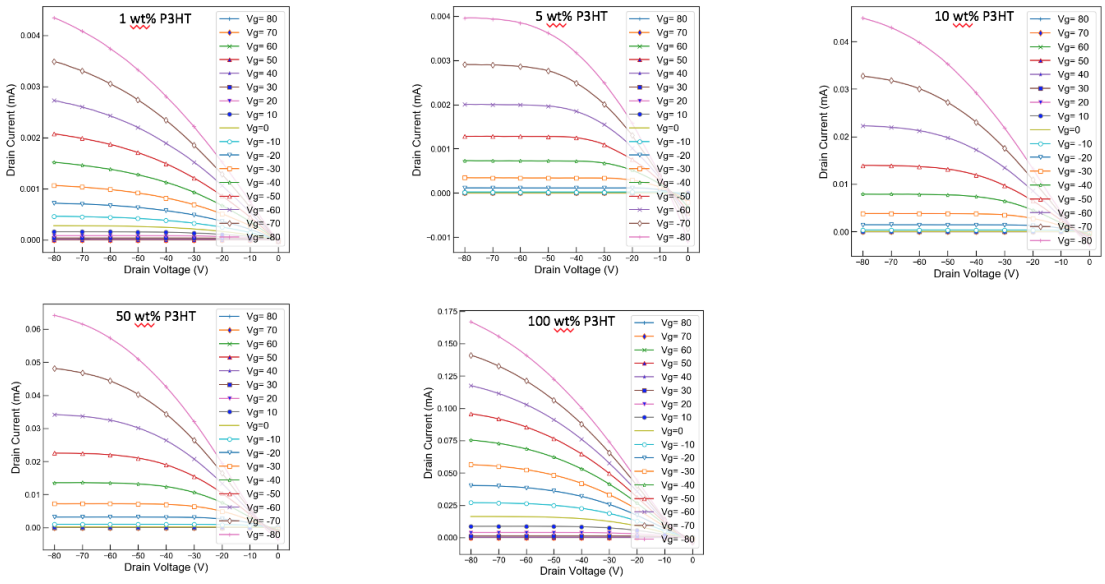

Figure C-15. Output Characteristics for UV-irradiated neat P3HT and P3HT/PS blade coated OFETs at the range of blend compositions investigated.

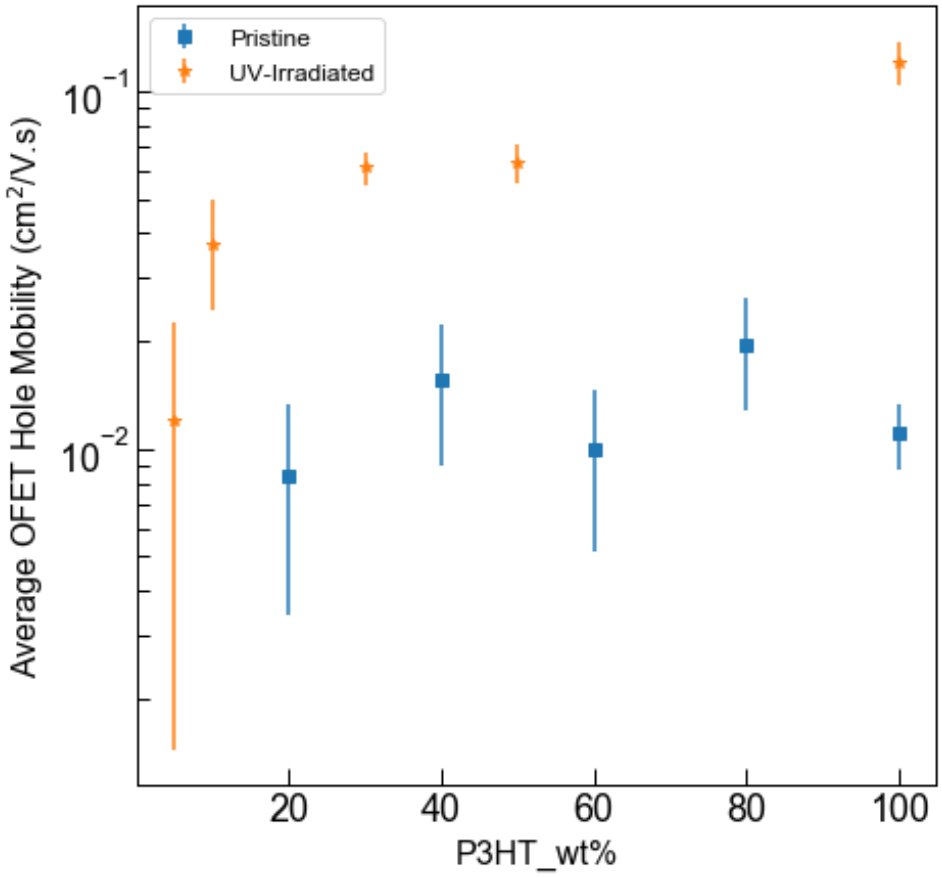

Figure C-16. Comparison of average FET hole mobilities of blade coated P3HT/PS blend films and P3HT/PS blend films from 8-min UV-irradiated blend solutions as a function of the weight percentage of P3HT in the blend solution plotted in log scale. The mobilities were extracted from the backward sweep transfer curve (V_{DS} = -80 V) and the error bars here represent 95% confidence intervals averaged over 18 OFET devices.

Table C-2. Threshold voltage obtained from forward and backward transfer curves and I_{on}/I_{off} ratio for blade coated untreated neat P3HT and P3HT/PS OFETs at the range of compositions investigated for OCAT experiments.

P3HT wt%	V_t forward	V_t backward	I_{on}/I_{off}
20	29 ± 17	9 ± 11	2×10^3
40	35 ± 12	21 ± 7	3×10^3
60	32 ± 4	20 ± 3	6×10^2
80	40 ± 12	26 ± 5	3×10^3
100	22 ± 14	15 ± 5	2×10^3

Table C-3. Threshold voltage obtained from forward and backward transfer curves and I_{on}/I_{off} ratio for blade coated UV-irradiated neat P3HT and P3HT/PS OFETs at the range of compositions investigated for OCAT experiments.

P3HT wt%	V_t forward	V_t backward	I_{on}/I_{off}
5	38 ± 7	24 ± 5	10^5
10	25 ± 8	15 ± 7	1.8×10^4
30	3 ± 7	-2 ± 4	3×10^4
50	4 ± 8	-2 ± 5	3.4×10^4
100	25 ± 7	17 ± 7	2.8×10^4

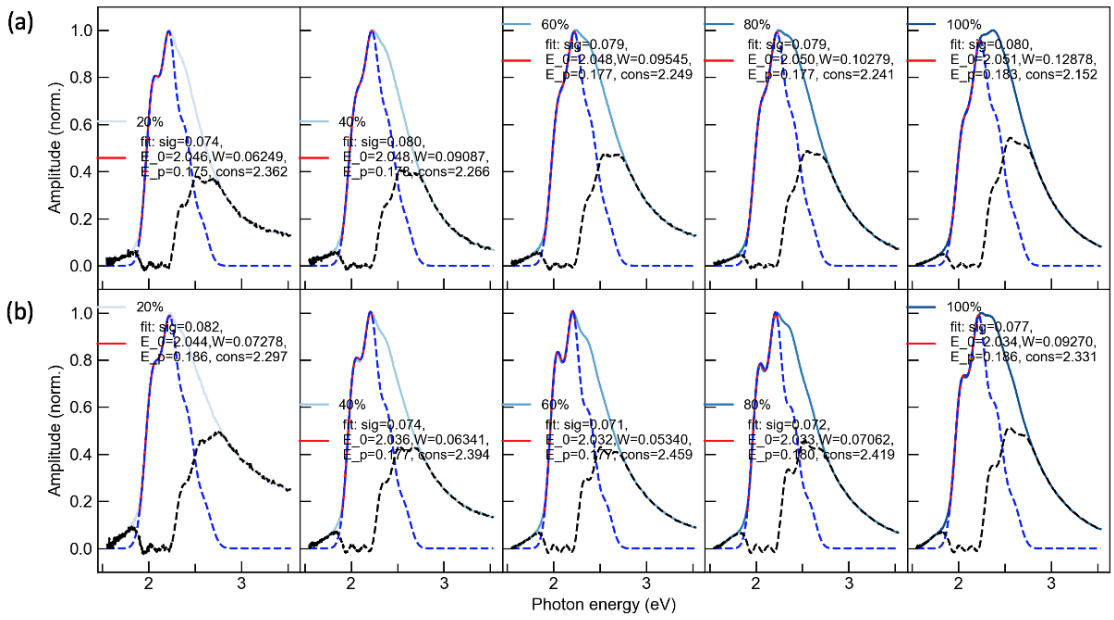

Figure C-17. Modified FC fit for all absorption spectra of the blended thin films prepared from different weight percentages of (a) untreated P3HT and (b) UV-irradiated P3HT. Dark blue dashed lines are the simulated FC curve. Light blue solid line is the experimentally obtained absorption spectra of the thin film. Black dashed lines are the absorption spectra of amorphous regions. Red curve is the part of the experimental spectra chosen for fitting. Sig represents the widths of the Gaussian inhomogeneous distribution used to describe the energetic disorder. E_0 represents the energy of the 0-0 vibronic transition. W is the exciton bandwidth. Ep represents the energy of the vibrational mode coupled to the electronic transition. Cons represents the fit constant. Except for the fit constant, all other parameters are displayed in units of eV.

REFERENCES

1. Gao, D.; Zhou, Z., Silicon-based optoelectronics: progress towards large scale optoelectronic integration and applications. *Frontiers of Optoelectronics* **2022,** *15* (1), 27.

2. Raman, S.; A, R. S.; M, S., Advances in silicon nanowire applications in energy generation, storage, sensing, and electronics: a review. *Nanotechnology* **2023,** *34* (18), 182001.

3. Venema, L., Silicon electronics and beyond. *Nature* **2011,** *479* (7373), 309-309.

4. Baran, D.; Corzo, D.; Blazquez, G., Flexible Electronics: Status, Challenges and Opportunities. *Frontiers in Electronics* **2020,** *1*.

5. Kenry; Yeo, J. C.; Lim, C. T., Emerging flexible and wearable physical sensing platforms for healthcare and biomedical applications. *Microsystems & Nanoengineering* **2016,** *2* (1), 16043.

6. Luo, Y.; Abidian, M. R.; Ahn, J.-H.; Akinwande, D.; Andrews, A. M.; Antonietti, M.; Bao, Z.; Berggren, M.; Berkey, C. A.; Bettinger, C. J.; Chen, J.; Chen, P.; Cheng, W.; Cheng, X.; Choi, S.-J.; Chortos, A.; Dagdeviren, C.; Dauskardt, R. H.; Di, C.-a.; Dickey, M. D.; Duan, X.; Facchetti, A.; Fan, Z.; Fang, Y.; Feng, J.; Feng, X.; Gao, H.; Gao, W.; Gong, X.; Guo, C. F.; Guo, X.; Hartel, M. C.; He, Z.; Ho, J. S.; Hu, Y.; Huang, Q.; Huang, Y.; Huo, F.; Hussain, M. M.; Javey, A.; Jeong, U.; Jiang, C.; Jiang, X.; Kang, J.; Karnaushenko, D.; Khademhosseini, A.; Kim, D.-H.; Kim, I.-D.; Kireev, D.; Kong, L.; Lee, C.; Lee, N.-E.; Lee, P. S.; Lee, T.-W.; Li, F.; Li, J.; Liang, C.; Lim, C. T.; Lin, Y.; Lipomi, D. J.; Liu, J.; Liu, K.; Liu, N.; Liu, R.; Liu, Y.; Liu, Y.; Liu, Z.; Liu, Z.; Loh, X. J.; Lu, N.; Lv, Z.; Magdassi, S.; Malliaras, G. G.; Matsuhisa, N.; Nathan, A.; Niu, S.; Pan, J.; Pang, C.; Pei, Q.; Peng, H.; Qi, D.; Ren, H.; Rogers, J. A.; Rowe, A.; Schmidt, O. G.; Sekitani, T.; Seo, D.-G.; Shen, G.; Sheng, X.; Shi, Q.; Someya, T.; Song, Y.; Stavrinidou, E.; Su, M.; Sun, X.; Takei, K.; Tao, X.-M.; Tee, B. C. K.; Thean, A. V.-Y.; Trung, T. Q.; Wan, C.; Wang, H.; Wang, J.; Wang, M.; Wang, S.; Wang, T.; Wang, Z. L.; Weiss, P. S.; Wen, H.; Xu, S.; Xu, T.; Yan, H.; Yan, X.; Yang, H.; Yang, L.; Yang, S.; Yin, L.; Yu, C.; Yu, G.; Yu, J.; Yu, S.-H.; Yu, X.; Zamburg, E.; Zhang, H.; Zhang, X.; Zhang, X.; Zhang, X.; Zhang, Y.; Zhang, Y.; Zhao, S.; Zhao, X.; Zheng, Y.; Zheng, Y.-Q.; Zheng, Z.; Zhou, T.; Zhu, B.; Zhu, M.; Zhu, R.; Zhu, Y.; Zhu, Y.; Zou, G.; Chen, X., Technology Roadmap for Flexible Sensors. *ACS Nano* **2023,** *17* (6), 5211-5295.

7. Tilli, M.; Haapalinna, A., Chapter 1 - Properties of silicon. In *Handbook of Silicon Based MEMS Materials and Technologies (Third Edition)*, Elsevier: 2020; pp 3-17.

8. Xu, X.; Zhao, Y.; Liu, Y., Wearable Electronics Based on Stretchable Organic Semiconductors. *Small* **2023,** *19* (20), 2206309.

9. Kelley, T. W.; Baude, P. F.; Gerlach, C.; Ender, D. E.; Muyres, D.; Haase, M. A.; Vogel, D. E.; Theiss, S. D., Recent Progress in Organic Electronics: Materials, Devices, and Processes. *Chemistry of Materials* **2004,** *16* (23), 4413-4422.

10. Ponomarenko, S.; Kirchmeyer, S., Recent advances in organic electronics materials and devices. *Polymer Science Series C* **2014,** *56* (1), 1-3.

11. Alan Heeger, A. M., and Hideki Shirakaw, The Nobel Prize in Chemistry 2000. **2016**.

12. Agbolaghi, S.; Zenoozi, S., A comprehensive review on poly(3-alkylthiophene)-based crystalline structures, protocols and electronic applications. *Elsevier Ltd* **2017,** *51*, 362-403.

13. Nielsen, C. B.; Turbiez, M.; McCulloch, I., Recent Advances in the Development of Semiconducting DPP-Containing Polymers for Transistor Applications. *Advanced Materials* **2013,** *25* (13), 1859-1880.

14. Quinn, J. T. E.; Zhu, J.; Li, X.; Wang, J.; Li, Y., Recent progress in the development of n-type organic semiconductors for organic field effect transistors. *Journal of Materials Chemistry C* **2017,** *5* (34), 8654-8681.

15. Facchetti, A., π-Conjugated Polymers for Organic Electronics and Photovoltaic Cell Applications. *Chemistry of Materials* **2011,** *23* (3), 733-758.

16. Gopalakrishnan, V.; Balaji, D.; Dangate, M. S., Review—Conjugated Polymer Photovoltaic Materials: Performance and Applications of Organic Semiconductors in Photovoltaics. *ECS Journal of Solid State Science and Technology* **2022,** *11* (3), 035001.

17. Günes, S.; Neugebauer, H.; Sariciftci, N. S., Conjugated Polymer-Based Organic Solar Cells. *Chemical Reviews* **2007,** *107* (4), 1324-1338.

18. Braga, D.; Horowitz, G., High-Performance Organic Field-Effect Transistors. *Advanced Materials* **2009,** *21*, 1473-1486.

19. Holliday, S.; Donaghey, J. E.; McCulloch, I., Advances in Charge Carrier Mobilities of Semiconducting Polymers Used in Organic Transistors. *Chemistry of Materials* **2014,** *26* (1), 647-663.

20. Sirringhaus, H., 25th Anniversary Article: Organic Field-Effect Transistors: The Path Beyond Amorphous Silicon. *Advanced Materials* **2014,** *26* (9), 1319-1335.

21. Alsalhi, M. S.; Alam, J.; Dass, L. A.; Raja, M., Recent advances in conjugated polymers for light emitting devices. *Int J Mol Sci* **2011,** *12* (3), 2036-54.

22. Burroughes, J. H.; Bradley, D. D. C.; Brown, A. R.; Marks, R. N.; Mackay, K.; Friend, R. H.; Burns, P. L.; Holmes, A. B., Light-emitting diodes based on conjugated polymers. *Nature* **1990,** *347* (6293), 539-541.

23. Sekine, C.; Tsubata, Y.; Yamada, T.; Kitano, M.; Doi, S., Recent Progress of High Performance Polymer OLED and OPV Materials for Organic Printed Electronics. *Science and Technology of Advanced Materials* **2014,** *15* (3), 34203-34218.

24. Nguyen, T. N.; Phung, V. D.; Tran, V. V., Recent Advances in Conjugated Polymer-Based Biosensors for Virus Detection. *Biosensors (Basel)* **2023,** *13* (6).

25. Zhu, C.; Liu, L.; Yang, Q.; Lv, F.; Wang, S., Water-Soluble Conjugated Polymers for Imaging, Diagnosis, and Therapy. *Chemical Reviews* **2012,** *112* (8), 4687-4735.

26. Massiot, I.; Cattoni, A.; Collin, S., Progress and prospects for ultrathin solar cells. *Nature Energy* **2020,** *5* (12), 959-972.

27. Wang, Y. J.; Yu, G., Conjugated polymers: From synthesis, transport properties, to device applications. *Journal of Polymer Science Part B: Polymer Physics* **2019,** *57* (23), 1557-1558.

28. Zhou, J.; Li, D.; Wang, L.; Zhang, X.; Deng, N.; Guo, C.; Chen, C.; Gan, Z.; Liu, C.; Sun, W.; Liu, D.; Li, W.; Li, Z.; Wang, K.; Wang, T., Bicontinuous donor and acceptor fibril networks enable 19.2% efficiency pseudo-bulk heterojunction organic solar cells. *Interdisciplinary Materials* **2023,** *2* (6), 866-875.

29. Callaway, C. P.; Liu, A. L.; Venkatesh, R.; Zheng, Y.; Lee, M.; Meredith, J. C.; Grover, M.; Risko, C.; Reichmanis, E., The Solution is the Solution: Data-Driven Elucidation of Solution-to-Device Feature Transfer for π-Conjugated Polymer Semiconductors. *ACS Applied Materials & Interfaces* **2022,** *14* (3), 3613-3620.

30. Gu, X.; Shaw, L.; Gu, K.; Toney, M. F.; Bao, Z., The meniscus-guided deposition of semiconducting polymers. *Nature Communications* **2018,** *9* (1), 534.

31. Haase, K.; Hambsch, M.; Teixeira da Rocha, C.; Zessin, J.; Mannsfeld, S. C. B., 17 - Advances in solution processing of organic materials for devices. In *Handbook of Organic Materials for Electronic and Photonic Devices (Second Edition)*, Ostroverkhova, O., Ed. Woodhead Publishing: 2019; pp 551-577.

32. Liao, X.; Zhang, L.; Chen, L.; Hu, X.; Ai, Q.; Ma, W.; Chen, Y., Room temperature processed polymers for high-efficient polymer solar cells with power conversion efficiency over 9%. *Nano Energy* **2017,** *37*, 32-39.

33. Yi, H. T.; Payne, M. M.; Anthony, J. E.; Podzorov, V., Ultra-flexible solution-processed organic field-effect transistors. *Nature Communications* **2012,** *3* (1), 1259.

34. Chang, M.; Choi, D.; Wang, G.; Kleinhenz, N.; Persson, N.; Park, B.; Reichmanis, E., Photoinduced Anisotropic Assembly of Conjugated Polymers in Insulating Polymer Blends. *ACS Appl Mater Interfaces* **2015,** *7* (25), 14095-14103.

35. Kang, B.; Ge, F.; Qiu, L.; Cho, K., Effective Use of Electrically Insulating Units in Organic Semiconductor Thin Films for High-Performance Organic Transistors. *Advanced Electronic Materials* **2017,** *3* (2), 1600240.

36. Lei, Y.; Deng, P.; Li, J.; Lin, M.; Zhu, F.; Ng, T.-W.; Lee, C.-S.; Ong, B. S., Solution-Processed Donor-Acceptor Polymer Nanowire Network Semiconductors For High-Performance Field-Effect Transistors. *Scientific Reports* **2016,** *6* (1), 24476.

37. Pan, Y.; Yu, G., Multicomponent Blend Systems Used in Organic Field-Effect Transistors: Charge Transport Properties, Large-Area Preparation, and Functional Devices. *Chemistry of Materials* **2021,** *33* (7), 2229-2257.

38. Shayla Nikzad, H.-C. W., Jenny Kim, Christine M. Mahoney, James R. Matthews, Weijun Niu, Yang Li, Hongxiang Wang, Wen-Chang Chen, Michael F. Toney, Mingqian He,* and Zhenan Bao*, Inducing Molecular Aggregation of Polymer Semiconductors in a

Secondary Insulating Polymer Matrix to Enhance Charge Transport. *Chemistry of Materials* **2020,** *32* (2), 897–905.

39. Noriega, R.; Rivnay, J.; Vandewal, K.; Koch, F. P.; Stingelin, N.; Smith, P.; Toney, M. F.; Salleo, A., A general relationship between disorder, aggregation and charge transport in conjugated polymers. *Nat Mater* **2013,** *12* (11), 1038-44.

40. Pankow, R. M.; Thompson, B. C., The development of conjugated polymers as the cornerstone of organic electronics. *Polymer* **2020,** *207*, 122874.

41. Chang, M.; Choi, D.; Wang, G.; Kleinhenz, N.; Persson, N.; Park, B.; Reichmanis, E., Photoinduced Anisotropic Assembly of Conjugated Polymers in Insulating Polymer Blends. *ACS Appl Mater Interfaces* **2015,** *7* (25), 14095-103.

42. Chen, M.; Peng, B.; Huang, S.; Chan, P. K. L., Understanding the Meniscus-Guided Coating Parameters in Organic Field-Effect-Transistor Fabrications. *Advanced Functional Materials* **2020,** *30* (1), 1905963.

43. Kafle, P.; Zhang, F.; Schorr, N. B.; Huang, K.-Y.; Rodríguez-López, J.; Diao, Y., Printing 2D Conjugated Polymer Monolayers and Their Distinct Electronic Properties. *Advanced Functional Materials* **2020,** *30* (12), 1909787.

44. Li, M.; An, C.; Marszalek, T.; Baumgarten, M.; Yan, H.; Müllen, K.; Pisula, W., Controlling the Surface Organization of Conjugated Donor–Acceptor Polymers by their Aggregation in Solution. *Advanced Materials* **2016,** *28* (42), 9430-9438.

45. McBride, M.; Liu, A.; Reichmanis, E.; Grover, M. A., Toward Data-Enabled Process Optimization of Deformable Electronic Polymer-Based Devices. *Current Opinion in Chemical Engineering* **2020,** *27*, 72-80.

46. Li, J.; Zhao, Y.; Tan, H. S.; Guo, Y.; Di, C.-A.; Yu, G.; Liu, Y.; Lin, M.; Lim, S. H.; Zhou, Y.; Su, H.; Ong, B. S., A Stable Solution-Processed Polymer Semiconductor with Record High-Mobility for Printed Transistors. *Scientific Reports* **2012,** *2* (1), 754-763.

47. Liu, A. L.; Lee, M.; Venkatesh, R.; Bonsu, J. A.; Volkovinsky, R.; Meredith, J. C.; Reichmanis, E.; Grover, M. A., Conjugated Polymer Process Ontology and Experimental Data Repository for Organic Field-Effect Transistors. *Chemistry of Materials* **2023,** *35* (21), 8816-8826.

48. Fratini, S.; Nikolka, M.; Salleo, A.; Schweicher, G.; Sirringhaus, H., Charge transport in high-mobility conjugated polymers and molecular semiconductors. *Nature Materials* **2020,** *19* (5), 491-502.

49. Nikolka, M.; Broch, K.; Armitage, J.; Hanifi, D.; Nowack, P. J.; Venkateshvaran, D.; Sadhanala, A.; Saska, J.; Mascal, M.; Jung, S.-H.; Lee, J. K.; McCulloch, I.; Salleo, A.; Sirringhaus, H., High-mobility, trap-free charge transport in conjugated polymer diodes. *Nature Communications* **2019,** *10* (1), 2122.

50. Wunderlich, B., Crystal Structure, Morphology and Defects. In *Macromolecular Physics*, Wunderlich, B., Ed. Academic Press, New York: 1973; Vol. Vol.1

51. Grévin, B.; Rannou, P.; Payerne, R.; Pron, A.; Travers, J.-P., Scanning Tunneling Microscopy Investigations of Self-Organized Poly(3-hexylthiophene) Two-Dimensional Polycrystals. *Advanced Materials* **2003,** *15* (11), 881-884.

52. Abbaszadeh, D.; Kunz, A.; Kotadiya, N. B.; Mondal, A.; Andrienko, D.; Michels, J. J.; Wetzelaer, G.-J. A. H.; Blom, P. W. M., Electron Trapping in Conjugated Polymers. *Chemistry of Materials* **2019,** *31* (17), 6380-6386.

53. Clark, J.; Chang, J.-F.; Spano, F. C.; Friend, R. H.; Silva, C., Determining Exciton Bandwidth and Film Microstructure in Polythiophene Films using Linear Absorption Spectroscopy. *Applied Physics Letters* **2009,** *94* (16), 163306-163311.

54. Takacs, C. J.; Treat, N. D.; Krämer, S.; Chen, Z.; Facchetti, A.; Chabinyc, M. L.; Heeger, A. J., Remarkable Order of a High-Performance Polymer. *Nano Letters* **2013,** *13* (6), 2522-2527.

55. Zen, A.; Saphiannikova, M.; Neher, D.; Grenzer, J.; Grigorian, S.; Pietsch, U.; Asawapirom, U.; Janietz, S.; Scherf, U.; Lieberwirth, I.; Wegner, G., Effect of Molecular Weight on the Structure and Crystallinity of Poly(3-hexylthiophene). *Macromolecules* **2006,** *39* (6), 2162-2171.

56. Bao, Z.; Dodabalapur, A.; Lovinger, A. J., Soluble and Processable Regioregular Poly(3-hexylthiophene) for Thin Film Field-Effect Transistor Applications with High Mobility. *Applied Physics Letters* **1996,** *69* (26), 4108-4110.

57. Ong, B. S.; Wu, Y.; Liu, P.; Gardner, S., High-Performance Semiconducting Polythiophenes for Organic Thin-Film Transistors. *Journal of the American Chemical Society* **2004,** *126* (11), 3378-3379.

58. Sirringhaus, H.; Brown, P. J.; Friend, R. H.; Nielsen, M. M.; Bechgaard, K.; Langeveld-Voss, B. M. W.; Spiering, A. J. H.; Janssen, R. A. J.; Meijer, E. W.; Herwig, P.; de Leeuw, D. M., Two-Dimensional Charge Transport in Self-Organized, High-Mobility Conjugated Polymers. *Nature* **1999,** *401* (6754), 685-688.

59. Koch, F. P. V.; Rivnay, J.; Foster, S.; Müller, C.; Downing, J. M.; Buchaca-Domingo, E.; Westacott, P.; Yu, L.; Yuan, M.; Baklar, M.; Fei, Z.; Luscombe, C.; McLachlan, M. A.; Heeney, M.; Rumbles, G.; Silva, C.; Salleo, A.; Nelson, J.; Smith, P.; Stingelin, N., The impact of molecular weight on microstructure and charge transport in semicrystalline polymer semiconductors–poly(3-hexylthiophene), a model study. *Progress in Polymer Science* **2013,** *38* (12), 1978-1989.

60. Rivnay, J.; Noriega, R.; Northrup, J. E.; Kline, R. J.; Toney, M. F.; Salleo, A., Structural origin of gap states in semicrystalline polymers and the implications for charge transport. *Physical Review B* **2011,** *83* (12), 121306.

61. Chu, P.-H. In *Controlling morphology of conjugated polymers and the impact on charge transport in flexible organic field-effect transistors*, 2017.

62. Paterson, A. F.; Singh, S.; Fallon, K. J.; Hodsden, T.; Han, Y.; Schroeder, B. C.; Bronstein, H.; Heeney, M.; McCulloch, I.; Anthopoulos, T. D., Recent Progress in High-Mobility Organic Transistors: A Reality Check. *Advanced Materials* **2018,** *30* (36), 1801079.

63. Venkateshvaran, D.; Nikolka, M.; Sadhanala, A.; Lemaur, V.; Zelazny, M.; Kepa, M.; Hurhangee, M.; Kronemeijer, A. J.; Pecunia, V.; Nasrallah, I.; Romanov, I.; Broch, K.; McCulloch, I.; Emin, D.; Olivier, Y.; Cornil, J.; Beljonne, D.; Sirringhaus, H., Approaching disorder-free transport in high-mobility conjugated polymers. *Nature* **2014,** *515* (7527), 384-388.

64. Zhang, W.; Smith, J.; Watkins, S. E.; Gysel, R.; McGehee, M.; Salleo, A.; Kirkpatrick, J.; Ashraf, S.; Anthopoulos, T.; Heeney, M.; McCulloch, I., Indacenodithiophene Semiconducting Polymers for High-Performance, Air-Stable Transistors. *Journal of the American Chemical Society* **2010,** *132* (33), 11437-11439.

65. Zhang, X.; Bronstein, H.; Kronemeijer, A. J.; Smith, J.; Kim, Y.; Kline, R. J.; Richter, L. J.; Anthopoulos, T. D.; Sirringhaus, H.; Song, K.; Heeney, M.; Zhang, W.; McCulloch, I.; DeLongchamp, D. M., Molecular origin of high field-effect mobility in an indacenodithiophene–benzothiadiazole copolymer. *Nature Communications* **2013,** *4* (1), 2238.

66. Kang, I.; Yun, H.-J.; Chung, D. S.; Kwon, S.-K.; Kim, Y.-H., Record High Hole Mobility in Polymer Semiconductors via Side-Chain Engineering. *Journal of the American Chemical Society* **2013,** *135* (40), 14896-14899.

67. Lan, Y.-K.; Yang, C. H.; Yang, H.-C., Theoretical investigations of electronic structure and charge transport properties in polythiophene-based organic field-effect transistors. *Polymer International* **2010,** *59* (1), 16-21.

68. Mei, J.; Bao, Z., Side Chain Engineering in Solution-Processable Conjugated Polymers. *Chemistry of Materials* **2014,** *26* (1), 604-615.

69. Di, C.-a.; Yu, G.; Liu, Y.; Zhu, D., High-Performance Organic Field-Effect Transistors: Molecular Design, Device Fabrication, and Physical Properties. *The Journal of Physical Chemistry B* **2007,** *111* (51), 14083-14096.

70. Newman, C. R.; Frisbie, C. D.; da Silva Filho, D. A.; Brédas, J.-L.; Ewbank, P. C.; Mann, K. R., Introduction to Organic Thin Film Transistors and Design of n-Channel Organic Semiconductors. *Chemistry of Materials* **2004,** *16* (23), 4436-4451.

71. Chung, S.; Cho, K.; Lee, T., Recent Progress in Inkjet-Printed Thin-Film Transistors. *Advanced Science* **2019,** *6* (6), 1801445.

72. Diao, Y.; Shaw, L.; Bao, Z.; Mannsfeld, S. C. B., Morphology control strategies for solution-processed organic semiconductor thin films. *Energy & Environmental Science* **2014,** *7* (7), 2145-2159.

73. Park, K. S.; Kwok, J. J.; Dilmurat, R.; Qu, G.; Kafle, P.; Luo, X.; Jung, S.-H.; Olivier, Y.; Lee, J.-K.; Mei, J.; Beljonne, D.; Diao, Y., Tuning conformation, assembly, and charge transport properties of conjugated polymers by printing flow. *Science Advances* **2019,** *5* (8), eaaw7757.

74. Lu, Z.; Wang, C.; Deng, W.; Achille, M. T.; Jie, J.; Zhang, X., Meniscus-guided coating of organic crystalline thin films for high-performance organic field-effect transistors. *Journal of Materials Chemistry C* **2020,** *8* (27), 9133-9146.

75. Zheng, Y.-Q.; Yao, Z.-F.; Lei, T.; Dou, J.-H.; Yang, C.-Y.; Zou, L.; Meng, X.; Ma, W.; Wang, J.-Y.; Pei, J., Unraveling the Solution-State Supramolecular Structures of Donor–Acceptor Polymers and their Influence on Solid-State Morphology and Charge-Transport Properties. *Advanced Materials* **2017,** *29* (42), 1701072.

76. Venkatesh, R.; Zheng, Y.; Liu, A. L.; Zhao, H.; Silva, C.; Takacs, C. J.; Grover, M. A.; Meredith, J. C.; Reichmanis, E., Overlap concentration generates optimum device performance for DPP-based conjugated polymers. *Organic Electronics* **2023,** *117*, 106779.

77. Singh, C.; Hone, D., Temperature-dependent behavior of conjugated polymers in solution. *Synthetic Metals* **1994,** *62* (1), 61-70.

78. Kleinhenz, N.; Persson, N.; Xue, Z.; Chu, P. H.; Wang, G.; Yuan, Z.; McBride, M. A.; Choi, D.; Grover, M. A.; Reichmanis, E., Ordering of Poly(3-hexylthiophene) in Solutions and Films: Effects of Fiber Length and Grain Boundaries on Anisotropy and Mobility. *Chemistry of Materials* **2016,** *28* (11), 3905-3913.

79. Vezie, M. S.; Few, S.; Meager, I.; Pieridou, G.; Dörling, B.; Ashraf, R. S.; Goñi, A. R.; Bronstein, H.; McCulloch, I.; Hayes, S. C.; Campoy-Quiles, M.; Nelson, J., Exploring the origin of high optical absorption in conjugated polymers. *Nature Materials* **2016,** *15* (7), 746-753.

80. McBride, M.; Bacardi, G.; Morales, C.; Risteen, B.; Keane, D.; Reichmanis, E.; Grover, M. A., Control of Nucleation Density in Conjugated Polymers via Seed Nucleation. *ACS Appl Mater Interfaces* **2019,** *11* (41), 37955-37965.

81. Kwok, J. J.; Park, K. S.; Patel, B. B.; Dilmurat, R.; Beljonne, D.; Zuo, X.; Lee, B.; Diao, Y., Understanding Solution State Conformation and Aggregate Structure of Conjugated Polymers via Small Angle X-ray Scattering. *Macromolecules* **2022,** *55* (11), 4353-4366.

82. Venkatesh, R.; Zheng, Y.; Viersen, C.; Liu, A.; Silva, C.; Grover, M.; Reichmanis, E., Data Science Guided Experiments Identify Conjugated Polymer Solution Concentration as a Key Parameter in Device Performance. *ACS Materials Letters* **2021,** *3* (9), 1321-1327.

83. Hestand, N. J.; Spano, F. C., Expanded Theory of H- and J-Molecular Aggregates: The Effects of Vibronic Coupling and Intermolecular Charge Transfer. *Chemical Reviews* **2018,** *118* (15), 7069-7163.

84. Spano, F. C.; Silva, C., H- and J-Aggregate Behavior in Polymeric Semiconductors. *Annual Review of Physical Chemistry* **2014,** *65* (1), 477-500.

85. Niles, E. T.; Roehling, J. D.; Yamagata, H.; Wise, A. J.; Spano, F. C.; Moulé, A. J.; Grey, J. K., J-Aggregate Behavior in Poly-3-hexylthiophene Nanofibers. *The Journal of Physical Chemistry Letters* **2012,** *3* (2), 259-263.

86. Koch, S. W.; Kira, M.; Khitrova, G.; Gibbs, H. M., Semiconductor excitons in new light. *Nature Materials* **2006,** *5* (7), 523-531.

87. Clark, J.; Silva, C.; Friend, R. H.; Spano, F. C., Role of intermolecular coupling in the photophysics of disordered organic semiconductors: aggregate emission in regioregular polythiophene. *Phys Rev Lett* **2007,** *98* (20), 206406.

88. Spano, F. C., Modeling disorder in polymer aggregates: The optical spectroscopy of regioregular poly(3-hexylthiophene) thin films. *The Journal of Chemical Physics* **2005,** *122* (23).

89. Spano, F. C., Absorption in Regio-Regular Poly(3-hexyl)thiophene Thin Films: Fermi Resonances, Interband Coupling and Disorder. *Chemical Physics* **2006,** *325*, 22-35.

90. Berson, S.; De Bettignies, R.; Bailly, S.; Guillerez, S., Poly(3-hexylthiophene) Fibers for Photovoltaic Applications. *Advanced Functional Materials* **2007,** *17* (8), 1377-1384.

91. Moulé, A. J.; Meerholz, K., Controlling Morphology in Polymer–Fullerene Mixtures. *Advanced Materials* **2008,** *20* (2), 240-245.

92. Paquin, F.; Yamagata, H.; Hestand, N. J.; Sakowicz, M.; Bérubé, N.; Côté, M.; Reynolds, L. X.; Haque, S. A.; Stingelin, N.; Spano, F. C.; Silva, C., Two-Dimensional Spatial Coherence of Excitons in Semicrystalline Polymeric Semiconductors: Effect of Molecular Weight. *Physical Review B* **2013,** *88* (15), 155202-1:14.

93. Jo, G.; Jung, J.; Chang, M., Controlled Self-Assembly of Conjugated Polymers via a Solvent Vapor Pre-Treatment for Use in Organic Field-Effect Transistors. *Polymers (Basel)* **2019,** *11* (2).

94. Barford, W., Exciton transfer integrals between polymer chains. *The Journal of Chemical Physics* **2007,** *126* (13).

95. Beljonne, D.; Cornil, J.; Silbey, R.; Millié, P.; Brédas, J. L., Interchain interactions in conjugated materials: The exciton model versus the supermolecular approach. *The Journal of Chemical Physics* **2000,** *112* (10), 4749-4758.

96. Manas, E. S.; Spano, F. C., Absorption and spontaneous emission in aggregates of conjugated polymers. *The Journal of Chemical Physics* **1998,** *109* (18), 8087-8101.

97. Zhou, T.; Song, Z.; Sundmacher, K., Big Data Creates New Opportunities for Materials Research: A Review on Methods and Applications of Machine Learning for Materials Design. *Engineering* **2019,** *5* (6), 1017-1026.

98. Omar, Ö. H.; del Cueto, M.; Nematiaram, T.; Troisi, A., High-throughput virtual screening for organic electronics: a comparative study of alternative strategies. *Journal of Materials Chemistry C* **2021,** *9* (39), 13557-13583.

99. Gupta, T.; Zaki, M.; Krishnan, N. M. A.; Mausam, MatSciBERT: A materials domain language model for text mining and information extraction. *npj Computational Materials* **2022,** *8* (1), 102.

100. McBride, M.; Persson, N.; Reichmanis, E.; Grover, M. A., Solving Materials' Small Data Problem with Dynamic Experimental Databases. *Processes* **2018,** *6* (7), 79.

101. Shetty, P.; Rajan, A. C.; Kuenneth, C.; Gupta, S.; Panchumarti, L. P.; Holm, L.; Zhang, C.; Ramprasad, R., A general-purpose material property data extraction pipeline from large polymer corpora using natural language processing. *npj Computational Materials* **2023,** *9* (1), 52.

102. Swain, M. C.; Cole, J. M., ChemDataExtractor: A Toolkit for Automated Extraction of Chemical Information from the Scientific Literature. *J Chem Inf Model* **2016,** *56* (10), 1894-1904.

103. Zhang, R.; Zhang, J.; Chen, Q.; Wang, B.; Liu, Y.; Qian, Q.; Pan, D.; Xia, J.; Wang, Y.; Han, Y., A literature-mining method of integrating text and table extraction for materials science publications. *Computational Materials Science* **2023,** *230*, 112441.

104. Alstrup, J.; Jørgensen, M.; Medford, A. J.; Krebs, F. C., Ultra fast and parsimonious materials screening for polymer solar cells using differentially pumped slot-die coating. *ACS Appl Mater Interfaces* **2010,** *2* (10), 2819-27.

105. An, N. G.; Kim, J. Y.; Vak, D., Machine learning-assisted development of organic photovoltaics via high-throughput in situ formulation. *Energy & Environmental Science* **2021,** *14* (6), 3438-3446.

106. Gomez, I. J.; Wu, J.; Roper, J.; Beckham, H.; Meredith, J. C., High Throughput Screening of Mechanical Properties and Scratch Resistance of Tricomponent Polyurethane Coatings. *ACS Applied Polymer Materials* **2019,** *1* (11), 3064-3073.

107. Hoogenboom, R.; Meier, M. A. R.; Schubert, U. S., Combinatorial Methods, Automated Synthesis and High-Throughput Screening in Polymer Research: Past and Present. *Macromolecular Rapid Communications* **2003,** *24* (1), 15-32.

108. Kennedy, K.; Stefansky, T.; Davy, G.; Zackay, V. F.; Parker, E. R., Rapid Method for Determining Ternary-Alloy Phase Diagrams. *Journal of Applied Physics* **2004,** *36* (12), 3808-3810.

109. Liu, A. L.; Dogan-Guner, E. M.; McBride, M.; Venkatesh, R.; Gonzalez, M. A.; Reichmanis, E.; Grover, M.; Meredith, J. C., Composition Gradient High-Throughput Polymer Libraries Enabled by Passive Mixing and Elevated Temperature Operability. *Chemistry of Materials* **2022,** *34* (15), 6659-6670.

110. Meier, M. A. R.; Schubert, U. S., Combinatorial polymer research and high-throughput experimentation: powerful tools for the discovery and evaluation of new materials. *Journal of Materials Chemistry* **2004,** *14* (22), 3289-3299.

111. Meredith, J.; Alamgir, K.; Eric, A., High-Throughput Measurement of Polymer Blend Phase Behavior. **2000**.

112. Meredith, J. C.; Smith, A. P.; Karim, A.; Amis, E. J., Combinatorial Materials Science for Polymer Thin-Film Dewetting. *Macromolecules* **2000,** *33* (26), 9747-9756.

113. Miracle, D. B.; Miller, J. D.; Senkov, O. N.; Woodward, C.; Uchic, M. D.; Tiley, J., Exploration and Development of High Entropy Alloys for Structural Applications. *Entropy* **2014,** *16* (1), 494-525.

114. Reetz, M. T., Combinatorial and Evolution-Based Methods in the Creation of Enantioselective Catalysts. *Angewandte Chemie International Edition* **2001,** *40* (2), 284-310.

115. Rodríguez-Martínez, X.; Sevim, S.; Xu, X.; Franco, C.; Pamies-Puig, P.; Córcoles-Guija, L.; Rodriguez-Trujillo, R.; del Campo, F. J.; Rodriguez San Miguel, D.; deMello, A. J.; Pané, S.; Amabilino, D. B.; Inganäs, O.; Puigmartí-Luis, J.; Campoy-Quiles, M., Microfluidic-Assisted Blade Coating of Compositional Libraries for Combinatorial Applications: The Case of Organic Photovoltaics. *Advanced Energy Materials* **2020,** *10* (33), 2001308.

116. Smith, A. P.; Douglas, J. F.; Meredith, J. C.; Amis, E. J.; Karim, A., High-throughput characterization of pattern formation in symmetric diblock copolymer films. *Journal of Polymer Science Part B: Polymer Physics* **2001,** *39* (18), 2141-2158.

117. Sormana, J.-L.; Meredith, J. C., High-Throughput Discovery of Structure−Mechanical Property Relationships for Segmented Poly(urethane−urea)s. *Macromolecules* **2004,** *37* (6), 2186-2195.

118. Xiang, X.-D.; Sun, X.; Briceño, G.; Lou, Y.; Wang, K.-A.; Chang, H.; Wallace-Freedman, W. G.; Chen, S.-W.; Schultz, P. G., A Combinatorial Approach to Materials Discovery. *Science* **1995,** *268* (5218), 1738-1740.

119. Agrawal, A.; Choudhary, A., Perspective: Materials informatics and big data: Realization of the "fourth paradigm" of science in materials science. *APL Materials* **2016,** *4* (5), 053208.

120. Audus, D. J.; de Pablo, J. J., Polymer Informatics: Opportunities and Challenges. *ACS Macro Lett* **2017,** *6* (10), 1078-1082.

121. Callaghan, S., Toward machine learning-enhanced high-throughput experimentation for chemistry. *Patterns* **2021,** *2* (3), 100221.

122. Chen, G.; Shen, Z.; Iyer, A.; Ghumman, U. F.; Tang, S.; Bi, J.; Chen, W.; Li, Y., Machine-Learning-Assisted De Novo Design of Organic Molecules and Polymers: Opportunities and Challenges. *Polymers* **2020,** *12* (1).

123. Chibani, S.; Coudert, F.-X., Machine learning approaches for the prediction of materials properties. *APL Materials* **2020,** *8* (8).

124. Childs, C. M.; Washburn, N. R., Embedding domain knowledge for machine learning of complex material systems. *MRS Communications* **2019,** *9* (3), 806-820.

125. Deagen, M. E.; Walsh, D. J.; Audus, D. J.; Kroenlein, K.; de Pablo, J. J.; Aou, K.; Chard, K.; Jensen, K. F.; Olsen, B. D., Networks and interfaces as catalysts for polymer materials innovation. *Cell Reports Physical Science* **2022,** *3* (11), 101126.

126. Du, X.; Lüer, L.; Heumueller, T.; Wagner, J.; Berger, C.; Osterrieder, T.; Wortmann, J.; Langner, S.; Vongsaysy, U.; Bertrand, M.; Li, N.; Stubhan, T.; Hauch, J.; Brabec, C. J., Elucidating the Full Potential of OPV Materials Utilizing a High-Throughput Robot-Based Platform and Machine Learning. *Joule* **2021,** *5* (2), 495-506.

127. Jørgensen, P. B.; Mesta, M.; Shil, S.; García Lastra, J. M.; Jacobsen, K. W.; Thygesen, K. S.; Schmidt, M. N., Machine learning-based screening of complex molecules for polymer solar cells. *J Chem Phys* **2018,** *148* (24), 241735.

128. Kim, E.; Huang, K.; Saunders, A.; McCallum, A.; Ceder, G.; Olivetti, E., Materials Synthesis Insights from Scientific Literature via Text Extraction and Machine Learning. *Chemistry of Materials* **2017,** *29* (21), 9436-9444.

129. Liu, A. L.; Venkatesh, R.; McBride, M.; Reichmanis, E.; Meredith, J. C.; Grover, M. A., Small Data Machine Learning: Classification and Prediction of Poly(ethylene terephthalate) Stabilizers Using Molecular Descriptors. *ACS Applied Polymer Materials* **2020,** *2* (12), 5592-5601.

130. Lo, Y. C.; Rensi, S. E.; Torng, W.; Altman, R. B., Machine learning in chemoinformatics and drug discovery. *Drug Discov Today* **2018,** *23* (8), 1538-1546.

131. Mannodi-Kanakkithodi, A.; Pilania, G.; Huan, T. D.; Lookman, T.; Ramprasad, R., Machine Learning Strategy for Accelerated Design of Polymer Dielectrics. *Sci Rep* **2016,** *6*, 20952.

132. Martin, T. B.; Audus, D. J., Emerging Trends in Machine Learning: A Polymer Perspective. *ACS Polymers Au* **2023,** *3* (3), 239-258.

133. Nagarajan, H. P. N.; Mokhtarian, H.; Jafarian, H.; Dimassi, S.; Bakrani-Balani, S.; Hamedi, A.; Coatanéa, E.; Gary Wang, G.; Haapala, K. R., Knowledge-Based Design of Artificial Neural Network Topology for Additive Manufacturing Process Modeling: A New Approach and Case Study for Fused Deposition Modeling. *Journal of Mechanical Design* **2019,** *141* (2).

134. Raccuglia, P.; Elbert, K. C.; Adler, P. D.; Falk, C.; Wenny, M. B.; Mollo, A.; Zeller, M.; Friedler, S. A.; Schrier, J.; Norquist, A. J., Machine-learning-assisted materials discovery using failed experiments. *Nature* **2016,** *533* (7601), 73-6.

135. Rodríguez-Martínez, X.; Pascual-San-José, E.; Campoy-Quiles, M., Accelerating organic solar cell material's discovery: high-throughput screening and big data. *Energy & Environmental Science* **2021,** *14* (6), 3301-3322.

136. Wang, A. Y.-T.; Murdock, R. J.; Kauwe, S. K.; Oliynyk, A. O.; Gurlo, A.; Brgoch, J.; Persson, K. A.; Sparks, T. D., Machine Learning for Materials Scientists: An Introductory Guide toward Best Practices. *Chemistry of Materials* **2020,** *32* (12), 4954-4965.

137. Wang, Z.-L.; Ogawa, T.; Adachi, Y., Properties-to-microstructure-to-processing Inverse Analysis for Steels via Machine Learning. *ISIJ International* **2019,** *59* (9), 1691-1694.

138. Genzer, J., Surface-Bound Gradients for Studies of Soft Materials Behavior. *Annual Review of Materials Research* **2012,** *42* (1), 435-468.

139. Green, M. L.; Choi, C. L.; Hattrick-Simpers, J. R.; Joshi, A. M.; Takeuchi, I.; Barron, S. C.; Campo, E.; Chiang, T.; Empedocles, S.; Gregoire, J. M.; Kusne, A. G.; Martin, J.; Mehta, A.; Persson, K.; Trautt, Z.; Van Duren, J.; Zakutayev, A., Fulfilling the promise of the materials genome initiative with high-throughput experimental methodologies. *Applied Physics Reviews* **2017,** *4* (1), 011105.

140. Persson, N. E.; Rafshoon, J.; Naghshpour, K.; Fast, T.; Chu, P. H.; McBride, M.; Risteen, B.; Grover, M.; Reichmanis, E., High-Throughput Image Analysis of Fibrillar Materials: A Case Study on Polymer Nanofiber Packing, Alignment, and Defects in Organic Field Effect Transistors. *ACS Appl Mater Interfaces* **2017,** *9* (41), 36090-36102.

141. Sun, S.; Hartono, N. T. P.; Ren, Z. D.; Oviedo, F.; Buscemi, A. M.; Layurova, M.; Chen, D. X.; Ogunfunmi, T.; Thapa, J.; Ramasamy, S.; Settens, C.; DeCost, B. L.; Kusne, A. G.; Liu, Z.; Tian, S. I. P.; Peters, I. M.; Correa-Baena, J.-P.; Buonassisi, T., Accelerated Development of Perovskite-Inspired Materials via High-Throughput Synthesis and Machine-Learning Diagnosis. *Joule* **2019,** *3* (6), 1437-1451.

142. Taniike, T.; Kitamura, T.; Nakayama, K.; Takimoto, K.; Aratani, N.; Wada, T.; Thakur, A.; Chammingkwan, P., Stabilizer Formulation Based on High-Throughput Chemiluminescence Imaging and Machine Learning. *ACS Applied Polymer Materials* **2020,** *2* (8), 3319-3326.

143. Saeki, A.; Kranthiraja, K., A high throughput molecular screening for organic electronics via machine learning: present status and perspective. *Japanese Journal of Applied Physics* **2019,** *59* (SD), SD0801.

144. Hong, Z.; Ward, L.; Chard, K.; Blaiszik, B.; Foster, I., Challenges and Advances in Information Extraction from Scientific Literature: a Review. *JOM* **2021,** *73* (11), 3383-3400.

145. Landhuis, E., Scientific literature: Information overload. *Nature* **2016,** *535* (7612), 457-458.

146. Li, H.; Zhang, Z.; Zhao, Z.-Z., Data-Mining for Processes in Chemistry, Materials, and Engineering. *Processes* **2019,** *7* (3), 151.

147. Lu, W.; Xiao, R.; Yang, J.; Li, H.; Zhang, W., Data mining-aided materials discovery and optimization. *Journal of Materiomics* **2017,** *3* (3), 191-201.

148. Park, G.; Pouchard, L. In *Scientific Literature Mining for Experiment Information in Materials Design*, 2019 New York Scientific Data Summit (NYSDS), 12-14 June 2019; 2019; pp 1-4.

149. Persson, N.; McBride, M.; Grover, M.; Reichmanis, E., Silicon Valley Meets the Ivory Tower: Searchable Data Repositories for Experimental Nanomaterials Research. *Current Opinion in Solid State and Materials Science* **2016,** *20* (6), 338-343.

150. Huang, S.; Cole, J. M., A database of battery materials auto-generated using ChemDataExtractor. *Scientific Data* **2020,** *7* (1), 260.

151. Court, C. J.; Cole, J. M., Auto-generated materials database of Curie and Néel temperatures via semi-supervised relationship extraction. *Scientific Data* **2018,** *5* (1), 180111.

152. Kononova, O.; Huo, H.; He, T.; Rong, Z.; Botari, T.; Sun, W.; Tshitoyan, V.; Ceder, G., Text-mined dataset of inorganic materials synthesis recipes. *Scientific Data* **2019,** *6* (1), 203.

153. Shetty, P.; Ramprasad, R., Automated knowledge extraction from polymer literature using natural language processing. *iScience* **2021,** *24* (1), 101922.

154. Hachmann, J.; Olivares-Amaya, R.; Atahan-Evrenk, S.; Amador-Bedolla, C.; Sánchez-Carrera, R. S.; Gold-Parker, A.; Vogt, L.; Brockway, A. M.; Aspuru-Guzik, A., The Harvard Clean Energy Project: Large-Scale Computational Screening and Design of Organic Photovoltaics on the World Community Grid. *Journal of Physical Chemistry Letters* **2011,** *2*, 2241-2251.

155. Ai, Q.; Bhat, V.; Ryno, S. M.; Jarolimek, K.; Sornberger, P.; Smith, A.; Haley, M. M.; Anthony, J. E.; Risko, C., OCELOT: An infrastructure for data-driven research to discover and design crystalline organic semiconductors. *J Chem Phys* **2021,** *154* (17), 174705.

156. Casciato, M. J.; Kim, S.; Lu, J. C.; Hess, D. W.; Grover, M. A., Optimization of a Carbon Dioxide-Assisted Nanoparticle Deposition Process Using Sequential Experimental Design with Adaptive Design Space. *Industrial & Engineering Chemistry Research* **2012,** *51* (11), 4363-4370.

157. Gómez-Bombarelli, R.; Wei, J. N.; Duvenaud, D.; Hernández-Lobato, J. M.; Sánchez-Lengeling, B.; Sheberla, D.; Aguilera-Iparraguirre, J.; Hirzel, T. D.; Adams, R. P.; Aspuru-Guzik, A., Automatic Chemical Design Using a Data-Driven Continuous Representation of Molecules. *ACS Central Science* **2018,** *4* (2), 268-276.

158. Okuyama, M.; Nakazawa, Y.; Funatsu, K., A data-driven scheme to search for alternative composite materials. *Science and Technology of Advanced Materials: Methods* **2022,** *2* (1), 106-118.

159. Kouraytem, N.; Li, X.; Tan, W.; Kappes, B.; Spear, A. D., Modeling process–structure–property relationships in metal additive manufacturing: a review on physics-driven versus data-driven approaches. *Journal of Physics: Materials* **2021,** *4* (3), 032002.

160. Yeh, I. C., Modeling of strength of high-performance concrete using artificial neural networks. *Cement and Concrete Research* **1998,** *28* (12), 1797-1808.

161. Yan, W.; Lian, Y.; Yu, C.; Kafka, O. L.; Liu, Z.; Liu, W. K.; Wagner, G. J., An integrated process–structure–property modeling framework for additive manufacturing. *Computer Methods in Applied Mechanics and Engineering* **2018,** *339*, 184-204.

162. Sánchez-Díaz, A.; Rodríguez-Martínez, X.; Córcoles-Guija, L.; Mora-Martín, G.; Campoy-Quiles, M., High-Throughput Multiparametric Screening of Solution Processed Bulk Heterojunction Solar Cells. *Advanced Electronic Materials* **2018,** *4* (10), 1700477.

163. Jørgensen, P. B.; Mesta, M.; Shil, S.; García Lastra, J. M.; Jacobsen, K. W.; Thygesen, K. S.; Schmidt, M. N., Machine learning-based screening of complex molecules for polymer solar cells. *The Journal of Chemical Physics* **2018,** *148* (24), 241735.

164. Kim, N.-K.; Jang, S.-Y.; Pace, G.; Caironi, M.; Park, W.-T.; Khim, D.; Kim, J.; Kim, D.-Y.; Noh, Y.-Y., High-Performance Organic Field-Effect Transistors with Directionally Aligned Conjugated Polymer Film Deposited from Pre-Aggregated Solution. *Chemistry of Materials* **2015,** *27* (24), 8345-8353.

165. Noriega, R.; Rivnay, J.; Vandewal, K.; Koch, F. P. V.; Stingelin, N.; Smith, P.; Toney, M. F.; Salleo, A., A General Relationship Between Disorder, Aggregation and Charge Transport in Conjugated Polymers. *Nature Materials* **2013,** *12* (11), 1038-1044.

166. Kang, I.; An, T. K.; Hong, J.-a.; Yun, H.-J.; Kim, R.; Chung, D. S.; Park, C. E.; Kim, Y.-H.; Kwon, S.-K., Effect of Selenophene in a DPP Copolymer Incorporating a Vinyl Group for High-Performance Organic Field-Effect Transistors. *Advanced Materials* **2013,** *25* (4), 524-528.

167. Sarkar, T.; Schneider, S. A.; Ankonina, G.; Hendsbee, A. D.; Li, Y.; Toney, M. F.; Frey, G. L., Tuning Intra and Intermolecular Interactions for Balanced Hole and Electron Transport in Semiconducting Polymers. *Chemistry of Materials* **2020,** *32* (17), 7338-7346.

168. McBride, M.; Persson, N.; Reichmanis, E.; Grover, M. A., Solving Materials' Small Data Problem with Dynamic Experimental Databases. *Processes* **2018,** *6* (7), 79-96.

169. Afzal, T.; Iqbal, M. J.; Iqbal, M. Z.; Sajjad, A.; Raza, M. A.; Riaz, S.; Kamran, M. A.; Numan, A.; Naseem, S., Effect of post-deposition annealing temperature on the charge carrier mobility and morphology of DPPDTT based organic field effect transistors. *Chemical Physics Letters* **2020,** *750*, 137507.

170. Armin, A.; Wolfer, P.; Shaw, P. E.; Hambsch, M.; Maasoumi, F.; Ullah, M.; Gann, E.; McNeill, C. R.; Li, J.; Shi, Z.; Burn, P. L.; Meredith, P., Simultaneous

enhancement of charge generation quantum yield and carrier transport in organic solar cells. *Journal of Materials Chemistry C* **2015,** *3* (41), 10799-10812.

171. Baek, S. W.; Ha, J.-W.; Yoon, M.; Hwang, D.-H.; Lee, J., Shellac Films as a Natural Dielectric Layer for Enhanced Electron Transport in Polymer Field-Effect Transistors. *ACS Applied Materials & Interfaces* **2018,** *10* (22), 18948-18955.

172. Iqbal, M. J.; Haq, H.; Riaz, S.; Raza, M. A.; Iqbal, M. Z.; Chaudhry, M. U.; Naseem, S., On the Operational, shelf life and degradation mechanism in polymer field effect transistors. *Superlattices and Microstructures* **2019,** *126*, 125-131.

173. Lei, Y.; Wu, B.; Chan, W.-K. E.; Zhu, F.; Ong, B. S., Engineering gate dielectric surface properties for enhanced polymer field-effect transistor performance. *Journal of Materials Chemistry C* **2015,** *3* (47), 12267-12272.

174. Li, J.; Zhao, Y.; Tan, H. S.; Guo, Y.; Di, C.-A.; Yu, G.; Liu, Y.; Lin, M.; Lim, S. H.; Zhou, Y.; Su, H.; Ong, B. S., A stable solution-processed polymer semiconductor with record high-mobility for printed transistors. *Scientific Reports* **2012,** *2* (1), 754.

175. Park, H.; Yoo, S.; Won, J. C.; Kim, Y. H., Room-temperature, printed, low-voltage, flexible organic field-effect transistors using soluble polyimide gate dielectrics. *APL Materials* **2020,** *8* (1), 011112.

176. Qu, G.; Zhao, X.; Newbloom, G. M.; Zhang, F.; Mohammadi, E.; Strzalka, J. W.; Pozzo, L. D.; Mei, J.; Diao, Y., Understanding Interfacial Alignment in Solution Coated Conjugated Polymer Thin Films. *ACS Applied Materials & Interfaces* **2017,** *9* (33), 27863-27874.

177. Xi, Y.; Wolf, C. M.; Pozzo, L. D., Self-assembly of donor–acceptor conjugated polymers induced by miscible 'poor' solvents. *Soft Matter* **2019,** *15* (8), 1799-1812.

178. Xu, H.; Li, J.; Leung, B. H. K.; Poon, C. C. Y.; Ong, B. S.; Zhang, Y.; Zhao, N., A high-sensitivity near-infrared phototransistor based on an organic bulk heterojunction. *Nanoscale* **2013,** *5* (23), 11850-11855.

179. Zhang, G.; Lee, S.; Gutiérrez-Meza, E.; Buckley, C.; McBride, M.; Valverde-Chávez, D. A.; Kwon, Y. H.; Savikhin, V.; Xiong, H.; Dunn, T. J.; Toney, M. F.; Yuan, Z.; Silva, C.; Reichmanis, E., Robust and Stretchable Polymer Semiconducting Networks: From Film Microstructure to Macroscopic Device Performance. *Chemistry of Materials* **2019,** *31* (17), 6530-6539.

180. Zhang, G.; McBride, M.; Persson, N.; Lee, S.; Dunn, T. J.; Toney, M. F.; Yuan, Z.; Kwon, Y.-H.; Chu, P.-H.; Risteen, B.; Reichmanis, E., Versatile Interpenetrating Polymer Network Approach to Robust Stretchable Electronic Devices. *Chemistry of Materials* **2017,** *29* (18), 7645-7652.

181. DataThief. https://www.datathief.org (Accessed January 2024). www.datathief.org.

182. Zheng, Y.-Q.; Yao, Z.-F.; Lei, T.; Dou, J.-H.; Yang, C.-Y.; Zou, L.; Meng, X.; Ma, W.; Wang, J.-Y.; Pei, J., Unraveling the Solution-State Supramolecular Structures of Donor–Acceptor Polymers and their Influence on Solid-State Morphology and Charge-Transport Properties. *Advanced Materials* **2017,** *29* (42), 1701072-1701080.

183. Porter, R. S.; Johnson, J. F., The Entanglement Concept in Polymer Systems. *Chemical Reviews* **1966,** *66* (1), 1-27.

184. Lopes, L. F.; Silveira, B. M.; Moreno, R., Rheological Evaluation of HPAM fluids for EOR Applications. *International Journal of Engineering & Technology* **2014,** *14* (3), 35-41.

185. Wood, S.; Wade, J.; Shahid, M.; Collado-Fregoso, E.; Bradley, D. D. C.; Durrant, J. R.; Heeney, M.; Kim, J.-S., Natures of Optical Absorption Transitions and Excitation Energy Dependent Photostability of Diketopyrrolopyrrole (DPP)-Based Photovoltaic Copolymers. *Energy & Environmental Science* **2015,** *8* (11), 3222-3232.

186. Qarai, M. B.; Chang, X.; Spano, F. C., Vibronic Exciton Model for Low Bandgap Donor–Acceptor Polymers. *The Journal of Chemical Physics* **2020,** *153* (24), 244901-244917.

187. McRae, E. G.; Kasha, M., Enhancement of Phosphorescence Ability upon Aggregation of Dye Molecules. *The Journal of Chemical Physics* **1958,** *28* (4), 721-722.

188. Chen, H.; Guo, Y.; Yu, G.; Zhao, Y.; Zhang, J.; Gao, D.; Liu, H.; Liu, Y., Highly π-extended copolymers with diketopyrrolopyrrole moieties for high-performance field-effect transistors. *Adv Mater* **2012,** *24* (34), 4618-22.

189. Lei, T.; Dou, J.-H.; Pei, J., Influence of Alkyl Chain Branching Positions on the Hole Mobilities of Polymer Thin-Film Transistors. *Advanced Materials* **2012,** *24* (48), 6457-6461.

190. Matthews, J. R.; Niu, W.; Tandia, A.; Wallace, A. L.; Hu, J.; Lee, W.-Y.; Giri, G.; Mannsfeld, S. C. B.; Xie, Y.; Cai, S.; Fong, H. H.; Bao, Z.; He, M., Scalable Synthesis of Fused Thiophene-Diketopyrrolopyrrole Semiconducting Polymers Processed from Nonchlorinated Solvents into High Performance Thin Film Transistors. *Chemistry of Materials* **2013,** *25* (5), 782-789.

191. McCulloch, I.; Salleo, A.; Chabinyc, M., Avoid The Kinks when Measuring Mobility. *Science* **2016,** *352* (6293), 1521.

192. Hu, H.; Zhao, K.; Fernandes, N.; Boufflet, P.; Bannock, J. H.; Yu, L.; de Mello, J. C.; Stingelin, N.; Heeney, M.; Giannelis, E. P.; Amassian, A., Entanglements in Marginal Solutions: a Means of Tuning Pre-Aggregation of Conjugated Polymers with Positive Implications for Charge Transport. *Journal of Materials Chemistry C* **2015,** *3* (28), 7394-7404.

193. Zhao, K.; Khan, H. U.; Li, R.; Su, Y.; Amassian, A., Entanglement of Conjugated Polymer Chains Influences Molecular Self-Assembly and Carrier Transport. *Advanced Functional Materials* **2013,** *23* (48), 6024-6035.

194. Lei Sun, J.-n. Z., Wei-heng Huang, Wen-hua Zhang and Liang-bin Li, The Effect of Solution Solubility on the Order-Disorder Transition of Molecular Chains in Conjugated Polymer Solutions. *Acta Polymerica Sinica* **2019,** *50* (8), 834-840.

195. Boehm, B. J.; McNeill, C. R.; Huang, D. M., Competing single-chain folding and multi-chain aggregation pathways control solution-phase aggregate morphology of organic semiconducting polymers. *Nanoscale* **2022**.

196. Xu, Z.; Park, K. S.; Diao, Y., What Is the Assembly Pathway of a Conjugated Polymer From Solution to Thin Films? *Frontiers in Chemistry* **2020,** *8*.

197. Xu, Z.; Park, K. S.; Kwok, J. J.; Lin, O.; Patel, B. B.; Kafle, P.; Davies, D. W.; Chen, Q.; Diao, Y., Not All Aggregates Are Made the Same: Distinct Structures of Solution Aggregates Drastically Modulate Assembly Pathways, Morphology, and Electronic Properties of Conjugated Polymers. *Advanced Materials* **2022,** *34* (32), 2203055.

198. Li, M.; Bin, H.; Jiao, X.; Wienk, M. M.; Yan, H.; Janssen, R. A. J., Controlling the Microstructure of Conjugated Polymers in High-Mobility Monolayer Transistors via the Dissolution Temperature. *Angewandte Chemie International Edition* **2020,** *59* (2), 846-852.

199. Yao, Z.-F.; Zheng, Y.-Q.; Li, Q.-Y.; Lei, T.; Zhang, S.; Zou, L.; Liu, H.-Y.; Dou, J.-H.; Lu, Y.; Wang, J.-Y.; Gu, X.; Pei, J., Wafer-Scale Fabrication of High-Performance n-Type Polymer Monolayer Transistors Using a Multi-Level Self-Assembly Strategy. *Advanced Materials* **2019,** *31* (7), 1806747.

200. Rubinstein, M.; Colby, R., *Polymer Physics*. Oxford University Press: 2003.

201. Sperling, L. H., *Introduction to Physical Polymer Science*. 4 ed.; Wiley: 2005.

202. Zierenberg, J.; Marenz, M.; Janke, W., Dilute Semiflexible Polymers with Attraction: Collapse, Folding and Aggregation. *Polymers* **2016,** *8* (9), 333.

203. Kuei, B.; Gomez, E. D., Chain conformations and phase behavior of conjugated polymers. *Soft Matter* **2017,** *13* (1), 49-67.

204. Lopes, L.; Silveira, B. M.; Moreno, R. B. Z. L. In *Rheological Evaluation of HPAM fluids for EOR Applications*, 2014.

205. Maron, S. H.; Nakajima, N.; Krieger, I. M., Study of entanglement of polymers in solution by viscosity measurements. *Journal of Polymer Science* **1959,** *37* (131), 1-18.

206. Pierri, E.; Papanagopoulos, D.; Dondos, A., The influence of shear rate, temperature and chain conformation on the critical concentration c. *Colloid and Polymer Science* **1997,** *275* (8), 709-715.

207. Porter, R. S.; Johnson, J. F., The Entanglement Concept in Polymer Systems. *Chemical Reviews* **1966,** *66*, 1-27.

208. Wang, P.-S.; Lu, H.-H.; Liu, C.-Y.; Chen, S.-A., Gel Formation via Physical Cross-Linking in the Soluble Conjugated Polymer, Poly[2-methoxy-5-(2-ethylhexyloxy)-1,4-phenylenevinylene], in Solution by Addition of Alkanes. *Macromolecules* **2008,** *41* (17), 6500-6504.

209. Gupta, P.; Elkins, C.; Long, T. E.; Wilkes, G. L., Electrospinning of linear homopolymers of poly(methyl methacrylate): exploring relationships between fiber formation, viscosity, molecular weight and concentration in a good solvent. *Polymer* **2005,** *46* (13), 4799-4810.

210. Lopez, C. G.; Richtering, W., Viscosity of Semidilute and Concentrated Nonentangled Flexible Polyelectrolytes in Salt-Free Solution. *The Journal of Physical Chemistry B* **2019,** *123* (26), 5626-5634.

211. Shenoy, S. L.; Bates, W. D.; Frisch, H. L.; Wnek, G. E., Role of chain entanglements on fiber formation during electrospinning of polymer solutions: good solvent, non-specific polymer–polymer interaction limit. *Polymer* **2005,** *46* (10), 3372-3384.

212. Masuelli, M. A., Intrinsic Viscosity Determination of High Molecular Weight Biopolymers by Different Plot Methods. Chia Gum Case. *Journal of Polymer and Biopolymer Physics Chemistry* **2018,** *6* (1), 13-25.

213. Lamport, Z. A.; Haneef, H. F.; Anand, S.; Waldrip, M.; Jurchescu, O. D., Tutorial: Organic field-effect transistors: Materials, structure and operation. *Journal of Applied Physics* **2018,** *124* (7), 071101.

214. Chen, Z.; Lee, M. J.; Shahid Ashraf, R.; Gu, Y.; Albert-Seifried, S.; Meedom Nielsen, M.; Schroeder, B.; Anthopoulos, T. D.; Heeney, M.; McCulloch, I.; Sirringhaus, H., High-performance ambipolar diketopyrrolopyrrole-thieno[3,2-b]thiophene copolymer field-effect transistors with balanced hole and electron mobilities. *Adv Mater* **2012,** *24* (5), 647-52.

215. Li, M.; Balawi, A. H.; Leenaers, P. J.; Ning, L.; Heintges, G. H. L.; Marszalek, T.; Pisula, W.; Wienk, M. M.; Meskers, S. C. J.; Yi, Y.; Laquai, F.; Janssen, R. A. J., Impact of polymorphism on the optoelectronic properties of a low-bandgap semiconducting polymer. *Nat Commun* **2019,** *10* (1), 2867.

216. Spano, F. C., Absorption in regio-regular poly(3-hexyl)thiophene thin films: Fermi resonances, interband coupling and disorder. *Chemical Physics* **2006,** *325* (1), 22-35.

217. Qarai, M. B.; Chang, X.; Spano, F. C., Vibronic exciton model for low bandgap donor–acceptor polymers. *The Journal of Chemical Physics* **2020,** *153* (24), 244901-1:16.

218. Lin, H.-W.; Lee, W.-Y.; Chen, W.-C., Selenophene-DPP donor–acceptor conjugated polymer for high performance ambipolar field effect transistor and nonvolatile memory applications. *Journal of Materials Chemistry* **2012,** *22* (5), 2120-2128.

219. Yun, H.-J.; Kang, S.-J.; Xu, Y.; Kim, S. O.; Kim, Y.-H.; Noh, Y.-Y.; Kwon, S.-K., Dramatic Inversion of Charge Polarity in Diketopyrrolopyrrole-Based Organic Field-Effect Transistors via a Simple Nitrile Group Substitution. *Advanced Materials* **2014,** *26* (43), 7300-7307.

220. Zheng, Y.; Venkatesh, R.; Callaway, C. P.; Viersen, C.; Fagbohungbe, K. H.; Liu, A. L.; Risko, C.; Reichmanis, E.; Silva-Acuña, C., Chain Conformation and Exciton Delocalization in a Push–Pull Conjugated Polymer. *Chemistry of Materials* **2023,** *35* (23), 10258-10267.

221. Chang, M.; Choi, D.; Wang, G.; Kleinhenz, N.; Persson, N.; Park, B.; Reichmanis, E., Photoinduced Anisotropic Assembly of Conjugated Polymers in Insulating Polymer Blends. *ACS Applied Materials & Interfaces* **2015,** *7* (25), 14095-14103.

222. Choi, D.; Kim, H.; Persson, N.; Chu, P.-H.; Chang, M.; Kang, J.-H.; Graham, S.; Reichmanis, E., Elastomer–Polymer Semiconductor Blends for High-Performance Stretchable Charge Transport Networks. *Chemistry of Materials* **2016,** *28* (4), 1196-1204.

223. McBride, M.; Persson, N.; Keane, D.; Bacardi, G.; Reichmanis, E.; Grover, M. A., A Polymer Blend Approach for Creation of Effective Conjugated Polymer Charge Transport Pathways. *ACS Appl Mater Interfaces* **2018,** *10* (42), 36464-36474.

224. Nam, M.; Lee, C.; Ko, D.-H., Sequentially processed quaternary blends for high-performance indoor organic photovoltaic applications. *Chemical Engineering Journal* **2022,** *438*, 135576.

225. Root, S. E.; Savagatrup, S.; Printz, A. D.; Rodriquez, D.; Lipomi, D. J., Mechanical Properties of Organic Semiconductors for Stretchable, Highly Flexible, and Mechanically Robust Electronics. *Chemical Reviews* **2017,** *117* (9), 6467-6499.

226. Nikzad, S.; Wu, H.-C.; Kim, J.; Mahoney, C. M.; Matthews, J. R.; Niu, W.; Li, Y.; Wang, H.; Chen, W.-C.; Toney, M. F.; He, M.; Bao, Z., Inducing Molecular Aggregation of Polymer Semiconductors in a Secondary Insulating Polymer Matrix to Enhance Charge Transport. *Chemistry of Materials* **2020,** *32* (2), 897-905.

227. Qiu, L.; Lee, W. H.; Wang, X.; Kim, J. S.; Lim, J. A.; Kwak, D.; Lee, S.; Cho, K., Organic Thin-film Transistors Based on Polythiophene Nanowires Embedded in Insulating Polymer. *Advanced Materials* **2009,** *21* (13), 1349-1353.

228. Wei, P.; Shen, Z.; Qin, X.; Zhang, P.; Bu, L.; Chen, Q.; Roth, S. V.; Lu, G., Improving Charge Injection at Gold/Conjugated Polymer Contacts by Polymer Insulator-Assisted Annealing for Transistors. *Small* **2022,** *18* (9), 2105896.

229. Park, B.; Kang, H.; Ha, Y. H.; Kim, J.; Lee, J.-H.; Yu, K.; Kwon, S.; Jang, S.-Y.; Kim, S.; Jeong, S.; Hong, S.; Byun, S.; Kwon, S.-K.; Kim, Y.-H.; Lee, K., Direct Observation of Confinement Effects of Semiconducting Polymers in Polymer Blend Electronic Systems. *Advanced Science* **2021,** *8* (14), 2100332.

230. Janasz, L.; Borkowski, M.; Blom, P. W. M.; Marszalek, T.; Pisula, W., Organic Semiconductor/Insulator Blends for Elastic Field-Effect Transistors and Sensors. *Advanced Functional Materials* **2022,** *32* (7), 2105456.

231. Chua, L.-L.; Ho, P. K. H.; Sirringhaus, H.; Friend, R. H., Observation of Field-Effect Transistor Behavior at Self-Organized Interfaces. *Advanced Materials* **2004,** *16* (18), 1609-1615.

232. Kim, J.-S.; Ho, P. K. H.; Murphy, C. E.; Friend, R. H., Phase Separation in Polyfluorene-Based Conjugated Polymer Blends: Lateral and Vertical Analysis of Blend Spin-Cast Thin Films. *Macromolecules* **2004,** *37* (8), 2861-2871.

233. Nilsson, S.; Bernasik, A.; Budkowski, A.; Moons, E., Morphology and Phase Segregation of Spin-Casted Films of Polyfluorene/PCBM Blends. *Macromolecules* **2007,** *40* (23), 8291-8301.

234. Ren, F.; Ward, L.; Williams, T.; Laws, K. J.; Wolverton, C.; Hattrick-Simpers, J.; Mehta, A., Accelerated discovery of metallic glasses through iteration of machine learning and high-throughput experiments. *Science Advances* **2018,** *4* (4), eaaq1566.

235. Yin, X.; Yang, J.; Wang, H., Vertical Phase Separation Structure for High-Performance Organic Thin-Film Transistors: Mechanism, Optimization Strategy, and Large-Area Fabrication toward Flexible and Stretchable Electronics. *Advanced Functional Materials* **2022,** *32* (27), 2202071.

236. Chang, M.; Lee, J.; Chu, P. H.; Choi, D.; Park, B.; Reichmanis, E., Anisotropic assembly of conjugated polymer nanocrystallites for enhanced charge transport. *ACS Appl Mater Interfaces* **2014,** *6* (23), 21541-9.

237. Liu, A. L. Enabling Data-Driven Experimentation For High-Performance Polymer Thin Film Formulations. Georgia Institute of Technology, 2023.

238. Green, M. L.; Choi, C. L.; Hattrick-Simpers, J. R.; Joshi, A. M.; Takeuchi, I.; Barron, S. C.; Campo, E.; Chiang, T.; Empedocles, S.; Gregoire, J. M.; Kusne, A. G.; Martin, J.; Mehta, A.; Persson, K.; Trautt, Z.; Van Duren, J.; Zakutayev, A., Fulfilling the promise of the materials genome initiative with high-throughput experimental methodologies. *Applied Physics Reviews* **2017,** *4* (1).

239. Alstrup, J.; Jørgensen, M.; Medford, A. J.; Krebs, F. C., Ultra Fast and Parsimonious Materials Screening for Polymer Solar Cells Using Differentially Pumped Slot-Die Coating. *ACS Applied Materials & Interfaces* **2010,** *2* (10), 2819-2827.

240. Meredith, J. C.; Karim, A.; Amis, E. J., High-Throughput Measurement of Polymer Blend Phase Behavior. *Macromolecules* **2000,** *33* (16), 5760-5762.

241. Harillo-Baños, A.; Rodríguez-Martínez, X.; Campoy-Quiles, M., Efficient Exploration of the Composition Space in Ternary Organic Solar Cells by Combining High-Throughput Material Libraries and Hyperspectral Imaging. *Advanced Energy Materials* **2020,** *10* (1), 1902417.

242. Eyke, N. S.; Koscher, B. A.; Jensen, K. F., Toward Machine Learning-Enhanced High-Throughput Experimentation. *Trends in Chemistry* **2021,** *3* (2), 120-132.

243. Rodríguez-Martínez, X.; Pascual-San-José, E.; Campoy-Quiles, M., Accelerating organic solar cell material's discovery: high-throughput screening and big data. *Energy Environ Sci* **2021,** *14* (6), 3301-3322.

244. Tran, V. V.; Jeong, G.; Kim, K. S.; Kim, J.; Jung, H.-R.; Park, B.; Park, J.-J.; Chang, M., Facile Strategy for Modulating the Nanoporous Structure of Ultrathin π-Conjugated Polymer Films for High-Performance Gas Sensors. *ACS Sensors* **2022,** *7* (1), 175-185.

245. Cascarini de Torre, L. E.; Flores, E. S.; Bottani, E. J., Nitrogen Physisorption on Modified Silica Surfaces. *Langmuir* **2000,** *16* (4), 1896-1901.

246. Ibach, H.; Horn, K.; Dorn, R.; Lüth, H., The adsorption of oxygen on silicon (111) surfaces. I. *Surface Science* **1973,** *38* (2), 433-454.

247. Campos, A.; Riera-Galindo, S.; Puigdollers, J.; Mas-Torrent, M., Reduction of Charge Traps and Stability Enhancement in Solution-Processed Organic Field-Effect Transistors Based on a Blended n-Type Semiconductor. *ACS Applied Materials & Interfaces* **2018,** *10* (18), 15952-15961.

248. Goffri, S.; Müller, C.; Stingelin-Stutzmann, N.; Breiby, D. W.; Radano, C. P.; Andreasen, J. W.; Thompson, R.; Janssen, R. A. J.; Nielsen, M. M.; Smith, P.; Sirringhaus, H., Multicomponent semiconducting polymer systems with low crystallization-induced percolation threshold. *Nature Materials* **2006,** *5* (12), 950-956.

249. Kang, J.; Shin, N.; Jang, D. Y.; Prabhu, V. M.; Yoon, D. Y., Structure and properties of small molecule-polymer blend semiconductors for organic thin film transistors. *Journal of the American Chemical Society* **2008,** *130* (37), 12273-12275.

250. Madec, M.-B.; Crouch, D.; Llorente, G. R.; Whittle, T. J.; Geoghegan, M.; Yeates, S. G., Organic field effect transistors from ambient solution processed low molar mass semiconductor–insulator blends. *Journal of Materials Chemistry* **2008,** *18* (27), 3230-3236.

251. Ohe, T.; Kuribayashi, M.; Tsuboi, A.; Satori, K.; Itabashi, M.; Nomoto, K., Organic Thin-Film Transistors with Phase Separation of Polymer-Blend Small-Molecule Semiconductors: Dependence on Molecular Weight and Types of Polymer. *Applied Physics Express* **2009,** *2* (12), 121502.

252. Xu, J.; Wang, S.; Wang, G. N.; Zhu, C.; Luo, S.; Jin, L.; Gu, X.; Chen, S.; Feig, V. R.; To, J. W.; Rondeau-Gagné, S.; Park, J.; Schroeder, B. C.; Lu, C.; Oh, J. Y.; Wang, Y.; Kim, Y. H.; Yan, H.; Sinclair, R.; Zhou, D.; Xue, G.; Murmann, B.; Linder, C.; Cai, W.; Tok, J. B.; Chung, J. W.; Bao, Z., Highly stretchable polymer semiconductor films through the nanoconfinement effect. *Science* **2017,** *355* (6320), 59-64.

253. Zhao, K.; Ding, Z.; Xue, L.; Han, Y., Crystallization-Induced Phase Segregation Based on Double-Crystalline Blends of Poly(3-hexylthiophene) and Poly(ethylene glycol)s. *Macromolecular Rapid Communications* **2010,** *31* (6), 532-538.

254. Lamport, Z. A.; Haneef, H. F.; Anand, S.; Waldrip, M.; Jurchescu, O. D., Tutorial: Organic field-effect transistors: Materials, structure and operation. *Journal of Applied Physics* **2018,** *124* (7).

255. Sirringhaus, H., Device Physics of Solution-Processed Organic Field-Effect Transistors. *Advanced Materials* **2005,** *17* (20), 2411-2425.

256. An, T. K.; Kang, I.; Yun, H. J.; Cha, H.; Hwang, J.; Park, S.; Kim, J.; Kim, Y. J.; Chung, D. S.; Kwon, S. K.; Kim, Y. H.; Park, C. E., Solvent additive to achieve highly ordered nanostructural semicrystalline DPP copolymers: toward a high charge carrier mobility. *Adv Mater* **2013,** *25* (48), 7003-9.

257. Coveney, S., *Fundamentals of Phase Separation in Polymer Blend Thin Films*. 1 ed.; Springer Cham: 2015.

258. Snyder, H. L.; Meakin, P., Details of phase separation processes in polymer blends. *Journal of Polymer Science: Polymer Symposia* **1985,** *73* (1), 217-239.

259. Wei, P.; Li, X.; Wang, L.; Liu, N.; He, S.; Ren, Y.; Zhu, Y.; Yang, Y.; Lu, G.; Bu, L., Vertical-Resolved Composition and Aggregation Gradient of Conjugated-Polymer@Insulator-Matrix for Transistors and Memory. *Advanced Electronic Materials* **2020,** *6* (4), 1901156.

260. Gelles, R.; Frank, C. W., Effect of molecular weight on polymer blend phase separation kinetics. *Macromolecules* **1983,** *16* (9), 1448-1456.

261. Dobry, A.; Boyer-Kawenoki, F., Phase separation in polymer solution. *Journal of Polymer Science* **1947,** *2* (1), 90-100.

262. Lee, W. H.; Kwak, D.; Anthony, J. E.; Lee, H. S.; Choi, H. H.; Kim, D. H.; Lee, S. G.; Cho, K., The Influence of the Solvent Evaporation Rate on the Phase Separation and

Electrical Performances of Soluble Acene-Polymer Blend Semiconductors. *Advanced Functional Materials* **2012,** *22* (2), 267-281.

263. Tipduangta, P.; Belton, P.; McAuley, W. J.; Qi, S., The use of polymer blends to improve stability and performance of electrospun solid dispersions: The role of miscibility and phase separation. *International Journal of Pharmaceutics* **2021,** *602*, 120637.

264. Müller-Buschbaum, P.; Gutmann, J. S.; Stamm, M., Influence of Blend Composition on Phase Separation and Dewetting of Thin Polymer Blend Films. *Macromolecules* **2000,** *33* (13), 4886-4895.

265. Park, H.; Yoo, S.; Won, J. C.; Kim, Y. H., Room-temperature, printed, low-voltage, flexible organic field-effect transistors using soluble polyimide gate dielectrics. *APL Materials* **2020,** *8* (1).

266. Jaczewska, J.; Budkowski, A.; Bernasik, A.; Moons, E.; Rysz, J., Polymer vs Solvent Diagram of Film Structures Formed in Spin-Cast Poly(3-alkylthiophene) Blends. *Macromolecules* **2008,** *41* (13), 4802-4810.

267. Emerson, J. A.; Toolan, D. T. W.; Howse, J. R.; Furst, E. M.; Epps, T. H., Determination of Solvent–Polymer and Polymer–Polymer Flory–Huggins Interaction Parameters for Poly(3-hexylthiophene) via Solvent Vapor Swelling. *Macromolecules* **2013,** *46*, 6533-6540.

268. Chang, M.; Choi, D.; Fu, B.; Reichmanis, E., Solvent Based Hydrogen Bonding: Impact on Poly(3-hexylthiophene) Nanoscale Morphology and Charge Transport Characteristics. *ACS Nano* **2013,** *7* (6), 5402-5413.

269. Jaczewska, J.; Raptis, I.; Budkowski, A.; Goustouridis, D.; Raczkowska, J.; Sanopoulou, M.; Pamuła, E.; Bernasik, A.; Rysz, J., Swelling of poly(3-alkylthiophene) films exposed to solvent vapors and humidity: Evaluation of solubility parameters. *Synthetic Metals* **2007,** *157* (18), 726-732.

270. Tanaka, K.; Takahara, A.; Kajiyama, T., Film Thickness Dependence of the Surface Structure of Immiscible Polystyrene/Poly(methyl methacrylate) Blends. *Macromolecules* **1996,** *29* (9), 3232-3239.

271. Heriot, S. Y.; Jones, R. A., An interfacial instability in a transient wetting layer leads to lateral phase separation in thin spin-cast polymer-blend films. *Nat Mater* **2005,** *4* (10), 782-6.

272. Walheim, S.; Böltau, M.; Mlynek, J.; Krausch, G.; Steiner, U., Structure Formation via Polymer Demixing in Spin-Cast Films. *Macromolecules* **1997,** *30* (17), 4995-5003.

273. Chang, M.; Lee, J.; Kleinhenz, N.; Fu, B.; Reichmanis, E., Photoinduced Anisotropic Supramolecular Assembly and Enhanced Charge Transport of Poly(3-hexylthiophene) Thin Films. *Advanced Functional Materials* **2014,** *24* (28), 4457-4465.

274. Park, S. Y.; Kwon, E. H.; Park, Y. D., Effect of localized UV irradiation on the crystallinity and electrical properties of dip-coated polythiophene thin films. *RSC Advances* **2020,** *10* (56), 34130-34136.

275. Wang, G.; Persson, N.; Chu, P.-H.; Kleinhenz, N.; Fu, B.; Chang, M.; Deb, N.; Mao, Y.; Wang, H.; Grover, M. A.; Reichmanis, E., Microfluidic Crystal Engineering of π-Conjugated Polymers. *ACS Nano* **2015,** *9* (8), 8220-8230.

276. Clark, J.; Chang, J.; Spano, F. C.; Friend, R. H.; Silva, C., Determining exciton bandwidth and film microstructure in polythiophene films using linear absorption spectroscopy. *Applied Physics Letters* **2009,** *94*.

277. Xu, Y.; Liu, J.; Wang, H.; Han, Y., Hierarchical network-like structure of poly(3-hexlthiophene) (P3HT) by accelerating the disentanglement of P3HT in a P3HT/PS (polystyrene) blend. *RSC Advances* **2013,** *3* (38), 17195-17202.

278. Boehm, B. J.; McNeill, C. R.; Huang, D. M., Competing single-chain folding and multi-chain aggregation pathways control solution-phase aggregate morphology of organic semiconducting polymers. *Nanoscale* **2022,** *14* (48), 18070-18086.

279. Li, Z.; Wang, Y.; Ma, G.; Liao, Y.; Gu, X.; Xia, W., Probing conformational properties of conjugated polymers in dilute solutions under variable solvent quality via coarse-grained modeling. *Journal of Polymer Science n/a* (n/a).

280. Li, T.; Zhang, H.; Liu, B.; Ma, T.; Lin, J.; Xie, L.; Lu, D., Effect of Solvent on the Solution State of Conjugated Polymer P7DPF Including Single-Chain to Aggregated State Structure Formation, Dynamic Evolution, and Related Mechanisms. *Macromolecules* **2020,** *53* (11), 4264-4273.

281. An, T. K.; Kang, I.; Yun, H.-j.; Cha, H.; Hwang, J.; Park, S.; Kim, J.; Kim, Y. J.; Chung, D. S.; Kwon, S.-K.; Kim, Y.-H.; Park, C. E., Solvent Additive to Achieve Highly Ordered Nanostructural Semicrystalline DPP Copolymers: Toward a High Charge Carrier Mobility. *Advanced Materials* **2013,** *25* (48), 7003-7009.

282. Chen, Z.; Lee, M. J.; Shahid Ashraf, R.; Gu, Y.; Albert-Seifried, S.; Meedom Nielsen, M.; Schroeder, B.; Anthopoulos, T. D.; Heeney, M.; McCulloch, I.; Sirringhaus, H., High-Performance Ambipolar Diketopyrrolopyrrole-Thieno[3,2-b]thiophene Copolymer Field-Effect Transistors with Balanced Hole and Electron Mobilities. *Advanced Materials* **2012,** *24* (5), 647-652.

283. MaterialsMine https://materialsmine.org/nm/.

284. Jolliffe, I. T.; Cadima, J., Principal component analysis: a review and recent developments. *Philos Trans A Math Phys Eng Sci* **2016,** *374* (2065), 20150202.

285. Tharwat, A.; Gaber, T.; Ibrahim, A.; Hassanien, A. E., Linear discriminant analysis: A detailed tutorial. *AI Communications* **2017,** *30*, 169-190.

286. Lin, T.-S.; Coley, C. W.; Mochigase, H.; Beech, H. K.; Wang, W.; Wang, Z.; Woods, E.; Craig, S. L.; Johnson, J. A.; Kalow, J. A.; Jensen, K. F.; Olsen, B. D., BigSMILES: A Structurally-Based Line Notation for Describing Macromolecules. *ACS Central Science* **2019,** *5* (9), 1523-1531.

287. Kim, C.; Chandrasekaran, A.; Huan, T. D.; Das, D.; Ramprasad, R., Polymer Genome: A Data-Powered Polymer Informatics Platform for Property Predictions. *The Journal of Physical Chemistry C* **2018,** *122* (31), 17575-17585.

288. Scikit Learn. https://scikit-learn.org/stable/. (Accessed March 2024).

289. Keras. https://keras.io/ (Accessed March 2024).

290. Pytorch. https://pytorch.org/. (Accessed March 2024).

291. Hutter, F.; Kotthoff, L.; Vanschoren, J., *Automated Machine Learning - Methods, Systems, Challenges*. Springer.

292. JMP Auto Machine Learning. https://www.jmp.com/en_us/software/capabilities/predictive-modeling-and-machine-learning.html (Accessed February 2024).

293. Azure Auto Machine Learning. https://azure.microsoft.com/en-us/products/machine-learning/automatedml/. (Accessed February 2024).

294. H20 Auto Machine Learning. https://h2o.ai/platform/h2o-automl/ (Accessed February 2024).

295. Le, T. T.; Fu, W.; Moore, J. H., Scaling tree-based automated machine learning to biomedical big data with a feature set selector. *Bioinformatics* **2019,** *36* (1), 250-256.

296. Olson, R. S.; Moore, J. H., TPOT: A Tree-Based Pipeline Optimization Tool for Automating Machine Learning. In *Automated Machine Learning: Methods, Systems, Challenges*, Hutter, F.; Kotthoff, L.; Vanschoren, J., Eds. Springer International Publishing: Cham, 2019; pp 151-160.

297. Stine, R. A., Bootstrap Prediction Intervals for Regression. *Journal of the American Statistical Association* **1985,** *80* (392), 1026-1031.

298. Barredo Arrieta, A.; Díaz-Rodríguez, N.; Del Ser, J.; Bennetot, A.; Tabik, S.; Barbado, A.; Garcia, S.; Gil-Lopez, S.; Molina, D.; Benjamins, R.; Chatila, R.; Herrera, F., Explainable Artificial Intelligence (XAI): Concepts, taxonomies, opportunities and challenges toward responsible AI. *Information Fusion* **2020,** *58*, 82-115.

299. Tibshirani, R., Regression Shrinkage and Selection via the Lasso. *Journal of the royal statistical society series b-methodological* **1996,** *58*, 267-288.

300. Ouyang, R.; Curtarolo, S.; Ahmetcik, E.; Scheffler, M.; Ghiringhelli, L. M., SISSO: A compressed-sensing method for identifying the best low-dimensional descriptor in an immensity of offered candidates. *Physical Review Materials* **2018,** *2* (8), 083802.

301. Augusto, D. A.; Barbosa, H. J. C., Symbolic regression via genetic programming. *Proceedings. Vol.1. Sixth Brazilian Symposium on Neural Networks* **2000**, 173-178.

302. Lundberg, S.; Lee, S.-I. A Unified Approach to Interpreting Model Predictions 2017, p. arXiv:1705.07874. https://ui.adsabs.harvard.edu/abs/2017arXiv170507874L (accessed May 01, 2017).

303. Jablonka, K. M.; Jothiappan, G. M.; Wang, S.; Smit, B.; Yoo, B., Bias free multiobjective active learning for materials design and discovery. *Nature Communications* **2021,** *12* (1), 2312.

304. Kuenneth, C.; Rajan, A. C.; Tran, H.; Chen, L.; Kim, C.; Ramprasad, R., Polymer informatics with multi-task learning. *Patterns (N Y)* **2021,** *2* (4), 100238.

305. Tamasi, M. J.; Patel, R. A.; Borca, C. H.; Kosuri, S.; Mugnier, H.; Upadhya, R.; Murthy, N. S.; Webb, M. A.; Gormley, A. J., Machine Learning on a Robotic Platform for the Design of Polymer-Protein Hybrids. *Adv Mater* **2022,** *34* (30), e2201809.

306. Yang, J.; Tao, L.; He, J.; McCutcheon, J. R.; Li, Y. In *Discovery of Innovative Polymers for Next-Generation Gas-Separation Membranes using Interpretable Machine Learning*, 2021.

307. Settles, B., *Active Learning*. Morgan & Claypool Publishers: 2012.

308. Rasmussen, C. E., Gaussian Processes in Machine Learning. In *Advanced Lectures on Machine Learning: ML Summer Schools 2003, Canberra, Australia, February 2 - 14, 2003, Tübingen, Germany, August 4 - 16, 2003, Revised Lectures*, Bousquet, O.; von Luxburg, U.; Rätsch, G., Eds. Springer Berlin Heidelberg: Berlin, Heidelberg, 2004; pp 63-71.

309. Garnett, R., *Bayesian Optimization*. Cambridge University Press: Cambridge, 2023.

310. Choi, D.; Chu, P. H.; McBride, M.; Reichmanis, E., Best Practices for Reporting Organic Field Effect Transistor Device Performance. *Chemistry of Materials* **2015,** *27* (12), 4167-4168.

311. Borycz, J., Implementing Data Management Workflows in Research Groups Through Integrated Library Consultancy. *Data Science Journal* **2021,** *20* (1).

312. Stoudt, S.; Vásquez, V. N.; Martinez, C. C., Principles for data analysis workflows. *PLoS Comput Biol* **2021,** *17* (3), e1008770.

313. Smith, G. How sharing your data could increase your citations 2021. https://communities.springernature.com/posts/how-sharing-your-data-could-increase-your-citations#:~:text=A%20key%20study%20published%20in,available%20in%20a%20repository.

314. Brocke, J. v.; Lippe, S., Managing collaborative research projects: A synthesis of project management literature and directives for future research. *International Journal of Project Management* **2015,** *33* (5), 1022-1039.

315. Margaret H Burnette, S. C. W. H. J. I., From Plan to Action: Successful Data Management Plan Implementation in a Multidisciplinary Project. *Journal of eScience Librarianship* **2016,** *5* (1).

316. Protocols.io. https://www.protocols.io/. (Accessed February 2024).

317. Higgins, S. G.; Nogiwa-Valdez, A. A.; Stevens, M. M., Considerations for implementing electronic laboratory notebooks in an academic research environment. *Nature Protocols* **2022,** *17* (2), 179-189.

318. Christensen, M.; Yunker, L. P. E.; Adedeji, F.; Häse, F.; Roch, L. M.; Gensch, T.; dos Passos Gomes, G.; Zepel, T.; Sigman, M. S.; Aspuru-Guzik, A.; Hein, J. E., Data-science driven autonomous process optimization. *Communications Chemistry* **2021,** *4* (1), 112.

319. MacLeod, B. P.; Parlane, F. G. L.; Morrissey, T. D.; Häse, F.; Roch, L. M.; Dettelbach, K. E.; Moreira, R.; Yunker, L. P. E.; Rooney, M. B.; Deeth, J. R.; Lai, V.; Ng, G. J.; Situ, H.; Zhang, R. H.; Elliott, M. S.; Haley, T. H.; Dvorak, D. J.; Aspuru-Guzik, A.; Hein, J. E.; Berlinguette, C. P., Self-driving laboratory for accelerated discovery of thin-film materials. *Science Advances 6* (20), eaaz8867.

320. Roch, L. M.; Häse, F.; Kreisbeck, C.; Tamayo-Mendoza, T.; Yunker, L. P. E.; Hein, J. E.; Aspuru-Guzik, A., ChemOS: An orchestration software to democratize autonomous discovery. *PLoS One* **2020,** *15* (4), e0229862.

321. Seifrid, M.; Hickman, R. J.; Aguilar-Granda, A.; Lavigne, C.; Vestfrid, J.; Wu, T. C.; Gaudin, T.; Hopkins, E. J.; Aspuru-Guzik, A., Routescore: Punching the Ticket to More Efficient Materials Development. *ACS Central Science* **2022,** *8* (1), 122-131.

322. Seifrid, M.; Pollice, R.; Aguilar-Granda, A.; Morgan Chan, Z.; Hotta, K.; Ser, C. T.; Vestfrid, J.; Wu, T. C.; Aspuru-Guzik, A., Autonomous Chemical Experiments: Challenges and Perspectives on Establishing a Self-Driving Lab. *Accounts of Chemical Research* **2022,** *55* (17), 2454-2466.

323. Vriza, A.; Chan, H.; Xu, J., Self-Driving Laboratory for Polymer Electronics. *Chemistry of Materials* **2023,** *35* (8), 3046-3056.

324. Coley, C. W.; Eyke, N. S.; Jensen, K. F., Autonomous Discovery in the Chemical Sciences Part I: Progress. *Angewandte Chemie International Edition* **2020,** *59* (51), 22858-22893.

325. Stach, E.; DeCost, B.; Kusne, A. G.; Hattrick-Simpers, J.; Brown, K. A.; Reyes, K. G.; Schrier, J.; Billinge, S.; Buonassisi, T.; Foster, I.; Gomes, C. P.; Gregoire, J. M.; Mehta, A.; Montoya, J.; Olivetti, E.; Park, C.; Rotenberg, E.; Saikin, S. K.; Smullin, S.; Stanev, V.; Maruyama, B., Autonomous experimentation systems for materials development: A community perspective. *Matter* **2021,** *4* (9), 2702-2726.

326. Tabor, D. P.; Roch, L. M.; Saikin, S. K.; Kreisbeck, C.; Sheberla, D.; Montoya, J. H.; Dwaraknath, S.; Aykol, M.; Ortiz, C.; Tribukait, H.; Amador-Bedolla, C.; Brabec, C. J.; Maruyama, B.; Persson, K. A.; Aspuru-Guzik, A., Accelerating the discovery of materials for clean energy in the era of smart automation. *Nature Reviews Materials* **2018,** *3* (5), 5-20.

327. Li, J.; Ballmer, S. G.; Gillis, E. P.; Fujii, S.; Schmidt, M. J.; Palazzolo, A. M. E.; Lehmann, J. W.; Morehouse, G. F.; Burke, M. D., Synthesis of many different types of organic small molecules using one automated process. *Science* **2015,** *347* (6227), 1221-1226.

328. Pollice, R.; dos Passos Gomes, G.; Aldeghi, M.; Hickman, R. J.; Krenn, M.; Lavigne, C.; Lindner-D'Addario, M.; Nigam, A.; Ser, C. T.; Yao, Z.; Aspuru-Guzik, A., Data-Driven Strategies for Accelerated Materials Design. *Accounts of Chemical Research* **2021,** *54* (4), 849-860.

329. Epps, R. W.; Abolhasani, M., Modern nanoscience: Convergence of AI, robotics, and colloidal synthesis. *Applied Physics Reviews* **2021,** *8* (4), 041316.

330. Volk, A. A.; Epps, R. W.; Abolhasani, M., Accelerated Development of Colloidal Nanomaterials Enabled by Modular Microfluidic Reactors: Toward Autonomous Robotic Experimentation. *Advanced Materials* **2021,** *33* (4), 2004495.

331. Felbrich, B.; Schork, T.; Menges, A., Autonomous robotic additive manufacturing through distributed model-free deep reinforcement learning in computational design environments. *Construction Robotics* **2022,** *6* (1), 15-37.

332. Knox, S. T.; Parkinson, S. J.; Wilding, C. Y. P.; Bourne, R. A.; Warren, N. J., Autonomous polymer synthesis delivered by multi-objective closed-loop optimisation. *Polymer Chemistry* **2022,** *13* (11), 1576-1585.

333. Liang, J.; Xu, S.; Hu, L.; Zhao, Y.; Zhu, X., Machine-learning-assisted low dielectric constant polymer discovery. *Materials Chemistry Frontiers* **2021,** *5* (10), 3823-3829.

334. Reis, M.; Gusev, F.; Taylor, N. G.; Chung, S. H.; Verber, M. D.; Lee, Y. Z.; Isayev, O.; Leibfarth, F. A., Machine-Learning-Guided Discovery of 19F MRI Agents

Enabled by Automated Copolymer Synthesis. *Journal of the American Chemical Society* **2021,** *143* (42), 17677-17689.

335. Tamasi, M.; Kosuri, S.; DiStefano, J.; Chapman, R.; Gormley, A. J., Automation of Controlled/Living Radical Polymerization. *Advanced Intelligent Systems* **2020,** *2* (2), 1900126.

336. Xu, J., Darancet, P. T., Polybot; https://www.anl.gov/cnm/polybot (accessed February 2024).

337. Haleem, A.; Javaid, M.; Singh, R. P.; Rab, S.; Suman, R., Hyperautomation for the enhancement of automation in industries. *Sensors International* **2021,** *2*, 100124.

338. Assaad, Z.; Burken, C. B.-v., Ethics and Safety of Human-Machine Teaming. In *Proceedings of the First International Symposium on Trustworthy Autonomous Systems*, Association for Computing Machinery: <conf-loc>, <city>Edinburgh</city>, <country>United Kingdom</country>, </conf-loc>, 2023; p Article 17.

339. Duros, V.; Grizou, J.; Sharma, A.; Mehr, S. H. M.; Bubliauskas, A.; Frei, P.; Miras, H. N.; Cronin, L., Intuition-enabled machine learning beats the competition when joint human-robot teams perform inorganic chemical experiments. *Journal of chemical information and modeling* **2019,** *59* (6), 2664-2671.

340. Ososky, S.; Schuster, D.; Phillips, E.; Jentsch, F. G. In *Building appropriate trust in human-robot teams*, 2013 AAAI spring symposium series, 2013.

341. Langner, S.; Häse, F.; Perea, J. D.; Stubhan, T.; Hauch, J.; Roch, L. M.; Heumueller, T.; Aspuru-Guzik, A.; Brabec, C. J., Beyond Ternary OPV: High-Throughput Experimentation and Self-Driving Laboratories Optimize Multicomponent Systems. *Adv Mater* **2020,** *32* (14), e1907801.